

## Selective Oxidations using Nanostructured Heterogeneous Catalysts

Mielby, Jerrik Jørgen; Kegnæs, Søren; Riisager, Anders

*Publication date:*  
2014

*Document Version*  
Peer reviewed version

[Link back to DTU Orbit](#)

*Citation (APA):*

Mielby, J. J., Kegnæs, S., & Riisager, A. (2014). Selective Oxidations using Nanostructured Heterogeneous Catalysts. Technical University of Denmark, Department of Chemical Engineering.

### DTU Library

Technical Information Center of Denmark

---

#### General rights

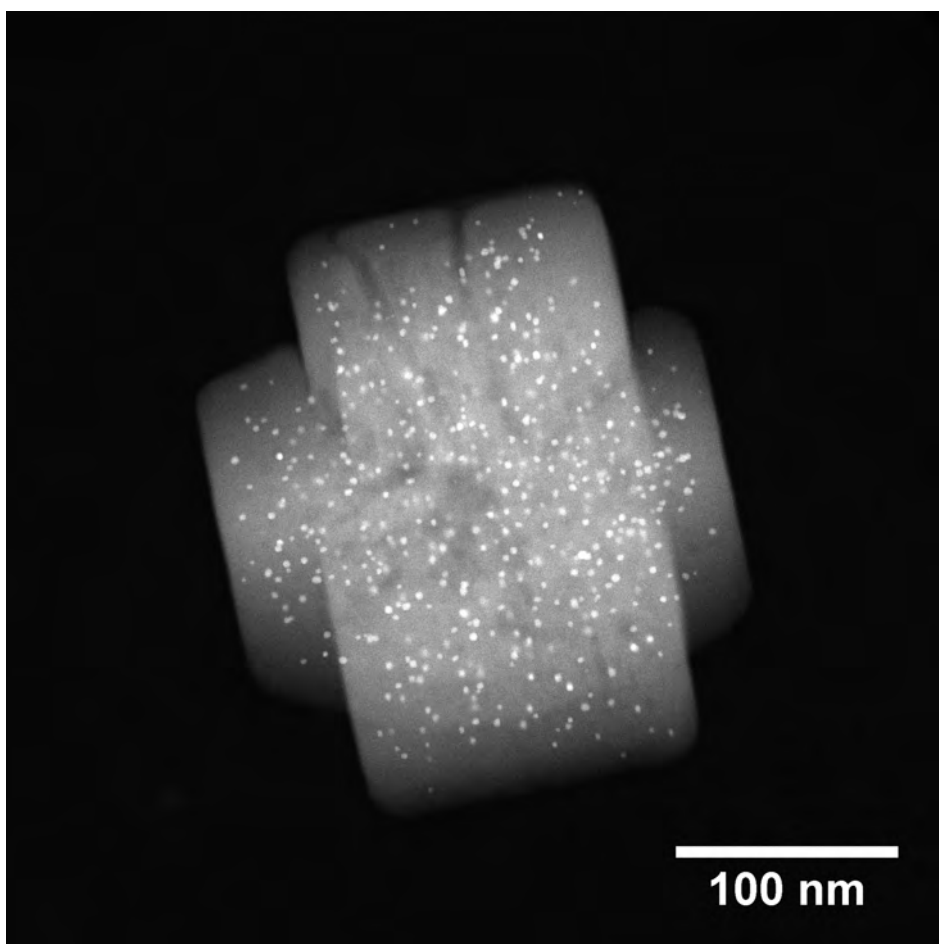
Copyright and moral rights for the publications made accessible in the public portal are retained by the authors and/or other copyright owners and it is a condition of accessing publications that users recognise and abide by the legal requirements associated with these rights.

- Users may download and print one copy of any publication from the public portal for the purpose of private study or research.
- You may not further distribute the material or use it for any profit-making activity or commercial gain
- You may freely distribute the URL identifying the publication in the public portal

If you believe that this document breaches copyright please contact us providing details, and we will remove access to the work immediately and investigate your claim.

# Selective Oxidations using Nanostructured Heterogeneous Catalysts

---



**Jerrik J. Mielby**

*Selective Oxidations using Nanostructured Heterogeneous Catalysts*

Ph.D. Thesis

Technical University of Denmark

E-mail address:

[jjmie@kemi.dtu.dk](mailto:jjmie@kemi.dtu.dk)

Jerrik J. Mielby, September 5, 2014

*Cover illustration:*

Scanning transmission electron microscopy image of  
2-3 nm gold nanoparticles encapsulated in silicalite-1.

## Preface

This thesis is submitted in candidacy for the Ph.D. degree from the Technical University of Denmark (DTU). The thesis is based on work carried out at the Centre for Catalysis and Sustainable Chemistry (CSC) at DTU Chemistry, from July 2011 to July 2014 under supervision of Associate Professor Søren Kegnæs and Associate Professor Anders Riisager. The project was funded by the Danish National Research Foundation and the Technical University of Denmark. The aim of the project was to investigate novel methods to oxidise alcohols and amines using heterogeneous catalysis and either O<sub>2</sub> or H<sub>2</sub>O<sub>2</sub> as oxidant. The main part of the experimental work has therefore been to synthesise, characterise and test heterogeneous catalysts for different oxidation reactions in liquid- and gas-phase.

First of all, I am grateful to Associate Professor Søren Kegnæs for sharing his immense knowledge in chemistry and for his friendly supervision, encouragement and never-ending support. It is a great experience and pleasure to be a part of his research group. I would also like to thank Associate Professor Anders Riisager, Associate Professor Susanne Mossin and Professor Rasmus Ferhmann for help and support during my studies and for creating an open and inspiring research atmosphere at CSC. I am grateful to Professor Dr Ferdi Schüth for letting me visit his group at Max-Planck-Institut für Kohlenforschung (KOFO) during my external stay in Germany from November 2012 to February 2013. At KOFO, I would also like to thank Dr Claudia Weidenthaler for XPS analysis and Dr Feng Wang for scientific discussions, inspiration and collaboration.

Most of the work in this project has been carried out in collaboration with other master and Ph.D. students at CSC. In particular, I would like to acknowledge and thank Raju Porreddy and Jacob Oskar Abildstrøm for their contributions to the project. Furthermore, I would like to thank Dr Takeshi Kasama for help with electron tomography and Associate Professor Peter Fristrup for help with DFT calculations. I would also like to thank Bodil Fliis Holten for keeping the labs running on a daily basis, Dr Uffe Mentzel and Dr Steffen Buus Kristensen for help with the plug-flow reactor, and all the undergraduate and fellow Ph.D. students at CSC for good company. Finally, I would like to thank Ane Falk Mouritsen for her endless patience, encouragement and support.

---

Jerrik J. Mielby  
Lyngby, September 5, 2014



## Abstract

The aim of this thesis is to investigate and develop new efficient methods to oxidise alcohols and amines using heterogeneous catalysts and either O<sub>2</sub> or H<sub>2</sub>O<sub>2</sub> as oxidants. From an economic and environmental point of view, these oxidants are ideal, because they are cheap and readily available and because they produce H<sub>2</sub>O as the only by-product.

Chapter 1 gives a short introduction to basic concepts in heterogeneous catalysis and green chemistry. Furthermore, the chapter gives an overview of the most important strategies to synthesise functional nanostructured materials and highlights how detailed understanding of size, shape and structure can help in the development of new and more efficient heterogeneous catalysts. The chapter is not intended to give a complete survey, but rather to introduce some of the recent developments in the synthesis of nanostructured heterogeneous catalysts. Finally, the chapter focuses on the use of supported metal catalysts for the selective oxidation of alcohols, which are currently dominated by the platinum group metals.

Chapter 2 deals with the most important methods to characterise heterogeneous catalysts, including X-ray powder diffraction, physisorption analysis and electron microscopy. In particular, the chapter gives an introduction to electron tomography, which makes it possible to visualise and analyse the detailed three-dimensional features of nanostructured heterogeneous catalysts.

Chapter 3 deals with the surprisingly high catalytic activity of supported gold nanoparticles with particular emphasis on the nature of the active site and the requirements needed to be considered when designing new catalytic systems. Furthermore, the chapter describes some of the most important methods to synthesise small and disperse gold nanoparticles on different supports.

Chapter 4 describes a novel method for the two-step synthesis of amides from alcohols and amines using Au/TiO<sub>2</sub> and base as catalysts. In the first step, a methyl ester is obtained by the gold-catalysed aerobic oxidation of the alcohol in methanol. Base is promoting this reaction. In the second step, the amine is added and the methyl ester undergoes base-catalysed aminolysis to give the desired amide. As the same base is used for both reactions, the synthesis could be performed in a convenient one-pot procedure. The oxidative coupling was applied to a number of different alcohols and amines to demonstrate the versatility of the reaction protocol to a broader range of substrates.

Chapter 5 describes the investigation of different silver catalysts for the synthesis of imines from alcohols and amines. The reactions were performed at relatively mild conditions (100°C and atmospheric pressure) without any additives or co-catalysts and afforded the desired imines with high selectivity (up to 99%). The highest catalytic activity was obtained with 5 wt% Ag/Al<sub>2</sub>O<sub>3</sub> in toluene with air as oxidant, although the reaction also occurred under inert atmosphere by releasing H<sub>2</sub> into the gas-phase.

Chapter 6 gives a short introduction to zeolites and the important concept of shape selectivity. Furthermore, the chapter describes the different strategies that can be used to overcome diffusion limitations.

Chapter 7 demonstrates that mesoporous titanium silicalite-1 prepared by carbon-templating is an efficient catalyst for oxidation of pyridines to pyridine *N*-oxides using aqueous H<sub>2</sub>O<sub>2</sub> as oxidant. The chapter begins with an introduction to *N*-oxides and an outline of recent development in the synthesis of ordered titanosilicates with focus on the efforts to overcome diffusion limitations.

Chapter 8 describes how the continuing technological developments in biomass processing have made bioethanol a promising platform molecule for the production of a variety of value-added chemicals. Furthermore, the chapter describes a simple and effective method to encapsulate gold nanoparticles into a MFI zeolite and demonstrate their remarkable stability, catalytic activity and selectivity for the gas-phase oxidation of bioethanol to acetaldehyde, which may become a favourable and green alternative to the ethylene route.

## Dansk Resumé

Formålet med denne afhandling er at undersøge og udvikle nye effektive metoder til at oxidere alkoholer og aminer ved hjælp af heterogen katalyse med enten  $O_2$  eller  $H_2O_2$  som oxidationsmiddel. Ud fra et økonomisk og miljømæssigt synspunkt er disse oxidationsmidler ideelle, fordi de er billige, let tilgængelige og producerer  $H_2O$  som eneste biprodukt.

Kapitel 1 giver en kort introduktion til grundlæggende begreber inden for heterogen katalyse og grøn kemi. Endvidere giver kapitlet et overblik over de vigtigste strategier ved syntetise af funktionelle nanostrukturerede materialer og omtaler, hvordan detaljeret forståelse af størrelse, form og struktur kan fremme udviklingen af nye og mere effektive heterogene katalysatorer. Kapitlet udgør ikke et komplet litteraturstudie, men er tænkt som en kort introduktion til den seneste udvikling indenfor syntese af nanostrukturerede heterogene katalysatorer. Endeligt fokuserer kapitlet på anvendelsen af metal-nanopartikler til selektiv oxidation af alkoholer, som hidtil har været domineret af platin gruppe metallerne.

Kapitel 2 omhandler nogle af de vigtigste metoder til at karakterisere heterogene katalysatorer, herunder røntgen diffraktion, fysisorption og elektronmikroskopi. Desuden giver kapitlet en introduktion til elektron-tomografi, som gør det muligt at visualisere og analysere fine tredimensionelle detaljer i heterogene nanostrukturerede katalysatorer.

Kapitel 3 beskriver den katalytiske aktivitet af guld-nanopartikler med særlig vægt på det aktive site og de betingelser, der er nødvendige for designet af nye katalytiske systemer. Endvidere beskriver kapitlet nogle af de vigtigste metoder ved syntese af små og veldistribuerede guld-nanopartikler på forskellige bærematerialer.

Kapitel 4 beskriver en ny to-trins syntese til fremstilling af amider fra alkoholer og aminer ved brug af en base og en  $Au/TiO_2$  katalysator. I det første trin, oxideres alkoholen i methanol, hvilket resulterer i dannelsen af en methylester. Basen er nødvendig for at fremme denne reaktion. I det andet trin tilsættes amin og ved basekatalyseret aminolyse omdannes methylesteren til det ønskede amid. Da basen anvendes i begge reaktioner, kan amid-syntesen foretages i én og samme glaskolbe. Denne simple metode er blevet testet på en række forskellige alkoholer og aminer. Metoden viste sig at være generel og forenelig med et bredt udvalg af substrater.

Kapitel 5 beskriver en direkte syntese af iminer ud fra alkoholer og aminer med forskellige sølv-katalysatorer. Reaktionen blev udført under relativt milde betingelser



(100°C og atmosfærisk tryk) uden additiver eller co-katalysatorer og resulterede i høj selektivitet (op til 99 %). Den højeste aktivitet blev opnået med 5 vægt% Ag/Al<sub>2</sub>O<sub>3</sub> i toluen og med luft som oxidationsmiddel, selvom reaktionen også forløb under inerte atmosfære ved fraspaltning af H<sub>2</sub>.

Kapitel 6 giver en kort introduktion til zeolitter og nogle af deres mest vigtige egenskaber såsom størrelses-selektivitet. Endvidere beskriver kapitlet de forskellige strategier, der kan anvendes til at overvinde diffusionsbegrænsninger i zeolitter.

Kapitel 7 beskriver, hvordan mesoporøs titanium silikalite-1, der er fremstillet med en kulstof-template, er en effektiv katalysator til oxidation af pyridiner med H<sub>2</sub>O<sub>2</sub> som oxidationsmiddel. Kapitlet begynder med en introduktion til *N*-oxider og en kort beskrivelse af den seneste udvikling indenfor syntese af titanium silikater med fokus på forsøget på at overvinde diffusionsbegrænsninger.

Kapitel 8 beskriver, hvordan den fortsatte teknologiske udvikling i forarbejdning af biomasse har gjort bioethanol til et lovende platform-molekyle til produktion af en lang række af mere værdifulde kemikalier. Desuden beskriver kapitlet en enkel og effektiv metode til at indkapsle guld-nanopartikler i zeolitter og demonstrerer deres bemærkelsesværdige stabilitet og katalytiske aktivitet for selektiv oxidation af bioethanol til acetaldehyde. På sigt kan dette blive et attraktivt og grønt alternativ til den nuværende fremstillingsproces, der er baseret på ethylen.

# Contents

Preface	iii
Abstract	v
Dansk Resumé	vii
<b>1. Introduction</b>	<b>1</b>
1.1. Basic concepts in heterogeneous catalysis	1
1.2. A note on green chemistry and catalysis	6
1.3. The search for new heterogeneous catalysts	7
1.4. Functional nanostructured materials in catalysis	7
1.5. Selective catalytic oxidation	16
1.5.1. Model compounds	19
1.6. Experimental section	20
1.6.1. Synthesis of silica aerogel	20
1.6.2. Synthesis of ordered mesoporous carbon	21
1.6.3. Synthesis of Pd/PPhen	21
1.6.4. Synthesis of Pd/C and Pd/PDVB	21
1.7. Summary	22
<b>2. Characterisation</b>	<b>23</b>
2.1. X-ray powder diffraction	23
2.2. Nitrogen physisorption	24
2.2.1. The BET equation	26
2.2.2. The t-plot method	27
2.2.3. The BJH method	28
2.3. Scanning electron microscopy	28
2.4. Transmission Electron Microscopy	30
2.4.1. Scanning transmission electron microscopy	32
2.5. Electron tomography	33
2.6. Experimental section	38
2.6.1. Synthesis of Ag/Al <sub>2</sub> O <sub>3</sub> hollow spheres	38
<b>3. Supported gold nanoparticles</b>	<b>39</b>
3.1. Introduction	39
3.2. The reactivity of gold	40
3.3. The support material	42
3.4. Effect of base	43
3.5. Preparation	45
3.5.1. Impregnation	45
3.5.2. Co-precipitation	45
3.5.3. Deposition-precipitation	45
3.6. Experimental section	46
3.6.1. General method for impregnation	46
3.6.2. General method for deposition-precipitation	46
3.7. Summary	47
<b>4. One-pot synthesis of amides</b>	<b>49</b>
4.1. Introduction	49
4.2. Oxidative coupling of alcohols and amines	50
4.2.1. Experimental section	50
4.2.2. Results and discussion	51
4.2.3. Hammett study	56
4.3. Summary	58

<b>5. Selective formation of imines</b>	<b>61</b>
5.1. Introduction	61
5.2. Experimental section	62
5.2.1. Catalyst preparation	62
5.2.2. Characterisation	63
5.2.3. Standard oxidation procedure	63
5.3. Results and discussion	63
5.4. Summary	71
<b>6. Zeolites</b>	<b>73</b>
6.1. Introduction	73
6.2. Zeolite catalysis	74
6.3. Zeolite synthesis	76
6.4. Diffusion in zeolites	77
6.5. Summary	81
6.6. Experimental section	81
6.6.1. Materials	81
6.6.2. Synthesis of silicalite-1	81
6.6.3. Synthesis of mesoporous silicalite-1	82
6.6.4. Synthesis of recrystallized silicalite-1	82
<b>7. Synthesis of N-oxides</b>	<b>83</b>
7.1. Introduction	83
7.1.1. Titanium Silicalite-1	84
7.2. Experimental section	84
7.2.1. Materials	84
7.2.2. Synthesis of conventional titanium silicalite-1 (TS-1)	85
7.2.3. Synthesis of carbon templated titanium silicalite-1 (cTS-1)	85
7.2.4. Synthesis of desilicated titanium silicalite-1 (dTS-1 and cdTS-1)	85
7.2.5. Characterisation	85
7.2.6. Standard oxidation procedure	86
7.3. Results and discussion	86
7.4. Summary	92
<b>8. Oxidation of bioethanol</b>	<b>93</b>
8.1. Introduction	93
8.2. Experimental section	96
8.2.1. Materials	96
8.2.2. Synthesis of Au/S1	97
8.2.3. Synthesis of Au/Meso-S1	97
8.2.4. Synthesis of Au/APS-S1	97
8.2.5. Synthesis of Au/Recryst-S1	97
8.2.6. Synthesis of Au/Al <sub>2</sub> O <sub>3</sub> , Au/ZrO <sub>2</sub> and Au/CeO <sub>2</sub> by deposition precipitation	98
8.2.7. Gas-phase oxidation of ethanol	98
8.2.8. A note on catalyst testing	100
8.3. Results and discussion	102
8.3.1. X-ray powder diffraction	102
8.3.2. Nitrogen physisorption	103
8.3.3. Transmission electron microscopy	105
8.3.4. X-ray photoelectron spectroscopy	107
8.3.5. High-angle annular dark-field scanning transmission electron microscopy and electron tomography	108
8.3.6. Catalytic activity	111
8.4. Summary	114
<b>9. Conclusion</b>	<b>117</b>
A. Publications	133
A.1-6. Article 1-6	135

# Chapter 1

## Introduction

---

This chapter gives a short introduction to basic concepts in catalysis and green chemistry. Furthermore, the chapter gives an overview of the most important strategies to synthesise functional nanostructured materials and highlights how detailed understanding of size, shape and structure can help to develop new and more efficient heterogeneous catalysts. The chapter is not intended to give a complete survey, but rather to give a short introduction to some of the recent developments in the synthesis of nanostructured heterogeneous catalysts.

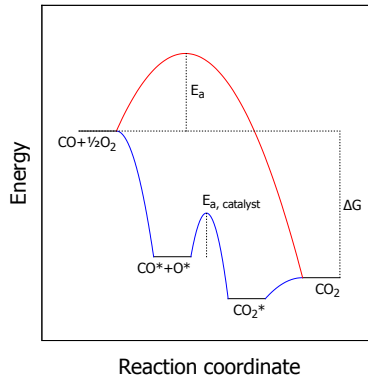
---

### 1.1. Basic concepts in heterogeneous catalysis

Catalysis is used to convert raw materials into valuable chemicals, materials and fuels in an efficient and environmentally benign manner. Catalytic processes are therefore essential to the industry and the world economy. It has been estimated that around 90 % of all chemical processes relies on catalysis and that 60 % of all chemical products are made using catalysis in some step of the manufacturing process [1]. In addition to the production of commodity chemicals, materials and fuels, catalysis is also used in energy conversion (*e.g.* for water-splitting and fuel cells), in pollution control (*e.g.* for flue-gas cleaning or water purification) and in food production (*e.g.* to make fertilisers or hydrogenate oils).

By definition, a catalyst is a substance that increases the rate of a chemical reaction without being consumed in the process. The catalyst increases the reaction rate by offering an alternative reaction pathway that requires less free energy to reach the transition state of the rate-limiting step. For example Figure 1.1 shows how the activation energy  $E_a$  for the oxidation of CO to CO<sub>2</sub> is decreased when the reaction occurs on the surface of a heterogeneous catalyst. As the catalyst does not change the Gibbs free energy  $\Delta G$ , the catalyst only changes the kinetics of the reaction and not the thermodynamics.

Catalysts are used because of their ability to enhance the rate of chemical reactions, often by many orders of magnitude. However, catalysts are also important because of

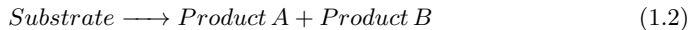


**Figure 1.1.:** The energy diagram for the oxidation of CO to CO<sub>2</sub> in gas phase and on the surface of a heterogeneous catalyst.

their selectivity, *i.e.* their ability to increase the rate of formation of one particular reaction product relative to other possible, but undesired by-products. The rate  $k$  of a chemical reaction is given by Arrhenius equation

$$k = Ae^{-E_a/RT} \quad (1.1)$$

where  $A$  is the pre-exponential factor,  $E_a$  is the activation energy,  $R$  is the gas constant and  $T$  is the temperature. Depending on the reaction condition, the selectivity of a catalytic reaction may be determined by either thermodynamic or kinetic reaction control. In the selective catalytic oxidation of hydrocarbons, for instance, the thermodynamics favour the ultimate formation of CO<sub>2</sub> and H<sub>2</sub>O. Therefore, the catalyst must strictly control the relative reaction rates that lead to the desired product and hinder those that lead to by-products. Consider for instance a reaction in which there are two possible products A and B



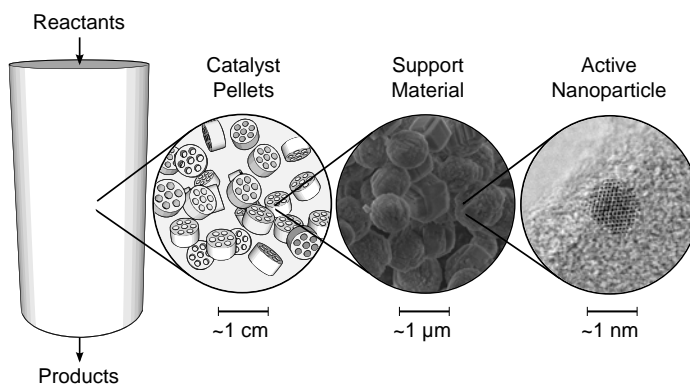
Under thermodynamic control the product distribution of product A and B is given by equation 1.3, while under kinetic control the distribution it is given by equation 1.4.

$$\ln \left( \frac{[A]}{[B]} \right) = \ln(K_{eq}) = -\frac{\Delta G^\circ}{RT} \quad (1.3)$$

$$\ln \left( \frac{[A]}{[B]} \right) = \ln \left( \frac{k_A}{k_B} \right) = -\frac{\Delta E_a}{RT} \quad (1.4)$$

Heterogeneous catalysis refers to the form of catalysis where the reactant and the catalyst are in different phases. Most often, the heterogeneous catalyst is a solid material while the reactants are in gas- or liquid-phase. Compared to homogeneous catalysis, where the catalyst and reactants are in the same phase, heterogeneous catalysts have an important advantage when it comes to separation. Heterogeneous gas phase reactions are typically performed in fixed- or fluidized bed reactors, while heterogeneous liquid phase reactions are often performed in batch reactors, where the catalyst can easily be separated from the product by sedimentation or filtration. Heterogeneous catalysts also have some disadvantages. For instance, heterogeneous catalyst can be difficult to apply for traditional organic reactions and to tune properties towards a desired reactivity is at best very complicated. Homogeneous catalysts have well-defined active sites and tuning the ligands and coordination environment with respect to the reaction mechanism is better understood. Furthermore, homogeneous catalyst does not suffer from mass and heat transfer limitations as they are dissolved in the reaction medium.

From the outside of a chemical reactor a catalytic process may seem very simple. Reactants enter the reactor and products leave it. On the inside, however, things are more complicated. The reactants must first diffuse to the catalyst and adsorb on the surface, reach an active site, react and then desorb again to make room for a new reactant. All these steps happen on the molecular or microscopic level on the surface of the catalyst. In addition to the microscopic level, physical interactions at the macroscopic level of the catalyst also effect the efficiency of the catalyst. A successful catalytic process on an industrial scale therefore involves design on many different length scales, all the way from the reactor on a macroscopic level to the active site on the atomic level [2], see Figure 1.2.



**Figure 1.2.:** *The different length scales involved in the design of a catalytic process.*

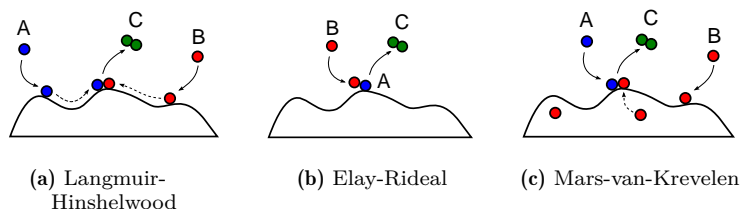
Although reactor design and catalyst forming are critical for practical industrial applications, in this thesis, the description is limited to a brief note on proper catalyst testing in Chapter 8. Instead, the thesis focuses on catalyst design on the microscopic level, *i.e.* on the composition, morphology and surface properties of the heterogeneous catalyst.

A heterogeneous catalysed reaction usually consists of a series of elementary steps. The first step in heterogeneous catalysed reaction mechanism is adsorption of at least one of the reactants on the surface of the catalyst. Depending on the strength of interaction, adsorption may be divided into physisorption caused by weak van der Waals forces and chemisorption that involves stronger interactions such as actual chemical bonds or dissociation.

For many reactions, the most important steps include dissociation of the reacting molecule and removal of the dissociated products. The rate of dissociation is determined by the activation energy  $E_a$  while the rate of the removal is determined by the surface energy of the intermediate  $\Delta E$ . It has long been known that a good catalyst has adsorbate-surface interactions of moderate strength (Sabatier's principle), *i.e.* a low activation and a weak intermediate binding energy, but only recently it has been shown that there is a linear Brønsted-Evans-Polanyi relationship between  $E_a$  and  $\Delta E$  [3]. For a number of reactions the simple relation between activation energy and binding energy leads to the well-known volcano curve [1], which is obtained when the activity of the catalyst is plotted against some parameter that determines the catalysts ability to bind the reactant, reaction intermediate or product. Information about the binding energy related to the rate-determining step from experimental or computational methods such as *e.g.* density functional theory (DFT) are therefore becoming useful guidelines in the search for new catalysts [4].

Although the detailed molecular details of a heterogeneous reaction are difficult to investigate, the general mechanism often depends on the nature of the adsorption, see Figure 1.3. A typical situation is described by the Langmuir-Hinshelwood mechanism, where two reactants adsorb to the surface of the catalyst before they meet and the reaction occurs. Another typical situation is described by the Eley-Rideal mechanism, where only one of the reactants adsorbs to the surface and the other reactant react with it directly from the gas-phase. Finally, the Mars-van-Krevelen mechanism describes a situation, where the reactant undergoes a reaction and leaves the surface with a constituent of the catalyst, *e.g.* a surface oxide species in an oxidation reaction. The catalyst is then regenerated (re-oxidised) in a subsequent step.

Although a catalyst is not consumed by the reaction itself, the activity of the catalyst may decrease over time. This deactivation is caused by one or more secondary processes, including chemical deactivation through reversible or irreversible poisoning,



**Figure 1.3.:** Three common reaction mechanisms in heterogeneous catalysis.

thermal deactivation through sintering, loss of active material through leaching or steaming and mechanical deactivation through attrition or erosion. Eventually, these processes may deactivate the catalyst to such a degree that the catalyst need reactivation or (if the damage is irreversible) replacement. Catalyst stability is therefore an important issue in all catalytic processes. The time of deactivation can range from a few hours to several years. In Fluid Catalytic Cracking (FCC) the deactivation happens so fast that the fluidised catalyst bed is constantly exchanged with regenerated catalyst as an integrated part of the process [1].

In the search for catalytic data it quickly becomes apparent that the large variety of reaction conditions and methods for rate calculation makes the comparison of different catalytic systems quite difficult. The activity of a catalyst is normally defined as the number of revolutions of the catalytic site per unit time as given by the turnover frequency (TOF) [5].

$$TOF = \frac{\text{moles of substrate converted}}{\text{moles of active sites} \times \text{time}} \quad (1.5)$$

Since the number of active sites is difficult to determine for *e.g.* supported metal catalyst, the TOF in heterogeneous catalysis is often reported on the basis of the surface or total number of metal atoms. Frequently, the TOF is replaced by the site time yield (STY), which is a related quantity defined by the number of molecules of the desired product produced per catalytic active site, number of surface or total metals atoms and per unit time. In general, chemical reaction rates should be compared with care and always be reported with detailed units and a description of the reaction conditions. Furthermore, the selectivity of a catalyst should always be compared at a similar degree of conversion.

Many of the petrochemical processes that provide the basis of our chemical infrastructure have been optimised for decades. However, with the increasing environmental concerns and continuing depletion of fossil resources, the future chemical industry must gradually rely on renewable resources such as biomass for production of bulk and fine chemicals. This development clearly requires that new efficient heterogeneous catalysts



are available. The following section gives an introduction to the important concept of green chemistry, while section 1.4 gives an overview of the most important strategies to synthesise nanostructured materials and highlights how detailed understanding of size, shape and structure can help in the development of new efficient catalysts.

## 1.2. A note on green chemistry and catalysis

Green chemistry is an important concept in chemical research and engineering that encourages development of products and processes that minimise the use and generation of harmful materials. There are several forces that drive the green chemistry initiative, including governmental legislation, societal pressure and economic benefit. Chemists are therefore constantly challenged to consider more environmentally friendly methods to produce and transform chemicals and to optimise the chemical production in terms of atom efficiency and step economy. Often, these objectives is best achieved by means of a catalyst and the field of catalysis has therefore been referred to as the 'foundational pillar of green chemistry' [6].

It is difficult to quantify just how green or environmental friendly a chemical reaction or product can claim to be. However, the atom efficiency and the  $E$ -factor at least give a rough idea. The atom efficiency is defined as the molecular mass,  $M$  of the desired product with respect to the molecular mass of all reactants. If all substrates are incorporated in the product the atom efficiency is 100%, see equation 1.6

$$\text{atom economy} = \frac{M(\text{product})}{\sum M(\text{reactants})} \quad (1.6)$$

The  $E$ -factor was introduced by Roger A. Sheldon in 1992 and is defined as the mass ratio of waste to a desired product [7]. Table 1.1 show the annual production and  $E$ -factor in different sectors of the chemical industry.

**Table 1.1.:** Typical production and  $E$ -factor in the chemical industry [8]

Products	Annual tonnage	$E$ -factor
Petrochemicals	$10^6 - 10^8$	$< 0.1$
Bulk Chemicals	$10^4 - 10^6$	$1 - 5$
Fine Chemicals	$10^2 - 10^4$	$5 - 50$
Pharmaceuticals	$10 - 10^3$	$20 - 100$

It is important to underline that there are many different kind of waste and that some are more harmful than others. This led Sheldon to introduce the Environmental Quotient ( $EQ$ ), which is obtained by multiplying the  $E$ -factor with an arbitrarily assigned unfriendliness quotient ( $Q$ ) that depends on the type of waste [9]. Although unfriendliness quotients are difficult to assign, the environmental impact of chemical processes is, in principle, possible to asses and quantify.

### 1.3. The search for new heterogeneous catalysts

As mentioned in the previous sections the development of new heterogeneous catalysts are needed to meet the increasing demands for a more sustainable chemical industry, environmental remediation, exploitation of renewable carbon resources and efficient energy transformations. Even today, however, catalysts are primarily developed by an intuitive trial-and-error approach [10]. This approach has recently been revolutionised by the introduction of parallel synthesis and high-throughput screening methods [11]. The widespread use of high-throughput methods may dramatically increase our empirical knowledge and help to optimise or even discover new catalysts. On the other hand, the implementation of high-throughput methods also presents a significant challenge, since the catalytic activity often depends on the structure of the catalyst and not only the composition. Although a *hit* definitely represent an interesting composition, it cannot be concluded that a composition that did not result in such a hit could not become a potential new catalyst [10]. The development of detailed molecular understanding, advanced synthetic methods and computational methods are therefore needed in order to obtain full benefit of the high-throughput methods. It is therefore clear that the search for new heterogeneous catalysts is a highly multi-disciplinary research field that depends on theory and experiments within chemistry, physics, nanotechnology, surface science and engineering.

### 1.4. Functional nanostructured materials in catalysis

Essentially, nanotechnology is about manipulating and making materials on the nanometre level, *i.e.* from around  $1\text{-}100\cdot 10^{-9}\text{m}$ . While this is considered as cutting-edge when it comes to consumer products, catalysis researchers have been working on this for decades. Already in the 1950s researchers were able to synthesize and characterize supported precious metal catalyst with particle sizes less than 10 nm [12]. In the following decades, researchers also started to understand how to control the molecular structure of nanostructured materials. In the 1960s, Barrer and Denny [13] prepared the first synthetic zeolites using organic structure directing agents and in the 1970s researchers at Mobil Oil Co. [14] synthesised the highly acidic zeolite ZSM-5 by increasing the Si/Al ratio. Zeolites have since revolutionised the petrochemical industry and is used to process several billion barrels of oil each year [15]. A more detailed introduction to zeolites is given in Chapter 6.

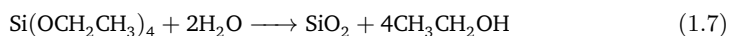
With the exception of *e.g.* zeolites, heterogeneous catalysts often consist of metal nanoparticles supported on high-surface area metal oxides. This is done to in order to increase and stabilise the dispersion of small nanoparticles and thereby expose as many active metal atoms as possible. The catalysts are often made using simple synthetic routes

such as impregnation, which often gives limited control over the size and distribution of nanoparticles. The individual nanoparticles may therefore have significantly different activity and selectivity, while the overall catalytic properties appear as an average. Only within the last 20 years, the continued developments in nanotechnology have made it possible to make detailed correlations between size and reactivity [16]. A particularly interesting example is the surprisingly high catalytic activity of supported gold nanoparticles. Supported gold nanoparticles have played a significant role in this Ph.D. project and a separate introduction to heterogeneous gold catalysis is therefore given in Chapter 3.

In addition to the size, the activity and selectivity has also been related to the shape of nanoparticles. From model reactions on single crystals it is known that different crystal facets have different activity and selectivity [17]. It is therefore likely that this effect can be exploited in practical heterogeneous catalysts. Recently, the control of nanoparticle shape has been accomplished by colloidal method using surfactants that selectively bind to crystal facets with a specific crystallographic orientation [15]. However, it is still difficult to control size and shape independently, which is required to fully separate the effect from shape and size.

The support material plays an essential role for many heterogeneous catalysts. First of all the support material provides a high surface area that facilitate the formation of small and disperse nanoparticles and keeps them separated under rough reaction conditions. Furthermore, the support material may contribute to the catalytic activity through electronic effects, through activation of the substrate or through the special chemical properties of the metal-support interfacial sites.

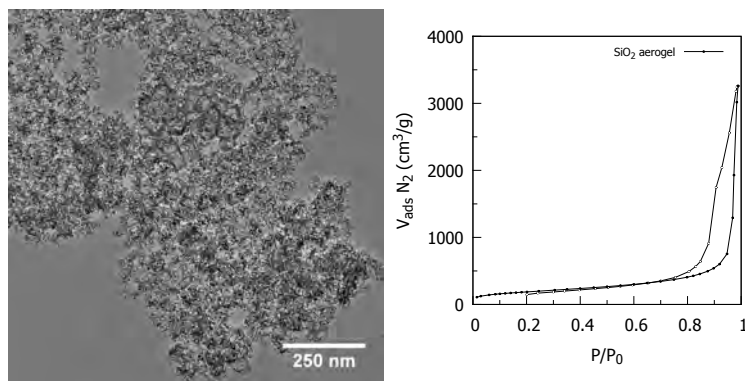
A well-known method to synthesise high surface area metal oxides is the sol-gel process. In a typical synthesis, a metal alkoxide is hydrolysed in an alkaline or acidic aqueous solution. The hydrolysis of a typical metal oxide, *i.e.* tetraethyl ortosilicate (TEOS), which is often used for sol-gel synthesis of  $\text{SiO}_2$  is shown below.



During the hydrolysis the solution gradually becomes a gel-like system containing both a liquid and a solid phase. The gel is then aged, dried and calcined. The nature of the final product can be controlled by adjusting several parameters during the synthesis, including the pH, the stoichiometry of reagents, the gelation temperature, ageing time and the solvent. Sol-gel methods are sometimes used to encapsulate metal nanoparticles and have also been used to protect supported nanoparticles against sintering. Unfortunately, this form for encapsulation may cause severe diffusion limitation and decreased activity. For instance, Zhu *et al.* [18] reported that when a sol-gel silica layer was added to a Au/TiO<sub>2</sub> catalyst, the catalyst was stable for CO oxidation up to 700°C, while the

activity was totally suppressed below 200°C.

Figure 1.4 shows an example on a high-surface area aerogel prepared by supercritical CO<sub>2</sub> drying of a silica sol-gel. By going from liquid to supercritical CO<sub>2</sub>, it is possible to remove the solvent from the sol-gel without causing stress from the liquid-solid surface tension. Under conventional drying, such surface tension may cause the structure to collapse. As a consequence, it is possible to synthesise aerogels with very high pore volumes and surface areas up to 1000 m<sup>2</sup>/g [19].



**Figure 1.4:** Transmission electron microscopy image and N<sub>2</sub> physisorption isotherm of a high surface area (680 m<sup>2</sup>/g) aerogel prepared by supercritical CO<sub>2</sub> drying.

In addition to the synthesis of high-surface area materials, much effort has also been devoted to porous materials. These materials are interesting because of their ability to interact with molecules not only at their surfaces, but also throughout the bulk of the material. According to the IUPAC definition, porous materials are microporous if the pores are <2 nm, mesoporous if the pores are 2-50 nm and macroporous if the pores are >50 nm [20]. The size, shape and volume of the pores directly relates to the properties of the porous material. For instance, zeolites can be used as molecular sieves. While small and linear molecules easily diffuses through the zeolite, more bulky molecules are selectively excluded from entering the well-defined micropore system. In addition to the pore size, the chemical composition of the pores are also important. For example, zeolites comprising pure silica are hydrophobic and can adsorb organic molecules from water, whereas zeolites comprising aluminosilicate are hydrophilic and can be used to adsorb water from organic solvent [21]. Another emerging type of microporous materials is metal organic frameworks (MOFs). One of the first MOFs (MOF-5) consists of Zn<sup>2+</sup> and 1,4-benzenedicarboxylate and has a larger pore volume than any known zeolite (>1 cm<sup>-3</sup>/g[22]). Because of their limited stability and high cost MOFs are unlikely to compete with zeolites and other porous metal-oxides for catalytic application in high-temperature processes. Nevertheless, MOFs gives perfect control over porosity, which may open up

for many interesting applications in *e.g.* gas separation and storage.

In principle there are two methods to obtain a high surface area material. The material can be divided into small particles or the material can be made porous. A simple example is to consider a sphere with the specific surface area  $A = 4\pi r^2/m$ . Since the mass of the sphere is given by  $m = \frac{4}{3}\rho\pi r^3$  the following equation is obtained

$$A = \frac{3}{\rho r} \quad (1.8)$$

where  $\rho$  is the density and  $r$  is the radius. With a density of  $3 \text{ g/cm}^3$  and a radius of  $1 \text{ cm}$  the specific area becomes  $1 \text{ cm}^2/\text{g}$ . If the radius of the spherical particle is decreased to  $1 \text{ }\mu\text{m}$ , the specific surface area  $A$  becomes  $100 \text{ m}^2/\text{g}$ , and if  $r$  is  $1 \text{ nm}$ ,  $A$  becomes  $1000 \text{ m}^2/\text{g}$  [23]. In other words, a material must comprise some nanostructured features in order to have a high surface area.

Many high surface area metal oxides have been developed by systematic optimisation of the synthetic parameters rather than by means of actual design principles. However, with the increasing demands for porous materials such principles are getting more and more important. One of the most efficient methods to control porosity is to use a template. The template can have several different functions, such as structure directing, space filling or size confining.

In synthesis of microporous zeolite the templates are often amines or quaternary ammonium salts, such as tetrapropylammonium hydroxide (TPAOH) in the synthesis of zeolite ZSM-5 or tetraethylammonium hydroxide (TEAOH) in the synthesis of zeolite BETA. In the remaining of this thesis these templates are referred to as structure directing agents (SDA) to distinguish them from other pore generating templates. The role of the SDAs are not fully understood, but they may help to 1) stabilise framework constituent to form more open structures, 2) control chemical equilibria, 3) pre-organise solution species to favour nucleation of a specific structure and 4) form porosity by acting as a space filling template [23].

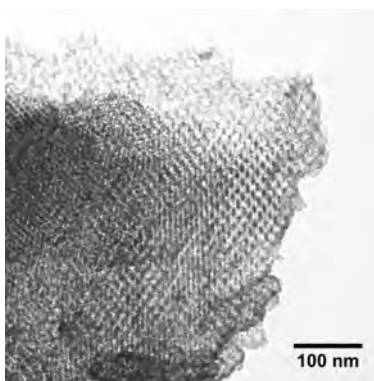
The use of structure directing agents is also important in the synthesis of ordered mesoporous materials. The first breakthrough in synthesis of ordered mesoporous materials was reported in 1992, when researchers at Mobil Oil Company disclosed their discovery of MCM-41 [24]. At that time, the most striking thing about this new material was that it possessed uniform mesopores, high surface area (up to  $1000 \text{ m}^2/\text{g}$ ) and long range order although it consisted of amorphous silica. MCM-41 was prepared using an alkyltrimethylammonium surfactant as the structure directing agent. Most likely, the formation of MCM-41 is based on a cooperative assembly process, which is caused by interactions between the positively charged surfactant micelles and the negatively charged silicate species in solution [25]. The pore diameter of MCM-41 can be changed from around 2-20 nm by changing the length of the surfactants alkyl chain. These relatively

large pores can help to overcome diffusion limitations [26], accommodate large organo-metallic complexes [27] or increase the dispersion and thermal stability of supported metal nanoparticles [28].

The cooperative interactions with the surfactant and the hydrolysis of the metal precursor are often more difficult to control for transition metal oxides than for silica. The synthesis of non-silica ordered mesoporous materials are therefore typically based on the method developed for another ordered mesoporous silica SBA-15 [23], where a non-ionic triblockcopolymer is used as structure directing agent [29; 30]. In this case, the surfactant and the inorganic solution species interact through hydrogen bonds, which make the method more versatile with respect to the metal precursor. Furthermore, non-silica ordered mesoporous materials are often synthesised using chloride metal precursors in alcoholic solvents.

Another approach to mesoporous materials is to use larger particles during the synthesis. For instance, polymer spheres can be used to synthesise mesoporous silica, while colloidal silica can be used to synthesise mesoporous carbon [31]. After the synthesis, the templates can be removed by calcination or dissolution in HF, respectively. It is important to mention that there often need to be a favourable interaction between the template and the forming solid in order to prevent phase separation. This requirement is particularly important for fine colloidal particles that have a relatively high interfacial area [23].

As an example of a three-dimensional ordered mesoporous material, Figure 1.5 show a TEM image of a mesoporous carbon prepared by carbonisation of poly(furfuryl alcohol) using 20 nm silica nanoparticles as template. After the carbonisation the silica was removed with base. The TEM image shows how the synthesised material is an almost perfect replica of the silica template. Experimental details are given in section 1.6.2.



**Figure 1.5.:** *Ordered mesoporous carbon prepared as a replica of 20 nm silica nanoparticles.*

Carbon templating has also been used for synthesis of zeolites that has an additional system of mesoporous. The method was first reported by researchers at Haldor Topsøe in 2000 [32]. In a typical synthesis, a carbon template, such as carbon black or carbon nanotubes [33], is impregnated with the zeolite precursor solution. The material is then subjected to steam assisted hydrothermal synthesis followed by calcination, which removes both the SDA and the carbon template. The carbon template results in intercrystalline mesopores, which shows that the zeolite crystallisation is not strongly affected by the presence of the template. Synthesis of mesoporous zeolites by carbon templating is an interesting alternative to post-synthesis methods, such as steaming or leaching, and has therefore been a key method to synthesise mesoporous zeolites in this project. A more detailed introduction to mesoporous zeolites is given in Chapter 6.

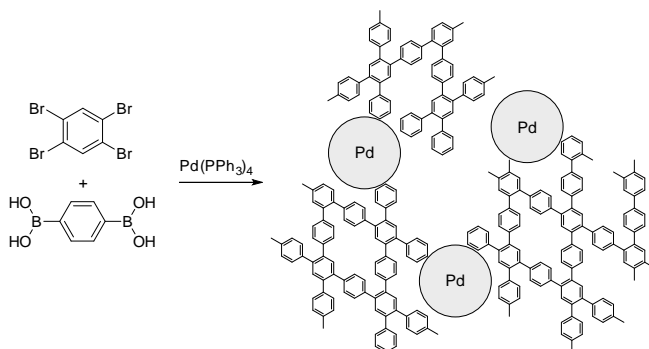
An alternative method to synthesise zeolites with a high external surface is to synthesise nano-sized zeolites by *e.g.* confined space synthesis. In this method the growth of the zeolite is limited by a carbon template during synthesis [34; 35]. For example, Fan *et al.* [36] used an ordered mesoporous carbon material as template for the confined space synthesis of silicalite-1. The mesoporous carbon was synthesised using colloidal silica nanoparticles, which resulted in a perfect carbon replica of the packed opal-like structure of the silica nanoparticles. The ordered mesoporous carbon was then used as template for the confined space synthesis of uniform silicalite-1 nanocrystals, which could be tuned from 10-40 nm by changing the size of the silica nanoparticles. This sophisticated synthesis takes advantage of three types of templating, including the structure directing agent as template for the zeolite synthesis, the space-filling silica spheres as template for the synthesis of the ordered mesoporous carbon and the ordered mesoporous carbon as template for the confined space synthesis of the nano-sized zeolites.

Another nanostructured design that has attracted much attention recently is the core-shell structure. In these materials, a transition metal nanoparticle is encapsulated by an outer layer of a porous oxide, sometimes in a yolk-shell or rattle-type configuration [37]. Typically, the materials are prepared by coating a colloidal solution of metal nanoparticles (gold has been studied most often) with a thin layer of silica using a variation of the well-known Stöber process [38], where TEOS is added to a colloidal aqueous solution of the nanoparticles in the presence of ethanol and  $\text{NH}_4\text{OH}$ . The silica encapsulated metal nanoparticles are then coated with another metal oxide in presence of a surfactant or co-block polymer template and finally the silica is removed by leaching with NaOH before the catalyst is calcined in order to remove the template. The outer shell can prevent sintering, enhance the selectivity or be functionalized to change the solubility or introduce new chemical properties. For instance, Schüth *et al.* [39] showed that Au nanoparticle encapsulated in hollow mesoporous  $\text{ZrO}_2$  spheres remained active for CO oxidation even after calcination at  $800^\circ\text{C}$ . In order to confirm the stabilising effect of the

ZrO<sub>2</sub> hollow spheres, the activity of the encapsulated Au nanoparticles was compared to a sample that was crushed under a static pressure of 1 GPa before calcination, which resulted in a significant increase in the particle sizes and, consequently, a marked decrease in catalytic activity.

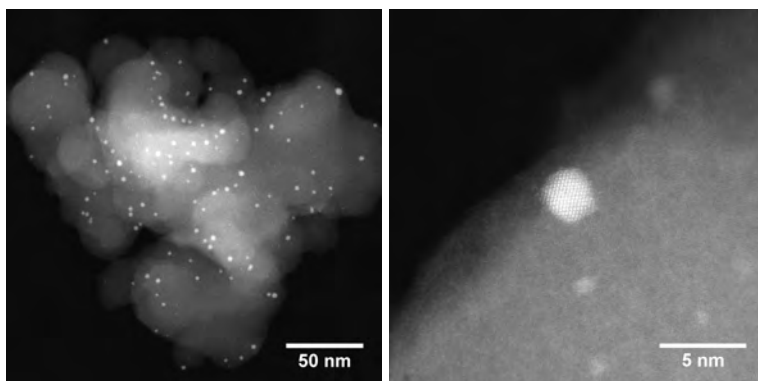
Although it is often desired to have small nanoparticles dispersed on a high and exposed surface area, the activity is not exclusively dependent on the dispersion. An important feature is also the chemical composition of the support materials and the support-metal interaction. For instance, Rolison *et al.* [40] have shown that ~6 nm Au nanoparticle dispersed in a TiO<sub>2</sub> aerogel exhibited high catalytic activity toward CO oxidation at room temperature, which matched previous results with optimally sized 3 nm Au particles on impregnated Au/TiO<sub>2</sub> catalysts [41]. Based on the detailed TEM investigations, Rolison *et al.* noted that the aerogel nanoarchitecture provided multiple Au-TiO<sub>2</sub> interfacial sites, which in contrast with the single interfacial perimeter of impregnated Au catalysts could minimise diffusion path length of relevant species and therefore be responsible for the high catalytic activity [42].

Compared to inorganic metal oxides, organic polymers are only rarely investigated as support materials, although they offer many interesting properties with respect to their tunable morphology, porosity and surface functionalization [43]. In collaboration with researchers at Max-Planck-Institute für Kohlenforschung we recently investigated a novel nanostructured material comprised of Pd nanoparticles supported on a polyphenylene polymer support (Pd/PPhen), which we found to be a surprisingly active catalyst for several challenging Suzuki coupling reactions in water [44]. The catalyst itself was synthesised by a Pd catalysed Suzuki coupling reaction between 1,2,4,5-tetrabromobenzene and benzene-1,4-diboronic acid, which resulted in the direct formation of palladium nanoparticles that were evenly distributed throughout the porous polyphenylene network, see Figure 1.6 and 1.7.



**Figure 1.6.:** Direct synthesis of Pd nanoparticles supported on polyphenylene by Pd(PPh<sub>3</sub>)<sub>4</sub> catalysed Suzuki coupling of 1,2,4,5-tetrabromobenzene and benzene-1,4-diboronic acid.






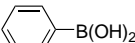

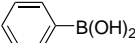
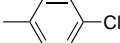
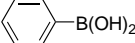
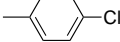
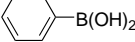
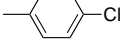
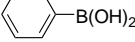
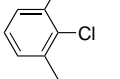
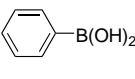
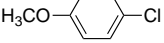
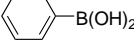
**Figure 1.7.:** Scanning transmission electron microscopy images of the prepared catalyst.

The remarkable catalytic activity of Pd/PPhen catalyst was in stark contrast to the poor results obtained with conventional catalysts such as  $\text{Pd}(\text{PPh}_3)_4$  and  $\text{Na}_2\text{PdCl}_4$  as well as Pd nanoparticles supported on carbon (Pd/C) and alternative porous polymer supports, such as polydivinylbenzene (Pd/PDVB), see Table 1.2. The cross-linked three-dimensional polyphenylene polymer had a surface area of  $1010 \text{ m}^2/\text{g}$  and a total pore volume of  $0.46 \text{ cm}^3/\text{g}$  which resulted from equal contributions of micropores ( $<1.5 \text{ nm}$ ) and supermicropore ( $1.5\text{-}2 \text{ nm}$ ). The strong support effect indicate that the high activity of Pd/PPhen may be related to its unique conjugated aromatic structure, which is not present in carbon or PDVB, and which may allow for strong  $\pi\text{-}\pi$  interactions with the substrate, similarly to the proposed effect of conjugated aromatic ligands in C-C coupling reactions catalysed by palladium complexes [45]. Although the polyphenylene support is partially hydrogenated compared to carbon, it is noteworthy that the polyphenylene support only consists of  $sp^2$  hybridised carbon atoms, which makes it highly stable and able to withstand temperatures up to  $400^\circ\text{C}$  in air and up to  $600^\circ$  in Ar.

In some reactions, the support material not only activate the substrate, but also catalyse the reaction. For instance, bifunctional catalysts comprised of noble metal nanoparticles supported on acid zeolites are widely used for reforming processes such as isomerisations and dehydrocyclisations [46], which for instance are used to increase the so-called *octane number* in gasoline. While the metal nanoparticles catalyse hydrogenation-dehydrogenation reactions, the main isomerisation takes place on the acid zeolite catalyst.

New methods have also been developed to control the composition and structure of bimetallic nanoparticles. By combination of several transition metals it may be possible to fine-tune the electronic structure in order to increase the reactivity or change the selectivity towards the desired product [47]. Furthermore, the alloying of metals

**Table 1.2.:** Suzuki coupling of different Pd catalysts, aryl chlorides and arylboronic acids.<sup>a</sup>

Entry	Chloride	Boronic acid	Catalyst	Yield (%)
1			2.7 wt% Pd/PPhen	82
2 <sup>b</sup>			Pd(PPh <sub>3</sub> ) <sub>4</sub>	n.d.
3 <sup>b</sup>			Na <sub>2</sub> PdCl <sub>4</sub>	n.d.
4			2.7 wt% Pd/C	n.d.
5			2.7 wt% Pd/PDVB	n.d.
6			2.7 wt% Pd/PPhen	55
7			2.7 wt% Pd/PPhen	20

<sup>a</sup> Reaction conditions: aryl chloride (0.5 mmol), arylboronic acid (0.75 mmol), NaOCH<sub>3</sub> (1.5 mmol), catalyst (0.8 mol% to aryl chloride), polyvinylpyrrolidone (0.5 mg, added to enhance dispersion), water (5 ml), 3 h at 80° under argon. <sup>b</sup> Tetrabutylammonium bromide (0.3 mmol, added as phase transfer catalyst).

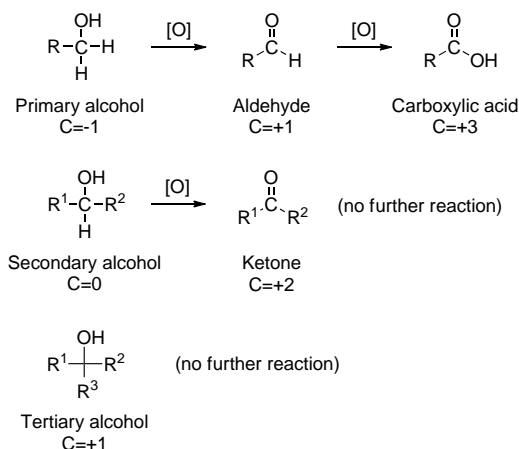
can help to prevent catalyst deactivation. For instance, Prati *et al.* have shown that bimetallic nanoparticle consisting of Pd and Au can prevent leaching of Pd from the support [48] and significantly change the catalytic activity and selectivity compared to the pure metals in the liquid phase oxidation of both aromatic and aliphatic alcohols [49]. Bimetallic nanoparticles comprised of Pd and Au are also highly active and selective catalysts for the generation of H<sub>2</sub>O<sub>2</sub>. H<sub>2</sub>O<sub>2</sub> is an important commodity chemical with extensive application in the production of bulk and fine chemicals. Up to 50% of all H<sub>2</sub>O<sub>2</sub> is used in pulp and paper industry [50], while another important application is for the manufacture of sodium percarbonate and sodium perborate which are used as mild bleaches in laundry detergents. Although H<sub>2</sub>O<sub>2</sub> can be produced in large amounts by the indirect anthraquinone process, the discovery that Au were active in the direct synthesis of H<sub>2</sub>O<sub>2</sub> from H<sub>2</sub> and O<sub>2</sub> [51] have initiated intensive research in this area and opened up for new interesting applications. For instance, Au supported on titanium silicalite-1 has shown to be a promising bifunctional catalyst for *in situ* generation of H<sub>2</sub>O<sub>2</sub> for epoxidation of propylene to propylene oxide [52], which is used in large amounts for the production of polyurethane and propylene glycol. Interestingly, the enhanced effect of using Pd-Au on conversion and selectivity not only depends on the composition and support material, but also on the structure of the individual nanoparticles. In particular, Hutching *et al.* [53] have shown that small and homogeneous Pd-Au alloy nanoparticles

are more efficient than Pd-Au alloys with a core-shell morphology consisting of a Au-rich core and a Pd-rich shell.

## 1.5. Selective catalytic oxidation

The range of different chemical products is enormous, but unfortunately the many manufacturing processes also lead to vast amounts of waste. An important chemical transformation that is used in the production of both bulk and fine chemicals is the selective oxidation of alcohols. The oxidation of alcohols over supported metal catalysts has been thoroughly investigated in the past years and many excellent books and reviews are available [54; 55].

Basically, the selective oxidation of alcohols involves the loss of hydrogen to form the corresponding carbonyl compound. While primary alcohols ( $R-CH_2-OH$ ) form aldehydes ( $R-CHO$ ) or carboxylic acids ( $R-COOH$ ) with further oxidation, secondary alcohols form ketones ( $R^1R^2=O$ ). Tertiary alcohols ( $R^1R^2R^3-OH$ ) are generally resistant to selective oxidation. Unselective oxidation may result in undesired by-products or in formation of  $CO_2$ , which is often referred to as *deep oxidation*.



**Figure 1.8.:** Selective oxidation of primary, secondary and tertiary alcohols, respectively.

Although standard organic textbook continues to recommend classical oxidation methods using stoichiometric high-valent inorganic oxidants such as permanganate or chromate reagents, it should always be stressed that these methods results in large amounts of toxic metal waste. From an economic viewpoint, this may be tolerable if the product is produced in small amounts and the added value is high, but because of the increasing environmental concerns it is getting more and more difficult to carry out industrial oxidations in such a manner [56]. The state-of-the-art in oxidation catalysis fortunately offers many, more environmentally friendly alternatives [57].

Table 1.3 shows a selection of common oxidants that can be used for the selective oxidation of alcohols. The problem with the inorganic oxidants is the relatively high cost, low active oxygen content and the large amounts of toxic waste. In contrast, molecular oxygen is readily available, inexpensive and produce water as the only by-product. From an environmental and economic point of view, molecular oxygen is therefore the ideal oxidant.

**Table 1.3.:** *A selection of terminal oxidants and their active oxygen content.*

Oxidant	Reaction/name	Active oxygen content (wt%) <sup>a</sup>	Typical waste
O <sub>2</sub>		50.0	H <sub>2</sub> O
H <sub>2</sub> O <sub>2</sub>		47.1	H <sub>2</sub> O
N <sub>2</sub> O		36.4	N <sub>2</sub> , H <sub>2</sub> O
CrO <sub>3</sub>	Jones oxidation	24.0	Cr <sub>2</sub> (SO <sub>4</sub> ) <sub>3</sub> , H <sub>2</sub> O
NaOCl	TEMPO	21.5	NaCl, H <sub>2</sub> O
C <sub>2</sub> O <sub>2</sub> Cl <sub>2</sub>	Swern oxidation	12.6	CO, CO <sub>2</sub> , Me <sub>2</sub> S, HCl, H <sub>2</sub> O
KMnO <sub>4</sub>		15.2	MnO <sub>2</sub> , KOH, H <sub>2</sub> O
KHSO <sub>5</sub>	Oxone	10.5	KHSO <sub>4</sub> , H <sub>2</sub> O

<sup>a</sup> The molar mass of active oxygen divided by the total molar mass of the oxidant.

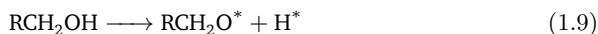
Because of their ability to adsorb and activate molecular oxygen, the platinum group metals, including Ru, Rh, Pd and Pt, are the dominating metals used for the selective oxidation of alcohols. The most investigated catalysts consists of Pt or Pd as the active metal with either Bi or Pb as promoters. Typically, the metals are supported on high surface area alumina or carbon. Beside Bi and Pb, many other promoter metals have been reported, including Cd, Co, Cu, Se, Ce, Te, Sn, Au and Ru, which all influence the activity and selectivity of the catalyst in some way or another. The other platinum group metals, including Ru and Rh, are usually used without promoters [54].

The liquid phase oxidation of alcohols with platinum-group metals is typically carried out at 25-100°C in batch reactors under O<sub>2</sub> or atmospheric air and because of the relative mild reaction conditions the range of application is therefore relatively broad. An important advantage of the supported metal catalysts is that they are active and selective in water, although conventional organic solvents are also often employed. In particular, organic solvents and high temperatures are sometimes needed for the selective synthesis of aldehydes in order to remove water and prevent hydration and subsequent dehydrogenation to the acid. When the carboxylic acid is the desired product, it is important to control the pH during reaction in order to facilitate product desorption from the active site and avoid metal leaching.

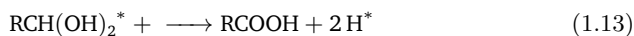
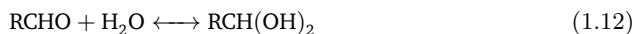
The most common reason for deactivation of platinum-group metals is over-oxidation of the active site [58]. In general, the rate of alcohol oxidation is highest on a reduced metal surface, which means that the catalyst often has to be reduced under

hydrogen before the reaction. Furthermore, the reactor should preferably be operated under conditions where the rate of oxygen supply is lower than the rate of alcohol dehydrogenation. Deactivation by the formation of strongly adsorbed by-products and CO are also frequently reported [54]. Furthermore, the supported metal catalyst may be irreversibly deactivated by *e.g.* sintering or metal leaching.

According to the classical dehydrogenation mechanism, the liquid phase oxidation of alcohols on platinum-group metals proceed via dehydrogenation followed by oxidation of the adsorbed hydrogen by adsorbed and dissociated oxygen [59].



If water is present in the reaction, the aldehyde may be hydrated to form a geminal diol, which can be dehydrogenated to form the corresponding acid.



Basically this mechanism shows that the alcohol is dehydrogenated in two elementary steps. In the first step, the alcohol O-H bond is dissociated to form an adsorbed alkoxide and an adsorbed hydrogen. The electron-withdrawing oxygen atom of the adsorbed alkoxide then weakens the  $\beta$ -C-H bond in rate-determining second dehydrogenation step. The dehydrogenation is generally favoured at high pH. Adsorbed oxygen or surface OH species is then needed to oxidise the adsorbed hydrogen, which drives the equilibrium towards the product aldehyde and frees the metal active site. The indirect role of oxygen in this model is supported by the observation that oxygen can be replaced by other hydrogen acceptors, including alkenes [60]. A possible variation of the mechanism has been proposed for some catalysts that exhibit Langmuir-Hinshelwood-type kinetics and therefore are likely to involve partial oxygen coverage on the metal surface [61]. It has also been proposed that the most important role of oxygen is to suppress catalyst deactivation by removing strongly adsorbed by-products [62].

Since the discovery of the unexpectedly high activity of supported gold nanoparticles for low-temperature CO oxidation [63], much research has also been to investigate the use of supported gold nanoparticles for liquid-phase oxidation of alcohols [64]. In general, the activity of Au strongly depends on the particle size, which can be controlled by

the preparation method and the catalyst support. A crucial and not fully understood question is why small Au nanoparticles exhibit such radically different catalytic properties from that of bulk Au. This fundamental question is discussed in more detail in Chapter 3. Compared to the platinum-group metals, the application range of supported gold nanoparticles is still not as broad. Under mild reaction conditions the liquid phase oxidation of alcohols requires a strongly alkaline solution. The need for base may represent a significant limitation, because various base-catalysed side-reactions may decrease the selectivity. On the other hand, comparative studies with Pt, Pd and Au have shown that Au was the most selective and least prone to metal leaching, over-oxidation and deactivation by strongly adsorbed by-products [65]. For this reason, supported gold nanoparticles offers many great properties as a catalyst and is now at a stage where it can contribute to the sustainable development of chemical processes, in particular selective oxidations [55].

### 1.5.1. Model compounds

One of the most studied alcohols to test for catalytic activity is benzyl alcohol. The reason why benzyl alcohol is used so often, is not because benzaldehyde or benzoic acid is particularly important products, but rather because of its high reactivity. Furthermore, the oxidation of benzyl alcohol can only result in a limited number of by-products since benzaldehyde cannot form the corresponding enol tautomer. In general, high yield of both benzyl aldehyde and benzylic acid can be obtained with both Pt, Pd, Au, Ag and mixtures thereof [66]. In particular, Enache *et al.* have reported good yields and a very high TOF of  $24 \text{ s}^{-1}$  (mmol substrate/mmol metal) at relatively mild conditions ( $100^\circ$  and 0.1 MPa  $\text{O}_2$ ) over a bimetallic Au-Pd/ $\text{TiO}_2$  catalyst. Like benzyl alcohol, cinnamyl alcohol is highly reactive and is also often investigated together with benzyl alcohol. Compared to benzyl alcohol the C=C double bond in cinnamyl alcohol can undergo side reaction such as hydrogenation or hydrogenolysis, which makes it somewhat more demanding with respect to the selectivity [66]. Another typical model compound is octanol, which is often used to investigate the catalytic activity with respect to aliphatic alcohols [66]. In general, the reactivity of octanol is much lower than *e.g.* benzyl alcohol. High rates have been obtained with bimetallic catalysts consisting of Pd-Au and Pt-Au on carbon, which resulted in TOFs of  $0.3 \text{ s}^{-1}$  and  $0.2 \text{ s}^{-1}$ , respectively, when the reaction were performed in  $\text{H}_2\text{O}$  with 4 equivalents of NaOH at  $50^\circ\text{C}$  [67]. Under the same conditions, but in absence of added base, the reaction rate decreased by an order of magnitude. The role of base was also significant for the monometallic Au catalyst, which was almost inactive in absence of base, but had some activity in the presence of 4 equivalents of NaOH. On the other hand, the addition of base to the monometallic Pd and Pt catalysts had no significant effect on the initial reaction rate. Another simple model compound is ethanol.

Zope *et al.* reported the oxidation of ethanol over supported Au and Pt catalysts [68] and found that the TOF of the Au catalyst was up to an order of magnitude higher than the Pt catalyst when 2 equivalents of NaOH was employed at 60°. Consistent with previous results, Zope *et al.* found that the Au catalysts were inactive in the presence of base, whereas the Pt catalysts remained somewhat active. Jørgensen *et al.* investigated the oxidation of aqueous ethanol over Au/TiO<sub>2</sub> and achieved up to 95% acetic acid at 150° and 3.0 MPa O<sub>2</sub> [69]. Although attempts were made to reuse the catalyst, the catalyst suffered from a significant decrease in catalytic activity, possibly caused by aggregation of the supported Au nanoparticles, which increased from 3-6 nm before the reaction to 5-7 nm after the reaction. Furthermore, Christensen *et al.* [70] compared the yields from Au/MgAl<sub>2</sub>O<sub>4</sub> (97% conversion and 86% selectivity), Pd/MgAl<sub>2</sub>O<sub>4</sub> (93% conversion and 65% selectivity) and Pt/MgAl<sub>2</sub>O<sub>4</sub> (82% conversion and 20% selectivity) and found that the highest yield was obtained with the Au catalyst at the same reaction conditions (150°C and 3.5 MPa O<sub>2</sub>).

## 1.6. Experimental section

### 1.6.1. Synthesis of silica aerogel

The silica aerogel was synthesised from the following three solutions

- A) 1.852 g NH<sub>4</sub>F, 100 ml H<sub>2</sub>O and 22.78 ml 25% NH<sub>3</sub> in H<sub>2</sub>O
- B) 4.7 g TEOS and 11 ml absolute ethanol.
- C) 7 ml H<sub>2</sub>O, 11 ml absolute ethanol and 0.370 ml of solution A.

A freshly prepared solution B was added to solution C under shaking, which resulted in formation of solid gel after ~10 min. The gel was left to age for 1 hour and then submersed in absolute ethanol to remove the water. Over the next 5 days the ethanol was replaced 5 times. The gel was then transferred to an autoclave. The autoclave was cooled to ~10°C in an ice bath and then filled with liquid CO<sub>2</sub> from a gas bottle equipped with a dip tube. A mixture of CO<sub>2</sub> and ethanol was released from the bottom of the autoclave and the autoclave was then refilled with CO<sub>2</sub>.

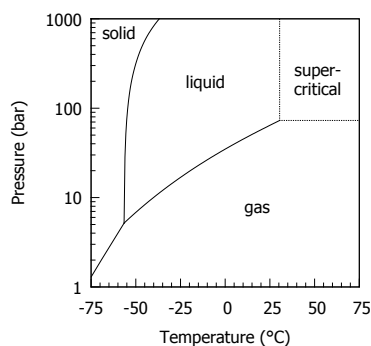


Figure 1.9.: CO<sub>2</sub> phase diagram.

This procedure was repeated several times until no ethanol could be seen in the released CO<sub>2</sub> upon sublimation. The autoclave was then heated through the critical point of CO<sub>2</sub> (31.1 °C and 72.9 bar) to ~50°C while maintaining a pressure of around 90-100 bar. The autoclave was then depressurised slowly to keep the temperature around 50°C. The dried silica aerogel was almost transparent with a characteristic blue cast from Rayleigh scattering.

### 1.6.2. Synthesis of ordered mesoporous carbon

Silica nanospheres (~20 nm in diameter) were prepared according to the following procedure. Lysine (160 mg) was dissolved in demineralised H<sub>2</sub>O(150 ml) and heated to 90°C in a 250 ml round-bottom flask with stirring around 500 rpm. TEOS (12 ml) was mixed with ethanol and added drop-wise. The round-bottom flask was then fitted with a condenser and left for stirring at 90°C for 2 days. The colloidal solution was then transferred to a Teflon lined autoclave and aged for 24 hours at 100°C. The product was then recovered by a rotary evaporator and calcined at 550°C for 12 hours. 3 g of the calcined silica nanospheres were transferred to a 50 ml centrifuge tube together with oxalic acid (20 mg) and 5 ml furfuryl alcohol. The mixture was shaken and then centrifuged so that excess furfuryl alcohol could be removed by decantation. The tube was then closed with a lid and then heated to 90° for 2 days. The resulting composite material was then cured under Ar for 2 hours at 200°C and then carbonised at 900°C for 3 hours (heating 5°C/min). The material was then transferred to a Teflon lined autoclave with 100 ml 6 M KOH and heated to 180° for 24 hours to remove the silica. The final product was washed with water (until neutral pH) and then dried at room temperature.

### 1.6.3. Synthesis of Pd/PPhen

The 2.7 wt% Pd/PPhen catalyst were prepared according to the following procedure: 1,2,4,5-tetrabromobenzene (0.765 g, 1.94 mmol) and benzene-1,4-diboronic acid (0.645 g, 3.89 mmol) were added to 60 ml dimethylformamide. The mixture was degassed through three freeze-pump-thaw cycles. K<sub>2</sub>CO<sub>3</sub> (2.0 M, 7.5 ml) and Pd(PPh<sub>3</sub>)<sub>4</sub> (0.225 g, 0.19 mmol) were added with subsequent three freeze-pump-thaw cycles. The mixture was then purged with Ar and heated to 150°C for 20 hours under stirring. The product was precipitated in water and washed with water, dichloromethane and methanol and then dried at room temperature.

### 1.6.4. Synthesis of Pd/C and Pd/PDVB

The 2.7 wt% Pd/C and Pd/PDVB was prepared according to the following procedure: Pd(PPh<sub>3</sub>)<sub>4</sub> (30 mg) was dissolved in CH<sub>2</sub>Cl<sub>2</sub> and impregnated on the C or PDVB support



(100 mg) by dropwise addition. Subsequently, the catalyst was dried and calcined under 20% H<sub>2</sub> in Ar at 250°C for 3 hours.

## **1.7. Summary**

In summary, the controlled synthesis of high-surface area and porous materials holds many promises for the development on novel heterogeneous catalysts. There are many different strategies to design and synthesise nanostructured materials and this section has only mentioned some of the many recent examples from the literature of how catalytic conversion and selectivity can be enhanced by control of the local size, shape, structure and composition of the catalyst particle. Advance in synthesis and characterisation constantly improves our understanding of the catalytic properties of nanostructured materials and help catalyst researchers to reach the ultimate goal of successfully exploit nanoscale phenomena in the development of new heterogeneous catalysts and green catalytic processes.

## Chapter 2

### Characterisation

---

This chapter gives a short introduction to some of the most important methods to characterise heterogeneous catalysts, including X-ray powder diffraction, physisorption analysis and electron microscopy. The chapter also gives an introduction to electron tomography, which makes it possible to visualise and analyse the detailed three-dimensional features of nanostructured heterogeneous catalysts.

---

#### 2.1. X-ray powder diffraction

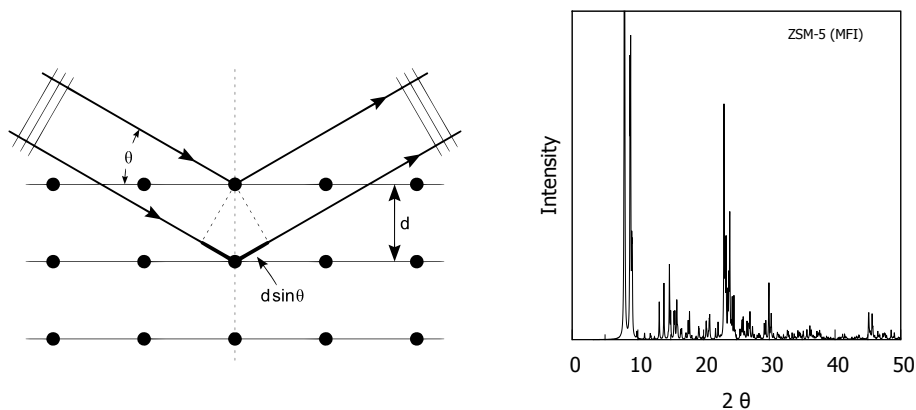
X-ray diffraction is the most important method to investigate and characterize the crystal structure of metal based catalysts. Figure 2.1 shows a schematic representation of X-ray diffraction in a sample. If the atoms of the sample are arranged in a periodic crystal lattice with a separation  $d$ , the scattered radiation will interfere constructively only in directions where the difference in path-length  $2d\sin(\theta)$  equals an integer  $n$  times the wavelength  $\lambda$ . In that case, the incident beam causes a diffraction spot at an angle of  $2\theta$  in the observed diffraction pattern. The relation is described by Bragg's law.

$$n\lambda = 2d\sin(\theta) \quad (2.1)$$

Ideally, a powder sample represents an even distribution of every possible crystalline orientation. This causes the three-dimensional reciprocal space, which is studied in single crystal X-ray diffraction, to be projected on a single dimension in X-ray powder diffraction (XRPD). In a powdered sample, the scattering therefore results in smooth diffraction rings as opposed to discrete diffraction spots. In practice, powder samples are often rotated in order to achieve more even distributions and a more uniform diffraction pattern.

Powder diffraction data is normally presented in a diffractogram, where the intensity is given as a function of  $2\theta$ . The powder diffractogram has several features such as the peak positions, their relative intensities, peak width and the background signal that all give information about the structure, size and quality of the samples. Figure 2.1 shows the XRPD pattern of a reference ZSM-5 zeolite (MFI) from the international zeolite

association [71]. In chapter 6 this characteristic diffraction pattern will be used as a fingerprint to identify the MFI structure.



**Figure 2.1.:** *Left: The geometry of Bragg diffraction. Right: X-ray powder diffraction pattern of calcined ZSM-5 zeolite. Adapted from [71].*

## 2.2. Nitrogen physisorption

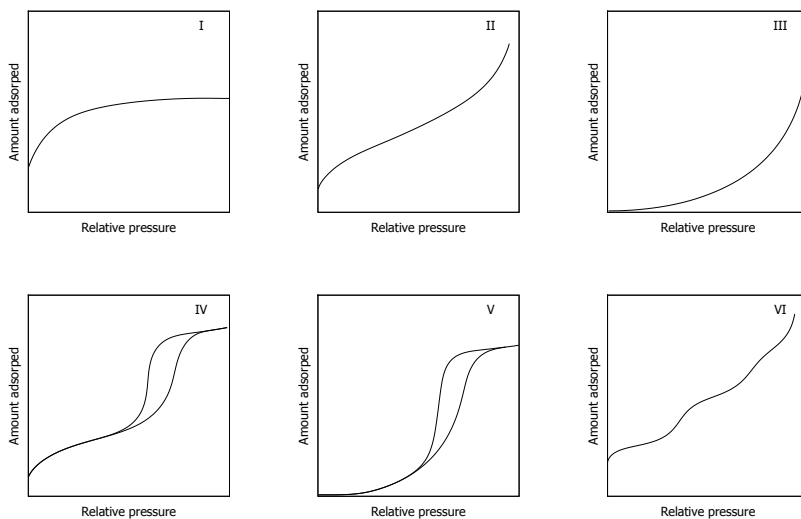
When a gas comes into contact with a solid, some of the gas molecules will stick to the surface of the solid. This phenomenon is known as physical adsorption or physisorption. Physisorption data is often presented in an adsorption isotherm that shows the amount of adsorbed gas over an interval of partial pressures at constant temperature. The amount of adsorbate is typically normalised by the mass of the adsorbent. The shape of the isotherm depends on both the adsorbate and the adsorbent, but in all cases the amount of adsorbed gasses increases with the pressure. At some point the adsorption becomes equivalent to a monolayer, eventually a multilayer and finally a condensed phase [72]. According to the IUPAC classification there are 6 types of different isotherms. The isotherms are shown in Figure 2.2 and briefly described below.

1. The type I isotherm in Figure 2.2 is sometimes called a Langmuir isotherm since the asymptotic value is related to a monolayer as described by the Langmuir equation

$$\frac{v}{v_m} = \theta = \frac{\alpha P}{1 + \alpha P} \quad (2.2)$$

where  $v$  is the volume of gas adsorped,  $v_m$  is the volume equivalent to a monolayer,  $P$  is the pressure of the gas,  $\theta$  is the fractional surface coverage and  $\alpha$  is a constant depending on the temperature. The type I isotherm is typical for microporous materials, such as zeolites or activated carbon.

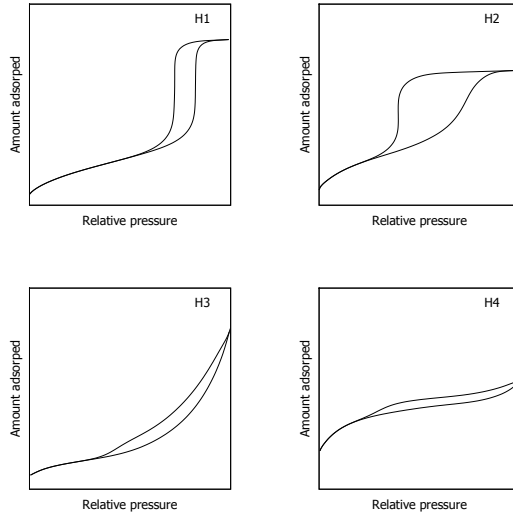
2. The type II isotherm is typical for nonporous or macroporous materials. The knee of the isotherm corresponds to the point where the adsorption is equivalent to a monolayer and multilayer adsorption begins to take place.
3. The type III isotherm is not common, but may occur for materials where the adsorbate-adsorbent interactions are relatively weak.
4. The type IV isotherm is similar to a type II (or type I) isotherm at low values of  $P/P_0$ , but exhibits a hysteresis loop over a range of high  $P/P_0$ . The hysteresis loop is associated with capillary condensation in mesoporous materials. Type IV isotherms are often encountered in heterogeneous catalysis.
5. The type V isotherm is not common, but may occur for certain porous materials with weak adsorbent-adsorbate interactions.
6. The type VI isotherm shows a step-wise multilayer adsorption on a non-porous material. Type VI isotherms are typically obtained from Ar physisorption on graphite.



**Figure 2.2.:** *The different types of isotherms according to the IUPAC classification. Adapted from [73].*

As mentioned above, the hysteresis loop observed in type IV isotherms is typically caused by capillary condensation in mesoporous materials. Hysteresis loops are normally divided into four different shapes, see Figure 2.3. While H1 loops is typically associated with porous materials that has a narrow pore size distribution, H2 loops are typical

for amorphous inorganic gels with a broader distribution of mesopores. H3 loops are typically observed in aggregates of plate-like particles with slit-shaped pores and H4 pores are typically observed in materials with narrow slit-like pores [73] and (in the case of type I isotherms) complex materials that comprise both micro- and mesopores [1].



**Figure 2.3.:** *The different types of hysteresis loops according to the IUPAC classification. Adapted from [73].*

A typical feature of many H2, H3 and H4 hysteresis loops is a steep region of the desorption branch. Furthermore, the closure point is often determined largely by the adsorbate rather than the porosity of the adsorbent (e.g.  $P/P_0=0.42$  for nitrogen at 77 K). Calculations based on the desorption branch alone may therefore lead to an artificial narrow peak in the pore size distribution [1].

### 2.2.1. The BET equation

There are several methods to analyse and quantify the physisorption data. Often, the surface area of the material is calculated by the Brunauer-Emmett-Teller (BET) method [74]. This BET method is an extension of the Langmuir equation for monolayer adsorption to multilayer adsorption and is based on the following assumptions: 1) the gas molecules adsorb in infinite layers, 2) there are no interaction between each layer and 3) the Langmuir equation can be applied to each layer. The resulting BET equation is given by

$$\frac{1}{v((P/P_0) - 1)} = \frac{c - 1}{v_m c} (P/P_0) + \frac{1}{v_m c} \quad (2.3)$$

where  $P$  and  $P_0$  is the equilibrium and saturated pressure, respectively,  $v$  is the volume of adsorbed gas at standard temperature and pressure,  $v_m$  is the volume equivalent to an adsorbed monolayer and  $c$  is the BET constant given by

$$c = \frac{H_1 - H_L}{RT} \quad (2.4)$$

where  $H_1$  is the heat of adsorption of the first layer and  $H_L$  is the heat of the second and higher layers and is equal to the heat of liquefaction. When  $1/v(P/P_0 - 1)$  is plotted against  $P/P_0$  in the range from around 0.05 to 0.30 [73] the plot should give a straight line with a slope equal to  $a = (c - 1)/v_m c$  and an intercept equal to  $b = 1/v_m c$ . The BET surface area can then be calculated by

$$v_m = \frac{1}{a + b} \quad (2.5)$$

$$S_{BET} = \frac{v_m N s}{m V_m}$$

where  $N$  is Avogadro's number,  $s$  is the cross section of the adsorbing molecule (0.162 nm<sup>2</sup> for N<sub>2</sub>),  $m$  is the mass of the adsorbent and  $V_m$  is the molar volume of the adsorbate.

Since several different parts of the BET plot may be reasonably linear (especially for microporous materials), it is sometimes useful to choose the best range of relative pressure according to the following selection criteria proposed by Rouquerol [75] *et al.*

1. The BET plot must have a positive intersect  $b$ , *i.e.* the BET constant  $c$  cannot be negative.
2. The term  $v_m(P_0 - P)$  must increase as function of  $P/P_0$ .

If these criteria are not fulfilled, the relative pressure range used for the BET calculation should be narrowed. It is important to underline that for microporous materials, such as zeolites, the physisorption is largely determined by the micropore volume rather than the surface area. The BET surface area of *e.g.* zeolites should therefore be interpret with care and not be confused with an actual (physical meaningful) surface area [73; 75].

### 2.2.2. The t-plot method

Another important method to analyse nitrogen physisorption data is the  $t$ -plot method, which was introduced by Lippens and de Boer [76]. In this method the multi-layer formation is modelled by a statistical thickness  $t$  as function of  $P/P_0$ , which is usually given by the Harkins-Jura equation

$$t = \left( \frac{13.99}{0.034 - \log(P/P_0)} \right)^{1/2} \quad (2.6)$$

It is then assumed that there is a region of the isotherm, where the micropores are saturated and the adsorption in the mesopores occurs according to the following linear equation.

$$v = S_{ext}t + v_{\mu} \quad (2.7)$$

where the intersection point  $v_{\mu}$  is the micropore volume and the slope  $S_{ext}$  is the external surface area. Normally, the thickness  $t$  is plotted from  $P/P_0=0.2$  to  $0.5$  and subsequently adjusted to find the best linear plot.

### 2.2.3. The BJH method

The pore size distribution can be estimated by the Barrett-Joyner-Halenda (BJH) method [77], which is based on a modified version of the Kelvin equation given by

$$r_k = -\frac{2\gamma v_l}{RT} \ln\left(\frac{P}{P_0}\right) \quad (2.8)$$

where  $r_k$  is the Kelvin radius,  $\gamma$  is the surface tension and  $v_l$  is the molar volume of the liquid adsorbate. The BJH method is based on the assumption that the pores are cylindrical and that the pore radius is equal to the sum of the Kelvin radius and the thickness of the film adsorbed on the pore wall. A relative pressure range of around 0.4-0.98 of the desorption branch is often used as initial data for BJH calculations, although the use of the adsorption branch is also possible.

The BJH method is generally valid for medium to large mesopores, but may underestimate the pore size of smaller mesopores. Therefore, the BJH method is sometimes replaced by non-local density functional theory (NLDFT) methods [78].

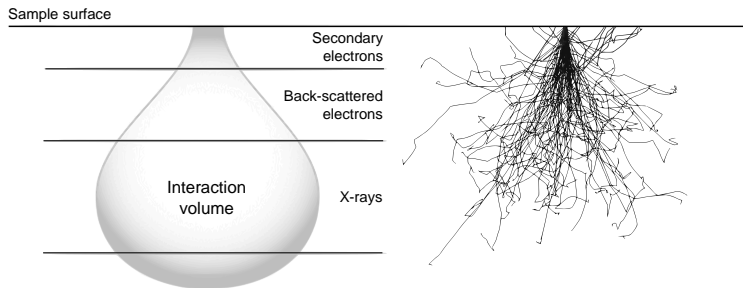
## 2.3. Scanning electron microscopy

Scanning electron microscopy (SEM) is based on the scattering of high-energy electrons by the atoms of a material. In the SEM microscope the electron beam is emitted from an electron source and accelerated to 1-30 keV. The electron source is normally a tungsten filament or a field emission gun (FEG). The electron beam is focused by one or two condenser lenses to a spot size of around 1-5 nm and then passed through a pair of scanning coils that deflect the beam in the  $x$  or  $y$  direction to analyse the surface in a raster scan.

When the electrons interact with the sample, the electron loses energy by a variety of mechanisms. The interactions can be elastic, which results in emission of high-energy backscattered electrons, or inelastic, which mostly result in heat. A small part of the energy that is lost by inelastic scattering may also escape as X-rays, light or low-energy

secondary electrons [79]. Normally, the back-scattered or secondary electrons are used for imaging, while the X-rays are used for chemical analysis. The region of the specimen that is penetrated by electrons is called the interaction volume. Even though radiation is generated within the entire interaction volume, the radiation will only be detected if it leaves the sample. The secondary electrons have less energy than the backscattered electrons, but originate from a region that is only a little larger than the incident beam and therefore gives a good resolution. The X-rays are not easily absorbed, and the detected X-rays will therefore originate from almost the entire interaction volume.

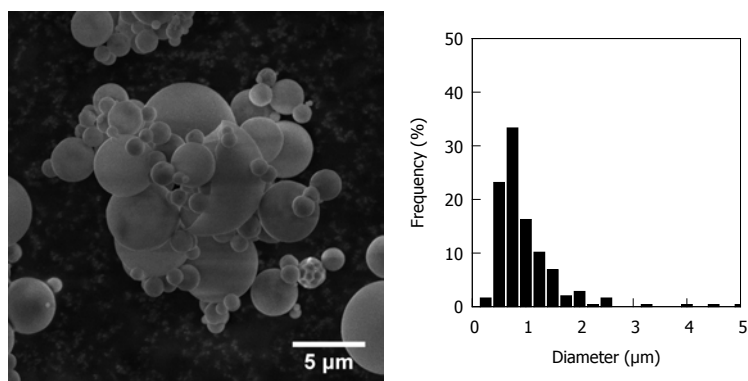
Figure 2.4 shows a schematic representation of the pear-shaped interaction volume together with a Monte Carlo simulation of the scattering of a 100 high-energy electrons in  $\text{SiO}_2$  (calculated in CASINO V2.42 [80]). The simulation illustrates that only a small fraction of the scattered electron will leave sample in the form of secondary or backscattered electrons. In general, the size of the interaction volume depends on the beam energy, the atomic number and the sample density.



**Figure 2.4.:** Schematic representation of the electron interaction volume (left) and a Monte Carlo simulation of the scattering of 100 high-energy electrons in  $\text{SiO}_2$  (right).

As example, Figure 2.5 show two SEM images of a nanostructured material comprised of Ag nanoparticles encapsulated in hollow spheres of  $\text{Al}_2\text{O}_3$  prepared by ultrasonic spray pyrolysis (for experimental details see section 2.6). The silver nanoparticles are smaller than the resolution of the SEM and cannot be seen. On the other hand, the SEM gives a good indication of the size and shape of the  $\text{Al}_2\text{O}_3$  particles.





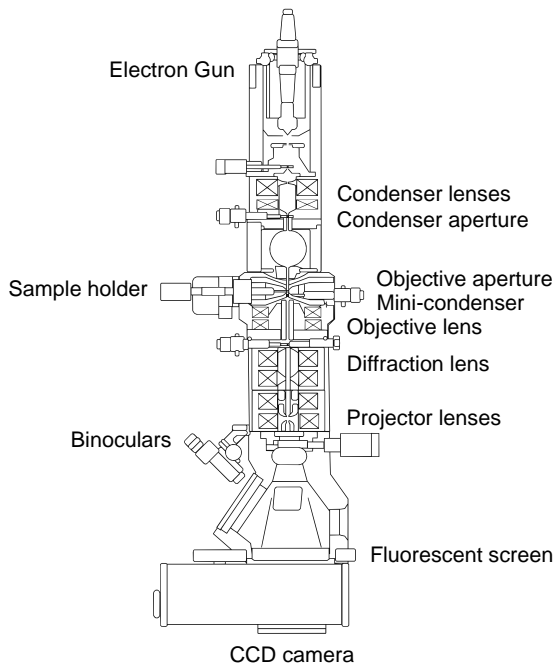
**Figure 2.5.:** SEM images of silver nanoparticles encapsulated in hollow  $\text{Al}_2\text{O}_3$  shells prepared by ultrasonic spray pyrolysis. Experimental details are given in section 2.6.

## 2.4. Transmission Electron Microscopy

One of the most important methods to investigate and characterise nanostructured heterogeneous catalysts is by transmission electron microscopy (TEM). In TEM, the electron beam is transmitted through the sample, which gives a two-dimensional image that is magnified and projected on a fluorescent phosphor screen or recorded using a charge-coupled device (CCD) camera. A fraction of the incident electrons will interact with the sample and give rise to a broad variety of scattered signals, including backscattered electrons, secondary electrons, elastic scattered electrons, inelastic scattered electrons, Auger electrons and X-rays [79]. In principle, all these signals can be detected and used to get information about the sample. In addition to the high resolution, which gives information about the size and shape of the sample, TEM analysis may therefore also be used to investigate the local crystal structure or chemical composition of a sample.

Figure 2.6 shows a schematic representation of a transmission electron microscope. The electron beam is emitted from the electron gun, which is connected to a high voltage source (typically at 100-300 kV). The beam is then passed through the electromagnetic condenser lenses and the condenser aperture, which controls the beam diameter and intensity. Generally, a large aperture gives high beam intensity and a less coherent beam, while a small aperture gives a low intensity and a more coherent beam. The electron beam is passed on through the mini-condenser and then through the two objective lenses, which are located on each side of the sample. An objective aperture is located in the back focal plane of the objective lens. The objective lenses control the focus while the objective aperture increases the contrast. Finally, the beam passes through the diffraction lens, which controls the focus in diffraction mode and a series of projective lenses that controls the magnification. In addition to the lenses and apertures a series of stigmators and deflection coils are mounted throughout the microscope. The stigmators

correct the electromagnetic lenses for inhomogenities and imperfections which may cause rotational asymmetry (astigmatism). The deflection coils are used to align the beam and magnification system. The entire microscope is normally operated under high vacuum.



**Figure 2.6.:** Schematic representation of a transmission electron microscope.

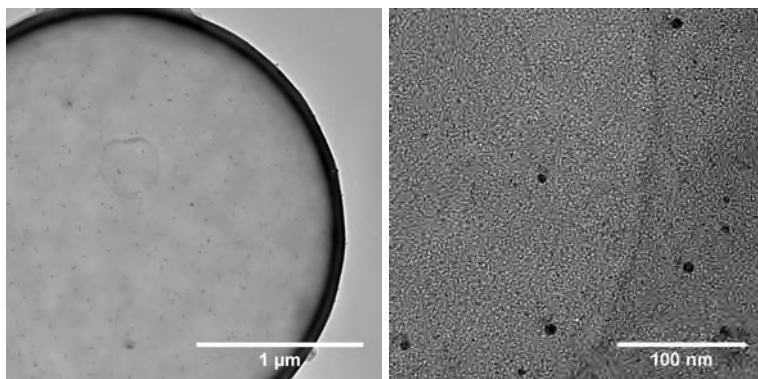
The generation of the TEM image depends on the mode of operation. The most common mode is the bright field imaging mode, where three types of contrast contribute to form the image. The most important type of contrast is the mass-thickness contrast, which is caused by elastic and inelastic scattering within the sample. Areas of the sample that are thicker or have higher density will scatter more strongly and appear dark in the bright field TEM image. Smaller apertures and low accelerating voltage normally increase the relative contrast, but decrease the intensity.

If the sample is crystalline, electron diffraction may contribute to the contrast in the TEM image. By inserting the objective aperture in the back focal plane, the diffracted electrons can be selected or excluded. If only the scattered electrons are selected and the beam of unscattered electrons is excluded, the areas with no sample will appear dark. This operation mode is therefore known as a dark-field imaging [79].

In high resolution transmission electron microscopy (HRTEM) the image formation relies on phase contrast [79], which is based on small differences in the phase, which is caused by electron wave interference. The transformation of the phase differences into

contrast and interpretation of the final image by phase contrast transfer functions can (at present) give a point resolution of around  $0.5 \text{ \AA}$ , which allow single atoms to be seen.

Figure 2.7 show two bright field TEM images of the same sample that was shown in Figure 2.5. In comparison to the SEM images 2.3, the TEM images indicate that the  $\text{Al}_2\text{O}_3$  spheres are hollow and contain small and disperse Ag nanoparticles.



**Figure 2.7.:** TEM images of Ag nanoparticles in hollow spheres of  $\text{Al}_2\text{O}_3$ .

#### 2.4.1. Scanning transmission electron microscopy

Scanning transmission electron microscopy (STEM) is a variation of TEM, where the electron beam is focused to a very small spot size. In a typical lens configuration the beam is focused using the mini-condenser. When the mini-condenser is switched 'optically on' the electron beam is in micro-probe mode and when the mini-condenser is 'optically off' the electron beam is in nano-probe mode.

The focused electron beam is then scanned across the sample (similar to SEM) while some signal is collected. The detected signals can for instance be X-rays, which can be used for high resolution elemental mapping, or high angle scattered electrons, which are highly sensitive to the atomic number (high Z-contrast). This latter method is also known as high-angle annular dark-field imaging or HAADF-STEM. Because the unscattered electrons are excluded and only the high angle scattered electrons are detected, sample areas of low density appear dark while areas with high density appear bright (opposite to BF-TEM).

Figure 2.8 show two HAADF-STEM images of the same sample that was shown in Figure 2.5 and 2.7. The HAADF-STEM images clearly show the distribution of Ag nanoparticles as bright white spots. Furthermore, the STEM images clearly show that the  $\text{Al}_2\text{O}_3$  spheres are hollow.

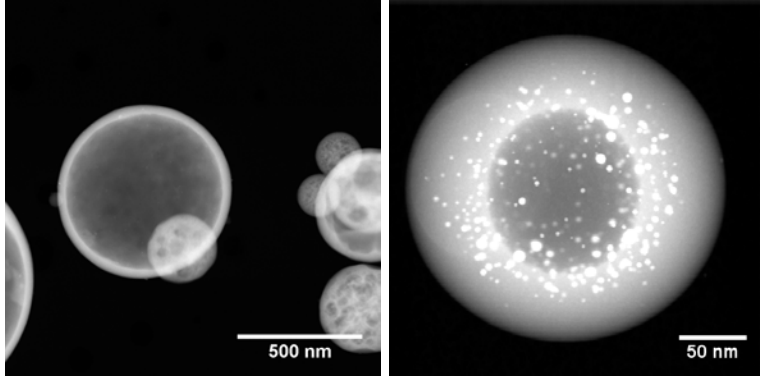


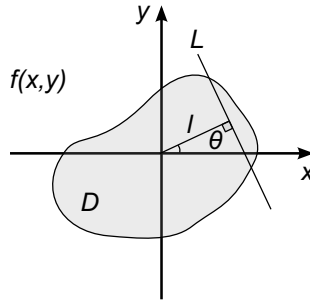
Figure 2.8.: STEM images of Ag nanoparticles in hollow spheres of  $Al_2O_3$ .

## 2.5. Electron tomography

Although the high resolution of TEM gives many detailed informations, it is important to remember that a TEM image is a projection of a 3D object on a 2D image. The projection may complicate accurate measurements of size and shape or cover up fine features, such as defects or small nanoparticles. Consider for instance a supported nanoparticle catalyst prepared by co-precipitation. While conventional TEM makes it possible to get accurate measurements of the size of the nanoparticles, information about their spatial distribution in or on the support is lost by the projection. To get this information the nanostructured catalyst must be visualised and analysed in 3D. In electron tomography, 3D information is obtained by digital reconstruction of a series of TEM images that is acquired by tilting the sample at incremental degrees of rotation while simultaneously correcting for image shift and focus changes. Typically, the tilt-series consist of around 50-150 TEM images. The mathematical basis for the tomographic reconstruction is the so-called Radon transform, which describes the mapping of an object  $D$  by a projection of line integrals through  $f$  along all possible lines  $L$  with unit length  $ds$

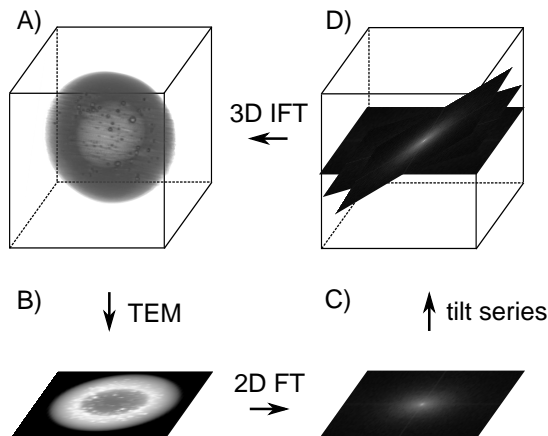
$$Rf = \int_L f(x, y) ds \quad (2.9)$$

The Radon transform convert the data into Radon space  $(l, \theta)$ , where  $l$  is the line perpendicular to the projection and  $\theta$  is the angle. A single projection of the object in real space therefore becomes a line at constant  $\theta$  in Radon space. The resulting map in Radon space is called a sinogram. With a sufficient number of projections, the object can then be reconstructed from the Radon space using the inverse Radon transform. Most conventional reconstruction algorithms in tomography are approximations, with varying complexity and accuracy, of this inverse Radon transformation [81]. The geometry of the Radon transform is illustrated in Figure 2.9.



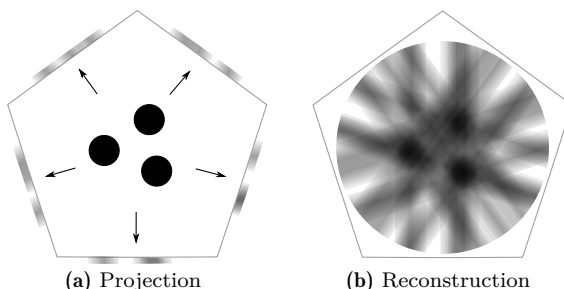
**Figure 2.9.:** Schematic illustration of the Radon transform.

The Radon transform is closely related to the so-called projection slice theorem (or central section theorem) which is based on the well-known Fourier transform and perhaps gives a better understanding of the reconstruction process. The projection slice theorem states that the Fourier transform of a 2D projection of a 3D object is equivalent to a 2D slice through the 3D Fourier space. By combining multiple projections it is therefore possible to sample the 3D Fourier space and reconstruct the 3D object by employing the 3D inverse Fourier transform. A schematic representation of the tomographic reconstruction using the projection slice theorem is shown in Figure 2.10.



**Figure 2.10.:** Schematic representation of tomographic reconstruction using the projection slice theorem. By combining Fourier transformed projections recorded at multiple tilt angles the object is sampled in Fourier space. The object is then reconstructed in real space by employing an inverse Fourier transform.

In practice, the tomographic reconstruction is often achieved using back-projection methods. In these methods the reconstruction is computed by an approach that is similar but reverse to the process that generated the projection, *i.e.* by smearing out the projection into the object space at the projection angle. With a sufficient number of projections from different tilt angles, the superposition of all back-projections will return the original object, see Figure 2.11. This reconstruction method is also known as direct back-projection [81].



**Figure 2.11.:** Schematic and simplified representation of the direct back-projection method. Adapted from [82].

Unfortunately, the direct back-projection proves to be quite unstable with the limited number of projections and relatively noisy data from TEM analysis. Even with regular sampling the direct back-projection appear to be blurred because of the relative higher sampling near the center of the Fourier space. Since the sampling is directly related to the angle and number of projections it is possible to introduce a correcting weighing filter, which improves the sample distribution in Fourier space and corrects the blurring in real space. This method is also known as weighted back-projection [83] and is probably one of the most used reconstruction methods today.

Blurring and other artifacts can also be decreased by using *a priori* information. A simple version of this method is to use the original projections to correct the reconstruction. When the projection of the imperfect reconstruction is compared to the original projection, the difference can be used to correct the reconstruction in consecutive computation. This procedure can then be repeated iteratively until the reconstruction fits the original projections in all directions. The most used iterative methods include the algebraic reconstruction techniques (ART) [84], which compares the reconstruction with a single projection at a time, and the simultaneous iterative reconstruction techniques (SIRT) [85], which compares all projections simultaneously [86]. For a comprehensive introduction to electron tomography in catalysis is referred to [87].

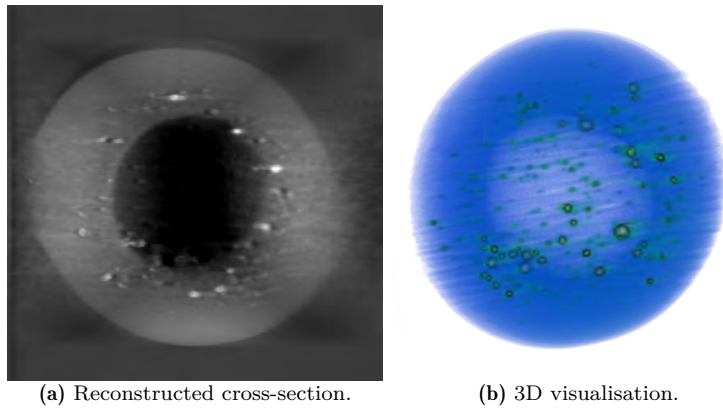
Before tomographic reconstruction, the tilt series has to be aligned with respect to a common tilt-axis and to account for errors in the positioning of the sample, which can occur

from thermal or mechanical drift during the acquisition. The alignment is very important to prevent artefacts and blurring of fine features in the reconstruction. Typically, the alignment is performed using 15-30 fiducial markers, such as gold nanoparticles, which are evenly distributed over the TEM grid. The relative position of the fiducial markers is tracked throughout the tilt series and then used to align the data for x-y shifts and a common tilt-axis. A good alignment can also be achieved by an iterative cross-correlation approach, where the shift from all iterations is added together before they are applied to the original data. The advantage of the iterative cross-correlation alignment is that it eliminates the need for the fiducial markers on the sample. However, the iterative cross-correlation is best suited for thin samples and if the sample has clear features that do not change significantly with the tilt angle [88]. However, if the sample is too thick and the images change drastically during tilting, the alignment is often still possible with fiducial markers, which makes it possible to compensate for image rotations and magnification changes and therefore gives a more accurate image alignment for images acquired under non-optimal conditions.

A good reconstruction with high resolution typically requires a high number of images and a high tilt angle range. Unfortunately, the tilt angle is often restricted in an electron microscope, which results in a *wedge* of missing information in the tilt-series. Such missing information can lead to artefacts and elongate the reconstruction in the direction of the missing wedge [89]. It has previously been suggested that a tilt range of around  $\pm 70$ - $80^\circ$  is required to allow reliable quantitative measurements [90]. An alternative method to minimise the missing wedge of information is to acquire images from a second tilt axis perpendicular to the first one, which requires a special double tilt sample holder.

In order to interpret the results, the tilt series requires that the intensity of the projected images vary monotonically with the material thickness. While BF-TEM and HRTEM often is the preferred method for acquisition of tomography tilt series in biology, these methods are in general not suitable to study crystalline materials because the diffraction contrast does not fulfil the so-called projection criterion [88]. On the other hand, HAADF-STEM almost completely eliminates diffraction and phase contrast. HAADF-STEM is therefore often the preferred mode of operation for tomography in material science and heterogeneous catalysis.


Figure 2.12 show the tomographic reconstruction and visualisation of Ag nanoparticles in a hollow  $\text{Al}_2\text{O}_3$  sphere. The tomography was performed by acquiring a tilt series of 76 STEM images from  $-74^\circ$  to  $+76^\circ$  in 2 degree steps while simultaneously correcting for image shift and focus changes. Alignment and tomographic reconstruction was performed in Inspect 3D (FEI Company) using the SIRT algorithm with 10 iterations. The visualisation was performed by volume and isosurface rendering in Avizo from FEI.



**Figure 2.12.:** *Electron tomography of Ag nanoparticles in hollow spheres of  $\text{Al}_2\text{O}_3$ .*

The tomographic data is also presented in the form of three movies, which gives a better impression of the distribution of Ag nanoparticles. The movies are available for download *via* the QR link in the last column of Table 2.1 or [91]. Movie 1 shows the aligned image stack of STEM images, while Movie 2 and Movie 3 show a 3D visualisation of the reconstructed data. The movies clearly show that the Ag nanoparticles are encapsulated inside a hollow shell of  $\text{Al}_2\text{O}_3$  with the exception of a few larger particles that are situated on the surface of the internal void. Please note that nanoparticles less than  $\sim 4$  nm may not be visualised in the 3D model.

**Table 2.1.:** *Electron tomography movies available for download [91].*

Movie	Content	Filename	File size	QR link
1	Aligned tilt-series	Movie1.mp4	0.82 MB	
2	3D model	Movie2.mp4	1.89 MB	
3	3D model (nanoparticles)	Movie3.mp4	1.47 MB	



## 2.6. Experimental section

### 2.6.1. Synthesis of Ag/Al<sub>2</sub>O<sub>3</sub> hollow spheres

AgNO<sub>3</sub> (0.016 g) and Al(O-i-Pr)<sub>3</sub> (3.832 g) was dissolved in HNO<sub>3</sub> (65%, 3 ml), acetic acid (4 ml) and ethanol (113 ml). The solution was stirred for 2 hours and then transferred to a ultrasonic nebuliser (Beurer LB 12). The nebulised aerosol was passed through a tube oven at 400° with a flow of air (around 2 l/min). The Ag/Al<sub>2</sub>O<sub>3</sub> hollow sphere was collected by filtration at the end of the oven. The material was calcined for 4 hours at 400° in air (heating 5°C/min) and then reduced for 4 hours at 400°C in Formier gas (10% H<sub>2</sub> in N<sub>2</sub>). The final product was a fine brown powder.

## Chapter 3

### Supported gold nanoparticles

---

Although gold is known as the most noble metal in the periodic table, supported gold nanoparticles are surprisingly active catalysts for a number of reactions in organic chemistry. Heterogeneous gold catalysis has recently been the subject of several excellent books and reviews, including [92–94]. The aim of this chapter is to give a short summary with particular emphasis on the requirements that are needed to be considered in the design of new catalytic systems.

---

#### 3.1. Introduction

Gold, silver and copper are often referred to as coinage metals and have been known as valuable metals for thousands of years. As far as catalysis concerns, they belong to a group of highly active redox metals. Cu and Ag are frequently used as heterogeneous catalysts in important industrial processes such as the synthesis of methanol and the epoxidation of ethylene with molecular oxygen, respectively. The oxidation state of gold ranges from -1 to +5 and although gold (especially  $\text{Au}^+$  and  $\text{Au}^{3+}$ ) has rich coordination and organo-metallic chemistry, solid  $\text{Au}^0$  is the most noble metal in the periodic table. For instance,  $\text{Au}_2\text{O}_3$  is the only metal oxide that has a positive formation enthalpy ( $\Delta H_f^\circ = 19.3 \text{ kJ/mol}$  [95]). For this reason Au appears to be chemically inert and has historically been regarded as a poor catalyst. This idea started to change in 1973 when Bond *et al.* [96] reported the hydrogenation of alkenes over a supported gold catalyst. Later, in the 1980s, Haruta *et al.* [63] discovered that supported gold can be a highly active catalyst for the oxidation of CO at low temperatures and that the preparation methods had a crucial impact on the catalytic activity. These discoveries triggered renewed interest for gold catalysis and it has since become well-known that supported gold nanoparticles (typically in the range of 1–5 nm) are surprisingly active and selective catalysts for a number of reactions in organic chemistry [94].

### 3.2. The reactivity of gold

As mentioned in the previous section, gold is the most noble metal in the periodic table. This means that most simple molecules, such as  $\text{H}_2$  or  $\text{O}_2$ , do not adsorb on a gold surface at room temperature. Table 3.1 show the calculated dissociative chemisorption energy of  $\text{O}_2$  on different transition metals relative to a free oxygen molecule [97]. The calculated energies show that Au is the only metal with where the dissociation is endothermic and that dissociative chemisorption of  $\text{O}_2$  is thermodynamically prohibited.

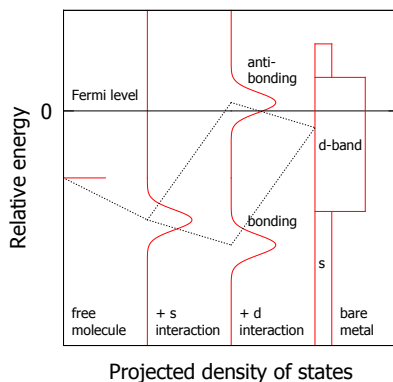
**Table 3.1:** Theoretical calculated energies (eV) for the dissociation of oxygen on transition metal surfaces. Adapted from [97].

Cr -	Mn -	Fe -6.30	Co -5.07	Ni -3.90	Cu -2.51
Mo -7.48	Tc -	Ru -4.62	Rh -4.03	Pd -1.20	Ag -0.65
W -8.62	Re -	Os -	Ir -4.65	Pt -2.17	Au <b>+0.54</b>

The weak interaction between oxygen and gold is essentially determined by the energy of the metal- $d$  band relative to the Fermi level. When the  $2p$  orbital of oxygen is interacting with a transition metal, the broad metal  $s$ -band leads to lowering and broadening of the energy levels, while the narrow metal  $d$ -band is splitting them into bonding and antibonding states. The bond strength is therefore determined by the filling of the metal- $d/2p$  antibonding orbitals, see Figure 3.1. If the metal  $d$ -band is close in energy to the Fermi level, the antibonding states are mostly empty and the metal-oxygen interaction is strong. For the noble metals to the right in the periodic table, the  $d$ -band is lower in energy, which causes a higher occupation of the antibonding states and a weaker metal-oxygen interaction. For gold, the  $d$ -band is at such a low energy that the metal- $d/2p$  antibonding orbitals are essentially filled, which prevent dissociative chemisorption [97].

Despite of the non-reactive nature of bulk gold, supported gold nanoparticles are highly active catalysts for a number of oxidation reactions. Since the first reports on low-temperature CO oxidation [63] there has been much debate about the origin of this surprising reactivity and many possible explanations have been proposed.

The first types of explanations is related to the high number of low-coordinated gold atoms found at steps, kinks and corners of small nanoparticles. This explanation is in good agreement with the fact that the ratio of low-coordinated corner atoms increases significantly when the size of the nanoparticle is decreased, while the fraction of total



**Figure 3.1.:** Schematic illustration of the formation of a chemical bond between an adsorbate valence states and the  $s$  and  $d$  states of a transition metal surface in the so-called  $d$ -band model. Adapted from [10].

surface atoms only changes slightly. It has previously been shown that the estimated fraction of corner atoms coincides with the catalytic activity for CO oxidation as function of the particle diameter [98]. By DFT calculation it has also been shown that there is a clear relation between the coordination number and the adsorption energy. The changes in the local electronic structure mean that the low-coordinated corner atoms have higher lying metal- $d$  states that are in a better position to interact with oxygen than the remaining surface atoms [97].

The second type of explanations are related to the possible indirect effects of the support material, including charge transfer to or from the support [99] and support induced strain [100].

The third type of explanations involves the support directly, for instance by transfer of activated oxygen [101]. It has also been proposed that it is the special chemical properties of the Au-support interfacial perimeter that is responsible for the high catalytic activity [102]. This idea has been supported by both experiments and theoretical calculations [103]. For instance, Haruta [104] compared the TOF for CO oxidation at 300 K over Au/TiO<sub>2</sub> and Pt/TiO<sub>2</sub> prepared by different methods, including deposition-precipitation, photo-deposition and impregnation. While the deposition-precipitation method resulted in hemispherical metal particles that were strongly attached to the support, photo-deposition and impregnation resulted in spherical particles. Since CO oxidation takes place on the Pt surfaces and the support material is not directly involved in the reaction, the activity of the Pt/TiO<sub>2</sub> catalysts was rather insensitive to the preparation method. On the other hand, the activity of the Au/TiO<sub>2</sub> catalysts was

highly dependent on the preparation method and differed by four orders of magnitude. The most active catalyst was comprised of hemispherical gold nanoparticles prepared by deposition-precipitation and exceeded the best Pt catalyst by one order of magnitude. It has also been proposed that the gold-support interaction can lead to the stabilisation of charged gold atoms. Evidence for the presence of charged gold atoms have been obtained by X-ray photoelectron spectroscopy (XPS) analysis of the Au  $4f_{7/2}$  level, which (sometimes) gives rise to a photopeak that can be assigned to the contribution of both Au, Au(I) and Au(III). Typically, Au(I) is present in smaller amounts than Au(III) [93].

Although the exact nature of the active site is still not fully understood, it is generally accepted that the number of low-coordinated Au atoms plays a crucial role. The most efficient way to increase the fraction of low-coordinated Au is to decrease the particle size, preferably to less than 10 nm. Apart from this general statement, it is also clear that the Au-support interaction has a large effect on the structural and chemical properties of the catalyst. During the synthesis of the catalyst, the surface properties of the support influence the size, dispersion and morphology of the Au nanoparticles. It has also been shown that the Au-support interphase enhance the binding of  $O_2$  [105] and therefore becomes a highly active region [103]. Furthermore, the Au-support interaction is also important for the stability of the nanoparticles and sintering can properly be partly suppressed by a strong interaction.

### 3.3. The support material

The most common support materials are metal oxides such as  $Al_2O_3$ ,  $Fe_2O_3$ ,  $SiO_2$ ,  $TiO_2$  and  $CeO_2$ . In general, the support materials must have a high surface area to expose as much gold as possible, but as discussed in the previous section, the support may also contribute to the catalytic activity through electronic effects, activation of the substrate or through the special chemical properties of the metal-support interfacial sites.

Based on pulsed isotopic labelling experiments with  $^{36}O_2$ , Schubert *et al.* [101] proposed that supported gold catalysts can be grouped into two categories with respect to the reaction mechanism. For gold nanoparticles supported on 'active' supports, such as  $Fe_2O_3$ ,  $TiO_2$  or  $CeO_2$ , the reactive oxygen may be provided through adsorption of mobile, molecular oxygen species on the support and dissociation on the gold-support interface. For gold nanoparticles supported on 'inactive' supports, such as  $SiO_2$  or  $Al_2O_3$ , which were found to be intrinsically less active, Schubert *et al.* proposed that the oxygen adsorption and activation may occur directly on the gold nanoparticles. More recent results have showed that gold nanoparticles with almost identical size distribution prepared by colloidal deposition on different metal oxides result in considerably different activity for CO oxidation. This confirms that the metal support interaction strongly influences the catalytic activity [106]. However, the effect did not follow the trend in

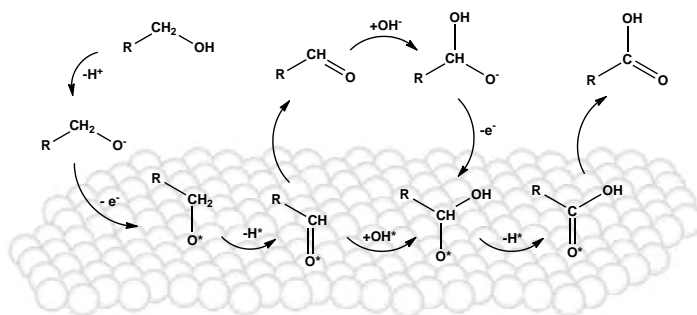
'active' and 'inactive' supports as proposed by Schubert *et al.* For instance, Comotti *et al.* [106] found that Au/TiO<sub>2</sub> (supposedly active) and Au/Al<sub>2</sub>O<sub>3</sub> (supposedly inactive) were much more active than Au/ZnO (supposedly active) and Au/ZrO<sub>2</sub> (supposedly inactive). On the other hand, the support seemed to influence the shape of the deposited particles, which may lead to the exposure of different facets and consequently different activity. In conclusion, the effect of the support is not understood in full detail and further experiments are still needed to unambiguously resolve the nature of the adsorbed species and the exact site and mechanism for the activation of oxygen.

### 3.4. Effect of base

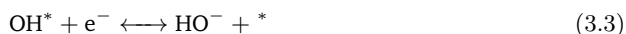
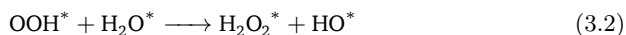
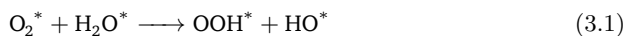
For most gold catalysed oxidations in liquid phase, no or little activity is observed without added base. This suggests that the role of hydroxide ions play an important role during the oxidation. Previous studies have shown that the oxidation of primary alcohols over supported metal catalysts proceeds by oxidative dehydrogenation to an aldehyde intermediate followed by oxidation to the acid [54]. The first step of the reaction therefore requires activation of the alcohol O-H bond, most likely by deprotonation. In aqueous solution, the deprotonation to form an alkoxide intermediate may occur at high pH according to the dissociation constant ( $pK_a$ ) of the alcohol. The initial activation of the O-H bond may also occur on a catalyst surface, although direct dissociative adsorption is energetically unfavourable on gold.

By means of DFT calculations Zope *et al.* [68] showed that the presence of surface bound hydroxide intermediate can facilitate O-H bond activation by a process similar to the proton transfer in solution. Furthermore, the adsorbed hydroxide can lower the activation energy for the subsequent C-H activation of the alkoxide intermediate to the aldehyde. The ability of adsorbed hydroxide to effectively activate the OH and CH bond may therefore explain the overall increase in catalytic activity of gold nanoparticles at high pH. Based on <sup>18</sup>O isotope labelling experiments Davis *et al.* also investigated if the O atom involved in the formation of carboxylic acid originates from O<sub>2</sub> or from the hydroxide ions. For instance, when the oxidation of ethanol was performed under <sup>18</sup>O<sub>2</sub> in an autoclave, no <sup>18</sup>O was observed in the product acetic acid by mass spectrometry. As no significant oxygen exchange was observed under reaction conditions in control experiments, the lack <sup>18</sup>O incorporation indicated that gold is unable to effectively dissociate O<sub>2</sub>. On the other hand, Zope *et al.* also performed the oxidation in labelled water (H<sub>2</sub><sup>18</sup>O) at high pH with <sup>16</sup>O<sub>2</sub> as the gas-phase oxidant, which resulted in incorporation of labeled <sup>18</sup>O in the product. Based on the important effect of base and the evidence of hydrogen peroxide formation in solution [107], Zope *et al.* therefore suggested that activation of O<sub>2</sub> occurs through the formation and dissociation of a peroxide (OOH<sup>\*</sup>) and a hydrogen peroxide (H<sub>2</sub>O<sub>2</sub><sup>\*</sup>) intermediate. In this mechanism the indirect role of O<sub>2</sub> is to remove

electrons from the metal surface and to close the catalytic cycle by regenerating hydroxide ions that are consumed in the reaction to produce the aldehyde or acid product.



**Figure 3.2.:** Proposed mechanism for the oxidation of alcohols to acids over a Au surface at high pH in  $H_2O$ . Adapted from [68].



Although alcohol and CO oxidation is difficult to compare, the promotional effect of hydroxyl species in liquid phase may also explain the importance of  $H_2O$  in gas-phase CO oxidation [108]. For instance, Okumura *et al.* investigated the effect of  $H_2O$  on the rate of CO oxidation over Au/ $Al_2O_3$  and Au/ $SiO_2$  at 273 K [109]. The results showed that increasing the concentration of  $H_2O$  from 0.3 to 200 ppm increased the reaction rate by 2 orders of magnitude for Au/ $SiO_2$  and 1 order of magnitude for Au/ $Al_2O_3$ . Furthermore, the oxidation of CO in liquid phase is also substantially promoted by high pH, even for Au nanoparticles supported on carbon, which normally has a low activity in gas-phase [110].

The effect of  $H_2O$  in gas-phase and  $OH^-$  in liquid phase suggests that the presence of hydroxyl groups substantially promotes the reaction rate, presumably by participating in the reaction mechanism. Recently, Ide and Davis [108] therefore proposed that adsorbed OH groups can react with CO to form COOH, which eventually decomposes to  $CO_2$  and that the observed particle size dependence for gas-phase oxidations over gold nanoparticles is most likely related to the optimum number of metal support interfacial sites that may be able to provide hydroxyl groups. These hydroxyl groups can also be supplied by increasing the pH, which makes the metal-support interfacial sites less important in liquid phase so that Au/C [111] or even bulk nanoporous gold [112] becomes active.

## 3.5. Preparation

There are several methods to synthesis small and disperse Au nanoparticles and as mentioned in section 3.2 the method of preparation often has a large effect on the activity. The three most common methods include impregnation, co-precipitation, and deposition-precipitation. Although several gold metal precursors are available, including  $\text{HAuCl}_4$ ,  $\text{HAu}(\text{NO}_3)_4$ ,  $\text{Au}(\text{CH}_3\text{COO})_3$  and  $\text{Au}(\text{CH}_3)_2(\text{acac})$ , the most used precursor is  $\text{HAuCl}_4$ .

### 3.5.1. Impregnation

In impregnation the support material is immersed in an aqueous solution of the  $\text{HAuCl}_4$  and the solution is evaporated to leave dispersed  $\text{HAuCl}_4$  on the surface of the support. Alternative gold precursors and organic solvents can also be used. The treated support is then calcined in air, usually at temperatures above 473K, or reduced in a stream of  $\text{H}_2$ . Unfortunately, this method often results in a broad size distribution of Au nanoparticles as the remaining chloride enhances aggregation by increasing the mobilisation of the gold atoms [93]. A variation of the impregnation is the so-called incipient wetness impregnation, where the amount of impregnation solution is adjusted to the pore volume of the support. In general, this method gives a better control of the dispersion and often results in nanoparticles <10 nm.

Another approach is to impregnate the support material with a colloidal solution of preformed gold nanoparticles. An effective method to synthesise small colloidal gold nanoparticles is to use polyvinylpyrrolidone (PVP) as protecting agent and  $\text{NaBH}_4$  as reducing agent [106].

### 3.5.2. Co-precipitation

In co-precipitation a solution of  $\text{HAuCl}_4$  and a soluble metal oxide precursor, most preferably nitrates, is poured into an alkaline solution (typically of  $\text{Na}_2\text{CO}_3$  or  $\text{NaOH}$ ) under vigorously stirring. The precipitates are then washed with water, filtered, dried and calcined to obtain the final catalyst. Often co-precipitation is a simple and convenient method for preparation of supported gold nanoparticles <10 nm. In general, the range of supports is limited to metal hydroxides or carbonates that can be precipitated with  $\text{Au}(\text{OH})_3$ . Moreover, the rate of precipitation and gold-support interaction has a large impact on the final catalyst.

### 3.5.3. Deposition-precipitation

Another important preparation method is deposition-precipitation, where a support material is stirred in a solution of  $\text{HAuCl}_4$ . As the pH is increased by addition of base,



solid  $\text{Au}(\text{OH})_3$  is deposited on the surface of the support as it precipitates. The material is then collected by filtration, washed with water to remove chloride and calcined, which decompose  $\text{Au}(\text{OH})_3$  into small Au nanoparticles. Systematic studies on the preparation of Au/ $\text{TiO}_2$  by deposition-precipitation [113] have shown that the size of the Au nanoparticles dependent on many different variables, including the concentration of  $\text{HAuCl}_4$ , the type of  $\text{TiO}_2$ , nature of the base, temperature, pH, washing and drying and on the conditions for the calcination.

The deposition-precipitation method requires that the  $\text{Au}(\text{OH})_3$  is deposited onto the support and is therefore highly depending on the isoelectric point of the surface. At low pH the surface of e.g.  $\text{TiO}_2$  is positively charged, while the species in solution are negatively charged. This means that the gold is deposited by electrostatic forces. This deposition of  $\text{Au}(\text{OH})_3$  is fast, but may result in relatively large particles with low activity. At high pH the deposited amount of gold decreases slightly, but typically results in smaller nanoparticles. At a pH value from 8-10 it is generally possible to deposit all the  $\text{Au}(\text{OH})_3$  on the support without precipitation in the solution. This  $\text{Au}(\text{OH})_3$  is essentially free from chloride and is deposited in small nanoparticles that lead to high activity [92].

On other supports, such as  $\text{SiO}_2$ , deposition-precipitation typically results in a low loading of Au because of the low isoelectric point of  $\text{SiO}_2$  (pI around 1.7-3.5 [114]). This means that the silica is negatively charged under the basic conditions needed to hydrolyse  $\text{HAuCl}_4$ , which causes the  $\text{Au}(\text{OH})_3$  to precipitate in solution rather than on the support [115].

## 3.6. Experimental section

### 3.6.1. General method for impregnation

The support material (0.9900 g) was impregnated with an aqueous solution of  $\text{HAuCl}_4 \cdot 3\text{H}_2\text{O}$  (0.0199 g) to incipient wetness. Preferably, the amount of water should be adjusted to the total pore volume of the support material. The impregnated material was dried at room temperature overnight and then reduced in Formier gas (10%  $\text{H}_2$  in  $\text{N}_2$ ) for 2 hours at  $350^\circ\text{C}$  (heating  $5^\circ\text{C}/\text{min}$ ) to give the final gold nanoparticle catalyst with a gold loading of 1 wt%.

### 3.6.2. General method for deposition-precipitation

The support material (0.9900 g) was added to a solution of  $\text{HAuCl}_4 \cdot 3\text{H}_2\text{O}$  (0.0199 g) in 5 ml  $\text{H}_2\text{O}$  under stirring. The pH was increased to 9 by addition of  $\sim 10$  drops of a saturated aqueous solution of  $\text{NaHCO}_3$  and the mixture was then stirred at  $50^\circ\text{C}$  for 1 hour in order to precipitate  $\text{Au}(\text{OH})_3$  on the support. During the reaction the colour of

the solution changed from yellow to colourless. The catalyst was collected by filtration and washed with water until no  $\text{Cl}^-$  could be detected upon addition of  $\text{AgNO}_3$  to the filtrate. The catalyst was dried at room temperature overnight and then reduced in Formier gas (10%  $\text{H}_2$  in  $\text{N}_2$ ) for 2 hours at  $350^\circ\text{C}$  (heating  $5^\circ\text{C}/\text{min}$ ) to give the final gold nanoparticle catalyst with a gold loading of 1 wt%.

### 3.7. Summary

The surprisingly high catalytic activity of supported gold catalysts are related to the number of low-coordinated gold atoms located at steps, kinks, and corners of the gold particles. These atoms are therefore also likely to constitute the active sites. Typically, gold nanoparticles are supported on high-surface area metal oxides that, besides from stabilising the nanoparticles, also influence the activity of the catalyst through a number of direct or indirect effects. For low-temperature CO oxidation in particular, the Au-support interfacial perimeter seems to bind  $\text{O}_2$  more strongly which make it a highly active region [105]. For liquid phase oxidations of alcohols, little activity is observed without added base, which suggest that  $\text{OH}^-$  plays a crucial role. In a possible reaction mechanism  $\text{O}_2$  is proposed to participate in the catalytic cycle not by dissociation to atomic oxygen, but by regenerating hydroxide ions which are formed via decomposition of a peroxide intermediate. Recent studies have pointed to the promotional effect of hydroxyl species, which also explains the importance of  $\text{H}_2\text{O}$  in gas-phase CO oxidation [108]. The conditions and method of preparation has a large effect on the size distribution and activity of supported gold nanoparticles. In general, the best preparation method depends on both the metal precursor and the nature of the support material.



## Chapter 4

### One-pot synthesis of amides

---

Amides constitute an important class of compounds in chemistry and biology that also finds use in many bulk and fine chemicals, including speciality chemicals and pharmaceuticals. This chapter describes a novel and efficient one-pot reaction protocol to synthesise amide from alcohols and amines. The reaction is based on intermediate formation of a methyl ester intermediate followed by aminolysis and uses a catalytic system comprised of supported gold nanoparticles and added base in methanol.

---

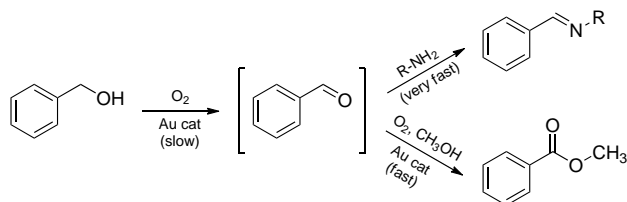
#### 4.1. Introduction

Supported gold catalysts have been tested in many different oxidation reactions under a broad variety of reaction conditions. For instance, gold catalysts have been successfully used in the oxidation of alcohols [92; 93; 116] to aldehydes [117], carboxylic acids [64; 118; 119] or esters [120; 121], in the oxidation of aldehydes to acids [122; 123] or esters [124; 125] and in the epoxidation of alkenes [126–128]. In addition to the above-mentioned reactions, interesting studies have recently been performed on oxidation of amines. Supported gold catalysts have been used in oxidation of amines to imines [129–131], azo-compounds [132] and - prior to this project - in formation of amides [133–135]. Although the application range of gold catalysed oxidations is still limited, the increasing number of reports on oxidation of nitrogen-containing compounds represents a very interesting development in this emerging field of organic chemistry.

Although the general developments in gold catalysis have been amply reviewed we therefore found it timely to summarise the efforts to synthesise nitrogen-containing compounds in a mini-review. Our mini-review entitled "Gold catalyzed formation of nitrogen-containing compounds – from mechanistic understanding to synthetic exploitation" is enclosed as publication A3.

## 4.2. Oxidative coupling of alcohols and amines

From previous experiments with gold catalysed synthesis of imines from alcohols and amines in methanol [131], we found that benzaldehyde and *N*-hexylamine reacted instantaneously to afford the corresponding imine, *N*-benzylidenehexane-1-amine. This indicated that the alcohol was first oxidised to an aldehyde intermediate over the supported gold catalyst. The aldehyde intermediate then reacted with the amine to form the corresponding imine by a condensation step that was substantially faster than the formation of other possible products, including methyl benzoate (which was formed in high yield when the oxidation was performed in absence of amine), see Figure 4.1.



**Figure 4.1.:** Possible reactions for the gold catalysed oxidation of benzyl alcohol in amine and methanol.

From GC-MS analysis we found that the only by-product was small amounts of *N*-hexylbenzamide. Apparently, no methyl benzoate was formed. The reaction was also performed in an autoclave under 10 bar  $O_2$ . Although the increased amount of oxygen had no significant effect on the conversion, the yield of imine was slightly decreased as more amide was formed. The increased formation *N*-hexylbenzamide could be explained by three possible situations. Either the amide was formed by 1) intermediate formation of benzoic acid followed by condensation with *N*-hexylamine, 2) oxidation of the hemiaminal intermediate or 3) intermediate formation of methyl benzoate followed by aminolysis. The following section describes how the last situation can be exploited to synthesise amides in an efficient one-pot reaction using a catalytic system comprised of supported gold nanoparticles and base in methanol.

### 4.2.1. Experimental section

All chemicals and reagents were used as received. The employed catalyst was a commercial 1 wt% Au/TiO<sub>2</sub> supplied by Mintek. In a typical experiment, alcohol (5 mmol), anisole (internal standard, 0.5 mmol), base (alkaline metal methoxide, 1.25 mmol) and methanol (50 mmol) were charged to a 20 ml reaction tube and connected to a reaction station providing stirring, heating and  $O_2$  for the oxidative esterification (atmospheric pressure). The system was flushed with  $O_2$  and 197 mg Au/TiO<sub>2</sub> catalyst was added (Au/substrate molar ratio of 1/500). After 24 hours, the amine (10 or 25 mmol) was added and the

reaction was either kept at 25°C or heated to 65°C to reflux methanol.

For the synthesis of benzamide, benzyl alcohol (5 mmol), KOMe (1.25 mmol) and methanol (50 mmol) were charged to a 20 ml pressure tube. After 24 hours of reaction at 25°C under oxygen the tube was cooled in an ice bath and bubbled through with ammonia for 20 min. The tube was then sealed and heated to 65°C for 24 hours. The reaction mixture was dissolved in water and neutralised to pH 7 by addition of an aqueous solution of 0.1 M HCl. The product benzamide was then extracted with ethyl acetate and isolated by evaporation of the solvent in a rotary evaporator.

During the reactions samples of 0.1 ml were periodically collected, filtered and analysed by GC-FID and GC-MS. The amount of substrates and reaction products were quantified using anisole as internal standard. The conversion, selectivity and yield were calculated from equation 4.1 to 4.3.

$$Yield = \frac{A(pro)_t}{A(pro)_{theo}} \quad (4.1)$$

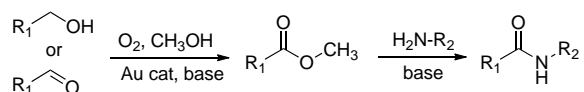
$$Conversion = 1 - \frac{A(sub)_t}{A(sub)_0} \frac{A(ref)_0}{A(ref)_t} \quad (4.2)$$

$$Selectivity = \frac{Yield}{Conversion} \quad (4.3)$$

where  $A(pro)$ ,  $A(sub)$  and  $A(ref)$  was the integrated GC peak area of the product, substrate and reference, respectively. The theoretical product peak area was determined from the response factor of the ester or amide product with respect to anisole.

#### 4.2.2. Results and discussion

Figure 4.2 show the synthesis of amides by oxidative coupling of alcohols using supported gold nanoparticles and base as catalyst.

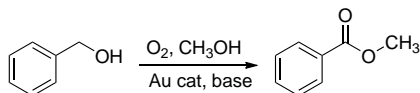


**Figure 4.2.:** *Synthesis of amides by oxidative coupling of alcohols or aldehydes with amines using supported gold nanoparticles and base as catalysts.*

In the first step of the reaction, the gold-catalysed oxidation of the alcohol or aldehyde is performed in methanol and therefore affords a methyl ester. In the second step, amine is added and the ester is converted into the corresponding amine by base-catalysed aminolysis. As the same base is promoting both steps, the synthesis can be performed in a one-pot reaction without isolation or purification of the intermediate. Initially, benzyl alcohol was used as a model substrate to study the formation of methyl

benzoate in methanol. Table 4.1 shows the results from the initial oxidation experiments using Au/TiO<sub>2</sub> as the heterogeneous catalyst.

**Table 4.1.:** Formation of methyl benzoate by aerobic oxidation of benzyl alcohol in methanol.<sup>a</sup>



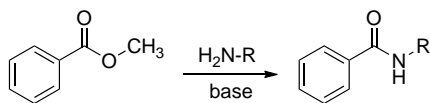
Entry	Catalyst	Base	Conv. (%)	Sel. (%)	Yield (%)
1	Au/TiO <sub>2</sub>	LiOMe	>99	84	84
2 <sup>b</sup>	Au/TiO <sub>2</sub>	LiOMe	>99	86	86
3 <sup>c</sup>	Au/TiO <sub>2</sub>	LiOMe	>99	89	89
4	Au/TiO <sub>2</sub>	NaOMe	>99	87	87
5	Au/TiO <sub>2</sub>	KOMe	>99	92	92
6	Au/TiO <sub>2</sub>	-	6	>99	6
7	TiO <sub>2</sub>	KOMe	0	0	0

Reaction conditions: <sup>a</sup> benzylalcohol (5 mmol), methanol (50 mmol), anisol (0.5 mmol, internal standard), base (1.25 mmol), catalyst (197 mg), 24 hours at 25 °C under O<sub>2</sub>. <sup>b</sup> methanol (75 mmol). <sup>c</sup> methanol (100 mmol).

Entries 1-3 show the effect of the amount of methanol on conversion and selectivity after 24 hours reaction at room temperature in presence of 20 mol% LiOMe and the Au/TiO<sub>2</sub> catalyst. As expected, the results show that the selectivity towards methyl benzoate was increased with increasing excess of methanol. All experiments were performed with 20 mol% base. The methoxide bases were chosen because they were readily available as methanol solutions, but in principle, hydroxide bases could also be used. Entry 1, 4 and 5 show that the yield of methyl ester was dependent on the alkali metal and that the trend in yield correlated well with the typical order of basicity in methanol, where KOMe > NaOMe > LiOMe [136]. Entry 6 show that the base was essential for the conversion of substrate as almost no benzyl alcohol was converted in the absence of base. Furthermore, pure TiO<sub>2</sub> did not result in any conversion which verified that gold nanoparticles were required to obtain catalytic activity.

Table 4.2 shows the results from the initial experiments with adding *N*-hexylamine to methyl benzoate under the same reaction conditions.

Entries 1-3 in Table 4.2 show the effect of the amount of methanol on conversion and selectivity after 24 hours reaction at room temperature and in presence of 20 mol% LiOMe. Increasing the amount of methanol from 50 to 75 and 100 mmol led to a decrease in yield from 82% to 69% and 59%, respectively. KOMe was found to be the best base, which suggested that the basicity of the solution had an important effect on the reaction rate. The reaction did not result in any conversion in absence of base. It is important to note that the selectivity remained high and unaffected by the presence of base in all reactions. Entry 7-11 show that it was possible to achieve full conversion in 24 hours

**Table 4.2.:** Formation of *N*-hexylbenzamide from methyl benzoate and *N*-hexylamine<sup>a</sup>,  $R=(CH_2)_5CH_3$ 

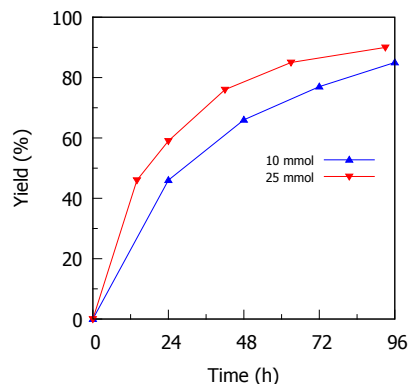
Entry	Catalyst	Base	Temp. (°C)	Conv. (%)	Sel. (%)	Yield (%)
1	-	LiOMe	25	82	>99	82
2 <sup>b</sup>	-	LiOMe	25	69	>99	69
3 <sup>c</sup>	-	LiOMe	25	59	>99	59
4	-	NaOMe	25	89	>99	89
5	-	KOMe	25	92	>99	92
6	-	-	25	0	0	0
7	-	LiOMe	65	>99	>99	>99
8	-	NaOMe	65	>99	>99	>99
9	-	KOMe	65	>99	>99	>99
10	Au/TiO <sub>2</sub>	-	65	15	>99	15
11	Au/TiO <sub>2</sub>	KOMe	65	>99	>99	>99

Reaction conditions: <sup>a</sup> methyl benzoate (5 mmol), *N*-hexylamine (10 mmol), methanol (50 mmol), anisol (0.5 mmol, internal standard), base (1.25 mmol), catalyst (197 mg), 24 hours. <sup>b</sup> methanol (75 mmol). <sup>c</sup> methanol (100 mmol).

by increasing the temperature from 25 to 65°C. Even at 65°C the presence of base was required to obtain full conversion. In presence of Au/TiO<sub>2</sub>, but absence of base, the yield was only 15%. Entry 11 in 4.2 shows that the gold catalyst had no apparent effect on the base-catalysed reaction. It is important to mention that an increased amount of methanol had a positive effect on the yield of the methyl ester, but a negative effect on the yield of amide. A possible improvement of the method could therefore be to remove methanol by reactive distillation during the base-catalysed aminolysis step.

The two individual steps were now combined in a one-pot reaction to synthesise *N*-hexylbenzamide. In the first step benzyl alcohol was oxidized to methyl benzoate. After 24 hours *N*-hexylamine was added and the temperature was increased to 65°C. Figure 4.3 shows the yield of amide during the second step of the reaction adding 10 and 25 mmol amine, respectively.

Notably, the yield after 24 hours with 10 mmol amine was only 46%, which was considerably lower than the result expected from the experiment with pure methyl benzoate (Table

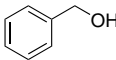
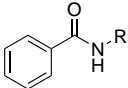
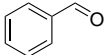
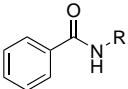
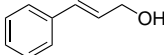
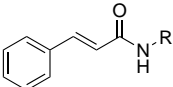
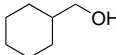
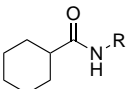
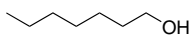
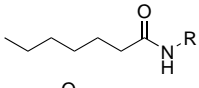
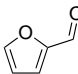
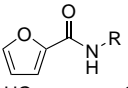
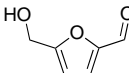
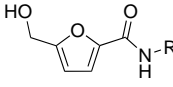
**Figure 4.3.:** Yield of *N*-hexylbenzamide with different amounts of amine.



4.2, Entry 11). The decrease in yield may be related to the formation of water during from the preceding oxidation step. Figure 4.3 also shows that the reaction rate increased with excess of amine. With 25 mmol of amine the reaction almost reached full conversion after 96 hours.

The one-pot synthesis was used for the oxidative coupling of different alcohols, aldehydes and amines. All reactions were performed under identical reaction conditions and no optimisation was attempted for the individual substrates. Table 4.3 compiles the results from oxidative coupling of different alcohols and aldehydes with *N*-hexylamine to form the corresponding *N*-hexylamides. All examined alcohols were oxidized with high selectivity to the methyl esters, but while the aromatic alcohols reached full conversion in 24 hours, 1-heptanol only reached 34% conversion at room temperature. Higher yield of aliphatic methyl esters have previously been reported at high temperatures and increased pressure of O<sub>2</sub> [137]. As expected, the oxidation of both aromatic aldehydes afforded methyl esters in high yield.

**Table 4.3:** Yield of ester and amide obtained in the oxidative coupling of alcohols and aldehydes with *N*-hexylamine,<sup>a</sup> R=(CH<sub>2</sub>)<sub>5</sub>CH<sub>3</sub>

Entry	Alcohol/Aldehyde	Product	Ester yield (%)	Amide yield <sup>b</sup> (%)
1			92	90 (59)
2			93	92 (64)
3			>99	46 (34)
4			74	74 (18)
5			34	34 (25)
6			>99	99 (84)
7			73	73 (73)

<sup>a</sup> Reaction conditions: alcohol or aldehyde (5 mmol), methanol (50 mmol), anisole (0.5 mmol), KOMe (1.25 mmol), Au/TiO<sub>2</sub> (197 mg). After 24 hours of oxidation at RT 25 mmol *N*-hexylamine was added and the mixture was heated to 65°C for additional 96 hours. <sup>b</sup> Number in parenthesis is the yield obtained after 24 hours.

Table 4.3 also show that all methyl esters reacted with *N*-hexylamine and afforded the corresponding amides with good yield. Notably, the reaction occurred with excellent selectivity (>99%) independent of the structure of the ester.

Table 4.4 compiles the results from the oxidative coupling of benzyl alcohol with different amines to form the corresponding amides. The reaction with benzylamine resulted in high yield of *N*-benzylbenzamide, while the more sterically demanding amines aniline and pentan-3-amine was unable to react under the given reaction conditions. As expected, the reaction with ammonia resulted in the formation of benzamide. It is expected that the yield of benzamide may be increased if the reaction is performed in an autoclave pressurised with ammonia or if the product recovery is optimised.

**Table 4.4.:** Yield of ester and amide obtained in the oxidative coupling of benzyl alcohol with amines,<sup>a</sup>  $R=(CH_2)_5CH_3$

Entry	Amine	Product	Ester yield (%)	Amide yield <sup>b</sup> (%)
1			92	90 (59)
2			92	54 (15)
3			92	38 (16)
4			92	-
5			92	-
6	NH <sub>3</sub>		92	41 <sup>c</sup>

<sup>a</sup> Reaction conditions: benzylalcohol (5 mmol), methanol (50 mmol), anisole (0.5 mmol), KOMe (1.25 mmol), Au/TiO<sub>2</sub> (197 mg). After 24 hours of oxidation at 25°C 25 mmol amine was added and the mixture was heated to 65°C for additional 96 hours. <sup>b</sup> Number in parenthesis is the yield obtained after 24 hours. <sup>c</sup> Isolated yield.

In order to study the structure-reactivity relationship we employed the well-known Hammett methodology [138] and focused our attention on a range of *para*-substituted benzyl alcohol derivatives, see Figure 4.4.

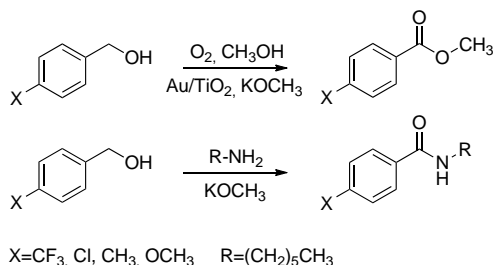


Figure 4.4.: An overview of the Hammett study.

### 4.2.3. Hammett study

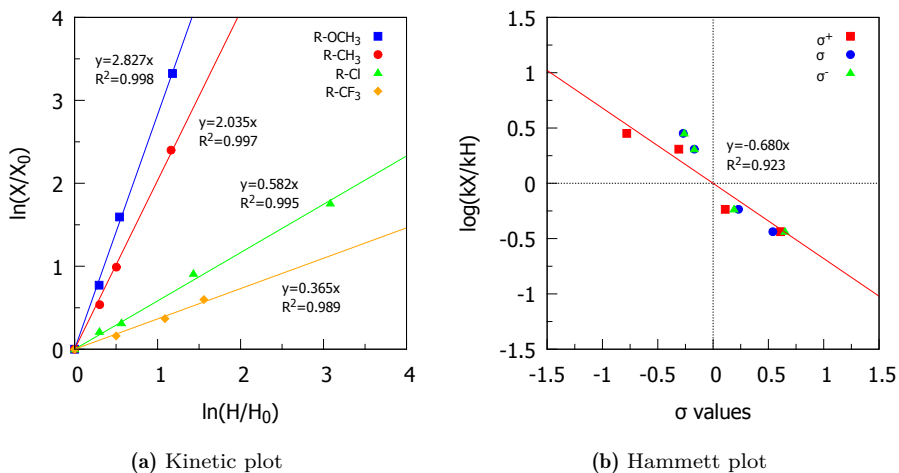
The Hammett study was performed through a series of competition experiments rather than by establishing absolute reaction rates for the individual substituents. There were several reasons to choose this approach. First of all, competition experiments are more robust towards small variations in the reaction conditions and allow the reaction to be followed to a high conversion without deviation from linearity. Furthermore, a competition experiment can be designed to investigate a different step than the overall rate-determining step. In this study, for instance, it was desirable to disregard any effects from *e.g.* activation of  $\text{O}_2$ .

Anisole (0.5 mmol), potassium methoxide (1.25 mmol) and methanol (50 mmol) were charged to a reaction tube together with benzyl alcohol (2.5 mmol) and either (4-methylphenyl)methanol, (4-methoxyphenyl)methanol, (4-chlorophenyl)methanol or (4-(trifluoromethyl)phenyl)methanol. The reaction tubes were connected to a reaction station providing stirring, heating and  $\text{O}_2$  for the oxidative esterification (atmospheric pressure). The system was flushed with  $\text{O}_2$  and 197 mg Au/ $\text{TiO}_2$  catalyst was added, corresponding to an Au/substrate molar ratio of 1/500. During the following two days, samples of 0.1 ml were periodically collected, filtered and analysed by GC-FID and GC-MS. When all reactions had reached full conversion, *N*-hexylamine (10 mmol) was added and the temperature was increased to 65°C. During the following two days more samples were collected and analysed.

In the first series of competition experiments, the oxidation of all *para*-substituted benzyl alcohols followed first order kinetics. This allowed the construction of the linear kinetic plots shown in Figure 4.5(a). From these plots the relative reactivity could be determined from the slope of the lines by linear regression [139]. The assumption that the oxidations followed first order kinetics could be justified from the good correlation coefficients ( $R^2 > 0.98$ ).

The reactivity of the *para*-substituted alcohols relative to benzyl alcohol was used to construct the Hammett plot in Figure 4.5(b) using three sets of  $\sigma$ -values from

the literature [140; 141]. The Hammett plot shows that the best linear correlation of  $\log(kX/kH)$  was obtained with the  $\sigma^+$ -values ( $R^2 = 0.922$ ), which resulted in a negative slope ( $\rho = -0.68$ ). The negative slope indicates that a partial positive charge builds up during the rate determining step, which corresponds to a hydride abstraction step.



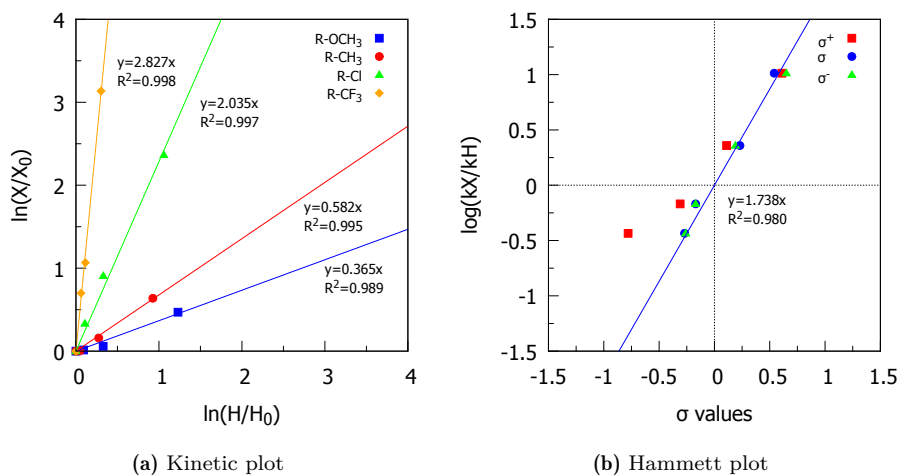
**Figure 4.5.:** Hammett study of the first step of the reaction showing the relative reactivity of four different para-substituted derivatives relative to benzyl alcohol.

Similar results have previously been reported from the gold-catalysed oxidation of benzyl alcohol to benzaldehyde ( $\rho = -1.10$ ) [142] and was further confirmed by a significant kinetic isotope effect when deuterated benzyl alcohol was investigated. Furthermore, Fristrup *et al.* investigated the oxidation of benzaldehyde to methyl benzoate and found a relatively large positive slope ( $\rho = 2.51$ ). These results confirm that the gold-catalysed esterification of benzyl alcohol with methanol occurs through an aldehyde intermediate and that the formation of the aldehyde is the rate determining step.

When the oxidative esterification reached full conversion, *N*-hexylamine was added to the reaction to follow the base-catalysed aminolysis. From the kinetic plots in Figure 4.6(a) it was possible to determine the relative reactivity and construct the Hammett plot in Figure 4.6(b).

Figure 4.6(b) shows that the best linear correlation was obtained with the neutral  $\sigma$ -values ( $R^2 = 0.980$ ), which resulted in a relatively large positive slope ( $R^2 = 1.738$ ). The positive slope indicated that the reaction was sensitive to the nature of the substituents and that negative charge was building up during the reaction.

Comparison of Figure 4.5(b) and 4.6(b) show that the substituent effects are oppo-



**Figure 4.6.:** Hammett study of the second step of the reaction showing the relative reactivity of four different *para*-substituted derivatives relative to methyl benzoate.

site in the two consecutive reactions. This means that electron withdrawing substituents decrease the reactivity in the oxidation step and increase the reactivity in the aminolysis step. On the other hand, electron donating groups increase the reactivity in the oxidation step and decrease the reactivity in the aminolysis step.

### 4.3. Summary

In summary, we have presented a novel approach for the two-step synthesis of amides *via* the corresponding methyl ester and showed that the combination of supported gold nanoparticles and base forms an efficient catalytic system for the reaction. As the same base is promoting both steps of the reaction, the synthesis can be performed in a convenient one-pot procedure without isolation or purification of the intermediate. The employed oxidant is pure molecular oxygen and the reactions can be performed under mild reaction conditions. Furthermore, the reactions can be performed with a number of substrates, which demonstrate the versatility of the method.

The one-pot synthesis of amides was also investigated in two consecutive Hammett studies. The studies were performed by competition experiments rather than by establishing absolute reaction kinetics and the investigated substrates were *para*-substituted benzyl alcohol derivatives. The result from the first Hammett study suggested that the gold-catalysed oxidation of benzyl alcohol occurs with build-up of positive charge in the benzylic position, which corresponds well to a H-abstraction step. The negative slope of the Hammett plot ( $\rho = -0.680$ ) was in good agreement with the generally accepted

perception that the gold catalysed esterification of alcohols with methanol occurs through the formation of an aldehyde intermediate and that this is the rate-determining step. The result from the second Hammett study showed that the rate of amide formation was very sensitive to substituent effects and that negative charge was formed during the reaction ( $\rho=1.738$ ).



## Chapter 5

### Selective formation of imines

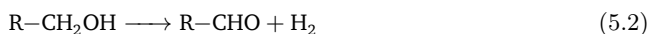
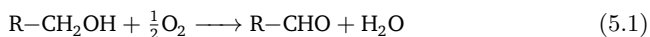
---

This chapter describes the investigation of different silver catalysts for the synthesis of imines from alcohols and amines. The reactions were performed at relatively mild conditions (100°C and atmospheric pressure) without any additives or co-catalysts and afforded the desired imines with high selectivity (up to 99%). The highest catalytic activity was obtained with 5 wt% Ag/Al<sub>2</sub>O<sub>3</sub> in toluene with air as oxidant, although the reaction also occurred under inert atmosphere by releasing H<sub>2</sub> into the gas phase.

---

#### 5.1. Introduction

As described in Chapter 1, much effort has been devoted to the development of aerobic oxidation of alcohols using molecular oxygen or air as the oxidant. Considering the atom efficiency, another attractive alternative is the oxidant-free dehydrogenation of alcohols to the corresponding carbonyl compounds and molecular H<sub>2</sub> [143]. Scheme 5.1 and 5.2 show the general synthesis of an aldehyde by oxidation and oxidant-free dehydrogenation of an alcohol, respectively.

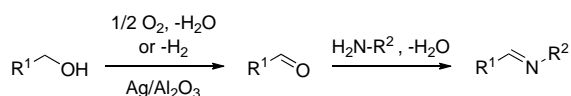


The catalytic dehydrogenation of primary and secondary alcohols is a well-known industrial process. The most important example is the silver metal catalysed dehydrogenation of methanol, which accounts for about 55% of the production of formaldehyde in Europe [144]. From a thermodynamic viewpoint, the dehydrogenation of alcohols is a reversible reaction. The direction of the process therefore depends on the temperature, which strongly influences the equilibrium. For methanol the reaction is typically performed at around 650°C.

Although tremendous advance have been achieved in the dehydrogenation of alcohols with homogeneous platinum-group metals [145–148], only a limited number of



heterogeneous catalysts that are effective under mild conditions in liquid phase have appeared to date. Recently, Kaneda *et al.* [149] used a hydrotalcite supported silver catalyst (Ag/HT) for the dehydrogenation of alcohols under oxidant-free conditions. The reaction afforded high yields of the corresponding aldehydes and ketones at 130°C with co-production of H<sub>2</sub>. Shimizu *et al.* [150] reported that Ag/Al<sub>2</sub>O<sub>3</sub> was more active than conventional catalysts based on conventional platinum group metals such as Rh/Al<sub>2</sub>O<sub>3</sub> and Pd/Al<sub>2</sub>O<sub>3</sub>. The high activity was explained by the presence sub-nanometer nanoparticles and the acidic and basic properties on Al<sub>2</sub>O<sub>3</sub>. Furthermore, Shimizu showed that Ag/Al<sub>2</sub>O<sub>3</sub> could be used for amide synthesis and also for the direct synthesis of secondary amines *via* intermediate formation of imine by the borrowing hydrogen mechanism. Although the number of reports is increasing, the application of supported Ag catalysts is still limited in liquid phase organic chemistry. The results in this chapter show that Ag/Al<sub>2</sub>O<sub>3</sub> is a highly active and selective catalyst for the formation of aldehydes from alcohols without the use of additives. Furthermore, Ag/Al<sub>2</sub>O<sub>3</sub> can be used for the direct formation of imines, see Figure 5.1.



**Figure 5.1.:** Formation of imines by oxidative dehydrogenation and condensation of alcohols and amines using Ag/Al<sub>2</sub>O<sub>3</sub> as heterogeneous catalyst.

## 5.2. Experimental section

### 5.2.1. Catalyst preparation

A series of supported Ag catalysts were prepared by incipient wetness impregnation of the support materials with an aqueous solution of AgNO<sub>3</sub> or HAuCl<sub>4</sub> resulting in 1, 5, or 10 wt% metal on the support. Before each reaction, the impregnated and dried silver catalysts were reduced with Formier gas (10% H<sub>2</sub> in N<sub>2</sub>) in a tube oven for 2 hours at 300°C (heating 5°C/min). The investigated support materials included a metal oxide (Al<sub>2</sub>O<sub>3</sub>), a spinel structure (MgAl<sub>2</sub>O<sub>4</sub>) and a layered double hydroxide (Mg<sub>6</sub>Al<sub>2</sub>(CO<sub>3</sub>)(OH)<sub>16</sub>, hydrotalcite, HT). All supports were purchased from commercial source (Saint-Gobain or Sigma Aldrich) and used without further purification or pretreatment.

A hydrotalcite catalyst with 5 wt% Ag was prepared by co-precipitation of AgNO<sub>3</sub> (0.158 g), Mg(NO<sub>3</sub>)<sub>2</sub> (2.250 g) and Al(NO<sub>3</sub>)<sub>3</sub> (1.955 g) in an aqueous alkaline solution of Na<sub>2</sub>CO<sub>3</sub> (1.276) and NaOH (1.668 g). The metal nitrates were dissolved in water and added drop-wise to the alkaline solution under vigorous stirring. After ageing for 24 hours, the catalyst was collected by filtration, washed with water and dried at 90°C overnight. The catalyst was then reduced with Formier gas (10% H<sub>2</sub> in N<sub>2</sub>) in a tube

oven for 2 hours at 300°C with a heating ramp of 5°C/min in agreement of the general reduction procedure.

### 5.2.2. Characterisation

The synthesised catalysts were characterised by nitrogen physisorption, X-ray powder diffraction and TEM as described in Chapter 2. Nitrogen physisorption analysis was performed with a Micromeritics ASAP 2020 Surface Area and Porosimetry Analyzer at 77K. The samples were outgassed in vacuum at 200°C prior to measurement and the total surface area was calculated according to the BET method. The XRPD analysis was carried out on a Huber G670 diffractometer operated in transmission mode with Cu  $K_{\alpha 1}$  irradiation from a focusing quartz monochromator. TEM was performed on a FEI Tecnai T20 G2 microscope operated at 200kV. All specimens were dispersed in ethanol and left to dry on the TEM grids at room temperature before the analysis. The particles size distributions were estimated by measurements of  $\sim 100$  particles.

### 5.2.3. Standard oxidation procedure

In a typical experiment, alcohol (2.0 mmol), amine (2.0 mmol), anisole (internal standard, 0.2 mmol), and toluene (6.0 ml) was charged into a reaction tube and connected to a reaction station (Radley Carrousel 12 Plus). The reaction station provided stirring, heating and an atmosphere of Ar, O<sub>2</sub> or atmospheric air at ambient pressure. The reaction tube was flushed with gas, heated to the desired temperature and then added 100 mg catalyst. Unless otherwise noted, the reactions were performed at 100°C for 24 h. During the reaction, samples of 0.1 ml were periodically collected, filtered and analysed by GC-FID and GC-MS. The amounts of substrates and products were quantified using anisole as internal standard. The conversions were calculated from the conversion of alcohol. The reported values were consistent with the corresponding values calculated from the conversion of amine within  $\pm 5\%$ .

## 5.3. Results and discussion

Table 5.1 shows an overview of the prepared catalysts. As expected, the surface areas of the Ag supported catalysts were similar to the parent support materials. The TEM images showed that the nanoparticle size distributions were relatively broad. As expected, the average size of the nanoparticles increased with the Ag loading. In general, the nanoparticles were evenly distributed over the support and  $<30$ ,  $<50$  and  $<70$  nm for the 1, 5 and 10 wt% catalyst, respectively.

**Table 5.1.:** Overview of the prepared catalysts.

Entry	Catalyst	Metal loading (wt%)	S <sub>BET</sub> (m <sup>2</sup> /g)	Size range (nm)
1	MgAl <sub>2</sub> O <sub>4</sub>	-	74	-
2	Ag/MgAl <sub>2</sub> O <sub>4</sub>	5	76	20-70
3	HT	-	135	-
4	Ag/HT	5	142	10-60
5	Ag/HT*	5	135	10-70
6	Al <sub>2</sub> O <sub>3</sub>	-	219	-
7	Ag/Al <sub>2</sub> O <sub>3</sub>	1	241	10-30
8	Ag/Al <sub>2</sub> O <sub>3</sub>	5	223	20-50
9	Ag/Al <sub>2</sub> O <sub>3</sub>	10	227	20-70
10	Au/Al <sub>2</sub> O <sub>3</sub>	5	217	10-50

\* Prepared by co-precipitation.

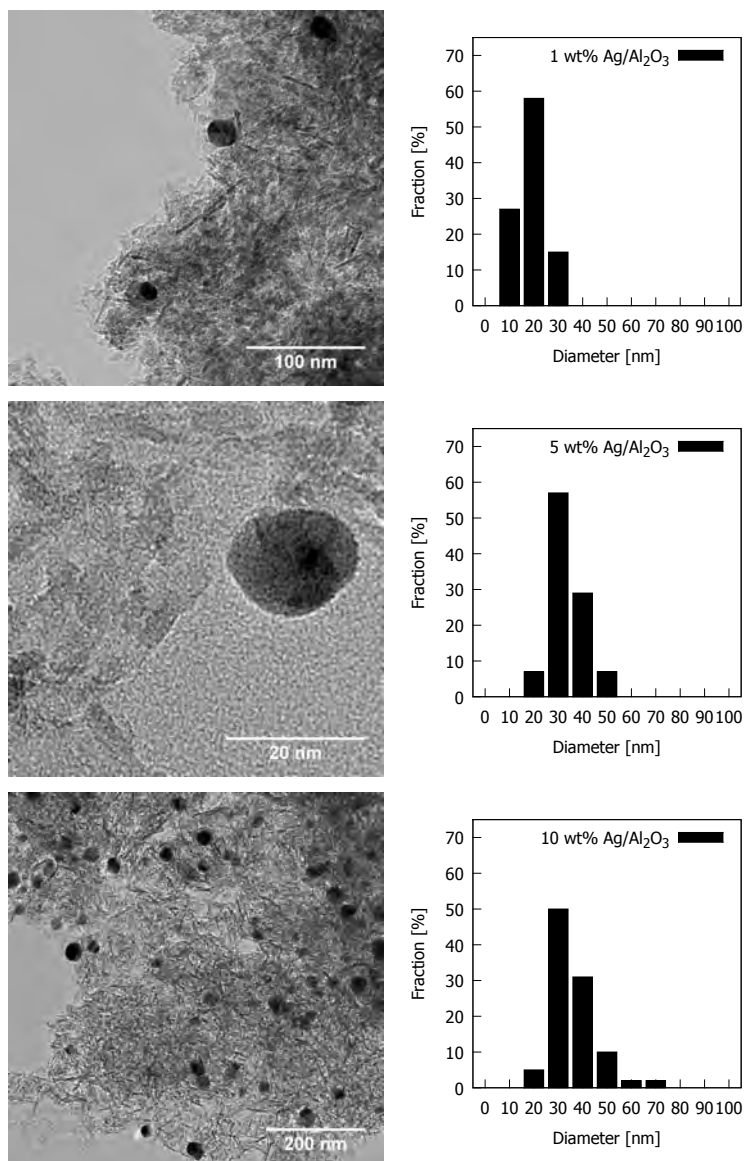
The dehydrogenation of benzyl alcohol to benzaldehyde was used as a model reaction to study the effect of the support materials and Ag loading. Table 5.2 shows the conversion, selectivity and yield from the dehydrogenation of benzyl alcohol under Ar (*i.e.* under oxidant-free conditions) after 24 hours at 100°. While no reaction occurred with the pure support materials, the Ag supported catalysts all afforded benzaldehyde in moderate to good yield. The activity of 5 wt% Ag/MgAl<sub>2</sub>O<sub>4</sub> and 5 wt% Ag/HT (Entry 2 and 4) resulted in 17-18% conversion with 70-72% selectivity, respectively. Surprisingly, the 5 wt% Ag/Al<sub>2</sub>O<sub>3</sub> (Entry 8) resulted in 60% conversion and 96% selectivity under the same reaction conditions. The co-precipitated hydrotalcite catalyst (Entry 5) did not result in any conversion, while the 5 wt% Au/Al<sub>2</sub>O<sub>3</sub> (Entry 10) only resulted in 8% yield. The main by-product in all reactions was benzyl benzoate.

**Table 5.2.:** Effect of support material and metal loading.

Entry	Catalyst	Conversion (%)	Selectivity (%)	Yield (%)
1	MgAl <sub>2</sub> O <sub>4</sub>	1	30	<1
2	Ag/MgAl <sub>2</sub> O <sub>4</sub>	17	70	12
3	HT	0	0	0
4	Ag/HT	18	72	13
5	Ag/HT*	0	0	0
6	Al <sub>2</sub> O <sub>3</sub>	5	20	1
7	Ag/Al <sub>2</sub> O <sub>3</sub>	28	3	1
8	Ag/Al <sub>2</sub> O <sub>3</sub>	60	96	57
9	Ag/Al <sub>2</sub> O <sub>3</sub>	15	60	9
10	Au/Al <sub>2</sub> O <sub>3</sub>	10	82	8
11	-	0	0	0

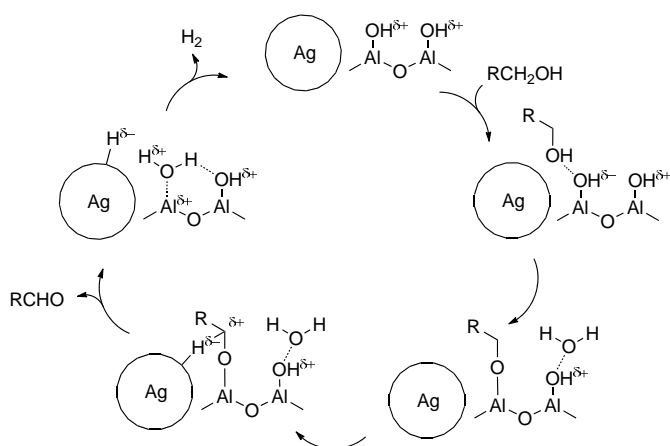
Reaction conditions: benzyl alcohol (2mmol), anisole (0.2 mmol), toluene (6ml), catalyst (100 mg), 24 h at 100°C under Ar.

The results in Table 5.2 also show the effect of the Ag loading. Since the same amount of catalyst was used in the reactions the increase in conversion from 1 to 5 wt% was expected. However, when the Ag loading was increased to 10 wt% the conversion and selectivity decreased significantly. This may be explained by the increased size of the nanoparticles as shown in Figure 5.2.



**Figure 5.2.:** TEM images and size distributions of 1 wt%, 5 wt% and 10 wt% Ag/Al<sub>2</sub>O<sub>3</sub>, respectively.

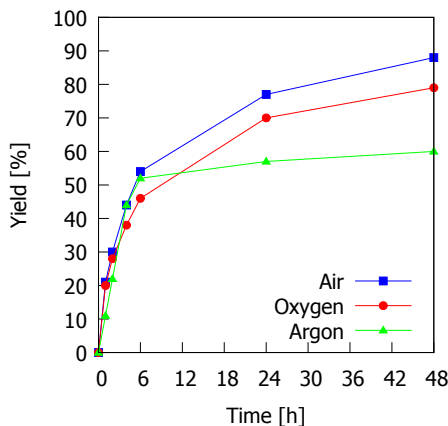
Shimizu *et al.* [150] previously proposed a mechanism where the dehydrogenation of alcohol is facilitated by the special acid-base sites on  $\text{Al}_2\text{O}_3$ . In this mechanism, the reaction proceeds in three steps, including 1) the reaction of the alcohol on a basic site to give an alkoxide and an adsorbed water molecule, 2) C-H activation of the alkoxide on the Ag nanoparticle to give a silver hydride species and a carbonyl compound and 3)  $\text{H}_2$  desorption from an alumina acid site, see Figure 5.3. The proposed mechanism may therefore explain the higher activity of Ag on  $\text{Al}_2\text{O}_3$  with respect to other supports. A similar mechanism has recently been proposed by Sushkevich *et al.* for the gas phase dehydrogenation of ethanol to acetaldehyde over  $\text{Ag}/\text{SiO}_2$  [151].



**Figure 5.3.:** Proposed mechanism for the dehydrogenation of alcohols on  $\text{Ag}/\text{Al}_2\text{O}_3$ . Adapted from [150].

As the dehydrogenation is dependent on the abstraction of hydrogen on the Ag atoms and a fast removal of this hydrogen is important for a high reaction rate, the reactions were also tested under atmospheric air and pure oxygen. Under these conditions, water is formed as by-product rather than molecular hydrogen. Figure 5.4 show the yield of benzaldehyde with reaction time over 5 wt%  $\text{Ag}/\text{Al}_2\text{O}_3$  in atmospheric air, pure oxygen and under an inert Ar atmosphere, respectively.

While the reaction rate was similar during the first 24 hours, the reaction performed in atmospheric air resulted in the highest yield after 48 hours. These results indicated that the presence of small amounts of  $\text{O}_2$  effectively increased the reaction rate, while too much  $\text{O}_2$  slightly decreased the catalytic activity, possibly due to formation of inactive silver oxide species [152].



**Figure 5.4.:** Yield of benzaldehyde as a function of reaction time using 5 wt% Ag/Al<sub>2</sub>O<sub>3</sub> at 100°C under atmospheric air, O<sub>2</sub> and Ar.

The effect of the reaction temperature was investigated under atmospheric air for 24 hours. As expected, the conversion decreased significantly as the temperature was decreased from 100 to 60°C. Furthermore, the formation of benzylbenzoate was suppressed at high temperatures, which resulted in 95% conversion and 97% selectivity at 100°C, see Table 5.3.

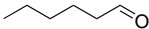
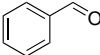
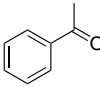
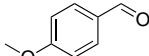
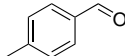
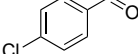
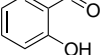

**Table 5.3.:** Effect of reaction temperature on the oxidation of benzyl alcohol to benzaldehyde.

Entry	Temperature (°C)	Conversion (%)	Selectivity (%)	Yield (%)
1	60	19	75	14
2	80	45	70	32
3	100	95	97	92

Reaction conditions: benzyl alcohol (2 mmol), anisole (0.2 mmol), toluene (6 ml), 5 wt% Ag/Al<sub>2</sub>O<sub>3</sub> (100 mg), 24 h under atmospheric air.

Table 5.4 compiles the conversion, selectivity and yield for a number of different alcohols. All reactions were carried out using 5 wt% Ag/Al<sub>2</sub>O<sub>3</sub> for 24 hours under atmospheric air at 100°C. All alcohols were converted into the corresponding carbonyl compounds. However, while benzyl alcohol almost reached full conversion in 24 hours, 1-hexanol only reached 27% conversion. In agreement with the results in Chapter 4, these results showed that the conversion of aliphatic alcohols were more difficult to oxidise than benzylic alcohols. The secondary alcohol 1-phenylethanol reached full conversion within 24 hours and afforded the corresponding ketone acetophenone in 94% yield.

**Table 5.4.:** Oxidation of different alcohols over 5 wt% Ag/Al<sub>2</sub>O<sub>3</sub> under atmospheric air <sup>a</sup>.

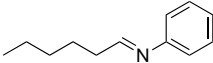
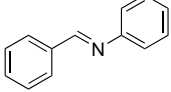
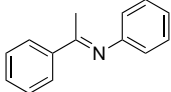
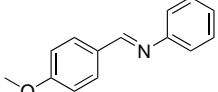
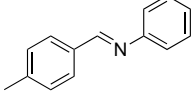
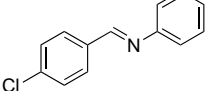
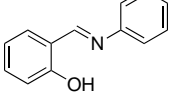
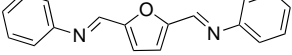
Entry	Product	Conversion (%)	Selectivity (%)	Yield (%)
1		27	74	20
2		95	97	92
3		100	99	99
4		100	98	98
5		96	98	94
6		46	97	45
7		100	99	99
8		23	73	17

<sup>a</sup> Reaction conditions: alcohol (2 mmol), anisole (0.2 mmol), toluene (6 ml), 5 wt% Ag/Al<sub>2</sub>O<sub>3</sub> (100 mg), 24 h at 100°C under atmospheric air.

Entries 4-6 in Table 5.4 show the substituent effect of different *para*-substituted benzyl alcohol derivatives. The decrease in conversion going from *p*-OCH<sub>3</sub> to *p*-CH<sub>3</sub> to *p*-Cl indicate a linear free energy relationship where substrates with electron donating substituents (*p*-OCH<sub>3</sub>) are more reactive than substrates with electron withdrawing substituents (*p*-Cl). These results suggest that a positive charge is build up in the benzylic position during the rate determining step, which is in good agreement with the hydrogen abstraction step proposed by Shimizu *et al.* [150]. Furthermore, furan-2,5-dicarbaldehyde was obtained in 17% yield from the oxidation of 5-hydroxymethylfurfural. Furthermore, the 5 wt% Ag/Al<sub>2</sub>O<sub>3</sub> catalyst was used to study the direct formation of imines by the oxidative dehydrogenation and condensation of alcohols and amines. All reactions were performed under the same reaction condition adding one equivalent of aniline as the amine substrate. No further optimisation was attempted for the individual substrates.

The results in Table 5.5 show that all substrates reacted to the corresponding imine, with the exception of 1-hexanol and aniline, which did not react under the given reaction conditions. Although the conversion of benzyl alcohol decreased slightly from 95% to 82%

**Table 5.5.:** Results from the oxidation of various alcohols in the presence of aniline over 5 wt% Ag/Al<sub>2</sub>O<sub>3</sub> under atmospheric air<sup>a</sup>.

Entry	Product	Conversion (%)	Selectivity (%)	Yield (%)
1		0	-	-
2		82	99	81
3		71	95	68
4		95	98	94
5		100	99	99
6		65	98	64
7		100	68	68
8		20	80	16

<sup>a</sup> Reaction conditions: alcohol (2 mmol), aniline (2 mmol), anisole (0.2 mmol), toluene (6 ml), 5 wt% Ag/Al<sub>2</sub>O<sub>3</sub> (100 mg), 24 h at 100°C under atmospheric air.

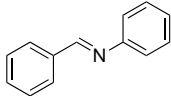
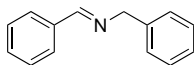
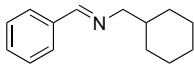
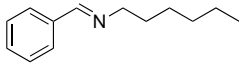
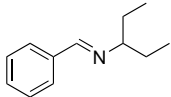
in the presence of aniline, the selectivity to the product *N*-benzylideneaniline increased as less benzyl benzoate was formed. The formation of benzyl benzoate in the oxidation of benzyl alcohol to benzaldehyde may be explained by the condensation of benzyl alcohol with benzoic acid (formed by over-oxidation or aldehyde disproportionation) or by the oxidation of a hemiacetal (formed by the reaction of benzyl alcohol and benzaldehyde). In both cases, the selectivity may be increased as the benzaldehyde intermediate reacts in fast condensation step to form the desired imine. For this reason, it is expected that even higher selectivity would be achieved by increasing the ratio of amine to alcohol. The same trend in yield was observed for the three *para*-substituted benzyl alcohols



derivatives, which confirmed that the oxidation of the alcohol is the rate determining step of the overall reaction. While 2-((phenylimino)methyl)phenol was obtained in 68% yield due to low selectivity (Entry 7), the diphenylimine of HMF was obtained in 16% yield due to low conversion (Entry 8).

Table 5.6 show the conversion selectivity and yield from the reaction of benzyl alcohol with different amines, including benzyl amine, cyclohexylmethanamine, hexan-1-amine, and pentan-3-amine. All amine substrates reacted with benzyl alcohols to afford the desired products with high selectivity (> 94%). While the reaction with benzyl amine and cyclohexylmethanamine resulted in 10% and 17% conversion, respectively, pentan-3-amine resulted in 32% conversion. The highest conversion of 82% was obtained with aniline, followed by hexan-1-amine with 66% conversion.

**Table 5.6.:** Results from the oxidation of benzyl alcohol in the presence of various amines over 5 wt% Ag/Al<sub>2</sub>O<sub>3</sub> under atmospheric air<sup>a</sup>.

Entry	Product	Conversion (%)	Selectivity (%)	Yield (%)
1		82	99	81
2		10	99	10
3		17	94	16
4		66	99	66
5		32	97	31

<sup>a</sup> Reaction conditions: alcohol (2 mmol), aniline (2 mmol), anisole (0.2 mmol), toluene (6 ml), 5 wt% Ag/Al<sub>2</sub>O<sub>3</sub> (100 mg), 24 h at 100°C under atmospheric air.

Compared to the previously reported results with Au catalysed imine synthesis [129–131; 153], the supported Ag catalysts are different in several aspects. In general, the Ag catalysts require higher temperatures than the Au catalysts that are active at room temperature. Furthermore, the Au catalysts are not deactivated by high partial pressures of oxygen. On the other hand, the Au catalysts require strongly alkaline conditions to obtain high yields. The need for base may be a problem in some systems as various base-catalysed side reactions may decrease the selectivity [54]. It is noteworthy that the supported Ag catalysts need no additives or co-catalysts and even were active under oxidant-free conditions with equimolar amounts of alcohol and amine.

## 5.4. Summary

Ag nanoparticles supported on  $\text{Al}_2\text{O}_3$  is an efficient catalyst for the oxidative dehydrogenation of alcohols to aldehydes and can also be used for the direct formation of imines from alcohols and amines. The highest catalytic activity was obtained with 5 wt% Ag/ $\text{Al}_2\text{O}_3$  in toluene using atmospheric air as oxidant. Under pure oxygen, the conversion was decreased, which indicated that the active Ag atoms may be oxidised to inactive silver oxide. The reactions could also be performed under oxidant-free conditions, where the reaction was driven to the product side by formation of  $\text{H}_2$  into the gas-phase. The reactions were performed at relatively mild conditions ( $100^\circ\text{C}$  and atmospheric pressure) without any additives or co-catalysts and afforded the desired imines with high selectivity (up to 99%) from equivalent amounts of alcohols and amines.



## Chapter 6

### Zeolites

---

This chapter gives an introduction to zeolites, which are used as catalysts and support materials in Chapter 7 and 8, respectively. The chapter begins with a general introduction to zeolites, zeolite synthesis and the possible strategies to optimise diffusion without compromising activity or shape selectivity. In the end of the chapter, the experimental section describes the synthesis of three silicalite-1 zeolites with very different morphology.

---

#### 6.1. Introduction

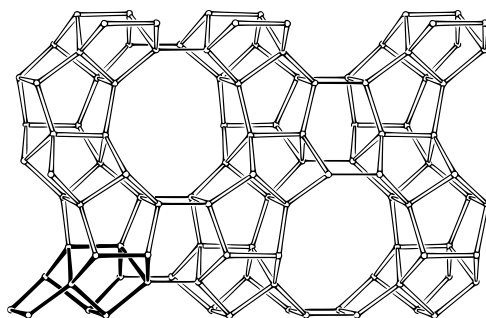
Zeolites are among the most used industrial catalysts and the application range from oil refining to synthesis of speciality chemicals and environmental catalysis. Structurally, zeolites are built from tetrahedral  $\text{TO}_4$  units (T=Si or Al) that are organized into a three-dimensional framework by sharing the oxygen atoms, which gives zeolites an overall composition of  $\text{TO}_2$ . In general, zeolites contain Si, Al and O, but it is also possible to make zeolites of pure  $\text{SiO}_2$  or to incorporate elements such as B, Ti, V, Fe, Ga, Ge or Sn. Strictly speaking, these materials are defined as zeotypes, but in the remaining of the thesis zeotypes are not distinguished from zeolites.

Zeolites are normally found to obey what is known as Lövensteins rule [154], which states that Al-O-Al linkage is forbidden in a zeolite framework. This means that the majority of the T atoms must be silica and that zeolites therefore can be regarded as silicates with a fraction of the Si substituted by *e.g.* Al atoms. As a result, the Si/Al ratio cannot be smaller than unity. All zeolites can be thought to consist of a large number of small building units that are assembled to form a crystalline solid with a high surface area and well-defined system of pores and cavities. The small units are known as secondary building units and can consist of as many as 16 T atoms (linked by oxygen). The diameters of the pores are determined by the number of T-atoms in the ring surrounding the pore. Zeolites are grouped into small-pore zeolites (up to 8 T-atoms), medium-pore zeolites (up to 10 T-atoms), large-pore zeolites (up to 12 T-atoms) and extra large-pore zeolites (up to 14 T-atoms or more). Since the dimensions of the micropores in zeolites are in the same order as small organic molecules (around

3-12 Å) and therefore can be used to separate compounds based on their size, zeolites are also known as molecular sieves.

In order to distinguish between the more than 218 unique zeolite structures known today, the international zeolite association [155] has assigned a three-letter code to each structure. While the code for the natural zeolites are based on the first three letters of the mineral name, such as STI for stilbite, the naming of synthetic zeolites are more complicated. For instance, the structure of the well-known ZSM-5 (five) zeolite has the three-letter code MFI. Furthermore, the three-letter code only takes the structure into account and not the chemical composition of the framework, which is typically reported as the metal or metal oxide ratio.

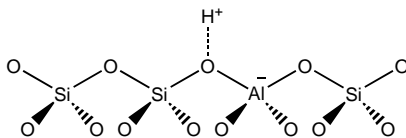
Figure 6.1 show the connection mode of a MFI structured zeolite and gives an impression of the uniform micropores that penetrates the crystal structure and gives rise to many of the interesting properties of zeolites. In principle, the MFI zeolite can be built from units of 12 T atoms (emphasised in black).



**Figure 6.1.:** *The connection mode and periodic building unit in a zeolite with MFI structure. Please note that the oxygen atoms are omitted for clarity. Adapted from [155].*

## 6.2. Zeolite catalysis

Since Al is a trivalent metal, the presence of tetrahedrally coordinated Al atoms in the zeolite framework results in a charge deficiency that must be compensated for by an organic or inorganic cation (such as an alkali or alkaline-earth cation). In principle, all cations which are small enough to fit into the zeolite micropores can be used as charge-compensating cations, which makes zeolites very useful ion-exchangers for instance in laundry detergents. It is also possible to substitute the cations to modify the catalytic properties of the zeolite. In particular, the cation may be exchanged with a proton which gives an acid site and is the basis for the important application of zeolites as solid acid catalysts.



**Figure 6.2.:** Schematic representation of a Brønsted acid site in an Al-containing zeolite.

The acidity of a zeolite depends on the number of acid sites and therefore on the degree of aluminium substitution. However, the strength of the individual acid site is also dependent on the presence of neighbouring Al atoms and the framework structure. Since the strength of the individual acid sites increases with the Si/Al ratio, the highest acidity is therefore typically obtained for zeolites with Si/Al > 10 [156]. Acidic zeolites are widely used as catalysts in the petrochemical industry, especially for isomerisation, fluid catalytic cracking and hydrocracking [1].

It is also possible to prepare zeolites of pure silica or to introduce other hetero atoms in the framework, including B, Ti, V, Fe, Ga, Ge or Sn [157]. The number and nature of the incorporated hetero atoms has a large effect on the stability and catalytic properties of the zeolite. For instance, the incorporation of trivalent metals such as Ga, Fe and B can be used to fine tune the Brønsted acid sites (Al > Ga > Fe > B), whereas the incorporation of tetravalent metals such as Ti or Sn can be used to introduce redox active sites and Lewis acid sites. While Sn-containing zeolites are promising catalysts for synthesis of lactic acid (or methyl lactate) from isomerisation of trioses [158] and even hexoses [159], titanium-containing zeolites are already widely used for a number of oxidation, ammoxidation and epoxidation reactions with H<sub>2</sub>O<sub>2</sub>. A more detailed introduction to titanium-containing zeolites is given in Chapter 7.

The size and shape of the zeolite micropores gives rise to another important feature of zeolite catalysts, namely the shape selectivity. Shape selectivity may cause the product distribution to deviate from the ideal distribution if the reactants, intermediates or products are inhibited by the spatial constraints of the zeolite micropores [160]. In general, there are three different types of shape selectivity, including 1) reactant, 2) product and 3) transition state selectivity. Reactant selectivity occurs when only small substrate molecules, that are able to diffuse sufficiently fast to the active site, are converted. However, the substrate not only needs to reach the active site, it also has to react and then diffuse out of the zeolite. Product selectivity occurs when several different products are possible, but the product distribution is determined by the diffusion of products leaving the zeolite. Eventually, the production of bulky products may deactivate the catalyst by pore blocking. If the change in product distribution arises from the actual product formation step, the effect is called transition state shape selectivity.

### 6.3. Zeolite synthesis

Zeolite synthesis is a crystallisation process, where the silica and metal precursors dissolve and react to form a less soluble crystalline metal silicate product. In general, zeolites are synthesised under hydrothermal conditions, *i.e.* under elevated temperature and autogenous pressure. Depending of the temperature and the gel composition, complete crystallisation may take place within a couple of hours or up to several days. A typical zeolite gel consists of a solvent, a metal precursor, a mineralisation agent and a structure directing agent (SDA) and may appear as a dry solid, a gel, a milky suspension or clear solution prior to the hydrothermal crystallization. Typical Si precursors include silica ( $\text{SiO}_2$ ), sodium silicate ( $\text{Na}_2\text{SiO}_3$ ), silicic acid ( $\text{H}_4\text{SiO}_4$ ) and metal alkoxides such as tetraethyl orthosilicate (TEOS), while typical Al precursors include sodium aluminate ( $\text{NaAlO}_2$ ), aluminium nitrate ( $\text{Al}(\text{NO}_3)_3$ ) and aluminium isopropoxide ( $\text{Al}(\text{O}-i\text{-Pr})_3$ ). The most used mineralising agent is the hydroxide ion and zeolite synthesis is therefore often performed at high pH. An alternative mineralising agent is the fluoride ion, which makes it possible to synthesise zeolites at neutral pH. The structure directing agent can be alkali metal ions such as  $\text{Na}^+$  and  $\text{K}^+$ , but is most often soluble organic species such as quaternary tetraalkylammonium cations. In synthesis of MFI zeolites tetrapropylammonium hydroxide is the preferred structure directing agent.

As mentioned in the introduction, the role of the SDA is not fully understood, although it may have several important functions. For instance it may help to 1) stabilise framework constituent to form more open structures, 2) control chemical equilibria, 3) pre-organise solution species to favour nucleation of a specific structure and 4) form porosity by acting as a space filling template [23]. The pre-organising and space filling function is particularly important in the synthesis of high silica zeolites, where charge interactions are absent [161]. For instance, it has been shown that the tetrapropylammonium cation is found to be located exactly in the intersection between the straight and sinusoidal channels of the MFI structured silicalite-1 [162].

In general, three basic chemical processes take place during the zeolite synthesis, including dissolution, nucleation and crystal growth. During the induction period, the precursor gel is dissolved to re-precipitate as an equilibrated gel. This gel may contain some degree of local order directed by the SDA. The equilibrated gel is sometimes allowed to age before the temperature and pressure is increased to induce the crystallisation. This ageing may cause a higher degree of order and more nucleation sites, which favour the formation of smaller zeolite crystals [163]. It is important to mention that the zeolite structure is a metastable phase during the hydrothermal synthesis, which means that the product is kinetically controlled and even slight variations in the synthesis conditions can therefore change the product significantly [164].

After the synthesis the autoclave is cooled to room temperature and the zeolite

product is washed with water and isolated by filtration or centrifugation. The product is then dried and calcined typically around 550°C in order to remove residual SDA and framework water.

## 6.4. Diffusion in zeolites

Although many of the remarkable properties zeolites are related to their microporous structure, the presence of micropores also limit their use when it comes to large and bulky molecules. The reason for this is that molecules that are about the same size of the micropores are almost always in contact with the pore wall which inevitable slows down the diffusion of substrates and products in and out of the zeolite. For this reason, the rate of diffusion within a zeolite can be orders of magnitude lower than molecular or Knudsen diffusion and is often referred to as configurational diffusion [165].

Consider for instance a first order reaction where diffusion is rate limiting. For a single cylindrical pore where the reaction takes place on the wall, the effectiveness factor  $\eta$  is given by

$$\eta = \frac{r_{observed}}{r_{intrinsic}} = \frac{\tanh(\phi)}{\phi} \quad (6.1)$$

where  $r$  is the reaction rate and  $\phi$  is the Thiele modulus defined by

$$\phi = \sqrt{\frac{k}{D_e/L^2}} \quad (6.2)$$

Here,  $L$  is the diffusion path length,  $k$  is the reaction rate constant and  $D_e$  is the effective diffusivity. The equations show that the effectiveness approaches unity if the Thiele modulus is decreased and there are two approaches to achieve this.

The first approach is to increase the effective diffusivity ( $D$ ) by increasing the pore size of the zeolite. Over the last 20 years, much effort has therefore been devoted to synthesise large- and extra-large pore zeolites [166]. This has resulted in a number of new structures with more than 12 T atoms in their pore rings, which are typically synthesised using even more complex structure directing agent [166]. In particular, the recent discovery of ITQ-43 which has 28 atoms in the pore ring and represent the first inherent hierarchical zeolite structure with interconnecting pores of around 2 and 0.6 nm [167]. However, beside the high cost of these SDAs, the increase in pore size may also compromise the activity, shape selectivity and stability of the catalysts, which may limit their general application [168].

The second approach is to decrease the mean diffusion path length ( $L$ ). This can be done by either decreasing the size of the zeolite crystals or by introducing an additional system of mesopores. In the last decade, much attention has been focused on synthesis of mesoporous zeolites, because they offer the possibility to combine the fast



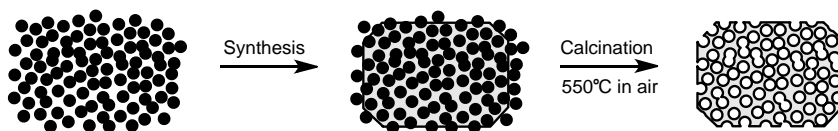
diffusion of mesoporous materials with the high stability, catalytic activity and selectivity of conventional microporous zeolites.

In order to synthesise nanosized zeolites, the reaction conditions has to be controlled in much detail. In particular, the homogeneity of the starting system and the simultaneity of event to form the precursor gel are very important. The synthesis is therefore often performed in highly diluted systems with large quantities of tetraalkylammonium hydroxide, which induces a fast nucleation and the formation of smaller crystals with a narrow particle distribution [169]. Furthermore, the synthesis is often carried out under mild condition, typically at temperatures  $<120^{\circ}\text{C}$ . Another important method to synthesise nanosized zeolites is the confined space synthesis which was briefly mentioned in section 1.4. Although nanosized zeolites have many interesting advantages, such as the controllable size, well-defined crystal morphology and a high colloidal stability, there are also some important drawbacks, including the difficult scale up, the low crystalline yield (typically  $<10\%$ ) and the difficult separation.

The different methods to synthesise mesoporous zeolites can be described as bottom-up and top-down approaches. The most common examples is modification of the preformed zeolite by demetallation or steaming (bottom-up) and the manipulation of the crystallisation process by carbon templating (top-down).

In demetallation parts of the preformed zeolite is removed by dissolution. For instance, a zeolite can be made mesoporous by a simply submersing the zeolite into a dilute aqueous solution of NaOH under moderate temperature. This post-synthesis treatment is also known as desilication. The greatest advantage of desilication is that the method is relatively cheap and the porosity can be tuned by simply changing the base, pH, temperature or reaction time. On the other hand, a significant drawback is that desilication is very dependent on the Si/Al ratio and may result in relatively low yields of recovered zeolite. Often the yield is only 40-90% of the parent zeolite, which may significantly increase the final cost of the overall process [170].

As mentioned in section 1.4, the preparation of mesoporous zeolites by carbon templating was first developed at Haldor Topsøe by Jacobsen *et al* [32]. The basic idea is that the zeolite precursors nucleating inside a carbon material so that the zeolite grows and partially encapsulates the carbon. After complete crystallisation, the carbon is removed by combustion. A schematic representation of the synthesis is shown in Figure 6.3

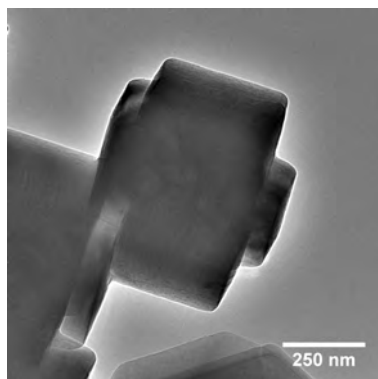


**Figure 6.3.:** Schematic representation of the synthesis of a mesoporous zeolite by carbon-templating.

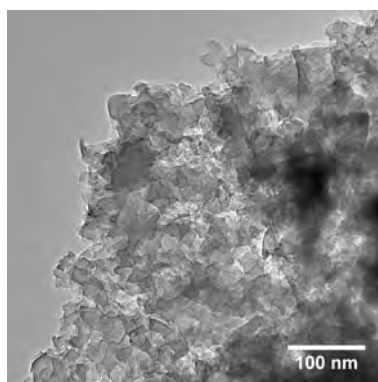
Compared to steaming and demetallation, carbon templating has several advantages. First of all, the method is independent of the zeolite structure and chemical composition. Furthermore, very high mesoporous volumes can be achieved and finally the size of mesopores can be controlled by using different carbon materials. The synthesis of pyridine *N*-oxide using mesoporous titanium silicalite-1 prepared by both desilication and carbon-templating is described in Chapter 7.

Another emerging method to synthesise mesoporous zeolites is recrystallization, which is basically a dissolution-reassembly process often performed in the presence of a surfactant, such as cetyl trimethylammonium bromide (CTAB). In the first step, dissolution in a dilute alkaline solution leads to partial dissolution of and extraction of zeolite fragments, which results in the perforation of the zeolite crystal by mesopores or to complete zeolite depolymerisation. The following step involves re-assembling of the dissolved species into a mesoporous structure under hydrothermal conditions. During the synthesis the main role of the surfactant is to protect the zeolite from non-uniform leaching [171]. Similar effects of controlled desilication have also been reported in the presence of tetraalkylammonium hydroxide such as tetrapropylammonium hydroxide (TPAOH) and tetrabutylammonium hydroxide (TBAOH) [172]. Another possible explanation was proposed by García-Martínez *et al.* [173], who proposed that the formation of the uniform porosity is generated through a surfactant-assisted crystal rearrangement mechanism. In this mechanism, the alkaline dissolution creates negatively charged sites inside the zeolite framework which attract the cationic surfactants. The electrostatic interactions then causes to the zeolite to rearrange around the surfactant micelles. Recently, Ivanova *et al.* [174] reported a detailed investigation of all intermediate products involved in the process and concluded that the recrystallization involves 1) fast ion-exchange with sodium cations and zeolite desilication, 2) diffusion of CTAB inside the pores and the ion-exchange of sodium with CTA-cations, 3) formation of micelles and condensation of siliceous species around the micelles both in the intracrystalline mesopores and on the external surface of the zeolite.

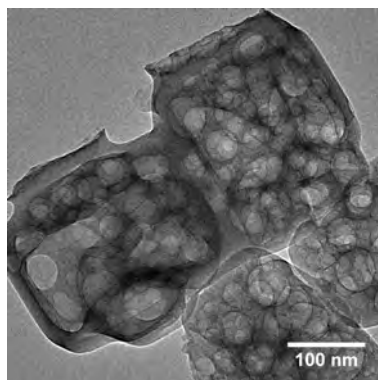
For comparison, Figure 6.4 shows three silicalite-1 samples with very different morphology. The first sample was prepared by a conventional hydrothermal synthesis, the second sample was prepared by carbon-templating and the third sample was prepared by prepared by recrystallization in TPAOH, see experimental section.



(a) Conventional



(b) Carbon templated



(c) Recrystallized in TPAOH

**Figure 6.4.:** *Three silicalite-1 samples with very different morphology.*

## 6.5. Summary

Much of the success of zeolites as heterogeneous catalysts can be attributed to their unique microporous structure and the possibility to tailor intrinsic properties, such as the number and strength of the acid sites, the redox properties, the hydrophobic/hydrophilic character and the pore architecture [175]. In particular, the microporous structure makes it possible to conduct shape selective catalysis, which is one of the most remarkable achievements in zeolite catalysis. On the other hand, the zeolite micropores also cause severe diffusion limitations when it comes to large and bulky substrates. In general, there are two possible strategies to overcome these diffusion limitations, including 1) to increase the diameter of the micropores or 2) to decrease the mean diffusion path length. Recently, the synthesis of mesoporous zeolites has received much attention as they offer optimum diffusion without compromising the activity or shape selectivity of the inherent zeolite micropores. The following two chapters will demonstrate how detailed control of the porosity can significantly increase the diffusion and facilitate the synthesis of small and disperse gold nanoparticles upon simple impregnation.

## 6.6. Experimental section

### 6.6.1. Materials

Commercial carbon black particles (Black Pearls 2000, Carbot Corporation) with an average particle diameter of around 12 nm were used as carbon-template for the synthesis of mesoporous silicalite-1. The carbon black particles were dried at 90°C for 24 h prior to use. All other reagents were of reagent grade and used without further purification or pretreatment: tetraethylorthosilicate (TEOS, Sigma-Aldrich), tetrapropylammonium hydroxide (TPAOH, 1M aqueous solution, Sigma-Aldrich) and deionized water.

### 6.6.2. Synthesis of silicalite-1

TEOS (4.465 ml) was added dropwise to TPAOH (1M, 7.265 ml) under stirring in a Teflon beaker. The mixture was stirred for 1 hour and then transferred to a Teflon-lined stainless steel autoclave (130 ml). The autoclave was heated to 180°C for 24 h under autogeneous pressure. The product was thoroughly washed with water, collected by filtration and washed again several times (until neutral pH). The product was dried at room temperature overnight and then calcined for 20 hours at 550°C (heating 5°C/min) to give a fine white powder.

### 6.6.3. Synthesis of mesoporous silicalite-1

Pre-dried carbon black (2 g) was put in a Teflon beaker, impregnated with TPAOH (1M, 7.265 ml) and dried at room temperature overnight. The material was then impregnated with TEOS (4.465 ml) and dried at room temperature overnight once more. The Teflon beaker was placed inside a Teflon-lined stainless steel autoclave (130 ml) containing enough water to produce saturated steam (15 ml) and heated to 180°C for 72 hours. The product was thoroughly washed with water, collected by filtration and washed again several times (until neutral pH). The product was dried at room temperature overnight and then calcined for 20 hours at 550°C (heating 5°C/min) to give a fine white powder.

### 6.6.4. Synthesis of recrystallized silicalite-1

Silicalite-1 (1 g) and TPAOH (1M, 6.05 ml) was added to a Teflon-lined autoclave and heated to 170°C for 24 h. The product was thoroughly washed with water, collected by filtration and washed again several times (until neutral pH). The product was dried at room temperature overnight and then calcined for 20 hours at 550°C (heating 5°C/min) to give a fine white powder.

# Chapter 7

## Synthesis of *N*-oxides

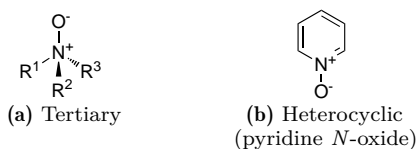
---

The results in this chapter demonstrate that mesoporous titanium silicalite-1 prepared by carbon-templating is an efficient catalyst for oxidation of pyridines to pyridine *N*-oxides using aqueous H<sub>2</sub>O<sub>2</sub> as oxidant. The chapter begins with an introduction to *N*-oxides and an outline of recent progress in the synthesis of ordered titanosilicates with focus on the efforts to overcome diffusion limitations.

---

### 7.1. Introduction

*N*-oxides cover a broad range on molecules with N-O bonds where the nitrogen atom is either sp<sup>3</sup> or sp<sup>2</sup> hybridised. The N-O bond has a strong dipole moment, which makes *N*-oxides highly soluble in water. *N*-oxides with a long hydrophobic alkyl tail are therefore often used as surfactants [176]. Furthermore, *N*-oxides are used in multiple organic reactions. In particular, pyridine *N*-oxide can be used as a oxidant [177], but also serves as an important intermediate for the activation and functionalization of the pyridine ring [178]. Figure 7.1 show the general molecular structure of a tertiary and a heterocyclic *N*-oxide (pyridine), respectively.



**Figure 7.1.:** The general molecular structure of *N*-oxides.

The conventional synthesis of *N*-oxides depends on the substrate, but typically relies on per-acids. While some amines can be oxidised with H<sub>2</sub>O<sub>2</sub> in acetic acid (peracetic acid) other requires peroxymonosulfuric acid (Caro's acid) or peracids like *tert*-butyl hydroperoxide (TBHP) or *meta*-chloroperoxybenzoic acid (mCPBA) [179].

### 7.1.1. Titanium Silicalite-1

As described in Chapter 6, the incorporation of isolated Al atoms in a zeolite framework results in a charge deficiency that must be compensated by *e.g.* a  $H^+$  cation, which gives a Brønsted acid site. Incorporation of other heteroatoms, may result in different catalytic properties than acidity. Among the possible heteroatoms, the incorporation of Ti in titanium silicalite-1 (TS-1) is probably one of the most successful examples. Since the discovery of TS-1, several industrial processes have been commercialised, including phenol hydroxylation [180], cyclohexanone ammoxidation [181] and propylene epoxidation [182].

In TS-1 only a small fraction of the tetrahedrally coordinated Si atoms is substituted by Ti. The Ti atoms do not result in a charge deficiency, such as Al, but act as strong Lewis acid sites. The combination of the Lewis acidity and the highly hydrophobic environment in silicalite-1 makes TS-1 an outstanding catalyst for oxidation of simple organic compounds with  $H_2O_2$ . TS-1 is a molecular sieve with MFI structure and medium sized micropores (10-membered rings of around  $5.1 \times 5.6 \text{ \AA}$ ). In order to improve the diffusion of large and non-linear molecules several research groups have made effort to design new and improved titanosilicate catalysts ranging from medium sized TS-1 materials to ultra-large pore ordered mesoporous materials [183]. Unfortunately, the special chemical properties generally seem to disappear as the pore dimension increases. Consequently, a compromise that relieves the diffusion restraints, while maintaining the high activity and shape selectivity of TS-1, is often more desirable [184]. Here, we demonstrate that mesoporous TS-1 prepared by carbon-templating is significantly more active than conventional TS-1 for the oxidation of pyridines to their corresponding N-oxides using aqueous  $H_2O_2$  as the oxidant.

## 7.2. Experimental section

### 7.2.1. Materials

Commercial carbon black particles (Black Pearls 2000, Carbot Corporation) with an average particle diameter of 12 nm were used as carbon-template. The carbon was dried at  $110^\circ\text{C}$  for at least 24 hours prior to use. All other reagents were of reagent grade and used without further purification: tetra-ethylorthosilicate (TEOS, 98 wt%), tetraethylorthotitanate (TEOT, 98 wt%), tetrapropylammonium hydroxide (TPAOH, 40 wt%), hydrogen peroxide ( $H_2O_2$ , 35 wt%), 1,4-dioxane (99.8%), pyridine (99.8%), 2-methylpyridine (98%), 4-methylpyridine (98%), 3,5-dimethylpyridine (98%), ethanol (99 wt%) and deionized water.

### 7.2.2. Synthesis of conventional titanium silicalite-1 (TS-1)

A mixture of TEOS (0.042 g) and TEOT (3.828) corresponding to a molar ratio of Si/Ti = 100 was added dropwise to a solution of TPAOH (40%, 3.40 g) and water. The mixture was stirred for 1 h and then transferred to a Teflon-lined stainless steel autoclave (130 ml). The autoclave was heated to 180°C for 24 h. The autoclaved was cooled to room temperature and the material was collected by filtration and washed with water (until neutral pH). The material was dried at room temperature overnight and then calcined for 24 h at 550°C (heating 2°C/min) to give TS-1 as fine white product.

### 7.2.3. Synthesis of carbon templated titanium silicalite-1 (cTS-1)

Pre-dried carbon black (2.00 g) was impregnated to incipient wetness with a solution of TPAOH (40%, 3.40 g), water and ethanol (3.00 g). After evaporation of the ethanol (24 h at room temperature), the particles were impregnated with a mixture of TEOT (0.042 g) and TEOT (3.828) corresponding to a molar ratio of Si/Ti=100. The impregnated carbon black was placed in a Teflon beaker and placed inside a Teflon-lined stainless steel autoclave (130 ml) containing enough water to produce saturated steam (15 ml) and heated to 180°C for 72 h. The obtained material was washed and calcined following the general procedure described in section 7.2.2, which resulted in cTS-1 as a fine white product.

### 7.2.4. Synthesis of desilicated titanium silicalite-1 (dTTS-1 and cdTTS-1)

TS-1 and cTS-1 was prepared and calcined according to the procedures described above. The catalysts were then treated with a 0.1 M solution of NaOH at 65°C for 30 min (8 mmol base/g catalyst). The desilicated catalysts were filtrated, thoroughly washed with water (until neutral pH) and dried at room temperature overnight to give dTTS-1 and cdTTS-1, respectively.

### 7.2.5. Characterisation

X-ray powder diffraction was measured in transmission mode using Cu-K $\alpha$  radiation from a focusing quartz monochromator and a HUBER G670 Guinier camera. Nitrogen adsorption and desorption measurements were performed at liquid nitrogen temperature (77 K) on a Micromeritics ASAP 2420. The samples were outgassed in vacuum at 300°C for 16 h prior to measurement. UV-Vis spectra were obtained with a VARIAN/CARY 5000 UV-Vis/NIR spectrophotometer equipped with diffuse reflectance unit (EL04114100), using deuterium (UV) and halogen quartz (Vis/NIR) as light sources and a photomultiplier and cooled PbS as detectors. Spectra were registered from 50,000 to 10,000 cm<sup>-1</sup> and obtained directly from the solid powder with no further treatment using Spectralon as



internal standard. Scanning electron microscopy (SEM) was performed on Quanta 200 ESEM FEG microscope with the samples supported on a double adhesive conducting carbon tape.

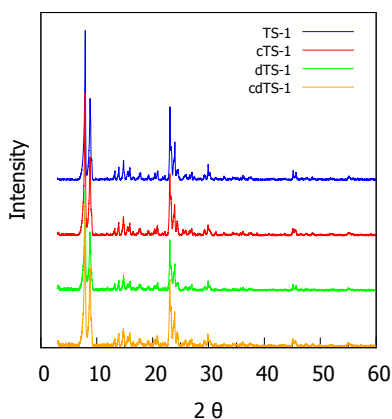
### 7.2.6. Standard oxidation procedure

In a typical experiment, amine (5 mmol), dioxane (internal standard, 0.5 mmol), water (5 ml) and 30 mg of catalysts were charged to a reaction tube together with a stirring bar. The reaction tube was closed with a rubber septum and put in a reaction station (Radley Carousel 12 Plus) that provided stirring and heating for several reactions at the same time. The system was heated to 60°C and the reaction time was started as hydrogen peroxide (7.5 mmol) was added to the reaction. Unless otherwise noted, the reactions were left for 24 h.

During the reactions, samples of 0.1 ml were periodically collected, filtered and analysed by a combined GC-FID/MS from Agilent Technologies. The amounts of substrate and product were quantified using dioxane as internal standard according to equation 4.1-4.3 in Chapter 4. Products other than the desired *N*-oxides were only observed in negligible amounts.

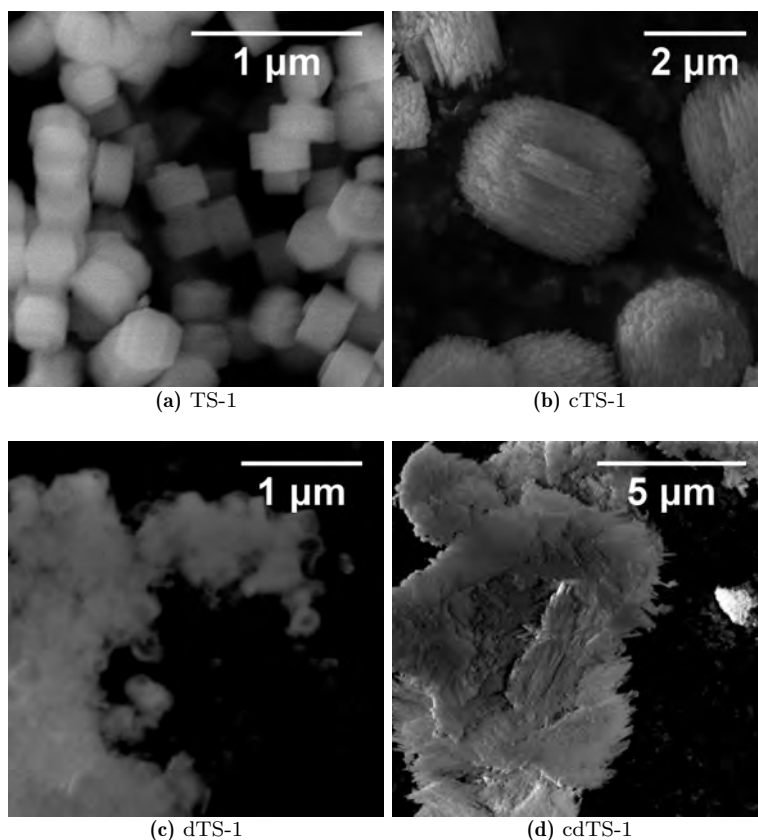
## 7.3. Results and discussion

Figure 7.2 show the X-ray powder diffraction patterns for the conventional (TS-1), carbon-templated (cTS-1), desilicated (dTS-1) and the catalyst prepared by both carbon-templating and desilication (cdTS-1). As expected, the diffractions showed that all samples were highly crystalline and possessed the characteristic MFI structure.



**Figure 7.2.:** X-ray powder diffraction patterns of the prepared TS-1 catalysts.

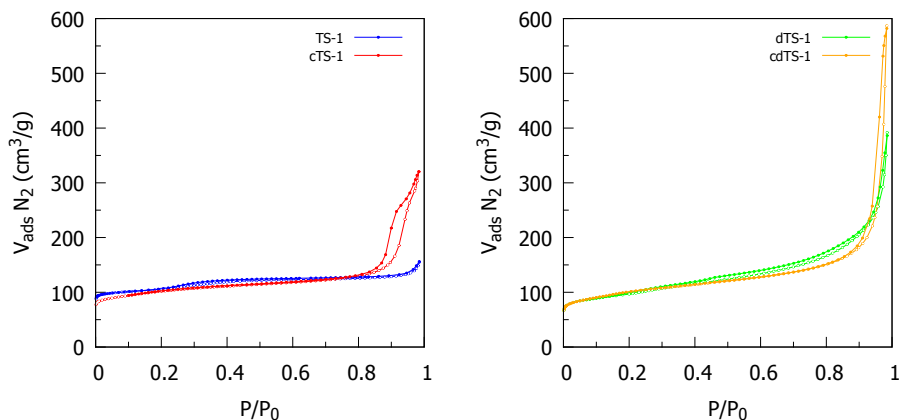
Figure 7.3 show the SEM images of the prepared catalyst. The images showed that the conventional TS-1 consisted of regular coffin shaped crystals that were 300-400 nm in length. The carbon-templated cTS-1 crystals were larger and more irregular in size and shape. Furthermore, the surface of the cTS-1 was perforated by non-crystallographic intracrystalline mesopores. The rough surface indicated that the cTS-1 catalysts were highly porous. The SEM images of the desilicated dTS-1 and cdTS-1 catalysts showed that the harsh alkaline desilication had destroyed most of the characteristic zeolite features.



**Figure 7.3.:** SEM images of the prepared catalysts.

Figure 7.4 show the nitrogen physisorption isotherm of the prepared catalysts. According to the IUPAC classification, the TS-1 catalyst has a typical type I isotherm with a large adsorption at  $P/P_0 < 0.1$  and almost no adsorption in the intermediate relative pressure range. At  $P/P_0 > 0.9$  the uptake of nitrogen may be related to the interparticle volume between the rather small zeolite crystals. In addition, the cTS-1, dTS-1 and

cdTS-1 catalysts also had some character of type IV isotherms with significant hysteresis loops, which is typical for mesoporous materials. The carbon-templated catalysts had hysteresis loops at  $P/P_0 > 0.86$  which could be attributed to the large pores that were observed in the SEM. The dTS-1 and cdTS-1 catalysts showed smaller hysteresis loops closing at  $P/P_0 > 0.42$ .



**Figure 7.4.:** Nitrogen adsorption/desorption isotherms of the investigated catalysts.

The (apparent) total surface area was calculated by the BET method. The micro-pore volume and external surface area were calculated by the  $t$ -plot method and the total pore volume were determined from the isotherm adsorption branch by a single point read at around  $P/P_0 = 0.95$ , see Table 7.1.

**Table 7.1.:** Results from  $N_2$  physisorption analysis.

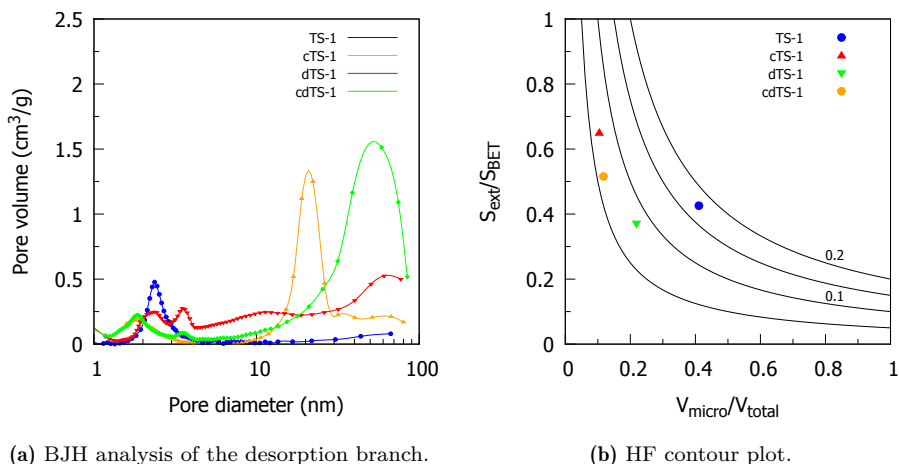
Catalyst	Carbon-templated (c)	Desilicated (d)	$S_{BET}^a$ ( $m^2/g$ )	$S_{ext}^b$ ( $m^2/g$ )	$V_{micro}^b$ ( $cm^3/g$ )	$V_{total}^c$ ( $cm^3/g$ )
TS-1	No	No	390	166	0.092	0.224
cTS-1	Yes	No	346	225	0.050	0.478
dTS-1	No	Yes	367	136	0.098	0.448
cdTS-1	Yes	Yes	353	182	0.073	0.622

<sup>a</sup> Calculated by the BET method. <sup>b</sup> Calculated by the  $t$ -plot method.

<sup>c</sup> Determined from the isotherm adsorption branch at around  $P/P_0 = 0.95$ .

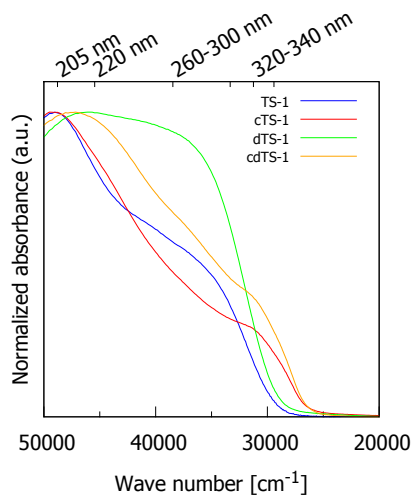
Figure 7.5(a) show the pore size distribution of the prepared catalysts as calculated by BJH analysis of the desorption branch. The carbon templated catalyst cTS-1 had mesopores of around 19 nm, while the subsequent desilication created larger macropores of around 60 nm in cdTS-1. The dTS-1 catalyst exhibited a broad range of meso- and macropores. Both dTS-1 and cdTS-1 had a small peak at around 3.5 nm which originated from the small hysteresis loops at around  $P/P_0 = 0.42$ . These loops may be caused

by the so-called tensile strength effect [185] and does not indicate any real porosity. Furthermore, Figure 7.5(b) show the hierarchy factor (HF) plotted in a contour plot as a function of the relative mesoporous surface area and the relative microporous volume [186]. The plot shows how the increase in the relative mesoporous surface area also causes a significant decrease in the relative microporous volume and, consequently, a lower hierarchy factor.



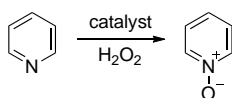
**Figure 7.5.:** Barrett-Joyner-Halenda pore size distribution from 1-100 nm and the hierarchy factor (HF) plotted in a contour plot as a function of the relative mesoporous surface area and the relative microporous volume.

The presence of tetrahedral coordinated Ti-atoms was investigated by ultraviolet-visible spectroscopy (UV-VIS), see Figure 7.6. The UV-vis spectrum of TS-1 had a maximum at around 205 nm, which is characteristic for the charge-transfer of oxygen 2*p* electrons to the empty 3*d* orbitals of tetrahedrally coordinated Ti(OSi)<sub>4</sub> species in the zeolite framework. The shift to 220 nm for the desilicated samples, dTS-1 and cdTS-1, indicated the simultaneous presence of tetrahedral tripodal Ti(OSi)<sub>3</sub>OH species [187]. As the same effect is not observed in cTS-1, the effect may be a consequence of an increased surface density of Ti species caused by the desilication process. Furthermore, dTS-1 showed a broad band at 260-300 nm that may be caused by partially polymerised Ti species, probably outside the zeolite framework [188; 189]. The carbon templated catalysts cTS-1 and cdTS-1 also had a broad band around 320-340 nm, which is typical for TiO<sub>2</sub>. As no diffraction peaks for TiO<sub>2</sub> was observed by XRPD, the band is proposed to be caused by small areas of high Ti density that may be formed during the combustion of the carbon template.



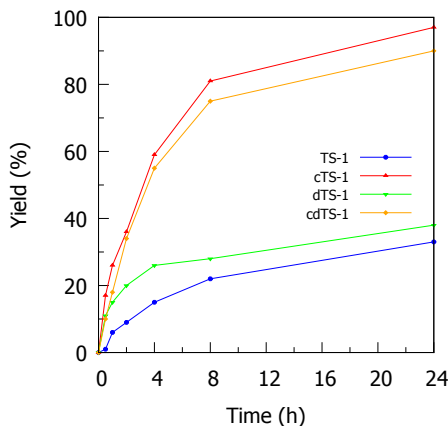
**Figure 7.6.:** *UV-Vis spectra of the prepared catalysts.*

The activity of the prepared titanium silicalite-1 catalysts were investigated for the oxidation of pyridine using aqueous  $\text{H}_2\text{O}_2$  as oxidant, see Figure 7.7. All catalysts afforded the corresponding pyridine *N*-oxides with excellent selectivity (>99%) and no by-products were observed by GC-FID/MS.



**Figure 7.7.:** *Catalytic oxidation of pyridine with  $\text{H}_2\text{O}_2$ .*

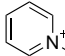
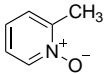
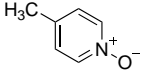
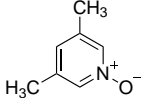
Figure 7.8 show the yield of pyridine *N*-oxide as function of the time. The introduction of additional porosity significantly increased the catalytic activity. While TS-1 resulted in 30% yield after 24 hours at  $60^\circ\text{C}$ , cTS-1 resulted in 97% yield. dTS-1 and cdTS-1 resulted in 37% and 94%, respectively. A blank experiment, with no added catalyst, resulted in 19% yield under the same reaction conditions. This showed that the reaction rate was significantly increased in the presence of a catalyst.



**Figure 7.8.:** Yield of pyridine *N*-oxide over time with TS-1 and cTS-1, respectively.

Table 7.2 compiles the results with different pyridine derivatives. All pyridines, including 2-methylpyridine, 4-methylpyridine and 3,5-dimethylpyridine were oxidised to the corresponding *N*-oxide with excellent selectivity (>99%). Pyridine and 4-methylpyridine were the only substrates that were also oxidised in the absence of catalyst.

**Table 7.2.:** Oxidation methyl-substituted pyridine derivatives<sup>a</sup>.

Entry	Product	Blank	TS-1	cTS-1	dTS-1	csTS-1
1		19	30	97	37	94
2		0	16	64	33	57
3		10	17	23	17	16
4		0	4	32	0	27

Reaction conditions: <sup>a</sup> amine (5 mmol), dioxane(0.5 mmol, internal standard), water (5 ml), H<sub>2</sub>O<sub>2</sub> (7.5 mmol), catalyst (30 mg), 24 h at 60°.

We speculate that the relatively low yield of 4-methylpyridine may be caused by steric hindrance near the Ti active sites or as a consequence of poor product diffusion. Disregarding any possible electronic substituent effects, which are expected to be small, the results indicate that the reaction rate is highly dependent on the size and spatial configuration of the substrates. It is however clear that the trend in yield with respect to

the catalyst is the same for all substrates, *i.e.* cTS-1 > cdTS-1 > dTS-1 > TS-1, except for 4-methylpyridine where the yield is highest for cTS-1 but more or less the same for cdTS-1, dTS-1 and TS-1.

A series of experiments were also performed in order to investigate other *para*-substituted pyridine derivatives, including *p*-CF<sub>3</sub>, *p*-OMe, *p*-Cl and more. While some of these substrates suffered from poor solubility in water, other substrates simply did not react under the given reaction conditions.

## 7.4. Summary

In summary, we have demonstrated that mesoporous TS-1 prepared by carbon templating is significantly more active than conventional TS-1 for the oxidation of pyridines to pyridine *N*-oxides using aqueous H<sub>2</sub>O<sub>2</sub> as oxidant. Furthermore, the carbon-templated catalyst was more active than desilicated TS-1. All catalysts were characterised by X-ray powder diffraction, scanning electron microscopy, UV-Vis spectroscopy and nitrogen physisorption. The results indicated that desilication may cause a surface densification of less active extra-framework Ti species, while carbon-templating is a more gentle and effective method to introduce mesopores and leaves the active tetrahedrally coordinated Ti sites essentially unchanged.

## Chapter 8

### Oxidation of bioethanol

---

With the continuing technological developments in biomass processing, bioethanol is becoming a promising platform molecule for the production of a variety of value-added chemicals. This chapter reports a novel and effective method to encapsulate gold nanoparticles in mesoporous zeolites and demonstrate their high stability, catalytic activity and selectivity for the selective gas-phase oxidation of aqueous bioethanol to acetaldehyde.

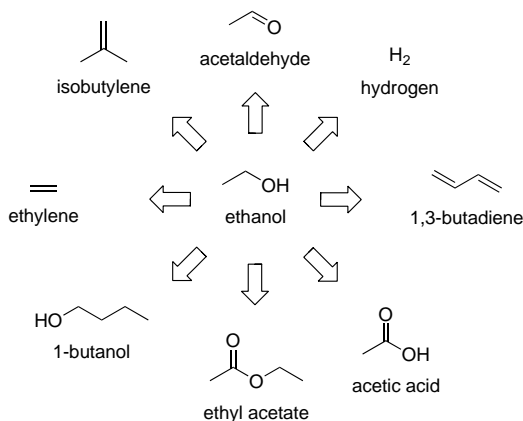
---

#### 8.1. Introduction

As a consequence of stricter environmental regulations and the continuing depletion of fossil resources, the future chemical industry must gradually rely on renewable resources such as biomass for production of bulk and fine chemicals. Bioethanol is already produced from biomass on a large scale and reached a production of 114 billion liters in 2013 [190; 191]. The conventional production of bioethanol is based on fermentation of edible biomass such as sugarcane in Brazil and corn in the United States. However, due to ethical considerations and concerns about ecological systems, much effort has been devoted to shift the bioethanol production towards lignocellulosic biomass feedstocks, such as agricultural waste, straw or wood chips [192].

Bioethanol is primarily used as fuel additive, although crude bioethanol contains up to 90% water which typically has to be removed before use. Simple flash-distillation results in a fraction of around 50 wt% water, while further water removal is a relatively energy demanding process [193]. It has therefore been suggested that bioethanol could be converted into higher value-added chemicals via reactions that are not sensitive to the water content [194]. In addition to the conversion into hydrocarbons [195], ethanol can also be used as a renewable resource for H<sub>2</sub> production by catalytic steam reforming [196] or for production of other oxygenates such as acetaldehyde [197], acetic acid [70] or ethyl acetate [198] by selective oxidation or dehydrogenation [199; 200]. Figure 8.1 show a selection of important bulk chemicals that can be produced from bioethanol.





**Figure 8.1.:** A selection of important bulk chemicals that can be produced from bioethanol. Adapted from [201].

Another promising opportunity is to use bioethanol for the production of acetonitrile. Acetonitrile is currently produced as a by-product from the ammoxidation of propylene to acrylonitrile [202]. The recent acetonitrile crisis of 2009 [203] highlights the need for an independent, efficient and sustainable process for the production of acetonitrile that is independent on the production of acrylonitrile and petrochemical resources. Although the direct ammoxidation of ethanol to acetonitrile is rather inefficient, ethylamine is presently produced on large scale from ethanol and ammonia, rendering it a readily available starting material [204] for a subsequent oxidative dehydrogenation to acetonitrile [205]. This chapter is, however, limited to the oxidation of bioethanol to acetaldehyde and acetic acid.

Currently, the main production of acetaldehyde is based on the oxidation of ethylene using a homogeneous catalytic system comprised of  $PdCl_2$  and  $CuCl_2$  (the Wacker process) while the main production of acetic acid is based on carbonylation of methanol using a homogeneous rhodium (the Monsanto process) or iridium catalyst (the Cativa process). Current market prices encourage the transformation of ethanol into acetaldehyde, but not into acetic acid [200] due to the low cost of methanol. As the cost of bioethanol is expected to decrease due to the technological developments in biomass processing, it seems likely that converting bioethanol to acetaldehyde may become a favourable and green alternative to the ethylene route. Clearly this development requires that highly efficient catalysts are available for the gas phase oxidation of bioethanol to acetaldehyde. Consistent with other alcohol oxidation reactions and the mechanisms discussed in section 1.5, ethanol is first oxidised to acetaldehyde and then to acetic acid. Further oxidation may lead to formation of  $CO_2$ . The general oxidation scheme for ethanol is shown in Figure 8.2.

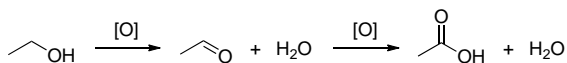


Figure 8.2.: Selective oxidation of ethanol.

As mentioned in section 3, supported gold nanoparticles are highly active and selective catalysts for the aerobic oxidation of alcohols, including ethanol, in both liquid [69; 70] and gas-phase [206; 207]. However, like other metal catalysts, supported gold nanoparticles are prone to sintering, a thermal deactivation caused by Ostwald ripening or particle migration and coalescence [208]. Because of melting-point depression [209], gold nanoparticles therefore tend to sinter even before the so-called Tammann temperature, which is approximately half the melting point of bulk gold in Kelvin (*i.e.* around 396°C). The stability may be improved by tuning the catalyst composition and metal-support interactions [210] or by optimising the three-dimensional distribution of the nanoparticles in ordered mesoporous materials [28]. Furthermore, highly stable catalysts have been achieved by encapsulation of individual nanoparticles in porous metal oxide core-shell materials [39]. In 2010, Laursen *et al.* [125] reported the encapsulation of colloidal gold nanoparticles in zeolites during the hydrothermal crystallisation and recently Li *et al.* [211] reported the synthesis of single nanoparticles in hollow zeolites. In an *in situ* TEM experiment Laursen *et al.* showed that the size of the gold nanoparticle did not increase significantly up to 500°C. Furthermore, the gold nanoparticles were only accessible through the zeolite micropores, which resulted in a remarkable size-selectivity for the aerobic oxidation of benzaldehyde over 3,5-di-*tert*-butylbenzaldehyd [125]. Li *et al.* achieved good control over the particle size as function of the concentration of  $\text{HAuCl}_4$  and have previously reported size-selective hydrogenation of toluene over mesitylene using zeolite encapsulated Pt nanoparticles prepared by the same synthetic approach [212].

The encapsulation of metal nanoparticles in zeolites is particularly interesting for a number of reasons. First of all, the zeolite micropores could increase the thermal stability by preventing the encapsulated nanoparticles from sintering, but still allow reactants and product to diffuse in and out of the zeolite crystal. Moreover, the zeolite micropores could introduce selectivity in terms of size- and shape selectivity or be functionalized to open up for bifunctional heterogeneous catalysis. Zeolite encapsulated metal nanoparticle therefore has a great potential in heterogeneous catalysis. Although encapsulation of single nanoparticles and bottom-up approaches are effective and elegant concepts, they often rely on complex synthetic procedures and expensive additives, which may prevent large-scale production and general implementation.

The following sections describe a novel and simple method to encapsulate gold nanoparticles in recrystallized silicalite-1 (denoted Au/Recryst-S1). The preparation of

the catalyst was based on impregnation of a sample of recrystallized silicalite-1 prepared by an alkaline dissolution-reassembly process in the presence of a surfactant. The alkaline dissolution was performed in an aqueous solution of ammonium hydroxide and cetyl trimethylammonium bromide (CTAB) and the reassembly was performed in an autoclave under hydrothermal conditions. The catalytic activity of the Au/Recryst-S1 catalyst was compared to three reference gold-zeolite catalysts prepared by conventional methods.

The first reference catalyst (denoted Au/S1) was prepared by impregnation of pure silicalite-1 followed by drying and reduction under hydrogen, see section 8.2.2.

The second reference catalyst (denoted Au/Meso-S1) was prepared by impregnation of a carbon-templated mesoporous silicalite-1 following the method developed by Jacobsen et al. [213], see section 8.2.3. As described in Chapter 7, it has previously been demonstrated that carbon-templating is an effective method to synthesise mesoporous zeolites and that the additional system of mesopores can increase the external surface area [214] and help to overcome diffusion limitations [215; 216].

The third reference catalyst (denoted Au/APS-S1) was prepared by impregnation of Silicalite-1 modified with 3-aminopropyl trimethoxysilane (APS) in refluxing toluene, see section 8.2.4. The surface modification was performed in order to improve the gold/support interaction [217] and assist the formation of small and disperse nanoparticles on the hydrophobic silicalite-1 zeolite.

Furthermore, the catalytic activity was compared to Au/Al<sub>2</sub>O<sub>3</sub>, Au/ZrO<sub>2</sub> and Au/CeO<sub>2</sub>, which was prepared by deposition-precipitation, and to a commercial Au/TiO<sub>2</sub> catalyst from Mintek, which was used as benchmark catalyst. Although deposition-precipitation is not compatible with high-silica zeolites (see section 3.5.3), it is often the best method for other metal oxides [218] and was therefore chosen for the preparation of the Al<sub>2</sub>O<sub>3</sub>, ZrO<sub>2</sub> and CeO<sub>2</sub> supported catalysts.

## 8.2. Experimental section

### 8.2.1. Materials

Commercial carbon black particles (Black Pearls 2000, Carbot Corporation) with an average particle diameter of around 12 nm were used as carbon-template for the synthesis of mesoporous silicalite-1. The carbon black particles were dried at 90°C for 24 hours prior to use. All other reagents were of reagent grade and used without further purification or pretreatment: HAuCl<sub>4</sub> · 3 H<sub>2</sub>O (Sigma-Aldrich), tetraethylorthosilicate (TEOS, Sigma-Aldrich), tetrapropylammonium hydroxide (TPAOH, 1M aqueous solution, Sigma-Aldrich), (3-aminopropyl)trimethoxysilane (APS, Sigma-Aldrich), toluene (Sigma-Aldrich), cetyl trimethylammonium bromide (CTAB, Sigma-Aldrich), ethanol (absolute, Sigma-Aldrich), deionised water and Formier gas (10% H<sub>2</sub> in N<sub>2</sub>).

### 8.2.2. Synthesis of Au/S1

Silicalite-1 was prepared according to the synthetic procedure described in section 6.6.2. Silicalite-1 (0.9900 g) pre-dried in a vacuum oven at 50°C was impregnated with an aqueous solution of  $\text{HAuCl}_4 \cdot 3\text{H}_2\text{O}$  (0.0199 g) to incipient wetness (corresponding to 1 wt% Au loading). The impregnated material was dried at room temperature overnight and then reduced in Formier gas for 2 hours at 350°C (heating 5°C/min) to give the final catalyst.

### 8.2.3. Synthesis of Au/Meso-S1

Mesoporous Silicalite-1 was prepared according to the synthetic procedure described in section 6.6.3. Pre-dried carbon black (2 g) was put in a Teflon beaker, impregnated with TPAOH (7.265 ml) and dried at room temperature overnight. The material was then impregnated with TEOS (4.465 ml) and dried at room temperature overnight once more. The Teflon beaker was placed inside a Teflon-lined stainless steel autoclave (130 ml) containing enough water to produce saturated steam (~15 ml) and heated to 180°C for 72 hours. The product was collected by filtration and washed with water (until neutral pH). The product was dried at room temperature overnight and then calcined for 20 hours at 550°C (heating 5°C/min) to give a fine white powder. The mesoporous zeolite (0.9900 g) was pre-dried in a vacuum oven at 50°C and then impregnated and reduced according to the general synthetic procedure described for the synthesis of Au/S1.

### 8.2.4. Synthesis of Au/APS-S1

Silicalite-1 (1.00 g, prepared according to section 6.6.2) and toluene (100 ml) was added to a round-bottom flask equipped with a Liebig condenser. APS (1 ml) was added dropwise under stirring and the mixture was refluxed for 4 hours (111°C). After cooling to room temperature, the product was precipitated by addition of water and collected by filtration. The surface functionalized zeolite was dried, impregnated and reduced according to the general synthetic procedure described for the synthesis of Au/S1.

### 8.2.5. Synthesis of Au/Recryst-S1

CTAB (0.70 g) was dissolved in an aqueous ammonia solution (100 ml, 2.5 wt%). Silicalite-1 (1.00 g, prepared according to section 6.6.2) was added and the suspension was stirred for 3 hours at room temperature. The mixture was then transferred to a Teflon-lined stainless steel autoclave and heated to 140°C for 24 hours. The product was collected by filtration, dried overnight and calcined at 550°C for 5 hours to remove the surfactant. The obtained material was then dried, impregnated and reduced according to the general synthetic procedure described for the synthesis of Au/S1.

### 8.2.6. Synthesis of Au/Al<sub>2</sub>O<sub>3</sub>, Au/ZrO<sub>2</sub> and Au/CeO<sub>2</sub> by deposition precipitation

Al<sub>2</sub>O<sub>3</sub>, ZrO<sub>2</sub> or CeO<sub>2</sub> (0.9900 g) was added to a solution of HAuCl<sub>4</sub> · 3 H<sub>2</sub>O (0.0199 g) in 5 ml H<sub>2</sub>O under stirring (1 wt% Au loading). The pH was increased to 9 by addition of ~10 drops of a saturated aqueous solution of NaHCO<sub>3</sub> and the mixture was heated to 50°C and stirred for 1 hour in order to precipitate Au(OH)<sub>3</sub> on the support. The catalyst was collected by filtration and washed with water until no Cl<sup>-</sup> could be detected upon addition of AgNO<sub>3</sub> to the filtrate. The catalyst was dried at room temperature overnight and then reduced in Formier gas for 2h at 350°C (heating 5°C/min).

### 8.2.7. Gas-phase oxidation of ethanol

The gas-phase oxidation of ethanol was performed in a continuous plug-flow reactor. In a typical experiment, an aqueous solution of 10% ethanol (0.05 ml/min) was pumped into an evaporator at 165°C together with a gas mixture of air (12.4 ml/min) and He (37.6 ml/min) corresponding to a molar ratio of O<sub>2</sub>/ethanol = 1. The gas was then passed through a 3 mm stainless steel plug-flow reactor containing a fixed-bed of 100 mg fractionated catalyst diluted with 100 mg of fractionated SiO<sub>2</sub> (180-355 μm). The weight hourly space velocity (WHSV) was 2.95 g ethanol/g catalyst h<sup>-1</sup>. The product gas was analysed periodically every 12 min by an online GC-FID equipped with a DB-1 non-polar column from Agilent Technologies. All products were identified from gas samples by GC-MS and by the retention time of authentic samples on the online GC-FID. CO and CO<sub>2</sub> were detected by an online NDIR detector (Rosemount GmbH). A simplified process diagram of the reactor setup is shown in Figure 8.3.

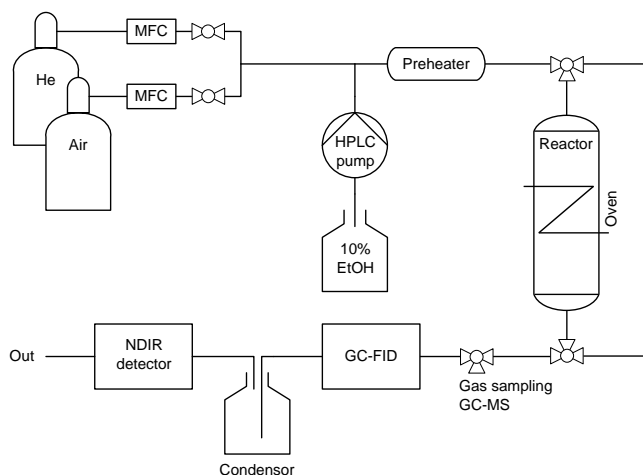
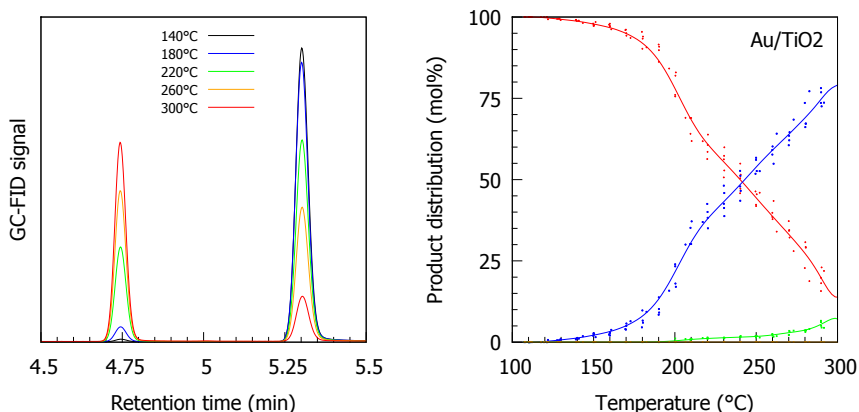


Figure 8.3.: Schematic illustration of the experimental flow-setup.

All catalysts were tested under the same reaction conditions using a pre-programmed temperature profile going from 110-300°C increasing in 10°C steps every hour to insure measurements at near steady state conditions. The reaction temperature was controlled with respect to a thermocouple positioned inside the reactor using a PID control loop feedback mechanism. All reaction parameters were controlled and logged in Labview.

For all investigated catalysts, the main products were acetaldehyde, acetic acid and CO<sub>2</sub>. Other possible by-products, such as ethylene or ethyl acetate were only observed in trace amounts at high temperatures over Au/Al<sub>2</sub>O<sub>3</sub>, probably due to the presence of Brønsted acid sites on the support (see section 5.1). Jørgensen *et al.* [69] investigated the liquid phase oxidation of aqueous ethanol to acetic acid over Au/TiO<sub>2</sub> at 90-200°C in an autoclave and found that the most important by-products were acetaldehyde, CO<sub>2</sub> and ethyl acetate. Because extending the reaction time showed no degradation of acetic acid, the formation of CO<sub>2</sub> likely occurred *via* over-oxidation of an intermediate species. In an attempt to increase the yield of ethyl acetate, Jørgensen *et al.* also found that the highest selectivity to ethyl acetate (50%) was achieved at 80-100% ethanol, which indicated that the acid to ester ratio was determined largely by thermodynamic equilibrium, which explain the limiting effect of water on the production of ethyl acetate. The product distribution was calculated from the GC-FID peak areas after subtracting the formation of CO and CO<sub>2</sub>, which was quantified by the NDIR detector. Figure 8.4(a) shows a section of 5 chromatograms from an experiment with 1 wt% Au/TiO<sub>2</sub>, which demonstrates how the acetaldehyde peak (retention time ~4.75 min) gradually increased as the ethanol peak decreased (retention time ~5.30 min) when the temperature was increased from around 140-300°C.



(a) GC peak areas of acetaldehyde (~4.75 min) and ethanol (~5.30 min) from 140-300°C. (b) Product distribution of ethanol (red), acetaldehyde (blue) and acetic acid (green)

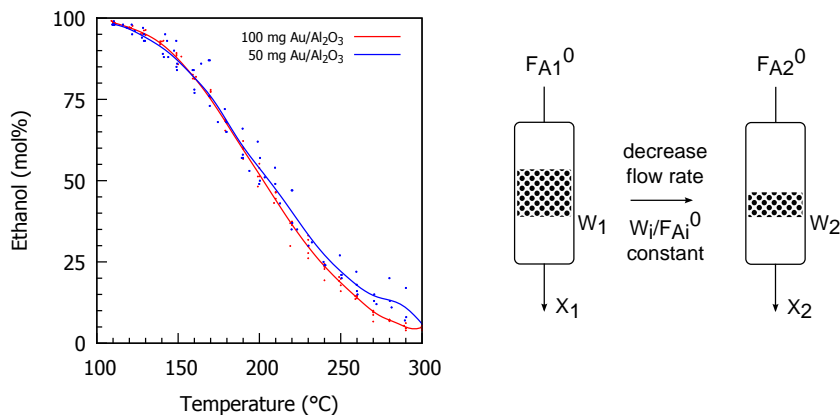
**Figure 8.4.** Results from the gas-phase oxidation of ethanol over 1 wt% Au/TiO<sub>2</sub>.

Figure 8.4(b) shows the corresponding product distribution and shows how the conversion of ethanol reached 50% conversion at around 240°C with 99% selectivity to acetaldehyde. No CO<sub>2</sub> was detected using Au/TiO<sub>2</sub> under the given reaction conditions, although acetic acid was formed in significant amounts above 260°C.

### 8.2.8. A note on catalyst testing

The choice of proper reaction conditions is fundamental in order to investigate the true intrinsic activity and selectivity of heterogeneous catalysts. A series of control experiments were therefore performed in order to exclude the presence of any mass- and heat transfer limitations under the given reaction conditions.

The first experiment was performed in order to determine whether the reaction was limited by external mass transfer limitations. Figure 8.5 shows the conversion of ethanol as function of the temperature with two different amounts of catalyst, but constant space-time  $W_i/F_{Ai}^0$ . As the mass transfer depends on the flow through the catalyst bed, external mass transfer may result in a change in conversion. However, since no significant change in conversion was observed, the experiment indicated that the reaction did not suffer from external mass transfer limitations under the given reaction conditions.



**Figure 8.5.:** Test for external mass transfer limitations.

The second experiment was performed in order to determine whether the reaction was limited by internal diffusion limitations. Figure 8.6 shows the conversion of ethanol as function of the temperature with two different particle size fractions, *i.e.* 180-355  $\mu\text{m}$  and 355-500  $\mu\text{m}$ . Under severe mass transfer limitations, the conversion is dependent on the particle size. However, since no significant changes in conversion was observed, the experiment indicated that the reaction did not suffer from internal mass transfer limitations.

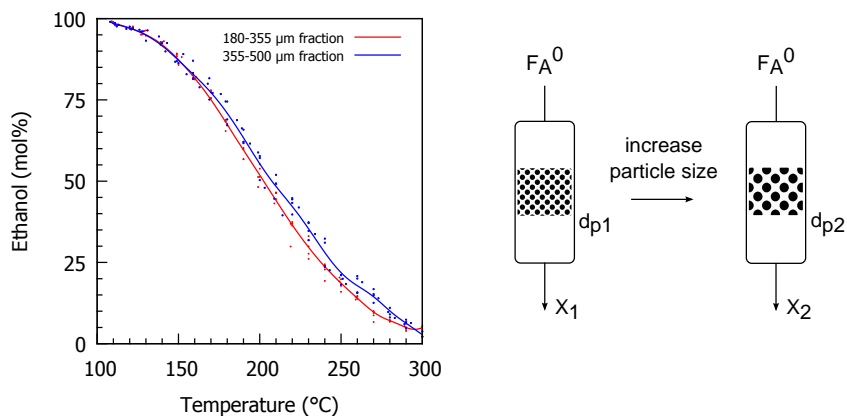


Figure 8.6.: Test for internal mass transfer limitations.

The third experiment was performed in order to determine whether the reaction was limited by heat transfer limitations. Figure 8.7 show the conversion of ethanol as function of the temperature with two different amounts of inactive quartz sand in the reactor. Upon dilution, heat transfer limitations would result in a lower conversion for exothermic reactions and in a higher conversion for endothermic reactions. Since the conversion did not change significantly when the ratio of quartz to catalyst was increased from 1 to 2, the experiment indicated that the reaction did not suffer from any heat transfer limitations. Based on these results we concluded that the reaction conditions were suitable for further catalytic tests.

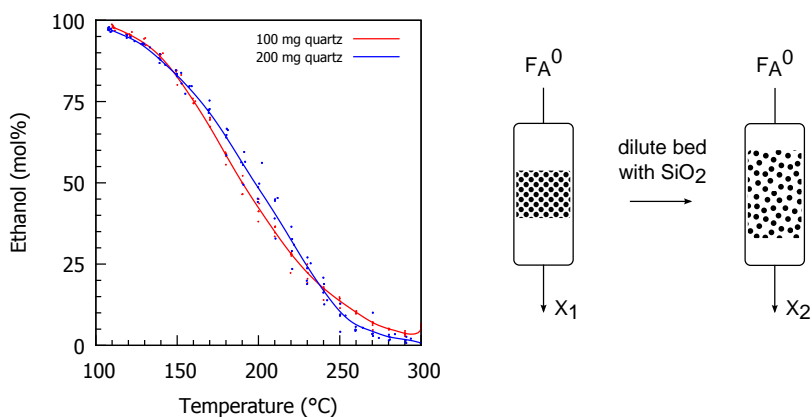


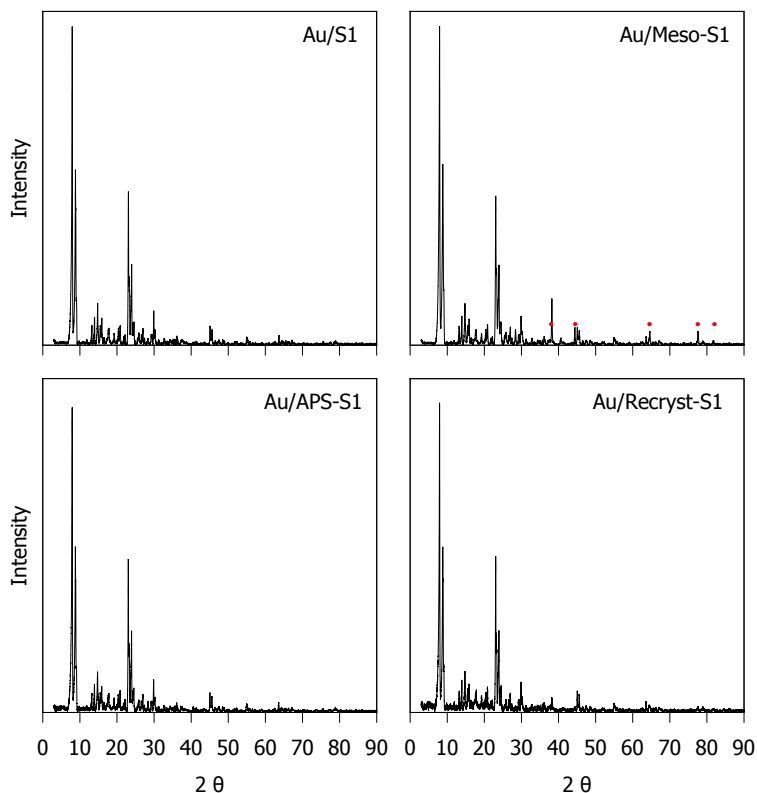
Figure 8.7.: Test for heat transfer limitations.



## 8.3. Results and discussion

### 8.3.1. X-ray powder diffraction

X-ray powder diffraction was measured in transmission mode using  $\text{Cu-K}\alpha$  radiation from a focusing quartz monochromator and a HUBER G670 Guinier camera. The diffraction data presented in Figure 8.8 has been corrected by background subtraction. In addition to the characteristic diffraction pattern of the MFI structured silicalite-1 (see section 2.1), the diffractogram for Au/Meso-S1 also showed diffraction peaks from gold (marked with red dots). The peaks may be assigned to a small number of large gold nanoparticles present in the sample.



**Figure 8.8.:** XRPD analysis of the prepared catalysts. Diffraction peaks from gold is marked with red dots for the Au/Meso-S1 catalyst.

### 8.3.2. Nitrogen physisorption

Nitrogen gas physisorption analysis was performed at 77 K on a Micromeritics ASAP 2020. Prior to the analysis, the samples were outgassed in vacuum for 16 h at 300°C. Figure 8.9 show the acquired nitrogen physisorption isotherms. While the isotherm of Au/S1 and Au/APS-S1 was type I isotherms, which is typical for microporous zeolites, the Au/Meso-S1 and Au/Recryst-S1 also possessed type IV character with corresponding hysteresis loops. The Au/Meso-S1 catalyst had a H1 hysteresis loop, which is typical for mesoporous zeolites with relatively narrow size distributions. The isotherm of the Au/Recryst-S1 catalyst had a H4 hysteresis loop that was almost parallel at  $P/P_0 > 0.45$ . As mentioned in section 2.2, the H4 hysteresis loop has often been observed in complex materials that comprise both micro- and mesopores [1].

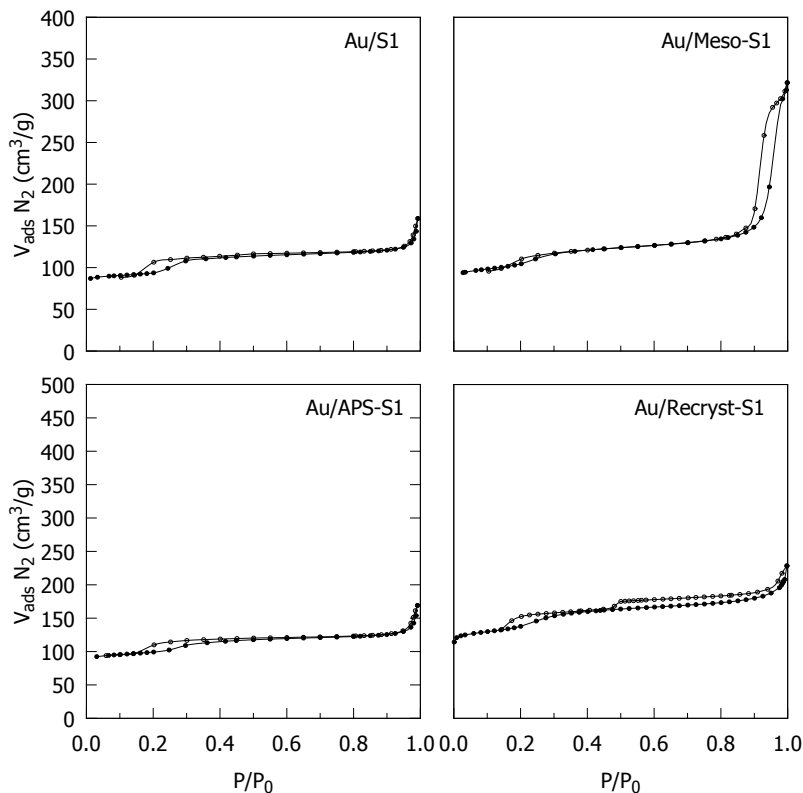
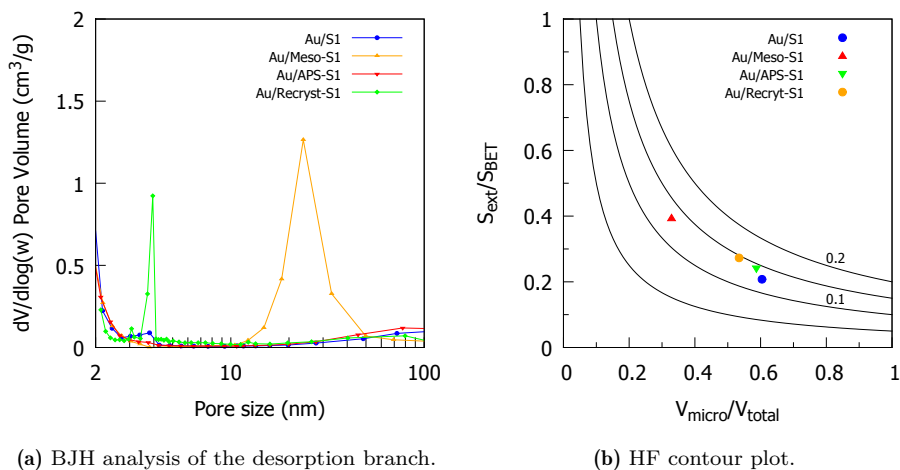


Figure 8.9.:  $N_2$  physisorption isotherms of the prepared catalysts.

The pore-size distribution in Figure 8.10(a) was derived from the desorption branch of the isotherm according to the BJH method. The results showed that Au/Meso-S1 possessed a broad distribution of mesopores around 24 nm. The pores size distribution of

Au/Recryst-S1 showed a narrow peak around 4 nm, which was consistent with previously reported results [173; 219]. However, since the same peak was not evident from the pore size distribution derived from the adsorption branch, it was therefore also possible that the peak was caused by the so-called tensile strength effect, which may be enhanced by an internal system of interconnected pores [185]. All isotherms had a small hysteresis loop around  $P/P_0 = 0.2$  that may be explained by a fluid-to-crystal-like phase transition, which is typical for nitrogen in MFI micropores [185].



**Figure 8.10.:** Barrett-Joyner-Halenda pore size distribution from 2-100 nm and the hierarchy factor ( $HF$ ) plotted in a contour plot as a function of the relative mesoporous surface area and the relative microporous volume.

The (apparent) total surface area was calculated by the BET method, the micropore volume and external surface area were calculated by the  $t$ -plot method and the total pore volume were determined from the isotherm adsorption branch by a single point read at around  $P/P_0 = 0.95$ . Table 8.1 shows a compilation of the physisorption data.

**Table 8.1.:** Results from  $N_2$  physisorption analysis.

Catalyst	$S_{BET}$ ( $m^2/g$ ) <sup>a</sup>	$S_{ext}$ ( $m^2/g$ ) <sup>b</sup>	$V_{micro}$ ( $m^3/g$ ) <sup>b</sup>	$V_{total}$ ( $m^3/g$ ) <sup>c</sup>	$HF^d$
1 wt% Au/S1	313	65	0.116	0.192	0.13
1 wt% Au/Meso-S1	353	139	0.100	0.304	0.13
1 wt% Au/APS-S1	333	80	0.118	0.201	0.14
1 wt% Au/Recryst-S1	374	102	0.124	0.232	0.15

<sup>a</sup> Calculated by the BET method. <sup>b</sup> Calculated by the  $t$ -plot method.

<sup>c</sup> Determined from the isotherm adsorption branch at around  $P/P_0 = 0.95$ .

<sup>d</sup> Hierarchy factor  $HF = (S_{ext}/S_{BET})(V_{micro}/V_{total})$  according to [186].

As expected, the unmodified Au/S1 catalyst had a relatively high micropore volume, while the carbon-templated mesoporous Au/Meso-S1 had the highest external surface area and total pore volume. The surface functionalized Au/APS-S1 catalyst was similar to Au/S1, although it had a slightly higher BET and external surface area. Surprisingly, the Au/Recryst-S1 catalyst had the highest micropore volume, although the BET surface area, external surface area and total pore volume was also increased by the alkaline dissolution-reassembly process. The highest HF factor was obtained with Au/Recryst-S1, which clearly shows how the relative mesoporous surface area was increased without a severe decrease in the relative micropore volume, see Table 8.1.

### 8.3.3. Transmission electron microscopy

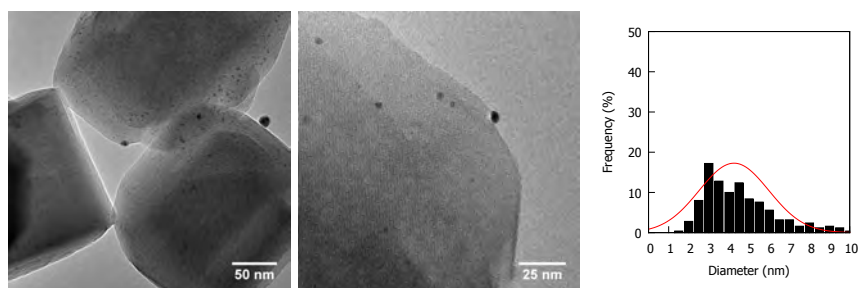
Bright field TEM was performed on a FEI Tecnai microscope operated at 200kV with the samples dispersed directly on holey carbon grids. Figure 8.11-8.14 show two representative TEM images of each of the investigated catalysts together with the particle size histogram and normal distribution. The mean diameter and standard deviation of the nanoparticles was calculated by measurements of  $\sim 250$  particles and is shown in Table 8.2.

**Table 8.2.:** Mean diameter and standard deviation of the supported Au nanoparticles.

Catalyst	Mean diameter (nm) <sup>a</sup>
1 wt% Au/S1	4.3 $\pm$ 1.7
1 wt% Au/Meso-S1	3.3 $\pm$ 1.4
1 wt% Au/APS-S1	2.4 $\pm$ 0.7
1 wt% Au/Recryst-S1	2.6 $\pm$ 0.5

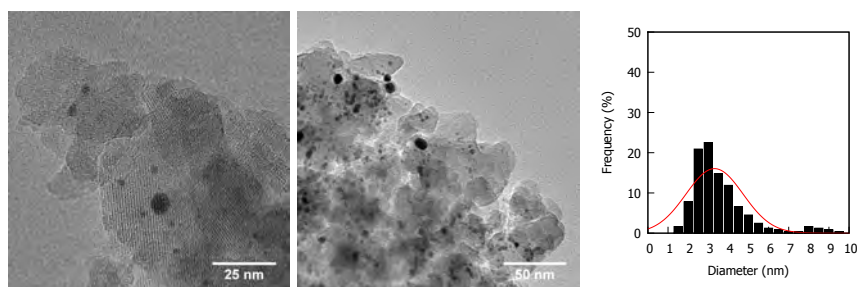
<sup>a</sup> Based on measurement of  $\sim 250$  particles

The TEM images of Au/S1 showed that the prepared silicalite-1 zeolites were uniform coffin-shaped crystals around 250-300 nm in length, see Figure 8.11. The gold nanoparticles were evenly distributed and clearly visible on the edges of the zeolite crystals. As expected, the Au/S1 catalyst had the largest and broadest distribution of Au nanoparticles (4.3 $\pm$ 1.7 nm)



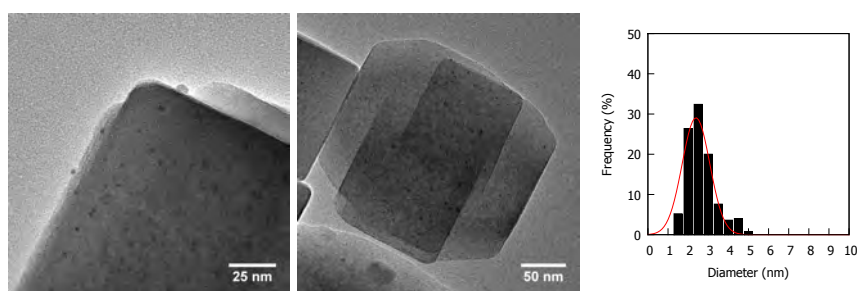
**Figure 8.11.:** TEM images of Au/S1 together with the particle size histogram and normal distribution.

A slightly better dispersion was obtained with the carbon-templated Au/Meso-S1 catalyst ( $3.3 \pm 1.4$  nm), which may be explained by the high external surface area. The TEM images also show how the carbon-template caused the formation of larger, but highly porous zeolite crystals, which were in good agreement with the  $N_2$  physisorption data, see Figure 8.12.



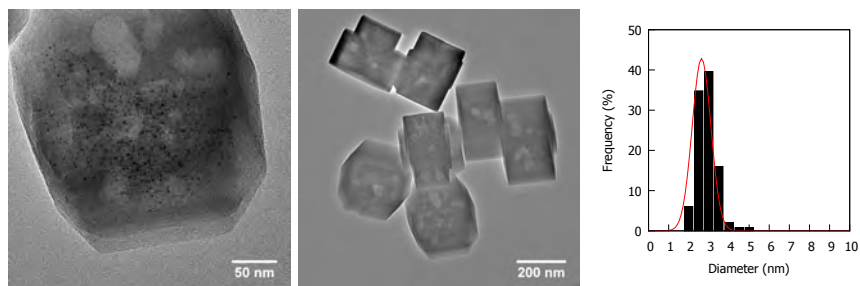
**Figure 8.12.:** TEM images of Au/Meso-S1 together with the particle size histogram and normal distribution.

As expected, the functionalization of S1 with (3-aminopropyl)trimethoxysilane in Au/APS-S1 resulted in a narrow size distribution of small nanoparticles, see Figure 8.13. The effect of the amine-groups may be related to a better dispersion of the  $HAuCl_4$  precursor on the support or by an improved gold/support interaction which may assist the formation of small and disperse nanoparticles upon reduction. In general, gold nanoparticles have poor affinity for silica because gold, unlike most other metals, does not form a passivating oxide film [217], see Chapter 3. Upon impregnation with  $HAuCl_4$  the APS may be protonated, which would result in a strong electrostatic interaction between the surface and the tetrachloroaurate anion [61].



**Figure 8.13.:** TEM images of Au/APS-S1 together with the particle size histogram and normal distribution.

The average size of the gold nanoparticles in Au/Recryst-S1 catalyst ( $2.4 \pm 0.7$  nm) were slightly larger than in Au/APS-S1 ( $2.6 \pm 0.5$ ), but had a very narrow size distribution, see Figure 8.14.



**Figure 8.14.:** TEM images of Au/Recryst-S1 together with the particle size histogram and normal distribution.

The TEM images of Au/Recryst-S1 showed some bright areas of different size and shape inside the silicalite-1 crystals. The bright areas (or low density) indicated a broad distribution of internal voids and mesopores, which was in good agreement with the  $N_2$  physisorption analysis. It is noteworthy that the outer surface of the recrystallized silicalite-1 crystals appeared unchanged by the dissolution reassembly process. Moreover, the gold nanoparticles seemed to be distributed inside the crystals. This first inference was based on the observation that only a small fraction of nanoparticles were found on the edges of the crystals when the sample was tilted in the microscope. Based on the BF-TEM images it was not possible to determine if there were any relation between the situation of the gold nanoparticles and the internal mesopores.

#### 8.3.4. X-ray photoelectron spectroscopy

XPS analysis was performed on a Kratos HSi spectrometer with a hemispherical analyser at Max-Planck-Institut für Kohlenforschung in Germany. The monochromatised Al  $K\alpha$  X-ray source ( $E=1486.6$  eV) was operated at 15 kV and 15 mA. For the narrow scans, an analyser pass energy of 40 eV was applied. The hybrid mode was used as lens mode. The base pressure during the experiment in the analysis chamber was better than  $4 \cdot 10^{-7}$  Pa. To account charging effects, all spectra were referred to C 1s at 284.5 eV. Figure 8.15 shows the measured intensities as function of the binding energy from 75-95 eV.

As opposed to Au/S1, Au/Meso-S1 and Au/APS-S1 that all showed two clear gold photopeaks at 90-80 eV (corresponding to the Au  $4f_{7/2}$  level), no gold signal was observed in the Au/Recryst-S1 catalyst. Since XPS is a surface-sensitive analysis, the absence of gold photopeaks was another indication that the gold nanoparticles were deposited inside the recrystallized silicalite-1 crystals rather than on the outer surface.

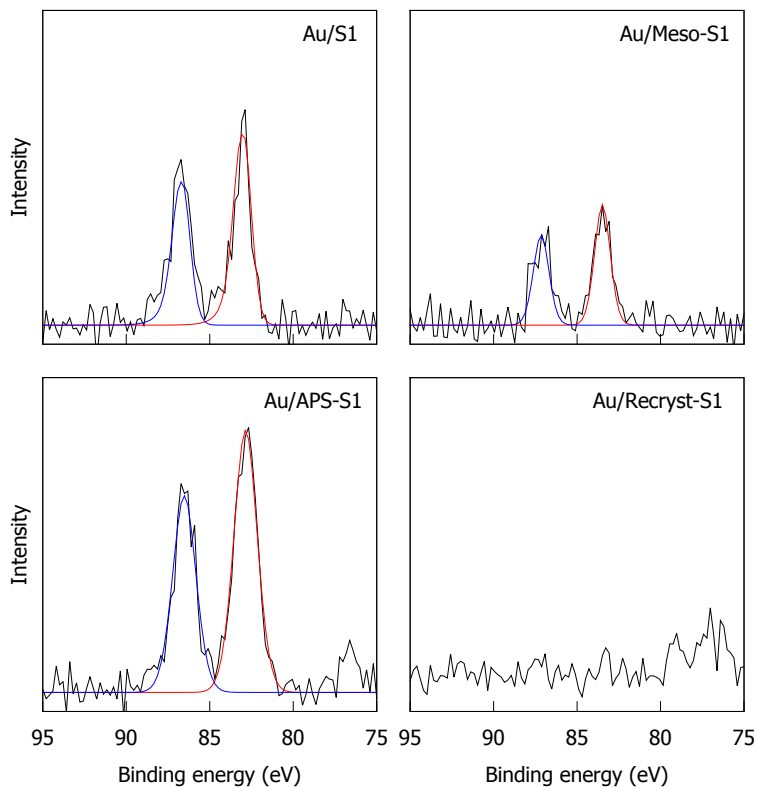
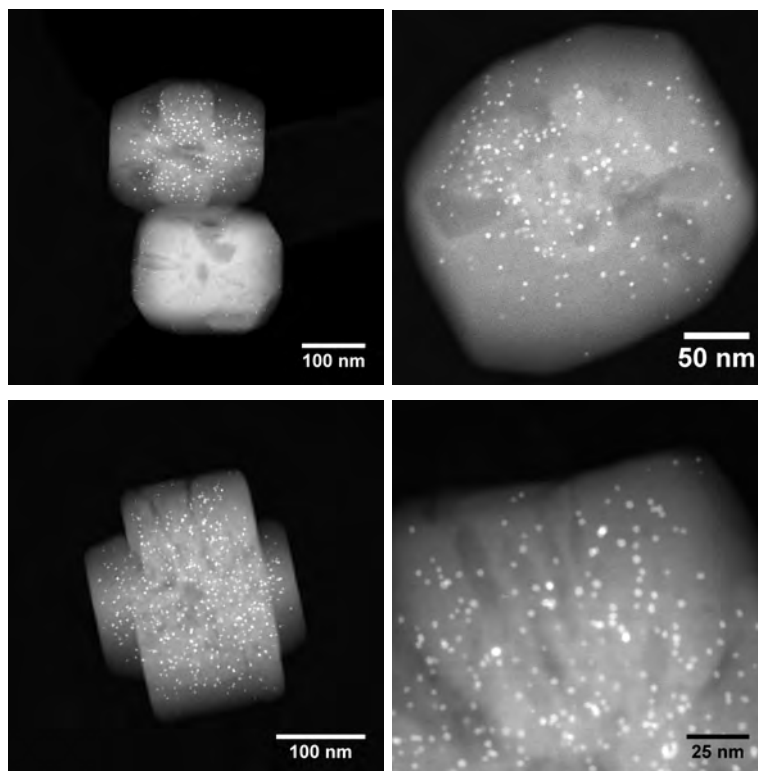


Figure 8.15.: XPS analysis of the prepared catalysts.

### 8.3.5. High-angle annular dark-field scanning transmission electron microscopy and electron tomography

More detailed information about the exact situation of the gold nanoparticles in the Au/Recryst-S1 catalyst was obtained by HAADF-STEM and electron tomography. The HAADF-STEM was performed in an FEI Titan 80-300ST field-emission-gun TEM operated at 300 kV. To avoid contamination from *e.g.* ethanol, the sample was dispersed directly on a holey carbon grid. Figure 8.16 shows three representative STEM images of the Au/Recryst-S1 catalyst. Because of the high Z-contrast, the gold nanoparticles appear as bright white spots on the STEM images. By increasing the focus depth (on account of resolution) it became clear that each individual zeolite crystal comprised up to several hundred gold nanoparticles.

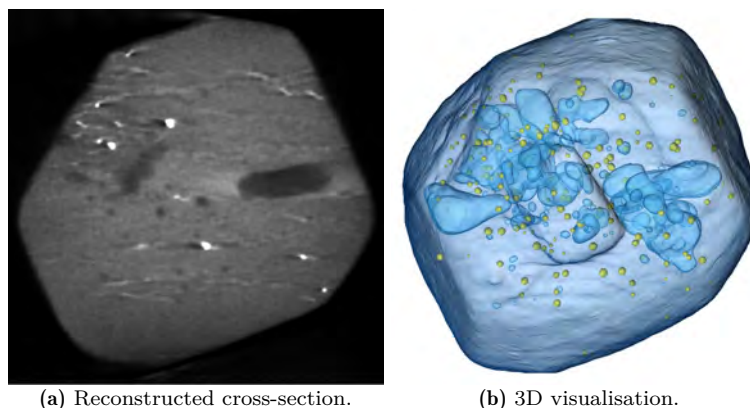


**Figure 8.16.:** Three representative STEM images of the Au/Recryst-S1 catalyst.

The electron tomography was performed by collecting STEM images at incremental degrees of rotation around the centre of the zeolite crystal shown in Figure 8.16. The crystal was selected on the basis of its optimal position on the TEM grid. In general, it is preferable if the investigated particle is more or less isolated in the middle of the holey carbon film somewhere along the rotation centre of the sample holder. The TEM grid was mounted on a single-tilt sample holder and the tilt-series was acquired over a range from  $-72^\circ$  to  $+76^\circ$  in  $2^\circ$  steps by simultaneously adjusting for image shift and focus changes. Alignment and reconstruction was performed in inspect 3D from FEI using the Simultaneous Iterative Reconstruction Technique (SIRT) algorithm. Segmentation and 3D visualisation of the reconstructed volume was performed in Avizo from FEI.

Figure 8.17(a) shows a reconstructed cross section of the Au/Recryst-S1 catalyst, which gives an impression of the position of the gold nanoparticles with respect to the intracrystalline porosity. Figure 8.17(b) shows a 3D model of the entire catalyst particle, which is made by segmentation and volume rendering of the reconstructed image stack. Although small voids  $<5$  nm were observed in the crystal, voids  $<10$  nm and gold






**Figure 8.17.:** *Electron tomography of Au/Recryst-S1.*

nanoparticles  $<1$  nm may not be visualised in the 3D model. The tomographic data is also presented in the form of three movies, which gives a better impression of the three-dimensional structure of the catalyst. The movies are available for download using the QR link in the last column of Table 8.3.

**Table 8.3.:** *Electron tomography movies available for download [220].*

Movie	Content	Filename	File size	QR link
1	Aligned tilt-series	Movie1.mp4	0.99 MB	
2	3D model	Movie2.mp4	5.13 MB	
3	3D model (nanoparticles)	Movie3.mp4	8.11 MB	

The tomographic data confirmed that the gold nanoparticles were indeed situated inside the silicalite-1 crystals. The gold nanoparticles were 2-3 nm in diameter and only a small fraction of the particles were situated on the surface of the zeolite. Furthermore, the tomographic reconstruction provided a unique insight into the voids and mesopores that were formed during the recrystallization process. Although there were no clear correlation between the location of the internal mesopores and the distribution of nanoparticles, the observed porosity were in good agreement with the  $N_2$  physisorption analysis.

Based on the detailed mechanism recently reported by Ivanova et al. [171; 174], we suggest that the alkaline treatment breaks Si-O-Si bond inside the zeolite, which causes the formation of intra-particle voids and mesopores. At this stage the surfactant may protect the zeolite from non-uniform leaching, which can result in formation of large meso- and macropores [221; 222]. Furthermore, the surfactant may diffuse into the zeolite where it (depending on the reaction conditions) can form micelles and serve as template

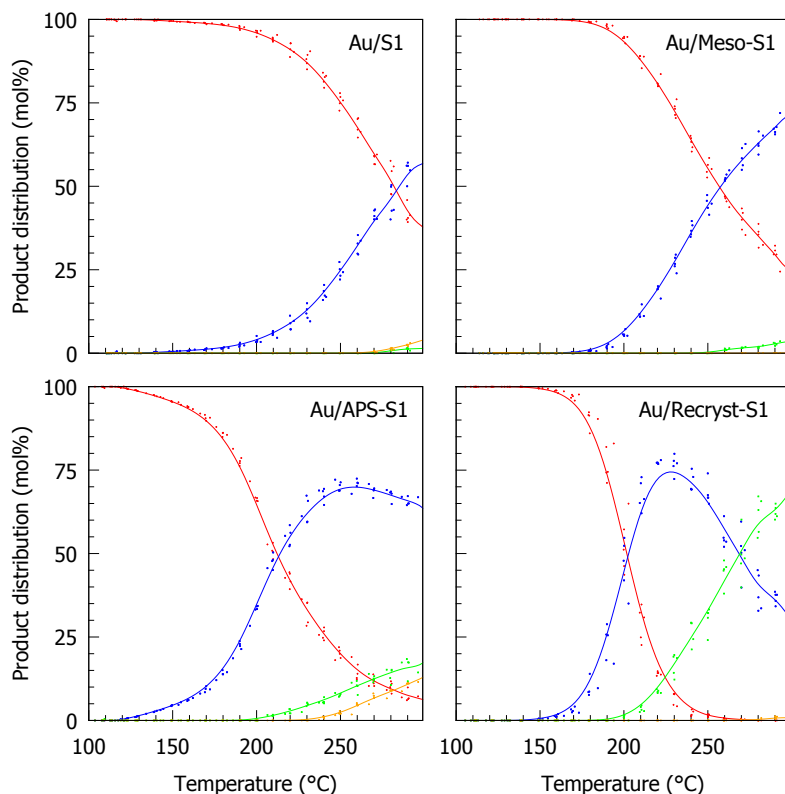
for the condensation of extracted siliceous species during the hydrothermal reassembly [171]. The recrystallized zeolite is then calcined in air to remove the surfactant, dried under vacuum and impregnated with an aqueous solution of  $\text{HAuCl}_4$  which fills up the voids and mesopores. As the material is dried and then reduced under hydrogen, the confined space of the zeolite framework provide ideal conditions for the preparation of small and disperse gold nanoparticles inside the zeolite crystals.

Since the largest sphere that can be included into a MFI framework is around 6.4 Å in diameter [155], it is noteworthy that the size of the nanoparticles was, in principle, too large to fit into silicalite-1. This suggests that the gold nanoparticles may be situated near small cracks or defects in the crystal structure. It is currently unclear if the defects are created during the recrystallization process or if they are present (but not accessible) in the parent silicalite-1 crystals. Further efforts to understand the formation and high dispersion of gold nanoparticles inside recrystallized zeolites is currently being undertaken in our group.

### 8.3.6. Catalytic activity

Figure 8.18 shows the product distribution as function of the reaction temperature for the investigated catalysts. All catalyst was impregnated with 1 wt% Au, which allowed a direct comparison of the catalytic activity with respect to conversion and selectivity. The Au/S1 catalyst was highly selective towards acetaldehyde, but only reached 50% conversion at 280°C. The Au/Meso-S1 catalyst was more active and reached 50% conversion at 250°C. Only small amounts of  $\text{CO}_2$  and acetic acid were observed at temperatures above 250°C. The slightly higher activity of the Au/Meso-S1 may be related to the increased external surface area with smaller and more dispersed Au nanoparticles [214]. The surface functionalized Au/APS-S1 catalyst was more active than both Au/S1 and Au/Meso-S1 and reached 50% conversion at 210°C. At temperatures above 240°C, however, the catalyst resulted in large amounts of acetic acid and  $\text{CO}_2$ , which significantly decreased the acetaldehyde yield. Au/Recryst-S1 was the most active catalyst and reached 50% conversion with 98% selectivity to acetaldehyde at 200°C. Above 200°C, the selectivity to acetaldehyde started to decrease due to formation of acetic acid. At 270°C both acetaldehyde and acetic acid was formed in 50% yield. Surprisingly, no  $\text{CO}_2$  was formed even at 300°C.

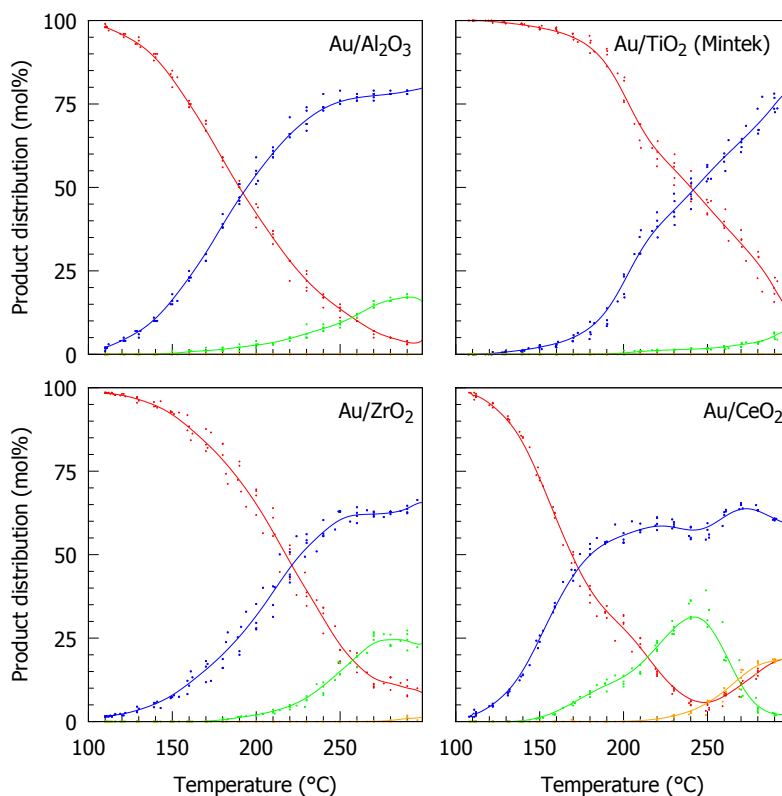
Because of its high surface area, thermal stability and mechanical strength,  $\text{SiO}_2$  is an attractive support material for heterogeneous metal nanoparticle catalysts. Unfortunately, it is often difficult to synthesise highly active Au catalysts by simple impregnation with  $\text{HAuCl}_4$  as residual chloride ions seems to facilitate agglomeration and sintering of the gold nanoparticles upon reduction [218]. Furthermore, deposition-precipitation is



**Figure 8.18.:** Product distribution of ethanol (red), acetaldehyde (blue), acetic acid (green) and  $\text{CO}_2$  (orange) as function of temperature.

difficult because of the low isoelectric point of  $\text{SiO}_2$ , which means that the silica surface is negatively charged under the basic condition used to precipitate  $\text{HAuCl}_4$ . Furthermore,  $\text{SiO}_2$  has often been described as an inert support because it does not contribute to the supply and activation of oxygen as opposed to reducible metal oxides such as  $\text{TiO}_2$ ,  $\text{CeO}_2$  or  $\text{Fe}_2\text{O}_3$  [101], see Figure 3.3. This does not mean that Au/ $\text{SiO}_2$  (here in the form of silicalite-1) cannot be active, but that high catalytic activity requires very small Au nanoparticles with a high number of metal-support interfacial sites. It has previously been suggested that these sites may provide hydroxyl groups that promote the reaction rate, presumably by participating in the reaction mechanism [68; 108], see section 3.4.

In order to investigate the effect of the support, the activity of the Au/Recryst-S1 catalyst was further compared to Au/ $\text{Al}_2\text{O}_3$ , Au/ $\text{TiO}_2$ , Au/ $\text{ZrO}_2$  and Au/ $\text{CeO}_2$  (all with 1 wt% metal loading), see Figure 8.19.

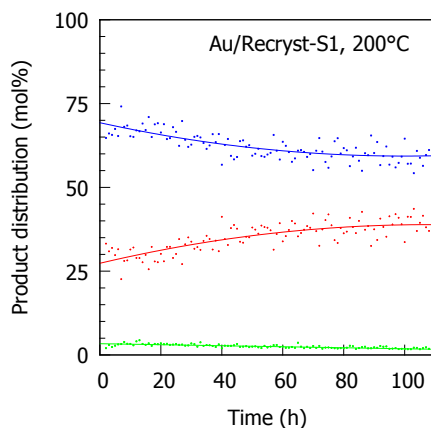


**Figure 8.19:** Product distribution of ethanol (red), acetaldehyde (blue), acetic acid (green) and CO<sub>2</sub> (orange) as function of temperature.

Figure 8.19 shows that the Au/Al<sub>2</sub>O<sub>3</sub> catalyst was highly active and selective and reached 50% conversion at 190°C. The commercial Au/TiO<sub>2</sub> catalyst from Mintek was highly selective towards acetaldehyde, but only reached 50% conversion at 240°C. Finally, Au/ZrO<sub>2</sub> and Au/CeO<sub>2</sub> resulted in 50% conversion at 220°C and 170°C, respectively. Above 200°C the Au/CeO<sub>2</sub> catalyst resulted in significant amounts of acetic acid and eventually CO<sub>2</sub>. Considering the limited amount of oxygen (O<sub>2</sub>/ethanol=1), the formation of CO<sub>2</sub> may explain the decrease in conversion above 250°C.

In terms of the temperature for 50% conversion, the Au/CeO<sub>2</sub> catalyst resulted in the highest catalytic activity. With respect to the selectivity and yield, however, it is important underline that the formation acetaldehyde and acetic acid is a consecutive oxidation process, see section 8.1, and that the overall productivity of each catalyst may be optimised by increasing the WHSV or O<sub>2</sub>/ethanol ratio.

The surprisingly high activity of the encapsulated nanoparticles in Au/Recryst-S1 demonstrate the importance of considering not only the size of the gold nanoparticles and the nature of the support material, but also the three-dimensional distribution and the structure of the gold-support interfacial sites. Furthermore, we are currently investigating if it is possible to increase the thermal stability of supported metal nanoparticles by encapsulation in zeolites. Figure 8.20 shows the distribution of products as function of time-on-stream for the Au/Recryst-S1 catalyst at 200°C. It is noteworthy that even after 100 hours of reaction the Au/Recryst-S1 catalyst was still far more active than the Au/TiO<sub>2</sub> benchmark catalyst.



**Figure 8.20.:** Product distribution of ethanol (red), acetaldehyde (blue) and acetic acid (green) as function of time-on-stream at 200°C using 1 wt% Au/Recryst-S1.

## 8.4. Summary

The production of chemicals only accounts for a fraction of the immense amounts of fossil resources that is processed each day - the rest is used for energy production and transportation fuels. Nevertheless, the production of these chemicals is essential for the well-being of humankind and represent great economic opportunities if they are produced by efficient synthetic routes. From this point of view, ethanol can be considered as one of the most promising bio-based chemicals, mainly because it has the potential to become a renewable and versatile platform molecule [201] and because its high-volume production is already well established [223]. One of the possible value-added products that can be produced from bioethanol (without energy demanding removal of water) is acetaldehyde. With the continued developments in biomass processing and decreasing price of bioethanol it seems likely that production of bioethanol may, eventually, become a

favourable and green alternative to the current ethylene route. Clearly, this development requires that efficient heterogeneous catalysts are available.

This chapter described a novel method to encapsulate Au nanoparticles in recrystallized MFI zeolite silicalite-1. The preparation of the catalyst is simple, effective and results in a narrow size distribution of small nanoparticles ( $2.6\pm 0.5$  nm) that are situated inside the zeolite crystals, but remain readily accessible through the inherent zeolite micropores. The encapsulated nanoparticles were demonstrated to be highly active and selective for the gas-phase oxidation of ethanol to acetaldehyde. The Au/Recryst-S1 catalyst resulted in 50% conversion and 98% selectivity at 200°C, which (under the given reaction conditions) corresponds to a site time yield of 617 mmol acetaldehyde/mmol Au hour<sup>-1</sup>.

In addition to the oxidation of bioethanol, the simple and effective method to encapsulate metal nanoparticles in zeolites opens up for many interesting applications, including size-selective and by-functional catalysis. We therefore hope that impregnation of recrystallized zeolites may become a helpful tool in the development of many new nanostructured materials with unprecedented catalytic properties.



## Chapter 9

### Conclusion

The synthesis of nanostructured materials holds great promises for the development of novel heterogeneous catalysts and many recent examples from the literature have shown how activity, selectivity and stability can be increased by controlling the size, shape and structure on the nanometre level. A particularly interesting size dependence is observed with gold. Bulk gold is chemically inert, but supported gold nanoparticles can promote several reactions under mild conditions. Since the discovery of the surprisingly high activity for low-temperature CO oxidation, the synthesis, characterisation and application of supported gold nanoparticles have therefore attracted much attention in the field of heterogeneous catalysis.

In this thesis, Chapter 4 describes a novel method for the two-step synthesis of amides from alcohols and amines using Au/TiO<sub>2</sub> and base as catalysts. In the first step, a methyl ester is obtained by the gold-catalysed aerobic oxidation of the alcohol in methanol. In the second step, amine is added and the methyl ester undergoes base-catalysed aminolysis to give the desired amide. As the same base promotes both reactions, the synthesis can be performed in a convenient one-pot procedure. The reaction protocol was applied to a number of different alcohols and amines to demonstrate the versatility of the method. Furthermore, the one-pot synthesis was investigated in two consecutive Hammett studies with different *para*-substituted benzyl alcohol derivatives. The result from the first Hammett study indicated that the gold-catalysed oxidation of benzyl alcohol occurs with build-up of positive charge in the benzylic position, which corresponds well with a H-abstraction step. Moreover, the negative slope of the Hammett plot ( $\rho = -0.680$ ) was in good agreement with the generally accepted perception that the gold-catalysed esterification of alcohols with methanol occurs through an aldehyde intermediate. The result from the second Hammett study showed that the rate of amide formation is very sensitive to substituent effects and that negative charge is formed during the reaction ( $\rho = 1.738$ ).

Chapter 5 describes the direct synthesis of imines by oxidative coupling of alcohols and amines using different supported silver catalysts. The reactions were performed at relatively mild conditions (100°C and atmospheric pressure) and afforded the desired imines with high selectivity (up to 99%). The highest catalytic activity was obtained



with 5 wt% Ag/Al<sub>2</sub>O<sub>3</sub> in toluene with air as oxidant. It is noteworthy that the supported Ag catalysts needed no additives or co-catalysts and were even active under oxidant-free conditions with only one equivalent of amine.

Chapter 7 describes the oxidation of pyridine to pyridine *N*-oxide using TS-1 and H<sub>2</sub>O<sub>2</sub> as oxidant. The results demonstrated that mesoporous TS-1 prepared by carbon templating was significantly more active than conventional TS-1. Furthermore, the carbon-templated catalyst was more active than a porous TS-1 catalyst prepared by desilication. The catalysts were characterised by UV-Vis spectroscopy, which indicated that desilication causes a surface densification of less active extra-framework Ti species, while carbon-templating is a more gentle and effective method to introduce mesopores and leaves the active tetrahedrally coordinated Ti sites essentially unchanged.

Finally, Chapter 8 describes how the continuing technological developments in biomass processing have made bioethanol to a promising platform molecule for the production of a variety of value-added chemicals. Furthermore, the chapter describes a simple and effective method to encapsulate gold nanoparticles into silicalite-1 and demonstrated their remarkable stability, catalytic activity and selectivity for the gas-phase oxidation of bioethanol to acetaldehyde, which may become a favourable and green alternative to the ethylene route. The silicalite-1 crystals were modified by recrystallization, which creates intraparticle voids and mesopores that facilitated the formation of small and disperse gold nano-particles upon simple impregnation. The gold nanoparticles were 2-3 nm in diameter and up to several hundred nanoparticles were situated inside each individual zeolite crystal. The encapsulated nanoparticles resulted in 50% conversion and 98% selectivity at 200°C, which (under the given reaction conditions) corresponded to a site time yield of 617 mmol acetaldehyde/mmol Au hour<sup>-1</sup>.

Although encapsulated metal nanoparticles have many potential applications, previous attempts to encapsulate metal nanoparticles in zeolites have relied on expensive additives and complex synthetic procedures. The exploration of these interesting materials has therefore been very limited. In contrast, our synthetic approach is simple, effective and scalable and we therefore hope that impregnation of recrystallized zeolites will become a helpful tool in the development of many new nanostructured materials with unprecedented catalytic properties.

## Bibliography

- [1] G. Ertl, H. Knözinger, F. Schüth, J. Weitkamp, *Handbook of heterogeneous catalysis*, Wiley-VCH, **2008**.
- [2] S. Mitchell, N.-L. Michels, K. Kunze, J. Pérez-Ramírez, *Nature Chemistry* **2012**, *4*, 825–831.
- [3] J. K. Nørskov, T. Bligaard, A. Logadottir, S. Bahn, L. B. Hansen, M. Bollinger, H. Bengaard, B. Hammer, Z. Sljivancanin, M. Mavrikakis, D. Xu, S. Dahl, C. J. H. Jacobsen, *Journal of Catalysis* **2002**, *209*, 275–278.
- [4] T. Bligaard, J. K. Nørskov, S. Dahl, J. Matthiesen, C. H. Christensen, J. Sehested, *Journal of Catalysis* **2004**, *224*, 206–217.
- [5] M. Boudart, *Chemical Reviews* **1995**, *95*, 661–666.
- [6] P. T. Anastas, M. M. Kirchhoff, T. C. Williamson, *Applied Catalysis A: General* **2001**, *221*, 3–13.
- [7] R. A. Sheldon, *Green Chemistry* **2007**, *9*, 1273–1283.
- [8] G. Rothenberg, *Catalysis: concepts and green applications*, Wiley-VCH, **2008**.
- [9] R. A. Sheldon, *Pure and Applied Chemistry* **2000**, *72*, 1233–1246.
- [10] C. H. Christensen, J. K. Nørskov, *The Journal of Chemical Physics* **2008**, *128*, 182503.
- [11] C. Hoffmann, A. Wolf, F. Schüth, *Angewandte Chemie* **1999**, *38*, 2800–2803.
- [12] L. Spenadel, M. Boudart, *The Journal of Physical Chemistry* **1960**, *64*, 204–207.
- [13] R. M. Barrer, P. J. Denny, *Journal of the Chemical Society* **1961**, 971.
- [14] R. Argauer, G. Landolt, *Crystalline zeolite zsm-5 and method of preparing the same*, **1972**, US Patent 3,702,886.
- [15] B. Zhou, S. Hermans, G. A. Somorjai, *Nanotechnology in catalysis*, Springer, **2007**.

- [16] M. Haruta, S. Tsubota, T. Kobayashi, H. Kageyama, M. J. Genet, B. Delmon, *Journal of Catalysis* **1993**, *144*, 175–192.
- [17] I. Lee, F. Delbecq, R. Morales, M. A. Albiter, F. Zaera, *Nature Materials* **2009**, *8*, 132–138.
- [18] H. Zhu, Z. Ma, S. H. Overbury, S. Dai, *Catalysis Letters* **2007**, *116*, 128–135.
- [19] A. C. Pierre, G. M. Pajonk, *Chemical Reviews* **2002**, *102*, 4243–4266.
- [20] J. Rouquerol, D. Avnir, C. Fairbridge, D. Everett, J. Haynes, N. Pernicone, J. Ramsay, K. Sing, K. Unger, *Pure and Applied Chemistry* **1994**, *66*, 1739–1758.
- [21] M. E. Davis, *Nature* **2002**, *417*, 813–821.
- [22] H. Li, M. Eddaoudi, M. O’Keeffe, O. M. Yaghi, *Nature* **1999**, *402*, 276–279.
- [23] F. Schüth, *Angewandte Chemie* **2003**, *42*, 3604–3622.
- [24] C. Kresge, M. Leonowicz, W. Roth, J. Vartuli, J. Beck, *Nature* **1992**, *359*, 710–712.
- [25] A. Monnier, F. Schüth, Q. Huo, D. Kumar, D. Margolese, R. Maxwell, G. Stucky, M. Krishnamurty, P. Petroff, A. Firouzi, M. Janicke, B. F. Chmelka, *Science* **1993**, *261*, 1299–1303.
- [26] G. De Cremer, M. B. Roeflaers, E. Bartholomeeusen, K. Lin, P. Dedecker, P. P. Pescarmona, P. A. Jacobs, D. E. De Vos, J. Hofkens, B. F. Sels, *Angewandte Chemie* **2010**, *122*, 920–923.
- [27] R. I. Kureshy, I. Ahmad, N. H. Khan, S. H. Abdi, K. Pathak, R. V. Jasra, *Journal of Catalysis* **2006**, *238*, 134–141.
- [28] G. Prieto, J. Zečević, H. Friedrich, K. P. de Jong, P. E. de Jongh, *Nature Materials* **2013**, *12*, 34–39.
- [29] D. Zhao, J. Feng, Q. Huo, N. Melosh, G. H. Fredrickson, B. F. Chmelka, G. D. Stucky, *Science* **1998**, *279*, 548–552.
- [30] K. Niesz, P. Yang, G. A. Somorjai, *Chemical Communications* **2005**, 1986–1987.
- [31] S. A. Johnson, P. J. Ollivier, T. E. Mallouk, *Science* **1999**, *283*, 963–965.
- [32] C. J. Jacobsen, C. Madsen, J. Houzvicka, I. Schmidt, A. Carlsson, *Journal of the American Chemical Society* **2000**, *122*, 7116–7117.
- [33] I. Schmidt, A. Boisen, E. Gustavsson, K. Ståhl, S. Pehrson, S. Dahl, A. Carlsson, C. J. Jacobsen, *Chemistry of Materials* **2001**, *13*, 4416–4418.

- [34] I. Schmidt, C. Madsen, C. J. Jacobsen, *Inorganic Chemistry* **2000**, *39*, 2279–2283.
- [35] W.-C. Li, A.-H. Lu, R. Palkovits, W. Schmidt, B. Spliethoff, F. Schüth, *Journal of the American Chemical Society* **2005**, *127*, 12595–12600.
- [36] W. Fan, M. A. Snyder, S. Kumar, P.-S. Lee, W. C. Yoo, A. V. McCormick, R. L. Penn, A. Stein, M. Tsapatsis, *Nature Materials* **2008**, *7*, 984–991.
- [37] C. Galeano, R. Güttel, M. Paul, P. Arnal, A.-H. Lu, F. Schüth, *Chemistry - A European Journal* **2011**, *17*, 8434–8439.
- [38] W. Stöber, A. Fink, E. Bohn, *Journal of Colloid and Interface Science* **1968**, *26*, 62–69.
- [39] P. M. Arnal, M. Comotti, F. Schüth, *Angewandte Chemie* **2006**, *118*, 8404–8407.
- [40] J. J. Pietron, R. M. Stroud, D. R. Rolison, *Nano Letters* **2002**, *2*, 545–549.
- [41] G. C. Bond, D. T. Thompson, *Gold Bulletin* **2000**, *33*, 41–50.
- [42] D. R. Rolison, *Science* **2003**, *299*, 1698–1701.
- [43] F. H. Richter, Y. Meng, T. Klasen, L. Sahraoui, F. Schüth, *Journal of Catalysis* **2013**, *308*, 341–351.
- [44] F. Wang, J. Mielby, F. Herrmann Richter, G. Wang, G. Prieto, T. Kasama, C. Weidenthaler, H. Bongard, S. Kegnae s, A. Fürstner, F. Schüth, *Angewandte Chemie* **2014**, (accepted).
- [45] D. W. Old, J. P. Wolfe, S. L. Buchwald, *Journal of the American Chemical Society* **1998**, *120*, 9722–9723.
- [46] A. Brito, F. García, M. Alvarez-Galván, M. Borges, C. Díaz, V. de la Peña O’Shea, *Catalysis Communications* **2007**, *8*, 2081–2086.
- [47] J. K. Nørskov, T. Bligaard, J. Rossmeisl, C. H. Christensen, *Nature Chemistry* **2009**, *1*, 37–46.
- [48] A. Villa, D. Wang, N. Dimitratos, D. Su, V. Trevisan, L. Prati, *Catalysis Today* **2010**, *150*, 8–15.
- [49] N. Dimitratos, A. Villa, D. Wang, F. Porta, D. Su, L. Prati, *Journal of Catalysis* **2006**, *244*, 113–121.
- [50] R. Hage, A. Lienke, *Angewandte Chemie* **2006**, *45*, 206–222.

- [51] P. Landon, P. J. Collier, A. J. Papworth, C. J. Kiely, G. J. Hutchings, *Chemical Communications* **2002**, 2058–2059.
- [52] N. Yap, R. Andres, W. Delgass, *Journal of Catalysis* **2004**, *226*, 156–170.
- [53] J. K. Edwards, G. J. Hutchings, *Angewandte Chemie* **2008**, *47*, 9192–9198.
- [54] T. Mallat, A. Baiker, *Chemical Reviews* **2004**, *104*, 3037–3058.
- [55] N. Dimitratos, J. A. Lopez-Sanchez, G. J. Hutchings, *Chemical Science* **2012**, *3*, 20–44.
- [56] W. F. Hoelderich, F. Kollmer *et al.*, *Pure and Applied Chemistry* **2000**, *72*, 1273–1287.
- [57] J.-E. Bäckvall, *Modern oxidation methods*, John Wiley & Sons, **2011**.
- [58] A. Markusse, B. Kuster, J. Schouten, *Catalysis Today* **2001**, *66*, 191–197.
- [59] M. Besson, P. Gallezot, *Catalysis Today* **2000**, *57*, 127–141.
- [60] C. Keresszegi, T. Mallat, A. Baiker, *New Journal of Chemistry* **2001**, *25*, 1163–1167.
- [61] S. Harish, R. Sabarinathan, J. Joseph, K. Phani, *Materials Chemistry and Physics* **2011**, *127*, 203–207.
- [62] C. Keresszegi, T. Bürgi, T. Mallat, A. Baiker, *Journal of Catalysis* **2002**, *211*, 244–251.
- [63] M. Haruta, N. Yamada, T. Kobayashi, S. Iijima, *Journal of Catalysis* **1989**, *115*, 301–309.
- [64] L. Prati, M. Rossi, *Journal of Catalysis* **1998**, *176*, 552–560.
- [65] C. Bianchi, F. Porta, L. Prati, M. Rossi, *Topics in Catalysis* **2000**, *13*, 231–236.
- [66] S. E. Davis, M. S. Ide, R. J. Davis, *Green Chemistry* **2013**, *15*, 17–45.
- [67] L. Prati, A. Villa, C. Campione, P. Spontoni, *Topics in Catalysis* **2007**, *44*, 319–324.
- [68] B. N. Zope, D. D. Hibbitts, M. Neurock, R. J. Davis, *Science* **2010**, *330*, 74–78.
- [69] B. Jørgensen, S. Egholm Christiansen, M. L. Dahl Thomsen, C. H. Christensen, *Journal of Catalysis* **2007**, *251*, 332–337.
- [70] C. H. Christensen, B. Jørgensen, J. Rass-Hansen, K. Egeblad, R. Madsen, S. K. Klitgaard, S. M. Hansen, M. R. Hansen, H. C. Andersen, A. Riisager, *Angewandte Chemie* **2006**, *45*, 4648–4651.

- [71] M. M. Treacy, J. B. Higgins, *Collection of Simulated XRD Powder Patterns for Zeolites Fourth (4th) Revised Edition*, Elsevier, **2001**.
- [72] M. Kustova, *Novel Zeolite Catalysts: Preparation, Characterization and Application*, Ph.D. thesis, Technical University of Denmark, **2006**.
- [73] K. S. W. Sing, D. H. Everett, R. A. W. Haul, L. Moscou, R. A. Pierotti, J. Rouquérol, T. Siemieniewska, *Pure and Applied Chemistry* **1985**, *57*, 603–619.
- [74] S. Brunauer, L. S. Deming, W. E. Deming, E. Teller, *Journal of the American Chemical Society* **1940**, *62*, 1723–1732.
- [75] J. Rouquerol, P. Llewellyn, F. Rouquerol, *Studies in Surface Science and Catalysis* **2007**, 49–56.
- [76] B. C. Lippens, J. De Boer, *Journal of Catalysis* **1965**, *4*, 319–323.
- [77] E. P. Barrett, L. G. Joyner, P. P. Halenda, *Journal of the American Chemical Society* **1951**, *73*, 373–380.
- [78] J. Landers, G. Y. Gor, A. V. Neimark, *Colloids and Surfaces A: Physicochemical and Engineering Aspects* **2013**, *437*, 3–32.
- [79] P. J. Goodhew, J. Humphreys, R. Beanland, *Electron microscopy and analysis*, CRC Press, **2000**.
- [80] D. Drouin, A. R. Couture, D. Joly, X. Tastet, V. Aimez, R. Gauvin, *Scanning* **2007**, *29*, 92–101.
- [81] P. Midgley, M. Weyland, *Ultramicroscopy* **2003**, *96*, 413–431.
- [82] A. H. Janssen, *Three-dimensional transmission electron microscopy of porous catalysts*, Ph.D. thesis, Utrecht University, **2003**.
- [83] M. Radermacher, *Journal of Electron Microscopy Technique* **1988**, *9*, 359–394.
- [84] G. T. Herman, A. Lent, S. W. Rowland, *Journal of Theoretical Biology* **1973**, *42*, 1–32.
- [85] P. Gilbert, *Journal of Theoretical Biology* **1972**, *36*, 105–117.
- [86] P. A. Midgley, S. Bals, *Handbook of Nanoscopy* **2012**.
- [87] H. Friedrich, P. E. de Jongh, A. J. Verkleij, K. P. de Jong, *Chemical Reviews* **2009**, *109*, 1613–1629.

- [88] C. Kübel, A. Voigt, R. Schoenmakers, M. Otten, D. Su, T.-C. Lee, A. Carlsson, J. Bradley, *Microscopy and Microanalysis* **2005**, *11*, 378–400.
- [89] P. A. Midgley, R. E. Dunin-Borkowski, *Nature Materials* **2009**, *8*, 271–280.
- [90] N. Kawase, M. Kato, H. Nishioka, H. Jinnai, *Ultramicroscopy* **2007**, *107*, 8–15.
- [91] *Electron tomographic movies available for download*, **2014**, [https://www.dropbox.com/sh/juu4ztq0qspccsn/AABcp\\_71vPqDxUViGpypgSjla](https://www.dropbox.com/sh/juu4ztq0qspccsn/AABcp_71vPqDxUViGpypgSjla).
- [92] A. S. K. Hashmi, G. J. Hutchings, *Angewandte Chemie* **2006**, *45*, 7896–7936.
- [93] A. Corma, H. Garcia, *Chemical Society Reviews* **2008**, *37*, 2096–2126.
- [94] Y. Zhang, X. Cui, F. Shi, Y. Deng, *Chemical Reviews* **2011**, *112*, 2467–2505.
- [95] G. C. Bond, *Catalysis Today* **2002**, *72*, 5–9.
- [96] G. C. Bond, P. A. Sermon, *Gold Bulletin* **1973**, *6*, 102–105.
- [97] T. V. Janssens, B. S. Clausen, B. Hvolbæk, H. Falsig, C. H. Christensen, T. Bligaard, J. K. Nørskov, *Topics in Catalysis* **2007**, *44*, 15–26.
- [98] B. Hvolbæk, T. V. Janssens, B. S. Clausen, H. Falsig, C. H. Christensen, J. K. Nørskov, *Nano Today* **2007**, *2*, 14–18.
- [99] A. Sanchez, S. Abbet, U. Heiz, W.-D. Schneider, H. Häkkinen, R. Barnett, U. Landman, *The Journal of Physical Chemistry A* **1999**, *103*, 9573–9578.
- [100] M. Mavrikakis, P. Stoltze, J. K. Nørskov, *Catalysis Letters* **2000**, *64*, 101–106.
- [101] M. M. Schubert, S. Hackenberg, A. C. Van Veen, M. Muhler, V. Plzak, R. J. Behm, *Journal of Catalysis* **2001**, *197*, 113–122.
- [102] H. Sakurai, T. Akita, S. Tsubota, M. Kiuchi, M. Haruta, *Applied Catalysis A: General* **2005**, *291*, 179–187.
- [103] I. X. Green, W. Tang, M. Neurock, J. T. Yates, *Science* **2011**, *333*, 736–739.
- [104] G. R. Bamwenda, S. Tsubota, T. Nakamura, M. Haruta, *Catalysis Letters* **1997**, *44*, 83–87.
- [105] L. Molina, B. Hammer, *Applied Catalysis A: General* **2005**, *291*, 21–31.
- [106] M. Comotti, W.-C. Li, B. Spliethoff, F. Schüth, *Journal of the American Chemical Society* **2006**, *128*, 917–924.

- [107] W. C. Ketchie, M. Murayama, R. J. Davis, *Topics in Catalysis* **2007**, *44*, 307–317.
- [108] M. S. Ide, R. J. Davis, *Accounts of chemical research* **2013**.
- [109] M. Daté, M. Okumura, S. Tsubota, M. Haruta, *Angewandte Chemie* **2004**, *43*, 2129–2132.
- [110] M. A. Sanchez-Castillo, C. Couto, W. B. Kim, J. A. Dumesic, *Angewandte Chemie* **2004**, *43*, 1140–1142.
- [111] F. Porta, L. Prati, *Journal of Catalysis* **2004**, *224*, 397–403.
- [112] H. Guo, A. Al-Hunaiti, M. Kemell, S. Rautiainen, M. Leskelä, T. Repo, *Chem-CatChem* **2011**, *3*, 1872–1875.
- [113] F. Moreau, G. C. Bond, A. O. Taylor, *Journal of Catalysis* **2005**, *231*, 105–114.
- [114] M. Kosmulski, *Chemical properties of material surfaces*, CRC press, **2001**.
- [115] Z. Ma, S. Dai, *Nano Research* **2011**, *4*, 3–32.
- [116] M. Haruta, *Gold Bulletin* **2004**, *37*, 27–36.
- [117] D. I. Enache, J. K. Edwards, P. Landon, B. Solsona-Espriu, A. F. Carley, A. A. Herzing, M. Watanabe, C. J. Kiely, D. W. Knight, G. J. Hutchings, *Science* **2006**, *311*, 362–365.
- [118] A. Abad, P. Concepción, A. Corma, H. García, *Angewandte Chemie* **2005**, *44*, 4066–4069.
- [119] S. Carrettin, P. McMorn, P. Johnston, K. Griffin, C. J. Kiely, G. J. Hutchings, *Physical Chemistry Chemical Physics* **2003**, *5*, 1329–1336.
- [120] T. Hayashi, T. Inagaki, N. Itayama, H. Baba, *Catalysis Today* **2006**, *117*, 210–213.
- [121] S. K. Klitgaard, A. T. DeLa Riva, S. Helveg, R. M. Werchmeister, C. H. Christensen, *Catalysis letters* **2008**, *126*, 213–217.
- [122] A. Corma, M. E. Domine, *Chemical Communications* **2005**, 4042–4044.
- [123] Y. Y. Gorbanev, S. K. Klitgaard, J. M. Woodley, C. H. Christensen, A. Riisager, *ChemSusChem* **2009**, *2*, 672–675.
- [124] C. Marsden, E. Taarning, D. Hansen, L. Johansen, S. K. Klitgaard, K. Egeblad, C. H. Christensen, *Green Chemistry* **2008**, *10*, 168–170.



- [125] A. B. Laursen, K. T. Højholt, L. F. Lundegaard, S. B. Simonsen, S. Helveg, F. Schüth, M. Paul, J.-D. Grunwaldt, S. Kegnaes, C. H. Christensen *et al.*, *Angewandte Chemie* **2010**, *122*, 3582–3585.
- [126] T. Hayashi, K. Tanaka, M. Haruta, *Journal of Catalysis* **1998**, *178*, 566–575.
- [127] M. Haruta, M. Daté, *Applied Catalysis A: General* **2001**, *222*, 427–437.
- [128] M. Turner, V. B. Golovko, O. P. Vaughan, P. Abdulkin, A. Berenguer-Murcia, M. S. Tikhov, B. F. Johnson, R. M. Lambert, *Nature* **2008**, *454*, 981–983.
- [129] A. Grirrane, A. Corma, H. Garcia, *Journal of Catalysis* **2009**, *264*, 138–144.
- [130] H. Sun, F.-Z. Su, J. Ni, Y. Cao, H.-Y. He, K.-N. Fan, *Angewandte Chemie* **2009**, *48*, 4390–4393.
- [131] S. Kegnaes, J. Mielby, U. V. Mentzel, C. H. Christensen, A. Riisager, *Green Chemistry* **2010**, *12*, 1437–1441.
- [132] A. Grirrane, A. Corma, H. García, *Science* **2008**, *322*, 1661–1664.
- [133] S. K. Klitgaard, K. Egeblad, U. V. Mentzel, A. G. Popov, T. Jensen, E. Taarning, I. S. Nielsen, C. H. Christensen, *Green Chemistry* **2008**, *10*, 419–423.
- [134] B. Xu, L. Zhou, R. J. Madix, C. M. Friend, *Angewandte Chemie* **2010**, *122*, 404–408.
- [135] Y. Wang, D. Zhu, L. Tang, S. Wang, Z. Wang, *Angewandte Chemie* **2011**, *123*, 9079–9083.
- [136] C. M. F. Paula, M. R. Castilho, J. Y. Crompton, *Journal of the Chemical Society Perkin Transactions 2* **1991**, 639–643.
- [137] I. S. Nielsen, E. Taarning, K. Egeblad, R. Madsen, C. H. Christensen, *Catalysis Letters* **2007**, *116*, 35–40.
- [138] L. P. Hammett, *Journal of the American Chemical Society* **1937**, *59*, 96–103.
- [139] P. Fristrup, D. Tanner, P.-O. Norrby, *Chirality* **2003**, *15*, 360–368.
- [140] C. Hansch, A. Leo, R. Taft, *Chemical Reviews* **1991**, *91*, 165–195.
- [141] C. Hansch, H. Gao, *Chemical Reviews* **1997**, *97*, 2995–3060.
- [142] P. Fristrup, L. B. Johansen, C. H. Christensen, *Catalysis Letters* **2008**, *120*, 184–190.
- [143] A. Friedrich, S. Schneider, *ChemCatChem* **2009**, *1*, 72–73.

- [144] M. Qian, M. Liauw, G. Emig, *Applied Catalysis A: General* **2003**, *238*, 211–222.
- [145] A. Maggi, R. Madsen, *Organometallics* **2011**, *31*, 451–455.
- [146] J. W. Rigoli, S. A. Moyer, S. D. Pearce, J. M. Schomaker, *Organic and Biomolecular Chemistry* **2012**, *10*, 1746–1749.
- [147] M. A. Esteruelas, N. Honczek, M. Oliván, E. Oñate, M. Valencia, *Organometallics* **2011**, *30*, 2468–2471.
- [148] B. Gnanaprakasam, J. Zhang, D. Milstein, *Angewandte Chemie* **2010**, *49*, 1468–1471.
- [149] T. Mitsudome, Y. Mikami, H. Funai, T. Mizugaki, K. Jitsukawa, K. Kaneda, *Angewandte Chemie* **2008**, *120*, 144–147.
- [150] K.-i. Shimizu, K. Sugino, K. Sawabe, A. Satsuma, *Chemistry - A European Journal* **2009**, *15*, 2341–2351.
- [151] V. L. Sushkevich, I. I. Ivanova, E. Taarning, *ChemCatChem* **2013**, *5*, 2367–2373.
- [152] W.-X. Li, C. Stampfl, M. Scheffler, *Physical Review Letters* **2003**, *90*, 256102.
- [153] J.-F. Soulé, H. Miyamura, S. Kobayashi, *Chemical Communications* **2013**, *49*, 355–357.
- [154] W. Löwenstein, *American Mineralogist* **1954**, *39*, 92–96.
- [155] *International Zeolite Association*, **2014**, <http://www.iza-online.org/>.
- [156] L. Pine, P. Maher, W. Wachter, *Journal of Catalysis* **1984**, *85*, 466–476.
- [157] C. T. Kresge, S. S. Dhingra, *Kirk-Othmer Encyclopedia of Chemical Technology* **2004**.
- [158] E. Taarning, S. Saravanamurugan, M. Spangenberg Holm, J. Xiong, R. M. West, C. H. Christensen, *ChemSusChem* **2009**, *2*, 625–627.
- [159] M. S. Holm, S. Saravanamurugan, E. Taarning, *Science* **2010**, *328*, 602–605.
- [160] B. Smit, T. L. Maesen, *Nature* **2008**, *451*, 671–678.
- [161] S. L. Burkett, M. E. Davis, *Chemistry of Materials* **1995**, *7*, 920–928.
- [162] K.-J. Chao, J.-C. Lin, Y. Wang, G. Lee, *Zeolites* **1986**, *6*, 35–38.
- [163] R. W. Broach, D.-Y. Jan, D. A. Lesch, S. Kulprathipanja, E. Roland, P. Kleinschmit, *Ullmann's Encyclopedia of Industrial Chemistry* **2012**.

- [164] C. S. Cundy, P. A. Cox, *Microporous and Mesoporous Materials* **2005**, *82*, 1–78.
- [165] S. Van Donk, A. H. Janssen, J. H. Bitter, K. P. de Jong, *Catalysis Reviews* **2003**, *45*, 297–319.
- [166] J. Jiang, J. Yu, A. Corma, *Angewandte Chemie* **2010**, *49*, 3120–3145.
- [167] J. Jiang, J. L. Jorda, J. Yu, L. A. Baumes, E. Mugnaioli, M. J. Diaz-Cabanas, U. Kolb, A. Corma, *Science* **2011**, *333*, 1131–1134.
- [168] K. Möller, T. Bein, *Chemical Society Reviews* **2013**, *42*, 3689–3707.
- [169] S. Mintova, J.-P. Gilson, V. Valtchev, *Nanoscale* **2013**, *5*, 6693–6703.
- [170] R. Chal, C. Gérardin, M. Bulut, S. van Donk, *ChemCatChem* **2011**, *3*, 67–81.
- [171] I. I. Ivanova, E. E. Knyazeva, *Chemical Society Reviews* **2013**, *42*, 3671–3688.
- [172] S. Abello, A. Bonilla, J. Perez-Ramirez, *Applied Catalysis A: General* **2009**, *364*, 191–198.
- [173] J. García-Martínez, M. Johnson, J. Valla, K. Li, J. Y. Ying, *Catalysis Science and Technology* **2012**, *2*, 987–994.
- [174] I. I. Ivanova, I. A. Kasyanov, A. A. Maerle, V. I. Zaikovskii, *Microporous and Mesoporous Materials* **2013**.
- [175] C. Perego, A. Carati, J. Čejka, J. Perez-Pariente, W. Roth, *Transworld Research Network Singapore* **2008**, 357.
- [176] S. K. Singh, M. Bajpai, V. Tyagi, *Journal of Oleo Science* **2006**, *55*, 99–119.
- [177] Y. Sawama, M. Takubo, S. Mori, Y. Monguchi, H. Sajiki, *European Journal of Organic Chemistry* **2011**, *2011*, 3361–3367.
- [178] G. Yan, A. J. Borah, M. Yang, *Advanced Synthesis and Catalysis* **2014**.
- [179] R. Abramovitch, E. M. Smith, *Chemistry of Heterocyclic Compounds: Pyridine and its Derivatives Supplement Part Two Volume 14* **1974**, 1–261.
- [180] B. Notari, *Studies in Surface Science and Catalysis* **1988**, *37*, 413–425.
- [181] M. Padovan, F. Genoni, G. Leofanti, G. Petrini, P. Roffia, A. Cesana, *Catalytic process for the manufacture of oximes*, **1990**, US Patent 4,968,842.
- [182] M. Taramasso, G. Perego, B. Notari, *Preparation of porous crystalline synthetic material comprised of silicon and titanium oxides*, **1983**, US Patent 4,410,501.

- [183] M. Moliner, A. Corma, *Microporous and Mesoporous Materials* **2014**, *189*, 31–40.
- [184] C. Perego, A. Carati, P. Ingallina, M. A. Mantegazza, G. Bellussi, *Applied Catalysis A: General* **2001**, *221*, 63–72.
- [185] J. C. Groen, L. A. Peffer, J. Pérez-Ramírez, *Microporous and Mesoporous Materials* **2003**, *60*, 1–17.
- [186] F. C. Meunier, D. Verboekend, J.-P. Gilson, J. C. Groen, J. Pérez-Ramírez, *Microporous and Mesoporous Materials* **2012**, *148*, 115–121.
- [187] P. Ratnasamy, D. Srinivas, H. Knözinger, *Advances in Catalysis* **2004**, *48*, 1–169.
- [188] G. Petrini, A. Cesana, G. D. Alberti, F. Genoni, G. Leofanti, M. Padovan, G. Parratto, P. Roffia, *Studies in Surface Science and Catalysis* **1991**, *68*, 761–766.
- [189] M. Bandyopadhyay, A. Birkner, M. Van Den Berg, K. Klementiev, W. Schmidt, W. Grünert, H. Gies, *Chemistry of Materials* **2005**, *17*, 3820–3829.
- [190] *Agricultural Outlook*, OECD Publishing, DOI: 10.1787/19991142, [http://www.oecd-ilibrary.org/agriculture-and-food/oecd-fao-agricultural-outlook-2013\\_agr\\_outlook-2013-en](http://www.oecd-ilibrary.org/agriculture-and-food/oecd-fao-agricultural-outlook-2013_agr_outlook-2013-en).
- [191] J. Goldemberg, *Science* **2007**, *315*, 808–810.
- [192] J. Sun, Y. Wang, *ACS Catalysis* **2014**, *4*, 1078–1090.
- [193] B. Jørgensen, S. B. Kristensen, A. J. Kunov-Kruse, R. Fehrmann, C. H. Christensen, A. Riisager, *Topics in Catalysis* **2009**, *52*, 253–257.
- [194] J. Rass-Hansen, H. Falsig, B. Jørgensen, C. H. Christensen, *Journal of Chemical Technology and Biotechnology* **2007**, *82*, 329–333.
- [195] R. Johansson, S. L. Hrubby, J. Rass-Hansen, C. H. Christensen, *Catalysis Letters* **2009**, *127*, 1–6.
- [196] G. Deluga, J. Salge, L. Schmidt, X. Verykios, *Science* **2004**, *303*, 993–997.
- [197] Y. Guan, E. J. Hensen, *Journal of Catalysis* **2013**, *305*, 135–145.
- [198] M. Nielsen, H. Junge, A. Kammer, M. Beller, *Angewandte Chemie* **2012**, *51*, 5711–5713.
- [199] M. Murdoch, G. Waterhouse, M. Nadeem, J. Metson, M. Keane, R. Howe, J. Llorca, H. Idriss, *Nature Chemistry* **2011**, *3*, 489–492.

- [200] T. Takei, N. Iguchi, M. Haruta, *Catalysis Surveys from Asia* **2011**, *15*, 80–88.
- [201] C. Angelici, B. M. Weckhuysen, P. C. Bruijninx, *ChemSusChem* **2013**, *6*, 1595–1614.
- [202] R. K. Grasselli, *Catalysis Today* **1999**, *49*, 141–153.
- [203] E. Rojas, M. O. Guerrero-Pérez, M. A. Bañares, *Catalysis Communications* **2009**, *10*, 1555–1557.
- [204] K. Hayes, *Applied Catalysis A: General* **2001**, *221*, 187–195.
- [205] E. C. Corker, U. V. Mentzel, J. Mielby, A. Riisager, R. Fehrmann, *Green Chemistry* **2013**, *15*, 928–933.
- [206] O. A. Simakova, V. I. Sobolev, K. Y. Koltunov, B. Campo, A.-R. Leino, K. Kordás, D. Y. Murzin, *ChemCatChem* **2010**, *2*, 1535–1538.
- [207] V. I. Sobolev, K. Y. Koltunov, O. A. Simakova, A.-R. Leino, D. Y. Murzin, *Applied Catalysis A: General* **2012**, *433*, 88–95.
- [208] T. W. Hansen, A. T. DeLa Riva, S. R. Challa, A. K. Datye, *Accounts of Chemical Research* **2013**, *46*, 1720–1730.
- [209] K. Dick, T. Dhanasekaran, Z. Zhang, D. Meisel, *Journal of the American Chemical Society* **2002**, *124*, 2312–2317.
- [210] J. A. Farmer, C. T. Campbell, *Science* **2010**, *329*, 933–936.
- [211] S. Li, L. Burel, C. Aquino, A. Tuel, F. Morfin, J.-L. Rousset, D. Farrusseng, *Chemical Communications* **2013**, *49*, 8507–8509.
- [212] S. Li, T. Boucheron, A. Tuel, D. Farrusseng, F. Meunier, *Chemical Communications* **2014**, *50*, 1824–1826.
- [213] M. Hartmann, *Angewandte Chemie* **2004**, *43*, 5880–5882.
- [214] C. H. Christensen, I. Schmidt, A. Carlsson, K. Johannsen, K. Herbst, *Journal of the American Chemical Society* **2005**, *127*, 8098–8102.
- [215] I. Schmidt, A. Krogh, K. Wienberg, A. Carlsson, M. Brorson, C. J. Jacobsen, *Chemical Communications* **2000**, 2157–2158.
- [216] J. Mielby, J. O. Abildstrøm, S. Pérez-Ferreras, S. B. Rasmussen, S. Kegnæs, *Journal of Porous Materials* **2014**, 1–7.

- [217] L. M. Liz-Marzán, M. Giersig, P. Mulvaney, *Langmuir* **1996**, *12*, 4329–4335.
- [218] M. Haruta, *Cattech* **2002**, *6*, 102–115.
- [219] R. Chal, T. Cacciaguerra, S. Van Donk, C. Gérardin, *Chemical Communications* **2010**, *46*, 7840–7842.
- [220] *Electron tomographic movies available for download*, **2014**, <https://www.dropbox.com/sh/88e77qbh7italq0/AABvP1FR37vfuJaiK0QYSRQIa>.
- [221] Y. P. Khitev, I. I. Ivanova, Y. G. Kolyagin, O. Ponomareva, *Applied Catalysis A: General* **2012**, *441*, 124–135.
- [222] V. Ordonsky, I. I. Ivanova, E. Knyazeva, V. Yuschenko, V. Zaikovskii, *Journal of Catalysis* **2012**, *295*, 207–216.
- [223] J. J. Bozell, G. R. Petersen, *Green Chemistry* **2010**, *12*, 539–554.



# Chapter A

## Publications

### Project related publications (enclosed in the thesis)

- 1 S. Kegnæs, J. Mielby, U. V. Mentzel, T. Jensen, P. Fristrup and A. Riisager, "One-pot synthesis of amides by aerobic oxidative coupling of alcohols or aldehydes with amines using supported gold and base as catalysts", *Chem. Commun.* **2012**, *48*, 2427-2429.
- 2 J. Mielby, A. Riisager, P. Fristrup and S. Kegnæs, "Mechanistic investigation of the one-pot formation of amides by oxidative coupling of alcohols with amines in methanol", *Catal. Today* **2013**, *203*, 211-216.
- 3 J. Mielby, S. Kegnæs and P. Fristrup, "Gold Nanoparticle-Catalyzed Formation of Nitrogen-containing Compounds – From Mechanistic Understanding to Synthetic Exploitation", *ChemCatChem* **2012**, *4*, 1037-1047.
- 4 J. Mielby, R. Poreddy, C. Engelbrekt and S. Kegnæs, "Highly selective formation of imines catalyzed by silver nanoparticles supported on alumina", *Chin. J. Catal.* **2014**, *35*, 769-775.
- 5 J. Mielby, J. O. Abildstrøm, S. Pérez-Ferreras, S. B. Rasmussen and S. Kegnæs, "Formation of N-oxides using Mesoporous Titanium Silicalite-1", *J. Porous Mat.*, **2014**, DOI: 10.1007/s10934-014-9800-0.
- 6 J. Mielby, J. O. Abildstrøm, F. Wang, T. Kasama, C. Weidenthaler and S. Kegnæs, "Oxidation of Bioethanol using zeolite encapsulated gold nanoparticles", *submitted*.

### Other publications

- 7 E. C. Corker, U. Mentzel, J. Mielby, A. Riisager and F. Fehrmann, "An alternative pathway for production of acetonitrile: ruthenium catalysed aerobic dehydrogenation of ethylamine" *Green Chem.* **2013**, *15*, 928-933.



- 8 J. Mielby and S. Kegnæs, "Epoxidation of Alkenes with Aqueous Hydrogen Peroxide and Quaternary Ammonium Bicarbonate Catalysts", *Catal. Lett.*, **2013**, *143*, 1162-1165.
- 9 F. Wang, J. Mielby, F. Herrmann Richter, G. Wang, G. Prieto, T. Kasama, C. Weidenthaler, H.-J. Bongard, S. Kegnæs, A. Fürstner and F. Schüth, "A polyphenylene support for Pd catalysts with exceptional catalytic activity", *Angew. Chem.*, **2014**, *accepted*.





Cite this: *Chem. Commun.*, 2012, **48**, 2427–2429

www.rsc.org/chemcomm

# One-pot synthesis of amides by aerobic oxidative coupling of alcohols or aldehydes with amines using supported gold and base as catalysts†

Søren Kegnæs, Jerrik Mielby, Uffe V. Mentzel, Thomas Jensen, Peter Fristrup and Anders Riisager\*

Received 1st November 2011, Accepted 10th January 2012

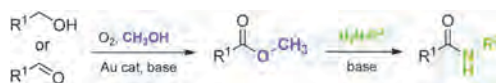
DOI: 10.1039/c2cc16768a

Synthesis of amides by aerobic oxidative coupling of alcohols or aldehydes with amines *via* intermediate formation of methyl esters is highly efficient and selective when using a catalytic system comprised of supported gold nanoparticles and added base in methanol.

Selective oxidation of alcohols is one of the most important reactions in organic chemistry and finds use in the manufacture of many bulk commodities, high-value fine chemicals, agrochemicals, and pharmaceuticals. Traditionally, oxidations of alcohols are performed with stoichiometric amounts of high-valent inorganic oxidants such as chromate or permanganate, which inevitably leads to the generation of large amounts of metal waste. In the search for a more sustainable chemical production, researchers have put considerable effort into the development of catalytic oxidations using air or molecular dioxygen as the stoichiometric oxidant.<sup>1,2</sup> From the standpoint of green chemistry these aerobic oxidations are attractive, because dioxygen is a cheap and abundant oxidant that produces water as the only by-product.

Since the first fundamental studies by Bond *et al.*,<sup>3</sup> Hutchings,<sup>4</sup> Haruta *et al.*,<sup>5</sup> and Prati and Rossi<sup>6</sup> supported gold nanoparticles have been recognised as surprisingly active and selective catalysts for a number of aerobic oxidations.<sup>7</sup> For instance, supported gold nanoparticles have been used for oxidation of alcohols to aldehydes,<sup>8</sup> carboxylic acids<sup>9</sup> and esters.<sup>10,11</sup> Furthermore, interesting results have been reported for the oxidation of amines and oxidative coupling of alcohols with amines. In particular, supported gold nanoparticles have been used in the synthesis of azo-compounds,<sup>12</sup> imines,<sup>13</sup> secondary amines,<sup>14</sup> and amides.<sup>15</sup>

Although the increasing number of reports on oxidations with nitrogen-containing compounds represents an interesting development, the field still needs further improvement in terms of catalytic efficiency and practical applicability. For instance, under mild reaction conditions the oxidation of alcohols often requires a strongly alkaline solution and in some systems this represents a strong limitation as various side reactions may decrease the selectivity.<sup>2</sup>



**Scheme 1** Synthesis of amides by aerobic oxidative coupling of alcohols or aldehydes with amines using supported gold nanoparticles and base as catalysts.

Here, we show that the combination of supported gold nanoparticles and base forms an efficient and highly selective catalytic system for the one-pot, two-step synthesis of amides by aerobic oxidative coupling of alcohols or aldehydes with amines, see Scheme 1.

In the first step of the reaction, the gold-catalysed oxidation of the alcohol or aldehyde in methanol yields a methyl ester.<sup>16</sup> In the second step, amine is added and the ester is converted into the desired amide by base-catalysed aminolysis. As the same base is promoting both steps of the reaction, the synthesis can be performed in a convenient one-pot procedure without cumbersome isolation or purification of the intermediate. The employed oxidant is pure dioxygen and the reaction can be performed under mild reaction conditions (25–65 °C, atmospheric pressure).

Initially, we used benzyl alcohol as a model compound to study the gold catalysed oxidative esterification in methanol. The results from these experiments showed that methyl benzoate could be obtained in 92% yield at full conversion after 24 hours employing KOMe as a base and Au/TiO<sub>2</sub> as a heterogeneous catalyst. Under the same reaction conditions, we found that addition of hexylamine to methyl benzoate resulted in the formation of *N*-hexylbenzamide (see ESI†).

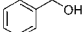
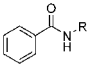
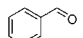
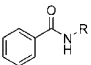
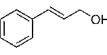
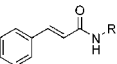
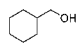
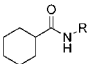
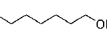
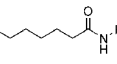
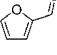
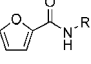
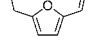
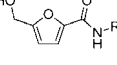
The two base-promoted reactions were combined in a novel one-pot reaction procedure and tested for the oxidative coupling of a number of substrates, including different alcohols, aldehydes and amines. All reactions were performed under identical reaction conditions and no optimisation was attempted for the individual substrates.

Table 1 compiles the results from the oxidative coupling of different alcohols and aldehydes with *N*-hexylamine to form the corresponding *N*-hexylamides. All examined alcohols, *i.e.* benzyl alcohol, cinnamyl alcohol, and 1-heptanol, were oxidised with high selectivity to form the corresponding methyl ester. While the oxidation of the aromatic alcohols achieved full conversion in 24 hours, 1-heptanol only achieved 34% conversion at room temperature (Table 1, entry 5). Higher yields of aliphatic

Centre for Catalysis and Sustainable Chemistry, Department of Chemistry, Technical University of Denmark, Building 207, 2800 Kgs. Lyngby, Denmark. E-mail: ar@kemi.dtu.dk

† Electronic supplementary information (ESI) available. See DOI: 10.1039/c2cc16768a

**Table 1** Yield of ester and amide obtained in the oxidative coupling of alcohols and aldehydes with *N*-hexylamine<sup>a</sup>

Entry	Alcohol/ aldehyde	Product	Ester yield [%]	Amide yield <sup>b</sup> [%]
1			92	90 (59)
2			93	92 (64)
3			> 99	46 (34)
4			74	74 (18)
5			34	34 (25)
6			> 99	99 (84)
7			73	73 (73)

<sup>a</sup> R = (CH<sub>2</sub>)<sub>5</sub>CH<sub>3</sub>. Reaction conditions: alcohol or aldehyde (5 mmol), methanol (50 mmol), anisole (0.5 mmol), KOMe (1.25 mmol), 1 wt% Au/TiO<sub>2</sub> (197 mg). After 24 hours 25 mmol amine was added and the mixture was heated to 65 °C for additional 96 hours. <sup>b</sup> Number in parenthesis is the yield obtained after 24 hours.

methyl esters have previously been reported at high temperatures and increased pressure of oxygen.<sup>11</sup> As expected, both aromatic aldehydes, *i.e.* benzaldehyde and furfural, were oxidised to the corresponding methyl esters in high yields (Table 1, entries 2 and 6).

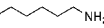
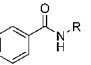
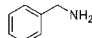
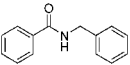
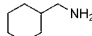
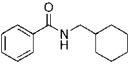
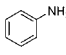
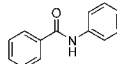
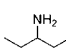
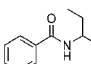
Table 1 also shows that all the investigated methyl esters reacted with *N*-hexylamine to form the corresponding amides in good yields. It is notable that the second step of the reaction occurred with excellent selectivity when using *N*-hexylamine (>99%) independent of the structure of the ester.

Table 2 summarises the results from the oxidative coupling of benzyl alcohol with different amines to form the corresponding amides. The reaction proceeded smoothly when employing benzylamine, while the more sterically demanding amines aniline and pentan-3-amine were unable to react under the applied reaction conditions. Furthermore, the oxidative coupling of benzyl alcohol with ammonia resulted in formation of benzamide.

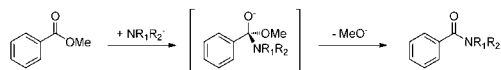
To investigate the observed structure–reactivity relationship for the aminolysis of methyl benzoate in Table 2 we performed a computational study. The exchange reaction is expected to take place *via* formation of an anionic, tetrahedral intermediate.<sup>17</sup> By determining the relative energies (in solution phase) of the methyl ester, tetrahedral intermediate and amide for the various amines we were aiming to correlate this with the experimental results. The overall process is illustrated in Scheme 2.

We investigated the reaction between methyl benzoate and ammonia, ethylamine, diethylamine, aniline and benzylamine. For the amines larger than NH<sub>3</sub> it was necessary to carry out a

**Table 2** Yield of ester and amide obtained in the oxidative coupling of benzyl alcohol with amines<sup>a</sup>

Entry	Amine	Product	Ester yield [%]	Amide yield <sup>b</sup> [%]
1			92	90 (59)
2			92	54 (15)
3			92	38 (16)
4			92	—
5			92	—
6	NH <sub>3</sub>	NH <sub>3</sub>	92	41 <sup>c</sup>

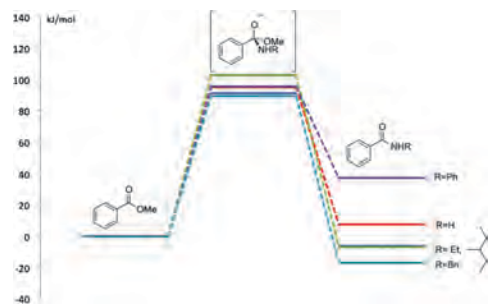
<sup>a</sup> R = (CH<sub>2</sub>)<sub>5</sub>CH<sub>3</sub>. Reaction conditions: benzyl alcohol (5 mmol), methanol (50 mmol), anisole (0.5 mmol), KOMe (1.25 mmol), 1 wt% Au/TiO<sub>2</sub> (197 mg). After 24 hours 25 mmol amine was added and the mixture was heated to 65 °C for additional 96 hours. <sup>b</sup> Number in parenthesis is the yield after 24 hours. <sup>c</sup> Isolated yield.

**Scheme 2** The reaction pathway from methyl ester to amide *via* an anionic, tetrahedral intermediate, which forms the basis for the computational study.

thorough conformational search, which was performed using the OPLS-2005 force-field<sup>18</sup> in MacroModel<sup>19</sup> with the built-in GB/SA solvation model (water).<sup>20</sup> The 10 best conformations was then subjected to further optimization using DFT/B3LYP<sup>21</sup> in Jaguar,<sup>22</sup> using the 6-31G\*\* basis set<sup>23</sup> in combination with the PBF continuum solvation model for methanol.<sup>24</sup> To account for the difference in protonation state we used hydroxide, hydronium and water, which were solvated by three additional water molecules.<sup>25</sup> The clusters were embedded in the same PBF solvation model for methanol.

The calculated energetic profiles of the aminolysis for the five different amines are shown in Fig. 1. The three successful examples (NH<sub>3</sub>, EtNH<sub>2</sub> and BnNH<sub>2</sub>) all have relatively low energies for both the tetrahedral intermediate and the amide product. In contrast, the amide formed from pentan-3-amine is also thermodynamically favoured by 7 kJ mol<sup>-1</sup> (similar to ethylamine), but the tetrahedral intermediate is disfavoured by 12 kJ mol<sup>-1</sup> relative to the one derived from ethylamine. This illustrates that the more sterically demanding pentan-3-amine cannot form the tetrahedral intermediate as the reaction is kinetically controlled.

With aniline the tetrahedral intermediate is similar in energy to the other mono-substituted amines, however, the amide product is almost 40 kJ mol<sup>-1</sup> higher in energy than the ester.



**Fig. 1** Calculated energetic profiles for the aminolysis of methyl benzoate using five different amines.

This energy penalty explains why aniline is incapable of converting the ester into the desired amide product.

In conclusion, we have presented a novel approach for the two-step synthesis of amides *via* the corresponding methyl ester and showed that the combination of supported gold nanoparticles and base forms an efficient catalytic system for the reaction. As the same base is promoting both steps of the reaction, the synthesis can be performed in a convenient one-pot procedure without isolation or purification of the intermediate. The employed oxidant is pure molecular oxygen and the reactions can be performed under mild reaction conditions. Furthermore, the reactions can be performed with a number of substrates, which demonstrates the versatility of the method. By employing theoretical DFT calculations we were able to rationalise the differences between successful and unsuccessful amine coupling partners based on a mechanism involving a tetrahedral, anionic intermediate. The good correlation between experiment and theoretical modelling obtained in this study allows us to use DFT calculations in a predictive manner when designing new experiments.

All chemicals and reagents were purchased from a commercial source and used without further purification. The employed catalyst was commercial gold on titanium dioxide (1 wt% Au/TiO<sub>2</sub>, supplied by Mintek) with a Brunauer–Emmett–Teller (BET) surface area of 49 m<sup>2</sup> g<sup>-1</sup>. The size of the gold nanoparticles has previously been determined to be 4–8 nm by means of transmission electron microscopy (TEM).<sup>26</sup>

In a typical experiment, alcohol or aldehyde (5 mmol), anisole (internal standard, 0.5 mmol), base (alkaline metal methoxide, 1.25 mmol) and methanol (50 mmol) were charged to a 20 ml reaction tube and connected to a reaction station providing stirring, heating and O<sub>2</sub> for the oxidation (atmospheric pressure). The system was flushed with O<sub>2</sub> and 197 mg Au/TiO<sub>2</sub> catalyst was added, corresponding to an Au/substrate molar ratio of 1/500. After 24 hours amine (10 or 25 mmol) was added and the reaction mixture was heated to 65 °C for methanol refluxing.

Samples were periodically collected, filtered and analysed by GC-FID and GC-MS using a HP-5 column from Agilent Technologies Inc. The amounts of substrates and reaction products were quantified by correlating to anisole as the internal standard.

The synthesis of benzamide (Table 2, entry 6) was performed in a pressure tube. After oxidising benzyl alcohol in methanol for 24 hours at room temperature under 1 bar of oxygen the tube was cooled in an ice bath and bubbled through with ammonia for 20 min. The tube was then sealed and heated

to 65 °C for 24 hours. The reaction mixture was dissolved in water and neutralised to pH 7 by addition of 0.1 M HCl. The product benzamide was recovered by extraction with ethyl acetate which was subsequently removed on a rotary evaporator to give 41% in isolated yield.

We gratefully acknowledge the support of the Danish Council for Independent Research, Grant No. 10-0937171.

## Notes and references

- G.-J. ten Brink, I. W. C. E. Arends and R. A. Sheldon, *Science*, 2000, **287**, 1636.
- T. Mallat and A. Baiker, *Chem. Rev.*, 2004, **104**, 3037.
- G. C. Bond, P. A. Sermon, G. Webb, D. A. Buchanan and P. B. Wells, *J. Chem. Soc., Chem. Commun.*, 1973, 444.
- G. Hutchings, *J. Catal.*, 1985, **96**, 292.
- M. Haruta, N. Yameda, T. Kobayashi and S. Iijima, *J. Catal.*, 1989, **115**, 301.
- L. Prati and M. Rossi, *J. Catal.*, 1998, **176**, 552.
- A. Stephen, K. Hashmi and G. J. Hutchings, *Angew. Chem., Int. Ed.*, 2006, **45**, 7896; C. Della Pina, E. Falletta, L. Prati and M. Rossi, *Chem. Soc. Rev.*, 2008, **37**, 2077; A. Wolf and F. Schüth, *Appl. Catal., A*, 2002, **226**, 1; G. Hutchings and M. Haruta, *Appl. Catal., A*, 2005, **291**, 2; G. J. Hutchings, *Catal. Today*, 2005, **100**, 55; A. Corma and H. Garcia, *Chem. Soc. Rev.*, 2008, **37**, 2096; M. Comotti, W.-C. Li, B. Spliethoff and F. Schüth, *J. Am. Chem. Soc.*, 2006, **128**, 917; N. Dimitratos, J. A. Lopez-Sanchez and G. J. Hutchings, *Chem. Sci.*, 2012, **3**, 20.
- D. I. Enache, J. K. Edwards, P. Landon, B. Solsona-Espriu, A. F. Carley, A. A. Herzing, M. Watanabe, C. J. Kiely, D. W. Knight and G. J. Hutchings, *Science*, 2006, **311**, 362.
- A. Abad, P. Concepción, A. Corma and H. Garcia, *Angew. Chem., Int. Ed.*, 2005, **44**, 4066.
- T. Hayashi, T. Inagaki, N. Itayama and H. Baba, *Catal. Today*, 2006, **117**, 210; E. Taarning, I. S. Nielsen, K. Egeblad, R. Madsen and C. H. Christensen, *ChemSusChem*, 2008, **1**, 75; B. Xu and C. M. Friend, *Faraday Discuss.*, 2011, **152**, 307.
- I. S. Nielsen, E. Taarning, K. Egeblad, R. Madsen and C. H. Christensen, *Catal. Lett.*, 2007, **116**, 35.
- A. Grirrane, A. Corma and H. Garcia, *Science*, 2008, **322**, 1661.
- A. Grirrane, A. Corma and H. Garcia, *J. Catal.*, 2009, **264**, 138; H. Sun, F.-Z. Su, J. Ni, Y. Cao, H.-Y. He and K.-N. Fan, *Angew. Chem., Int. Ed.*, 2009, **48**, 4390; S. Kegness, J. Mielby, U. V. Mentzel, C. H. Christensen and A. Riisager, *Green Chem.*, 2010, **12**, 1437; B. Xu, C. M. Friend and R. J. Madix, *Faraday Discuss.*, 2011, **152**, 241.
- T. Ishida, N. Kawakita, T. Akita and M. Haruta, *Gold Bull.*, 2009, **42**, 1.
- S. K. Klitgaard, K. Egeblad, U. V. Mentzel, A. G. Popov, T. Jensen, E. Taarning, I. S. Nielsen and C. H. Christensen, *Green Chem.*, 2008, **10**, 419; B. Xu, L. Zhou, R. J. Madix and C. M. Friend, *Angew. Chem., Int. Ed.*, 2010, **49**, 394; Y. Wang, D. Zhu, L. Tang, S. Wang and Z. Wang, *Angew. Chem., Int. Ed.*, 2011, **50**, 8917.
- P. Fristrup, S. Alvarez, L. B. Johansen and C. H. Christensen, *Chem. Commun.*, 2008, **7345**, 2750; P. Fristrup, L. B. Johansen and C. H. Christensen, *Catal. Lett.*, 2008, **120**, 184.
- M. L. Bender, *Chem. Rev.*, 1960, **60**, 53.
- G. A. Kaminski, R. A. Friesner, J. Tirado-Rives and W. L. Jorgensen, *J. Phys. Chem. B*, 2001, **2**, 6474.
- MacroModel version 9.9*, Schrödinger, LLC, New York, NY, 2011.
- W. C. Still, A. Tempczyk, R. C. Hawley and T. Hendrickson, *J. Am. Chem. Soc.*, 1990, **112**, 6127.
- A. D. Becke, *J. Chem. Phys.*, 1993, **98**, 5648; A. D. Becke, *J. Chem. Phys.*, 1993, **98**, 1372; C. Lee, W. Yang and R. G. Parr, *Phys. Rev. B: Condens. Matter Mater. Phys.*, 1988, **37**, 785.
- Jaguar version 7.8*, Schrödinger, LLC, New York, NY, 2011.
- R. Ditchfield, W. J. Hehre and J. A. Pople, *J. Chem. Phys.*, 1971, **54**, 724.
- B. Marten, K. Kim, C. Cortis, R. A. Friesner, R. B. Murphy, M. N. Ringnalda, D. Sitkoff and B. Honig, *J. Phys. Chem.*, 1996, **100**, 11775; D. J. Tannor, B. Marten, R. Murphy, R. A. Friesner, D. Sitkoff, A. Nicholls, B. Honig, M. Ringnalda and W. A. Goddard, *J. Am. Chem. Soc.*, 1994, **116**, 11875.
- V. S. Bryantsev, M. S. Diallo, A. C. T. van Duin and W. A. Goddard III, *J. Chem. Theory Comput.*, 2009, **5**, 1016.
- Y. Y. Gorbaney, S. K. Klitgaard, J. M. Woodley, C. H. Christensen and A. Riisager, *ChemSusChem*, 2009, **2**, 672.





## Mechanistic investigation of the one-pot formation of amides by oxidative coupling of alcohols with amines in methanol

Jerrick Mielby<sup>a,b</sup>, Anders Riisager<sup>a,b</sup>, Peter Fristrup<sup>b,\*</sup>, Søren Kegnæs<sup>a,b,\*\*</sup>

<sup>a</sup> Centre for Catalysis and Sustainable Chemistry

<sup>b</sup> Department of Chemistry, Technical University of Denmark, Building 207, DK-2800 Kgs. Lyngby, Denmark

### ARTICLE INFO

#### Article history:

Received 20 November 2011

Received in revised form 17 April 2012

Accepted 23 April 2012

Available online 23 June 2012

#### Keywords:

Gold catalysis  
Oxidative coupling  
Amide formation  
Mechanism  
Hammett study

### ABSTRACT

The one-pot formation of amides by oxidative coupling of alcohols and amines *via* intermediate formation of methyl ester using supported gold and base as catalysts was studied using the Hammett methodology. Determining the relative reactivity of four different *para*-substituted benzyl alcohol derivatives showed that the first step of the reaction generates a partial positive charge in the benzylic position (*i.e.* by hydride abstraction), while the second step of the reaction builds up negative charge in the rate determining step. The aminolysis of the methyl ester intermediate was further investigated by means of DFT/B3LYP. The transition state structures and energies were determined for both a concerted and a neutral two-step reaction mechanism. As expected, the base-promoted two-step mechanism was found to be the most energetically favourable and this reaction mechanism was used to construct a theoretical Hammett plot that was in good agreement with the one obtained experimentally.

© 2012 Elsevier B.V. All rights reserved.

### 1. Introduction

Formation of amides is a fundamental reaction in chemical synthesis and is used in the production of a broad range of bulk commodities, high-value fine chemicals, agrochemicals, and pharmaceuticals [1]. Amides are usually prepared by coupling of carboxylic acids and amines using a coupling reagent or by activation of the carboxylic acid. Alternative procedures include the Staudinger ligation [2], aminocarbonylation of aryl halides [3], and oxidative amidation of aldehydes [4]. Unfortunately, all these methods require the use of stoichiometric amounts of reagents, making them generally expensive and wasteful reactions [5]. In the search for a more sustainable chemical production, great efforts have been put into replacing the stoichiometric reagents with catalytic processes. This approach is not only cheaper and more environmentally friendly but also facilitates the possibility of starting from substrates other than carboxylic acids, thus paving the way for previously unavailable synthetic routes to amides [5].

In 2007 Milstein and co-workers [6] reported the first direct acylation of amines by alcohols under liberation of molecular hydrogen using a homogeneous ruthenium catalyst. Although this simple and highly atom-efficient reaction have inspired several other research

groups to further develop this reaction [7,8], the special handling of expensive metal complexes and ligands remains a limitation that may prevent general application. In contrast, the handling of a heterogeneous catalyst is usually more straightforward [9].

Since the first fundamental studies by Bond et al. [10], Hutchings [11], Haruta et al. [12], and Prati and Rossi [13], supported gold nanoparticles have been recognised as surprisingly active and selective heterogeneous catalysts for a number of aerobic oxidations using molecular oxygen (or even air) as the terminal oxidant [14,15]. From the standpoint of green and sustainable chemistry these oxidations are attractive, because oxygen is a cheap and abundant oxidant that produces water as the only by-product.

Recently, we reported that the combination of supported gold nanoparticles and base forms an efficient and highly selective catalytic system for the one-pot synthesis of amides by aerobic oxidative coupling of alcohols or aldehydes with amines in methanol [16] (see Scheme 1).

In the first step of this reaction, a methyl ester is obtained by the gold-catalysed aerobic oxidation of the alcohol or aldehyde in methanol [17,18]. It is notable that in this step the methanol serves as both solvent and reactant. In the second step of the reaction, addition of amine affords the amide by base-catalysed aminolysis of the methyl ester. As the same base promotes both steps of the reaction, the oxidative coupling can be performed in a convenient one-pot procedure under mild reaction conditions (25–65 °C, atmospheric pressure). It is important to mention that this approach is conceptually different from the gold-catalysed reactions previously reported by Wang et al. [19] and Soulé et al. [20], which are

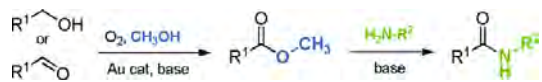
\* Corresponding author. Tel.: +45 45 25 21 23; fax: +45 45 88 31 36.

\*\* Corresponding author at: Centre for Catalysis and Sustainable Chemistry.

Tel.: +45 45 25 24 02; fax: +45 45 88 31 36.

E-mail addresses: [pf@kemi.dtu.dk](mailto:pf@kemi.dtu.dk) (P. Fristrup), [skk@kemi.dtu.dk](mailto:skk@kemi.dtu.dk) (S. Kegnæs).





**Scheme 1.** Synthesis of amides by aerobic oxidative coupling of alcohols or aldehydes with amines using supported gold and base as catalysts.

proposed to involve the formation and subsequent oxidation of a hemiaminal intermediate to the desired amide.

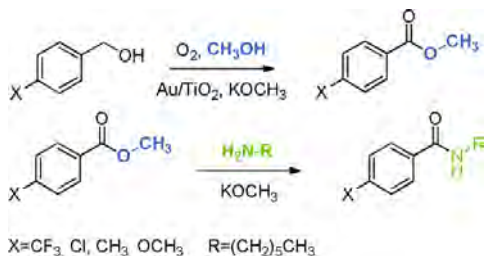
To study the structure-reactivity relationship we employed the well-known Hammett methodology [21] and focused our attention on a range of *para*-substituted benzyl alcohol derivatives (see Scheme 2).

In line with previous work [22,23], the results were obtained by performing competition experiments rather than establishing absolute kinetics. There were several reasons to choose this approach. First of all, a competition experiment is more robust towards small variations in the reaction conditions and allows the reaction to be followed to relatively high conversion without deviation from linearity. Secondly, a competition experiment can be designed to investigate a different step than the overall rate-determining step. In this study, we were interested in the elementary steps of the reaction that are directly involved in the activation of the substrates. It was therefore desirable to disregard any effects from steps involving, e.g. activation of dioxygen.

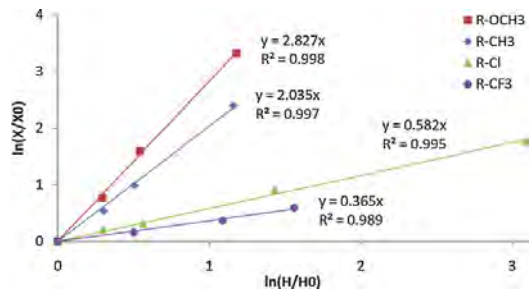
**2. Experimental study**

**2.1. Reaction procedure and analysis**

A series of competition experiments were performed to investigate the structure-reactivity relationship of the two consecutive steps of the oxidation-aminolysis reaction. In these experiments, anisole (0.5 mmol), potassium methoxide (1.25 mmol), and methanol (50 mmol) were charged to a reaction tube together with benzyl alcohol (2.5 mmol) and either (4-methylphenyl)methanol, (4-methoxyphenyl)methanol, (4-chloro-phenyl)methanol, or (4-(trifluoro-methyl)phenyl)methanol (2.5 mmol). The reaction tubes were connected to a reaction station providing stirring, heating and dioxygen gas for the oxidative esterification (atmospheric pressure). The system was flushed with O<sub>2</sub> before 197 mg 1 wt% Au/TiO<sub>2</sub> catalyst (Mintek) was added, corresponding to an Au/substrate molar ratio of 1/500. During the following two days, samples of 0.1 ml were periodically collected, filtered, and analysed by GC-FID and GC-MS using anisole as internal standard. When all reactions had reached full conversion, hexane-1-amine (10 mmol) was added and the temperature was increased to 65 °C (reflux temperature of methanol). During the following two days additional samples were collected and analysed.



**Scheme 2.** Overview of the competition experiments carried out to determine the relative reactivity of the various *para*-substituted benzyl methyl esters.



**Fig. 1.** Kinetic plot for the first step of the reaction showing the relative reactivity of four different *para*-substituted derivatives relative to benzyl alcohol.

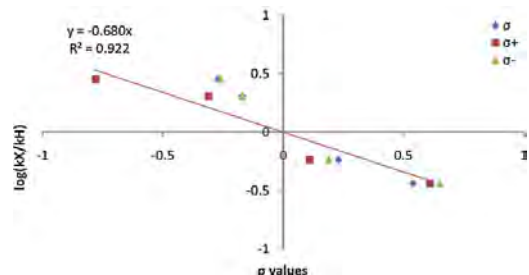
**2.2. Results and discussion**

In the first series of experiments, the conversion of all benzyl alcohols followed first order kinetics, which allowed the construction of the kinetic plots shown in Fig. 1. From these plots the relative reactivity could be determined as the slopes of the lines found by linear regression [24]. The assumption that the oxidation of all methyl esters followed first order kinetics could be justified from the good correlation coefficients ( $R^2 > 0.98$ ).

With the relative reactivity of the four different *para*-substituted methyl esters at hand, the Hammett plot could be constructed using three distinct sets of  $\sigma$ -values from literature [25,26] (Fig. 2).

Fig. 2 shows that the best linear correlation of  $\log(kX/kH)$  was obtained with the  $\sigma^+$ -values ( $R^2 = 0.922$ ), which resulted in a relatively large negative slope ( $\rho = -0.680$ ). A negative slope in the Hammett plot indicates that a positive charge is built up during substrate activation, which suggests that the reaction proceeded through the generation of a partial cation in the benzylic position, i.e. by  $\beta$ -hydride elimination.

Fristrup et al. [27] have previously reported a similar result from the gold-catalysed oxidation of benzyl alcohol to benzaldehyde ( $\rho = -1.10$ ). In that study the involvement of the  $\beta$ -hydride abstraction step was further confirmed by a significant kinetic isotope effect (KIE), when benzyl alcohol with deuterium incorporated in the  $\alpha$ -position was employed as substrate. Furthermore, Fristrup et al. [28] have investigated the conversion of benzaldehyde to methyl benzoate and found here a positive  $\rho$  value ( $\rho = 2.51$ ). These results suggest that the gold-catalysed esterification of alcohols with methanol occurs through the formation of an aldehyde intermediate and that this is the rate-determining step. The formation of an aldehyde intermediate also explains the formation of imines when the oxidation is carried out in presence of both methanol and amine [29].



**Fig. 2.** Hammett plot obtained using the relative reactivity determined during the oxidation of the benzyl alcohols.

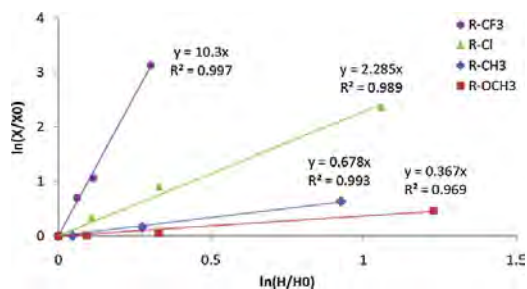


Fig. 3. Kinetic plot for the second step of the reaction showing the relative reactivity of four different *para*-substituted derivatives relative to methyl benzoate.

When all the oxidation reactions had reached full conversion, hexane-1-amine was added to the reactions and data for a second Hammett study could be obtained. Also here linear kinetic plots could be constructed from the conversion of substrate, which allowed determination of the relative reactivity (see Fig. 3). The corresponding Hammett plot is shown in Fig. 4.

Fig. 4 shows that the best linear correlation was obtained with the neutral  $\sigma$ -values ( $R = 0.980$ ), which resulted in a relatively large positive slope ( $\rho = 1.738$ ). The positive slope shows that a negative charge is building up during the reaction. A Hammett study was also performed starting with pure methyl benzoate esters. As expected these experiments showed that the water formed from the oxidation of the benzyl alcohols to the methyl esters had no significant effect on the relative reactivity (see Supporting information).

Comparison of Figs. 2 and 4 shows that the effect of the substituents are opposite in the two reactions. For instance, electron withdrawing substituents decrease the reactivity in the oxidation step but increase the reactivity in the consecutive aminolysis step – and vice versa.

### 3. Computational study

#### 3.1. DFT calculations

In order to understand the observed structure-reactivity relationship, the second step of the synthesis was modelled by means of Density Functional Theory (DFT) using the B3LYP functional [30,31] in line with earlier work [32,33]. The 6-31G\*\* basis set [34] was applied and solvation energies calculated using the built-in PCM model [35,36] with parameters suitable for methanol [37] as incorporated in Jaguar v. 7.8 release 109 from Schrödinger Inc. [38] All structures were optimised in gas phase and characterised by computations of the harmonic vibrational frequencies at the same level

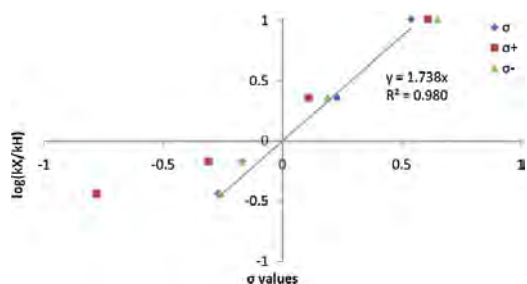


Fig. 4. Hammett plot obtained from the relative reactivity of the *para*-substituted methyl benzoates.

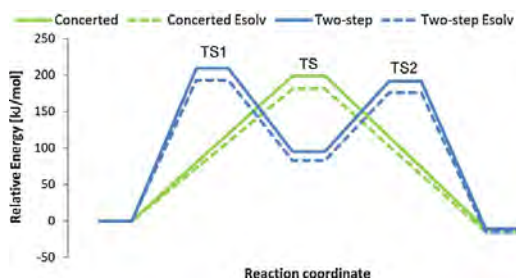


Fig. 5. Energy diagram for the concerted and two-step reaction mechanism, respectively.

of theory. Transition states were found to have one negative eigenfrequency, as required. Furthermore, the transition state structures were investigated by relaxation following the Intrinsic Reaction Coordinate (IRC), which lead to structures resembling pre-reactive and post-reactive complexes, as expected. Single-point solvation energies (methanol) were calculated for the structures optimised in gas phase. In order to avoid direct comparison between neutral and charged species we decided only to include neutral species in the investigated mechanisms (*vide infra*). Although recent developments have improved implicit solvation model tremendously, it is still doubtful whether a comparison between a neutral and a charged species is sufficiently accurate [39].

#### 3.2. Results and discussion

Initially, two possible mechanistic pathways were examined for the aminolysis of methyl benzoate with ammonia [40]. In the first reaction mechanism all bond forming and -breaking interactions were assumed to occur in a single step. The transition state of this “concerted” reaction mechanism involves simultaneous C–N bond formation, C–O cleavage and a proton transfer, as shown in Scheme 3.

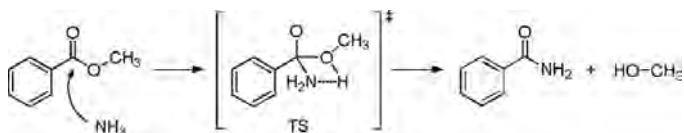
In the second mechanism under consideration the aminolysis was assumed to occur in two steps (Scheme 4). In the first step, a C–N bond is formed as a proton is transferred from ammonia to the oxygen atom of the C=O double bond. In the second step of the mechanism, the tetrahedral intermediate [41] is converted into benzamide and methanol by cleavage of the C–O bond, reformation of the C=O double bond, and a proton transfer between the two oxygen atoms.

The optimised structures of transition states; TS, TS1 and TS2 are shown in the supporting information together with the structure of the tetrahedral intermediate. A comparison of the relative energies, with and without a solvent model, is shown in Fig. 5.

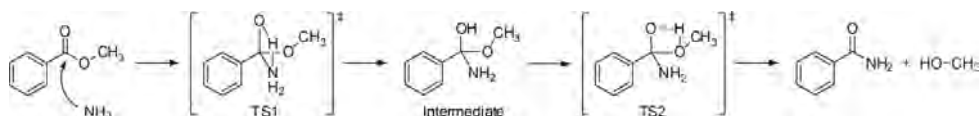
Fig. 5 shows that the concerted reaction is predicted to be the most energetically favourable mechanistic scenario. As expected, the implementation of the solvent model results in lowering of the relative energies.

Schaefer and co-workers [40] have previously investigated the aminolysis of methyl benzoate by DFT and *ab initio* methods and proposed a model, where considerable energy savings are realised by including an additional ammonia molecule in the computations. In this model, the additional  $\text{NH}_3$  molecule serves as an H-bridge that opens up the four-membered ring intermediate and favours the H-transfer between the hydroxylic oxygen atom and the methoxy group. The optimised transition state structures with an additional ammonia molecule are shown in Figs. 6 and 7, respectively.

Fig. 8 shows the effect of including an additional ammonia molecule in the model. Compared to the energy diagram in Fig. 5,



Scheme 3. Concerted reaction mechanism.



Scheme 4. Two-step reaction mechanism.

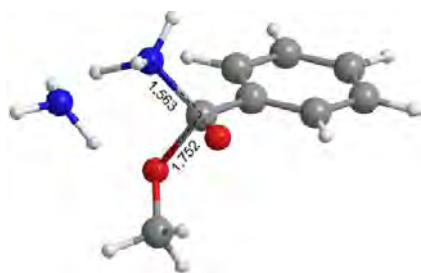


Fig. 6. The optimised transition state structure TS for the concerted mechanism.

**Table 1**  
Relative energies for the *para*-substituted methyl benzoate derivatives along the two-step mechanistic pathway.

Substituent	TS1 [kJ/mol]	Intermediate [kJ/mol]	TS2 [kJ/mol]
<i>p</i> -CF <sub>3</sub>	79.4	31.3	87.0
<i>p</i> -Cl	82.9	34.4	100.0
<i>p</i> -H	88.5	37.8	104.5
<i>p</i> -CH <sub>3</sub>	91.8	40.8	107.3
<i>p</i> -OCH <sub>3</sub>	95.0	44.4	111.0

the figure shows that besides stabilising the intermediate, the ammonia molecule also lowers the relative energy of the transition states. Interestingly, this effect is most profound for the two-step mechanism, which now becomes the energetically favourable mechanism. Furthermore, the figure shows that the second step of the mechanism is predicted to be rate-determining.

Fig. 8 shows how the additional ammonia molecule promotes both steps of the reaction and results in considerable lowering of the relative energies along the reaction pathway. Methanol has the same effect as ammonia, but although the first step is slightly lower in energy (4 kJ/mol) the ammonia-promoted mechanism is

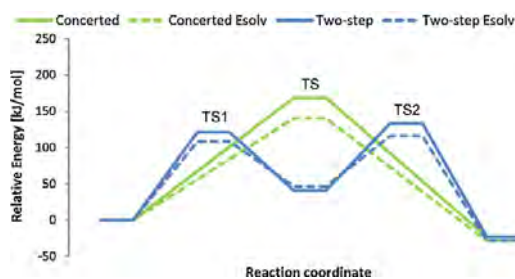


Fig. 8. Energy diagram for the concerted mechanism with an additional ammonia molecule.

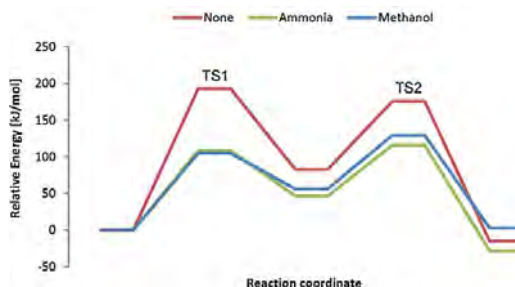


Fig. 9. Energy diagram showing the promoting effect of ammonia and methanol.

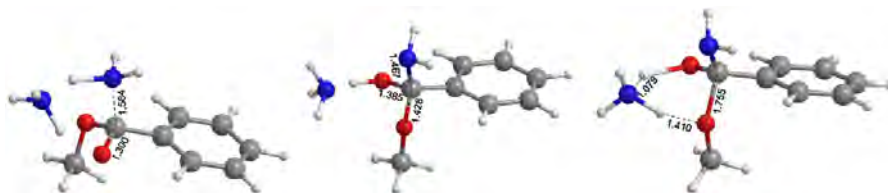


Fig. 7. The optimised structure of TS1 (left), the intermediate (middle) and TS2 (right) for the two-step mechanism.

the most favourable when it comes to the second step (13 kJ/mol) (see Fig. 9).

In order to compare the theoretical calculations with the experimental results, the ammonia molecule was replaced with an amine. To limit the number of possible conformations we chose methylamine instead of hexane-1-amine (which was used for the

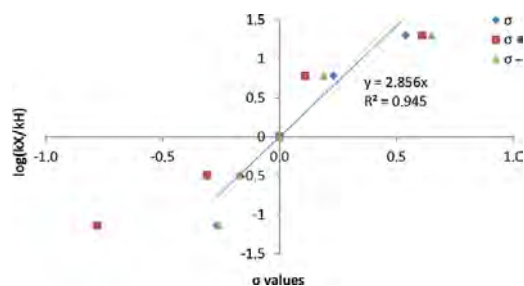


Fig. 10. Theoretically calculated Hammett plot.

Hammett study). Table 1 compiles the relative energies computed from the transition state structures of the five *para*-substituted derivatives that were used in the experimental Hammett study.

The energies in Table 1 were used to construct the Hammett plot in Fig. 10 using the Arrhenius equation. The best linear correlation of  $\log(kX/kH)$  was obtained with the  $\sigma$ -values ( $R^2 = 0.945$ ) which resulted in a line with a relatively large positive slope ( $\rho = 2.855$ ). On the other hand, poor correlations were obtained with the corresponding  $\sigma^-$ -values ( $R^2 = 0.883$ ,  $\rho = 2.476$ ) and  $\sigma^+$ -values ( $R^2 = 0.877$ ,  $\rho = 1.762$ ).

The limitations of the B3LYP functional are well known and have been addressed earlier by adding either classical dispersion terms [42] or by using improved exchange–correlation functionals that incorporate kinetic energy–density terms [43]. However, recalculation of the relative reaction rates in Fig. 10 using the M06 functional only resulted in a slight change of the corresponding reaction constant (from  $\rho_{\text{cal}} = 2.856$  to 2.894). As expected, these results show that the main contribution to the relative energies comes from electrostatic forces rather than dispersion forces. Compared with the experimental results described in the previous section ( $\rho_{\text{exp}} = 1.724$ ), the Hammett plot in Fig. 10 has a larger slope ( $\rho_{\text{cal}} = 2.856$ ). However, the resulting lines both have positive slopes in the same order of magnitude, which shows that the experiments and the model are in relatively good agreement.

#### 4. Conclusion

The one-pot synthesis of amides was investigated in two consecutive Hammett studies. The studies were performed by competition experiments rather than by establishing absolute reaction kinetics and the investigated substrates were *para*-substituted benzyl alcohol derivatives.

The result from the first Hammett study suggested that the gold-catalysed oxidation of benzyl alcohol occurs with build-up of positive charge in the benzylic position, which corresponds to a  $\beta$ -hydride abstraction step. The negative slope of the Hammett plot ( $\rho = -0.680$ ) was in good agreement with the generally accepted perception that the gold catalysed esterification of alcohols with methanol occurs through the formation of an aldehyde intermediate and that this is the rate-determining step.

The result from the second Hammett study showed that the reaction rate was very sensitive to the substituents and that negative charge is formed during the reaction ( $\rho = 1.738$ ). The aminolysis of the methyl ester intermediate was further investigated by means of Density Functional Theory. The transition state structures and energies were determined for both a concerted and a neutral two-step reaction mechanism. The base-promoted two-step

mechanism was found to be the most energetically favourable route, and using this mechanism it was possible to construct a theoretical Hammett plot that was in good agreement with the experimental results. The overall good correspondence between theory and experiment gives hope for the use of DFT calculations as a predictive tool to improve the reaction protocol, for instance by calculating the relative energy barriers when using ethanol instead of methanol. Furthermore, it could be envisioned that possible additives may be screened *in silico* to avoid time-consuming and waste-producing experiments.

#### Appendix A. Supplementary data

Supplementary data associated with this article can be found, in the online version, at <http://dx.doi.org/10.1016/j.cattod.2012.04.026>.

#### References

- [1] E. Valeur, M. Bradley, *Chemical Society Reviews* 38 (2009) 606.
- [2] M. Köhn, R. Breinbauer, *Angewandte Chemie International Edition* 43 (2004) 3106.
- [3] J.R. Martinelli, T.P. Clark, D.A. Watson, R.H. Munday, S.L. Buchwald, *Angewandte Chemie International Edition* 46 (2007) 8460.
- [4] W.-J. Yoo, C.-J. Li, *Journal of the American Chemical Society* 128 (2006) 13064.
- [5] C.L. Allen, J.M.J. Williams, *Chemical Society Reviews* 40 (2011) 3405.
- [6] C. Gunanathan, Y. Ben-David, D. Milstein, *Science* 317 (2007) 790.
- [7] L.U. Nordström, H. Vogt, R. Madsen, *Journal of the American Chemical Society* 130 (2008) 17672.
- [8] Y. Zhang, C. Chen, S.C. Ghosh, Y. Li, S.H. Hong, *Organometallics* 29 (2010) 1374.
- [9] S.K. Klitgaard, K. Egeblad, U.V. Mentzel, A.G. Popov, T. Jensen, E. Taarning, I.S. Nielsen, C.H. Christensen, *Green Chemistry* 10 (2008) 419.
- [10] G.C. Bond, P.A. Sermon, G. Webb, D.A. Buchanan, P.B. Wells, *Journal of the Chemical Society, Chemical Communications* (1973) 444b.
- [11] G.J. Hutchings, *Journal of Catalysis* 96 (1985) 292.
- [12] M. Haruta, N. Yameda, T. Kobayashi, S. Iijima, *Journal of Catalysis* 115 (1989) 301.
- [13] L. Prati, M. Rossi, *Journal of Catalysis* 176 (1998) 552.
- [14] A.S.K. Hashmi, G.J. Hutchings, *Angewandte Chemie International Edition* 45 (2006) 7896.
- [15] K.T. Højholt, A.B. Laursen, S. Kegnes, C.H. Christensen, *Topics in Catalysis* 54 (2011) 1026.
- [16] S. Kegnes, J. Mielby, U.V. Mentzel, T. Jensen, P. Fristrup, A. Riisager, *Chemical Communications* 48 (2012) 2427.
- [17] C. Marsden, E. Taarning, D. Hansen, L. Johansen, S.K. Klitgaard, K. Egeblad, C.H. Christensen, *Green Chemistry* 10 (2008) 168.
- [18] A.B. Laursen, K.T. Højholt, S.B. Simonsen, L.F. Lundegaard, S. Helveg, F. Schüth, M. Paul, J.-D. Grunwaldt, S. Kegnes, C.H. Christensen, K. Egeblad, *Angewandte Chemie International Edition* 49 (2010) 3504.
- [19] Y. Wang, D. Zhu, L. Tang, S. Wang, *Angewandte Chemie International Edition* 50 (2011) 1.
- [20] J.-F. Soulé, H. Miyamura, S. Kobayashi, *Journal of the American Chemical Society* 133 (2011) 18550.
- [21] L.P. Hammett, *Journal of the American Chemical Society* 59 (1937) 96.
- [22] P. Fristrup, S. Le Quement, D. Tanner, P.-O. Norrby, *Organometallics* 23 (2004) 6160.
- [23] L. Keinicke, P. Fristrup, P.-O. Norrby, R. Madsen, *Journal of the American Chemical Society* 127 (2005) 15756.
- [24] P. Fristrup, D. Tanner, P.-O. Norrby, *Chirality* 15 (2003) 360.
- [25] C. Hansch, A. Leo, R. Taft, *Chemical Reviews* 91 (1991) 165.
- [26] C. Hansch, H. Gao, *Chemical Reviews* 97 (1997) 2995.
- [27] P. Fristrup, L.B. Johansen, C.H. Christensen, *Catalysis Letters* 120 (2007) 184.
- [28] P. Fristrup, L.B. Johansen, C.H. Christensen, *Chemical Communications* (2008) 2750.
- [29] S. Kegnes, J. Mielby, U.V. Mentzel, C.H. Christensen, A. Riisager, *Green Chemistry* 12 (2010) 1437.
- [30] A.D. Becke, *Journal of Chemical Physics* 98 (1993) 5648.
- [31] C. Lee, W. Yang, R.G. Parr, *Physical Review B* 37 (1988) 785.
- [32] P. Fristrup, M. Kreis, A. Palmelund, P.-O. Norrby, R. Madsen, *Journal of the American Chemical Society* 130 (2008) 5206.
- [33] J.H. Dam, P. Fristrup, R. Madsen, *Journal of Organic Chemistry* 73 (2008) 3228.
- [34] R. Ditchfield, W.J. Hehre, J.A. Pople, *Journal of Chemical Physics* 54 (1971) 724.
- [35] B. Marten, K. Kim, C. Cortis, R.A. Friesner, R.B. Murphy, M.N. Ringnalda, D. Sitkoff, B. Honig, *Journal of Physical Chemistry* 100 (1996) 11775.
- [36] D.J. Tannor, B. Marten, R. Murphy, R.A. Friesner, D. Sitkoff, A. Nicholls, M. Ringnalda, W.A. Goddard III, B. Honig, *Journal of the American Chemical Society* 116 (1994) 11875.

- [37] Continuum dielectric constant: 33.62; Solvent probe molecule radius: 2.000 Å.
- [38] Jaguar, version 7.8, Schrodinger, LLC, New York, NY, 2010.
- [39] For a discussion, see P. Fristrup, M. Ahlquist, D. Tanner, P.-O. Norrby, *Journal of Physical Chemistry A* 112 (2008) 12862.
- [40] B. Galabov, Y. Atanasov, S. Ilieva, H.F. Schaefer, *Journal of Physical Chemistry A* 109 (2005) 11470.
- [41] M.L. Bender, *Chemical Reviews* 60 (1960) 53.
- [42] S. Grimme, *Journal of Computational Chemistry* 25 (2004) 1463.
- [43] Y. Zhao, D.G. Truhlar, *Theoretical Chemistry Accounts* 120 (2008) 215.

DOI: 10.1002/cctc.201200314

# Gold Nanoparticle-Catalyzed Formation of Nitrogen-containing Compounds—From Mechanistic Understanding to Synthetic Exploitation

Jerrick Mielby, Søren Kegnæs,\* and Peter Fristrup\*[a]

Dedicated to Professor Per-Ola Norrby on the occasion of his 50<sup>th</sup> birthday

During the last decade, heterogeneous catalysis using gold nanoparticles has gained importance as an efficient method for the oxidation of alcohols and aldehydes. The scope of these reactions has recently been extended to nitrogen-containing compounds, which is a particularly promising substrate class, as nitrogen is ubiquitous in both materials science and biology. It has been shown that gold nanoparticles can over-

come many of the frequently encountered difficulties caused by the coordinating properties of nitrogen when using homogeneous catalysis. This minireview is meant to serve as an entry point for new researchers in this emerging field and is divided into sections based upon which nitrogen-containing products are synthesized using gold nanoparticles in the critical reaction step.

## Introduction

For many years, the legendary noble character of gold discouraged the investigation of its potential catalytic activity.<sup>[1]</sup> Until 1973, only scattered reports had appeared in the literature when Bond et al.<sup>[2]</sup> reported the hydrogenation of olefins over a supported gold catalyst. A decade later, Hutchings<sup>[3]</sup> and Haruta et al.<sup>[4]</sup> reported remarkable results from using supported gold catalysts for hydrochlorination of acetylene and low-temperature oxidation of carbon monoxide, respectively. These fundamental studies triggered renewed interest in gold catalysis<sup>[5]</sup> and significant advances have been made both within homogeneous and heterogeneous catalysis.<sup>[6]</sup> In particular, it has been shown that supported gold nanoparticles (typically <5 nm) are surprisingly active and selective catalysts for a number of reactions in organic chemistry.<sup>[7–9]</sup>

Although the intimate mechanisms at the molecular level are still not fully understood, several factors have been identified as being critical for the catalytic activity of gold nanoparticles.<sup>[10]</sup> First and foremost the gold particles must be a few nm in diameter, so that under-coordinated, reactive gold atoms exist in large numbers at the edges and corners of the particles.<sup>[11]</sup> These gold atoms have often been described as being non-metallic,<sup>[12]</sup> and it has been shown that the appearance of the non-metallic character coincides with onset of catalytic activity. The high catalytic activity of supported gold has also been related to possible indirect effects of the support material, including charge transfer<sup>[13]</sup> and support-induced strain.<sup>[14]</sup> Furthermore, it has been suggested that the reaction involves the support more directly either by activation of the substrates<sup>[15]</sup> or by virtue of the special chemical properties of the gold/support interface.<sup>[16]</sup>

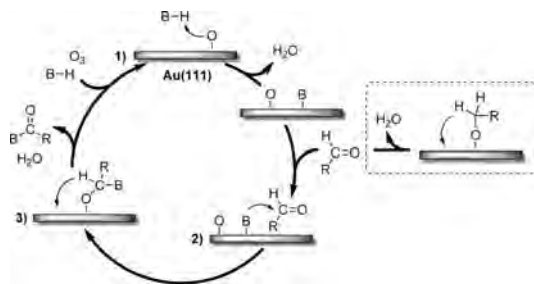
The mechanism for the activation of dioxygen has also been subject to significant debate and both peroxy and superoxy intermediates have been suggested.<sup>[17,18]</sup> A few reports have in-

dicated that gold-hydride species exists under catalytic reaction conditions,<sup>[19]</sup> and there have also been indications of carbonate or bicarbonate species.<sup>[20]</sup> Very recently, the importance of water has been highlighted in a combined experimental and theoretical study in which oxygen is regenerating hydroxide ions via a peroxide intermediate rather than participating directly.<sup>[21]</sup>

The mechanism of oxidation, as experienced by the substrate, has received far less attention. However, it has been shown that alcohol oxidation takes place via an initial  $\beta$ -hydride abstraction step.<sup>[22]</sup> Similarly, it has been shown that the oxidation of aldehydes exhibits a significant kinetic isotope effect (KIE), which also indicates an H-abstraction step. In this case, however, the Hammett study of a series of *para*-substituted benzaldehydes indicated that a radical mechanism may be operating.<sup>[23]</sup> Valuable mechanistic insight has also been gained from fundamental studies on gold single crystals.<sup>[24–26]</sup> Based on advanced experimental and theoretical investigations, Friend and co-workers<sup>[27]</sup> have proposed a general mechanistic framework for the oxidative coupling reactions of alcohols, aldehydes and amines over oxygen covered gold surfaces. In this framework, the acidic hydrogen abstraction through a Brønsted acid-base reaction, the nucleophilic attack, and the oxygen assisted  $\beta$ -H elimination are identified as the critical reaction steps, see Scheme 1.

In this minireview we have chosen to focus on the heterogeneous gold-catalyzed formation of nitrogen-containing com-

[a] J. Mielby, S. Kegnæs, Prof. P. Fristrup  
Department of Chemistry  
Technical University of Denmark  
Building 207, DK-2800 Kgs. Lyngby (Denmark)  
E-mail: skk@kemi.dtu.dk  
pf@kemi.dtu.dk



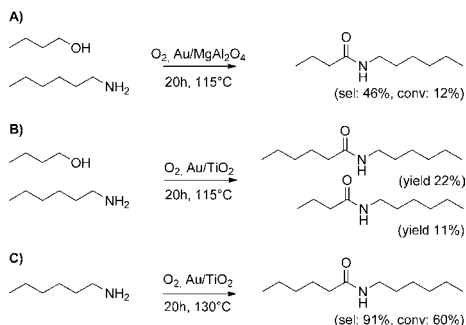
**Scheme 1.** The general mechanism for cross-coupling reactions with its three critical steps; 1) acidic hydrogen activation, 2) nucleophilic attack and 3)  $\beta$ -H elimination.

pounds. Nitrogen-containing compounds are ubiquitous in biochemistry and many important compounds in both the pharmaceutical industry and materials science contain nitrogen atoms. Unfortunately, many nitrogen-containing compounds are excellent  $\sigma$ -donors and coordinate strongly to transition metals, which complicates their synthesis by both homogeneous and heterogeneous catalysis. However, recent results have shown that many of these problems can be overcome using supported gold nanoparticles. We believe that the catalytic formation of nitrogen-containing compounds is an important new research direction within gold catalysis, and we hope that this minireview can serve as an entry point for new researchers in this emerging field. The remaining part of this review is divided into sections based upon which particular nitrogen-containing products are synthesized using gold in the critical reaction step.

## 1. Formation of amides

Supported gold nanoparticles have become well-known catalysts for the aerobic oxidation of alcohols or aldehydes to acids<sup>[28,29]</sup> or esters,<sup>[30–32]</sup> but only recently gold nanoparticles have been demonstrated to catalyze the direct formation of amides.

In 2008 Klitgaard et al.<sup>[33]</sup> showed that the oxidation of mixtures of amines and alcohols afforded different products when using supported gold nanoparticles on different supports as catalysts. When Au/MgAl<sub>2</sub>O<sub>4</sub> was used for the oxidation of mixtures of *N*-hexylamine and 1-butanol, *N*-hexylbutyramide was the main product, see Scheme 2A. However, when Au/TiO<sub>2</sub> was used as catalyst, both *N*-hexylbutyramide and *N*-hexylhexanamide were obtained, see Scheme 2B. The authors suggested that the formation of *N*-hexylbutyramide could be explained by two possible reaction mechanisms that involve either the oxidation of 1-butanol to butyl butyrate, followed by aminolysis to afford the amide, or the oxidation of the hemiaminal of butanol and *N*-hexylamine. However, the formation of *N*-hexylhexanamide could only be explained by oxidation of the amine. In fact, when the reaction was performed in absence of butanol, *N*-hexylamine was obtained with high selectivity (60% conversion, 91% selectivity), see Scheme 2C. Fur-

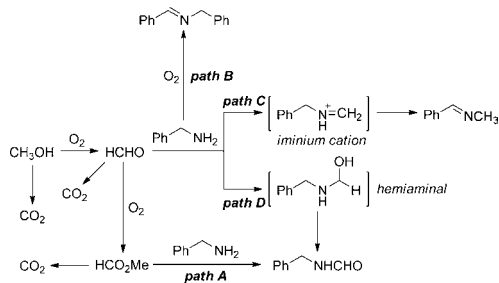


**Scheme 2.** Oxidation of mixtures of 1-butanol and hexylamine with A) Au/MgAl<sub>2</sub>O<sub>4</sub> and B) Au/TiO<sub>2</sub>, and C) hexylamine using Au/TiO<sub>2</sub>.

thermore, Klitgaard et al. showed that 1,6-hexanediamine could be oxidized to the corresponding amide, caprolactam, opening up a potential new route to nylon-6.

A better understanding of the mechanism for the direct amidation was given by Xu et al.<sup>[34]</sup> in 2010. Xu et al. showed that adsorbed dimethylamine on Au(111) selectively attacks the electron-deficient carbon in formaldehyde to yield *N,N*-dimethylformamide.

In 2009 Ishida and Haruta<sup>[35]</sup> reported that formamides could be synthesized directly from amines with methanol and molecular oxygen over supported gold nanoparticles, see Scheme 3.

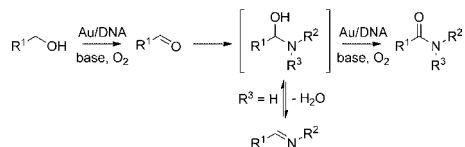


**Scheme 3.** Possible reaction pathways for *N*-formylation of benzylamine in methanol over supported gold nanoparticles.

Benzylamine, morpholine, aniline, and cyclohexylamine were converted into the corresponding formamides in moderate to good yield using Au/NiO as the heterogeneous catalyst. Also in this reaction, the authors found that the main products markedly changed with the choice of metal-oxide support. Au/NiO and Au/Al<sub>2</sub>O<sub>3</sub> enabled *N*-formylation by oxidation of methanol, whereas Au/TiO<sub>2</sub> seemed to have a higher affinity for amines, which consequently afforded the corresponding oxime as the main product. Ishida and Haruta also investigated the *N*-formylation reaction using formaldehyde, formic acid and methyl formate as formylating agents. Although formic acid and methyl formate only afforded formamides, formaldehyde

also afforded *N*-benzylidene-methylamine. These results suggested that the production of formamide could be ascribed to the in situ formation of formaldehyde or methyl formate. Scheme 3 shows the four possible reaction pathways for the reaction of benzylamine in methanol.

In 2011, Wang et al.<sup>[36]</sup> and Soulé et al.<sup>[37]</sup> investigated the direct conversion of alcohols and amines into amides using new and advanced gold nanoparticle catalysts. Wang et al. developed a heterogeneous catalyst comprised of gold supported on DNA. This unusual catalyst, prepared from a natural fish sperm DNA template and Au metal salt precursor, was stable in air and showed remarkable reversible solubility in water and ethanol. The catalytic activity of Au/DNA was investigated for the direct amidation of benzyl alcohol and aniline and compared to a series of catalysts comprised of gold nanoparticles supported on different water-soluble (PVA, PVP, starch, and Arabic gum) and insoluble materials (TiO<sub>2</sub>, SiO<sub>2</sub>, CeO<sub>2</sub>, Al<sub>2</sub>O<sub>3</sub>, and NiO). Under strongly basic conditions, all catalysts afforded phenylbenzamide in low to moderate yield. While most of the catalyst performed unsatisfactorily due to either poor stability under the reaction conditions (soluble catalysts) or poor dispersion of the catalyst in water (insoluble catalysts), Au/DNA afforded up to 91% amide after 12 h at 50 °C under optimized conditions. Furthermore, taking advantage of the reversible solubility of Au/DNA in water and ethanol, the catalyst could be recovered by simple phase separation and reused. The fact that oxygen, high pH and water were all essential for the reaction led the authors to suggest that hydroxides adsorbed at the gold/water interphase may promote the oxidation of the hemiaminal intermediate to the desired product, while the water is proposed to affect the equilibrium and prevent the formation of imine, see Scheme 4.

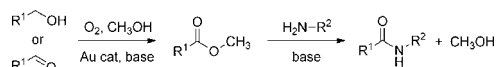


**Scheme 4.** Proposed mechanism of amination from alcohols and amines catalyzed by Au/DNA.

Under similar conditions, that is, using one equivalent of base, Soulé et al.<sup>[37]</sup> reported the general and selective amidation of a series of amines and alcohols. The amidations were catalyzed by gold- or bimetallic nanoparticles consisting of gold and inexpensive materials, such as nickel, iron, or cobalt, supported on polystyrene-based polymers. For the amidation of benzyl alcohol and benzyl amine, the authors found that the association between gold and nickel, iron, or cobalt had a positive effect on amide selectivity. In particular, gold and cobalt afforded the desired amide in 94% yield. Furthermore, the catalyst could be filtered and reused without significant loss of activity or leaching. As it was found that a low concentration of the aldehyde intermediate was required to obtain high selectivity, the authors suggested that the effect of Co

could be ascribed to a) decreased activity of Au the first step and b) increased stability of the hemiaminal intermediate.

Choosing a different approach, we recently reported a reaction protocol for the one-pot formation of amides via intermediate formation of methyl esters, Scheme 5.<sup>[38]</sup> In the first



**Scheme 5.** Synthesis of amides by aerobic oxidative coupling of alcohols or aldehydes with amines using supported gold and base as catalysts.

step of this reaction, the gold-catalyzed oxidation of an alcohol or aldehyde in methanol affords a methyl ester. In the second step, amine is added and the ester is converted into the desired amide by base-catalyzed aminolysis. As the same base is promoting both steps of the reaction, the synthesis can be performed in a convenient one-pot procedure without isolation or purification of the intermediate. However, while benzyl alcohol and *N*-hexylamine reacted to give the corresponding amide in 90% yield, the more sterically demanding amines like aniline were unable to react under the applied reaction conditions. By employing theoretical DFT calculations we were able to rationalize the differences between successful and unsuccessful amine coupling partners based on a mechanism involving a tetrahedral, anionic intermediate. As with the direct amidations, the reactions could be performed under mild reaction conditions using molecular oxygen as the terminal oxidant and with water being the only by-product, although only a catalytic amount of base was required.

In a subsequent Hammett study, we investigated the free-energy relationship of both steps of the reaction.<sup>[39]</sup> Determining the relative reactivity of four different *para*-substituted benzyl alcohol derivatives showed that the first step of the reaction generates a partial positive charge in the benzylic position (i.e., by hydride abstraction), while the second step of the reaction builds up negative charge in the rate determining step. The aminolysis of the methyl ester intermediate was further investigated by means of DFT. A base-promoted two-step mechanism was found to be the most energetically favorable and the energy of the rate determining step was used to construct a theoretical Hammett plot that was in good agreement with the one obtained experimentally.

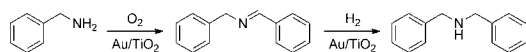
## 2. Formation of Imines

The two most used methods to synthesize imines using a heterogeneous gold catalyst are the condensation of amines with carbonyl compounds and the oxidation of secondary amines.

In 2009, Sun et al.<sup>[40]</sup> reported the synthesis of imines starting from alcohols and amines using different supported gold catalysts in toluene. Among the catalysts tested, Au supported on hydroxyapatite (HAP) showed the highest catalytic activity. For instance, benzylideneaniline was synthesized from benzyl alcohol and aniline in 98% yield. The higher activity of Au/HAP was ascribed to the special acid/base sites present on the hy-







**Scheme 9.** One-pot, two-step synthesis of secondary amines using Au/TiO<sub>2</sub> as catalyst.

Aschwanden et al.<sup>[48]</sup> showed that it is possible to arrive at an efficient catalyst without any of the conventional steps for preparation of the supported gold nanoparticles. The catalyst precursor Au(OAc)<sub>3</sub> and an oxide support were simply added to the reaction mixture which formed the active gold nanoparticles in situ. The gold catalyst showed good catalytic activity for the aerobic oxidative dehydrogenation of dibenzylamine and the product dibenzylimine was afforded in 58% yield. Moreover, oxidation of benzylamine afforded dibenzylimine in 89% yield. Filtration of the reaction mixture stopped the reaction progress and showed that the catalyst was indeed heterogeneous.

### 3. Formation of amines

The synthesis of amines using supported gold nanoparticles includes the reduction of nitrogen-containing compounds, such as imines, amides, or nitro compounds. Although the reduction of imines and amides results in formation of secondary amines, reduction of nitro compounds results in formation of primary amines. In addition, deoxygenations and aminations can lead to formation of tertiary amines.

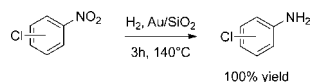
One of the first studies with nitrogen-containing compounds was made by Biella et al.<sup>[49]</sup> They investigated if the presence of basic amino group in amino-alcohols could promote the gold-catalyzed oxidation of the alcohol groups in absence of added base. As aliphatic amines were known to interact strongly with noble metals, the authors also wanted to compare the Au catalysts with Pd and Pt catalysts, see Table 1.

<b>Table 1.</b> Oxidation of 2-aminoethanol and 2-aminopropanol to the corresponding amino acids and carboxylates, respectively.			
Substrate	Catalyst	Conversion	Conversion with NaOH
	1 wt% Au/C	3	20
	5 wt% Pd/C	0	0
	5 wt% Pt/C	0	0
	1 wt% Au/Al <sub>2</sub> O <sub>3</sub>	–	23
	1 wt% Au/C	22	65
	5 wt% Pd/C	0	0
	5 wt% Pt/C	0	0
	1 wt% Au/Al <sub>2</sub> O <sub>3</sub>	–	100

Analysis of the results in Table 1 reveals that the catalytic activity of Au/C for the oxidation to aminoacids is sensitive to the nature of the substrate, such as low activity for 2-aminoethanol and higher for 2-aminopropanol. In both cases, Pd/C and Pt/C are inactive. Adding an equivalent amount of NaOH improved the conversion to the corresponding aminocarboxylate for Au/C, whereas Pd/C and Pt/C remained inactive.

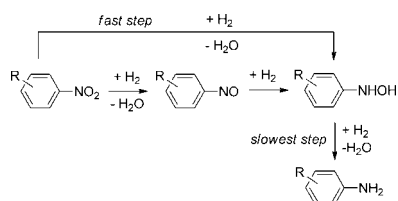
Changing the support material from carbon to alumina increased the conversion of 2-aminoethanol to 23% and the conversion of 2-aminopropanol to 100%.

In 2006, Chen et al.<sup>[50]</sup> reported a simple reduction method for supporting gold nanoparticles on silica. The reducing agent was different organosilanes introduced onto the silica in a sol-gel process stirring 3-glycidoxypropyltrimethoxysilane (GPTMS) and tetraethoxysilicate (TEOS) in an aqueous solution of ammonia. The modified silica (CH<sub>2</sub>O-SiO<sub>2</sub>) were suspended in a solution of HAuCl<sub>4</sub> and heated to 100 °C for 2 h to reduce the gold. The as-prepared Au/SiO<sub>2</sub> catalyst was tested for the catalytic hydrogenation of aromatic compounds. Although the applied reaction conditions were relatively harsh (140 °C, 40 bar H<sub>2</sub>) compared to, for example, Pd-based catalysts that are effective under milder reaction conditions, the supported gold nanoparticles showed higher chemoselectivity. For instance, the hydrogenation of chlorine-containing nitroaromatics proceeded to full conversion without any dechlorination to give 100% yield of the desired amines, see Scheme 10.



**Scheme 10.** Hydrogenation of chlorine-containing nitroaromatics to the corresponding amines.

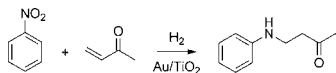
To unravel the reaction pathway of the gold-catalyzed reduction of nitro compounds, Corma et al.<sup>[51]</sup> combined in situ IR spectroscopy with macro-kinetic experiments to determine the reaction intermediates and relative rates of the elementary steps during the reaction. Based on these results the authors concluded that aromatic nitro compounds are hydrogenated on Au/TiO<sub>2</sub> by the reaction sequence shown in Scheme 11.



**Scheme 11.** Proposed reaction pathway for the hydrogenation of aromatic nitro compounds to aniline derivatives over Au/TiO<sub>2</sub>.

In a subsequent study, Corma and co-workers<sup>[42]</sup> applied gold catalysts in cascade-type reactions to synthesize different nitrogen-based compounds, including a number of imines and amines. The reduction of aromatic nitro compounds were carried out in presence of hydrogen or either an aldehyde,  $\alpha,\beta$ -unsaturated carbonyl compound or alkyne to afford the corresponding amines. The benefit of using gold nanoparticles for these reductions was most evident when other easily reducible groups such as double bonds or halide groups were present in

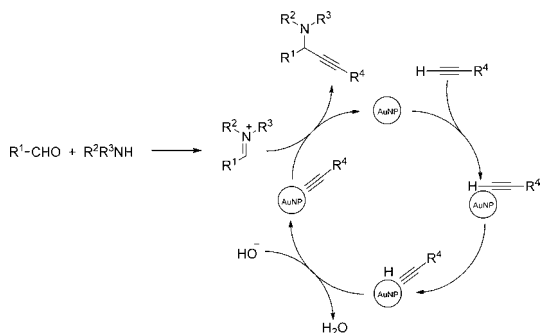
the substrates. In particular, the authors showed that Au/TiO<sub>2</sub> is an efficient and highly selective catalyst for the synthesis of  $\beta$ -amino carbonyl compounds starting directly from nitroaromatics and conjugated ketones, see Scheme 12.



**Scheme 12.** One-pot synthesis of a  $\beta$ -amino carbonyl compound from nitrobenzene and 1-buten-3-one using Au/TiO<sub>2</sub> as bi-functional heterogeneous catalyst.

Under H<sub>2</sub> pressure the supported Au nanoparticles selectively hydrogenate the nitro group into an amine, while the mild acidity of TiO<sub>2</sub> promotes the aza-Michael addition of the amine to the  $\alpha,\beta$ -unsaturated ketone affording the desired product in high yield (up to 91%).

In 2007, Kidwai et al.<sup>[52]</sup> reported that unsupported gold nanoparticles are efficient catalysts for the three-component coupling reaction of aldehydes, amines and alkynes to form the corresponding propargylamines (A<sup>3</sup> coupling). For instance, benzaldehyde, piperidine, and phenylacetylene reacted to form 2-propyn-1-amine in 78% yield after 12 h using 10 mol% gold nanoparticles around 18 nm in diameter. After completion of the reaction, the reaction mixture was centrifuged at 2000–3000 rpm. The organic phase was decanted off and the remaining gold nanoparticles could be collected and reused for up to seven runs without significant loss of activity. The authors proposed a mechanism where the alkyne C–H bond is activated by the gold nanoparticles, see Scheme 13. The acti-



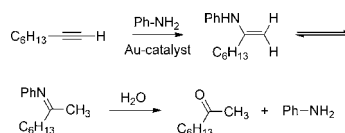
**Scheme 13.** Proposed mechanism for the gold nanoparticle-catalyzed A<sup>3</sup> coupling.

vated alkenyl–Au intermediate then reacts with the iminium ion (formed from the reaction of aldehydes with secondary amines), which gives the corresponding propargylamine and regenerates the gold nanoparticle.

More recently, Datta et al.<sup>[53]</sup> reported an approach for the encapsulation of gold nanoparticles in mesoporous carbon nitride with built-in functionalities that resulted in small and highly dispersed nanoparticles. The as-prepared catalysts were

shown to be efficient for the three-component coupling reaction and afforded propargylamine in 62% yield after 24 hour. Layek et al.<sup>[54]</sup> reported further improvements in the catalytic activity for the same reaction using a catalytic system containing gold nanoparticles supported on commercial nanocrystalline magnesium oxide (TONs up to 400).

Corma et al.<sup>[55]</sup> demonstrated that the supported gold nanoparticles are active and regioselective catalysts for the hydroamination of alkynes. For instance, 1-octyne and aniline reacted to form *N*-(2-octylidene) aniline and 2-octanone in different ratios. The formation of these products is consistent with the initial formation of the Markovnikov enamine, followed by tautomerization to *N*-(2-octylidene) aniline and possibly hydrolysis to form the ketone 2-octanone. The proposed reaction pathway is shown in Scheme 14.

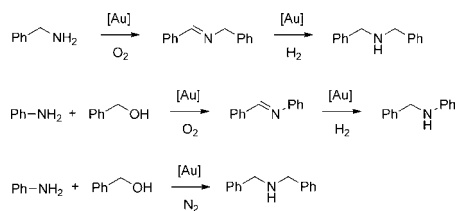


**Scheme 14.** Proposed reaction pathway for the hydroamination reaction of 1-octyne with aniline catalyzed by supported gold nanoparticles.

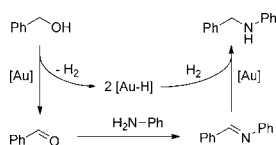
Unfortunately, agglomeration of the gold nanoparticles caused a decrease in the catalytic activity upon recycling of the catalyst. The authors found that gold supported on a composite formed by chitosan and silica resulted in the highest catalytic activity over time (TON up to 477), which suggested that the interaction of gold nanoparticles with the NH and OH groups of the bio-polymer may be responsible for stabilization of the gold nanoparticles against agglomeration or leaching.

Ishida et al.<sup>[56]</sup> deposited Me<sub>2</sub>Au(acac) on three kinds of porous coordination polymers (MOF-5, CPL-2, and Al-MIL53) by using the solid grinding method. After reduction in Formier gas at 120 °C for 2 h, the size of the nanoparticles increased in the order of Al-MIL53 < CPL-2 < MOF-5. The mean diameter of the gold particles supported on Al-MIL53 was estimated to be around 1.6 nm by means of HAADF-STEM. The prepared catalysts were tested for the one-pot synthesis of secondary amines from primary amines by a sequential oxidation/hydrogenation reaction and Al-MIL53 was shown to be the best support. For instance, Ishida et al. showed that dibenzylamine could be obtained from benzylamine in 91% yield via initial formation of benzylidenebenzylamine. The reaction was carried out at 120 °C over 2 mol% of Au in 5 bar O<sub>2</sub> for 2 h and then in 5 bar H<sub>2</sub> for 22 h. The authors also found that the small gold clusters promoted the N-alkylation of aniline with benzylalcohol in the presence of base under N<sub>2</sub> atmosphere, that is, without using O<sub>2</sub> and H<sub>2</sub> (Scheme 15).

Ishida et al. proposed a mechanism composed of 1) the dehydrogenation of alcohol to aldehyde with formation of Au–H species, 2) the formation of imine from the reaction of the aldehyde with amine and 3) the hydrogen transfer from Au–H to the imine affording the secondary amine (Scheme 16). The



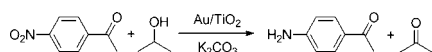
**Scheme 15.** Synthesis of secondary amines using supported gold nanoparticles by sequential oxidation/hydrogenation and direct N-alkylation, respectively.



**Scheme 16.** Proposed pathway for the N-alkylation of benzyl alcohol with aniline over Au/Al-MIL53.

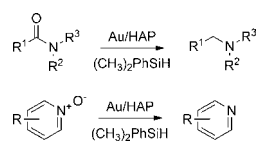
proposed hydrogen transfer mechanism was strengthened by the observation that 2-propanol could be used to reduce benzylidenebenzylamine to afford dibenzylamine and acetone, respectively. Interestingly, this reaction resembles the homogeneous iridium-catalyzed “borrowing hydrogen” methodology pioneered by Yamaguchi and co-workers.<sup>[57,58]</sup>

A similar result was reported by Su et al.<sup>[59]</sup> from the investigation of the transfer hydrogenation of nitro compounds to amines using 2-propanol as reductant and supported gold nanoparticles as catalyst. The results showed that the Au/TiO<sub>2</sub> was a very efficient catalyst for the selective reduction of nitro groups in the presence of carbonyl functionalities. Notably, 100% chemoselectivity in terms of –NO<sub>2</sub> reduction was achieved for the synthesis of 4-aminoacetophenone, see Scheme 17.



**Scheme 17.** Au/TiO<sub>2</sub>-catalyzed transfer hydrogenation of 4-nitroacetophenone.

Mikami et al.<sup>[60]</sup> reported that hydroxyapatite-supported gold nanoparticles (Au/HAP) are an efficient catalyst for the deoxygenation of amides, using silanes as reductants. Tertiary and secondary amides with benzylic, allylic, aliphatic, and heterocyclic amide substituents were all selectively converted into the corresponding amines with TONs up to 10000 (Scheme 18). For instance, *N,N*-dimethylbenzamide reacted to afford *N,N*-dimethyl-1-phenylmethanamine in 99% yield after 3 h at 110 °C in the presence of dimethylphenylsilane. High yields of amines were not limited to HAP, but could also be reached with Au



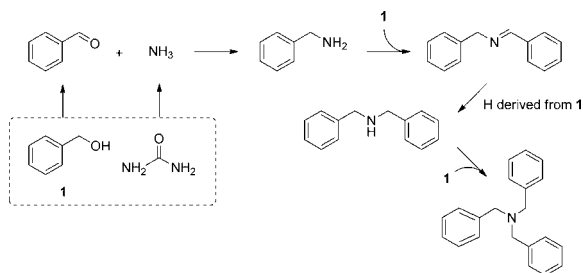
**Scheme 18.** Gold-catalyzed deoxygenation of amides and *N*-pyridine oxides.

supported on other supports such as TiO<sub>2</sub> or Al<sub>2</sub>O<sub>3</sub>. However, Au had the highest catalytic activity compared to other metal nanoparticles. Pd, Ag, and Pt nanoparticles resulted in low yields, whereas Ru and Rh showed no activity under the applied reaction conditions. The Au/HAP/silane system was also effective for the selective deoxygenation of sulfoxides and (in particular) pyridine *N*-oxides, even when the substrates contained other reducible functional groups such as cyano, olefin, or carbonyl as substituents.

He et al. reported the gold-catalyzed synthesis of tertiary and secondary amines from alcohols and urea.<sup>[59]</sup> The reaction of primary alcohols with urea exclusively gave tertiary amines, while those of secondary alcohols selectively afforded secondary amines. For instance, stoichiometric amounts of benzyl alcohol and urea (6:1 molar ratio) reacted to afford tribenzylamine in 92% yield after 10 h at 140 °C using Au/TiO<sub>2</sub> as the heterogeneous catalyst. The catalytic efficiency of Au/TiO<sub>2</sub> was significantly higher than gold supported on other materials. Au/Fe<sub>2</sub>O<sub>3</sub>, Au/CeO<sub>2</sub>, Au/ZnO, and Au/C resulted in low yields, whereas Au/Al<sub>2</sub>O<sub>3</sub> resulted in moderate yield. Control experiments showed that the inherent nature of the support material was critical in mediating the in situ formation of NH<sub>3</sub> involved in the amination reaction. Other noble metals (Pt, Pd, Ag, and Ru) supported on TiO<sub>2</sub> resulted in very limited conversion and selectivity towards the desired amine.

As several of the intermediates could be detected during the reaction, the time-conversion plot provided much information about the reaction pathway. Based on these results, the authors proposed that the reaction proceeds through three (or two) consecutive N-alkylation steps, see Scheme 19.

In the first step, the dehydrogenation of the alcohol gives the corresponding carbonyl compound that reacts with NH<sub>3</sub> and leads to the formation an imine intermediate. Hydrogen transfer followed by an additional N-alkylation step (if possible) affords the product amine.

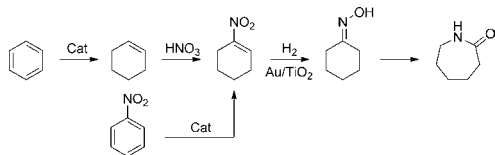


**Scheme 19.** Direct Au/TiO<sub>2</sub>-catalyzed synthesis of tribenzylamine from benzylalcohol and urea.

#### 4. Formation of Other Functional Groups

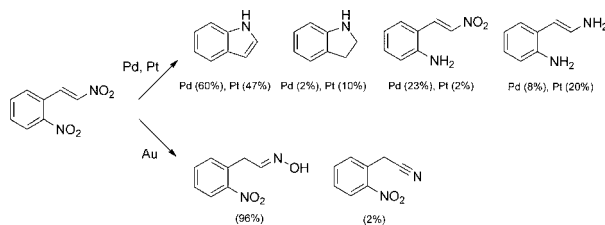
In addition to amides, imines, and amides, supported gold nanoparticles have also recently been used for the synthesis of other nitrogen-containing compounds, including oximes, *N*-oxides, quinolines, carbodiimides, carbamides, and azo compounds.

Corma et al.<sup>[61]</sup> investigated supported gold nanoparticles as catalysts for the chemoselective reduction of aryl nitro compounds with reducible substituents. Compared to Pt and Pd, Au showed high chemoselectivity for the reduction of the nitro groups without modifying the olefin, carbonyl, nitrile, or amide groups. Given the excellent chemoselectivity of gold, this system was proposed as an alternative catalytic route for the production of cyclohexanone oxime, an important molecule in the production of caprolactam (Scheme 20). Cyclohexanone oxime is currently manufactured industrially by the reaction of cyclohexanone and hydroxylamine.



**Scheme 20.** Possible reaction route for the production of caprolactam using a supported gold catalyst for the chemoselective hydrogenation of 1-nitrocyclohexene.

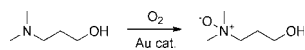
The process required the selective hydrogenation of 1-nitrocyclohexene with  $H_2$  into cyclohexanone oxime. Whereas Pt and Pd showed low selectivity even at relatively low conversion, selectivity > 90% was achieved with Au/TiO<sub>2</sub> at full conversion. In a subsequent study Corma et al.<sup>[62]</sup> investigated the hydrogenation of  $\alpha,\beta$ -unsaturated nitro compounds in further detail. Scheme 21 shows the distribution of products obtained from the hydrogenation of  $\beta,2$ -dinitrostyrene with  $H_2$  and demonstrates the unique chemoselectivity of Au compared to other noble metals such as Pt and Pd for this reaction. Combined with the Henry reaction, the selective hydrogenation of nitro compounds is an interesting alternative route to many complex molecules starting from aldehydes or ketones.



**Scheme 21.** Distribution of products for the hydrogenation of  $\beta,2$ -dinitrostyrene using Pd/C, Pt/C, and Au/TiO<sub>2</sub> catalysts.

During their investigation of the gold-catalyzed oxidation of alcohols in presence of amines, Sun et al.<sup>[40]</sup> also applied Au/HAP as catalyst for the tandem synthesis of oximes from alcohols and hydroxylamine. Aromatic, unsaturated and heterocyclic alcohols could all be converted into the corresponding oximes in high yield using only one equivalent of hydroxylamine. In the study of the *N*-formylation of amines over supported gold nanoparticles, Ishida and Haruta<sup>[35]</sup> also reported that Au/TiO<sub>2</sub> gave benzaldehyde oxime as the main product in the oxidation of benzylamine in methanol, whereas Au/Al<sub>2</sub>O<sub>3</sub> and Au/NiO gave formamide. Although titanium-silicate and TiO<sub>2</sub> has been reported to catalyze the oxidation of amines into oximes, the pure metal-oxides showed no catalytic activity under the same reaction conditions, confirming that the gold nanoparticles were responsible for the oxidation.

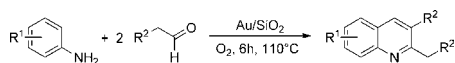
Supported gold nanoparticles and bimetallic catalysts have also been found to transform tertiary amines into *N*-oxides under mild reaction conditions.<sup>[63]</sup> Among the different combinations of metals and support materials tested, the highest catalytic activity for the synthesis of triethylamine *N*-oxide was achieved with Au-Rh supported on carbon (100% conversion). In fact, the bimetallic Au-Rh catalyst showed a clear synergistic effect compared to the low conversion of pure Au/C (46%) and pure Rh/C (26%). Furthermore, the effect of added base was investigated. Opposed to the promoting effect well-known from the liquid phase oxidation of for example, alcohols,<sup>[64]</sup> NaOH had a pronounced negative effect on the oxidation of triethylamine. The only exceptions were Au/C and Rh/C that for some reason showed increased catalytic activity. The role of base is still not understood. Pyridine was smoothly oxidized into pyridine *N*-oxide (100% yield) in presence of all the tested catalysts both with and without base. In line with the oxidation of primary aminoalcohols mentioned in Section 3 Della Pina et al.<sup>[63]</sup> also investigated the oxidation of tertiary aminoalcohols. Using 3-dimethylamino-1-propanol as model substrate, the authors found that the oxidation of the amino group was favored in the absence of base, where 100% chemoselectivity to the corresponding *N*-oxide was observed, see Scheme 22. High catalytic activity was, however, restricted to



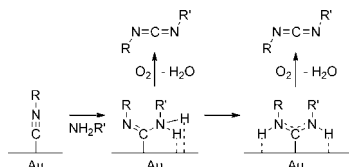
**Scheme 22.** Chemoselective oxidation of 3-dimethylamino-1-propanol to the corresponding *N*-oxide.

the gold-based catalysts; this is consistent with the observation that aliphatic amines interact strongly with traditional noble metals, which may result in catalyst deactivation.

So et al.<sup>[65]</sup> reported that gold nanoparticles supported on silica is an effective catalyst for the one-pot aerobic oxidative cyclization of anilines with aldehydes to form quinolines, see Scheme 23. The reaction was demonstrated to be general (20 different substrates with up to 95% yield) and the catalyst could be recovered by centrifugation and reused for



**Scheme 23.** Au/SiO<sub>2</sub>-catalyzed one-pot aerobic oxidative cyclization of anilines with aldehydes to quinolines.



**Scheme 24.** Proposed mechanism for the bulk gold-catalyzed oxidative amination of isocyanides.

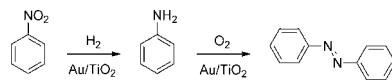
seven consecutive runs without significant loss of catalytic activity, although it was necessary to rinse the catalyst with piranha solution after each run.

Lazar and Angelici<sup>[44]</sup> reported that bulk gold catalyze the oxidative amination of isocyanides into carbodiimides. The employed catalyst was gold powder

with particle size approximately 1 μm. On the basis of infrared reflection absorption spectroscopy and kinetic studies, the authors proposed that the reaction occurs by initial η<sup>1</sup>-adsorption of the isocyanide on the Au surface, which activates the isocyanate to attack by the amine. This attack is the rate-determining step, which is very similar to the reactions of amines with coordinated isocyanides in transition metal complexes (Scheme 24). However, the metallic Au surface provides a reaction pathway that involves oxygen to give the carbodiimide products whereas homogeneous catalysts such as Au<sup>I</sup> or Au<sup>III</sup> complexes result in formamides.<sup>[66]</sup> Furthermore, Lazar et al.<sup>[45]</sup> investigated the reaction of secondary amines and isocyanides over bulk gold. The reactions were performed with a non-catalytic amount of gold (Au/substrate=500) and excess secondary amine, but afforded the desired carbamides with high selectivity under mild reaction conditions.

In 2008 Grirrane et al.<sup>[67,68]</sup> showed that gold nanoparticles supported on TiO<sub>2</sub> catalyze the aerobic oxidation of aromatic anilines to the corresponding azo compounds under mild reaction conditions. For instance, aniline reacted to give diphenyldiazene in 98% yield after 22 h at 100 °C and 5 bar O<sub>2</sub>. As Au/TiO<sub>2</sub> was able to catalyze both the aerobic oxidation of anilines and the chemoselective hydrogenation of nitro groups,<sup>[61]</sup> the authors also developed a single-pot process to produce azo compounds from nitroaromatics, (Scheme 25).

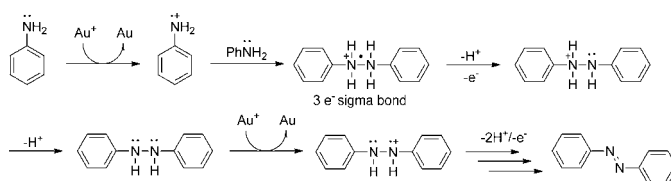
The proposed reaction mechanism involves the single-electron oxidation of aniline to the corresponding radical cation, mediated by the TiO<sub>2</sub>-sup-



**Scheme 25.** Two-step, one-pot process for the catalytic synthesis of azobenzene from nitrobenzene.

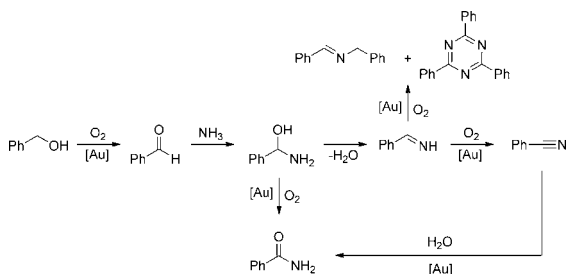
ported gold nanoparticles through undercoordinated gold sites and/or Au<sup>δ+</sup> species formed by interaction with the support. The radical cation of aniline then reacts with neutral aniline to form a three-electron sigma bond that eventually leads to the formation of hydrazine by loss of two protons and one electron. Once formed, the hydrazine is quickly oxidized to azobenzene, following a pathway that again involves alternating transfer of electrons and protons (Scheme 26).

Recently, Ishida et al.<sup>[69]</sup> reported that simple metal oxides



**Scheme 26.** Proposed reaction mechanism for the aerobic oxidation of aniline into diphenyldiazene using Au/TiO<sub>2</sub> as catalyst.

such as MnO<sub>2</sub>, Co<sub>3</sub>O<sub>4</sub>, and NiO are catalytically active for the ammoxidation of alcohols to nitriles. The deposition of gold nanoparticles on MnO<sub>2</sub> did not enhance the ammoxidation of benzyl alcohol but promoted the hydration to produce benzamide without further addition of water. On the other hand, gold supported on Al<sub>2</sub>O<sub>3</sub>, CuO, and CeO<sub>2</sub> catalyzed the ammoxidation of benzyl alcohol, whereas the pure support materials showed no catalytic activity. These results therefore show that gold is intrinsically active for ammoxidation of alcohols. The authors also showed that the main reaction route was dependent on the choice of support material. Where Au/CuO afforded benzonitrile as the major product, Au/Al<sub>2</sub>O<sub>3</sub> and Au/CeO<sub>2</sub> promoted either the dehydration of the nitrile or the oxidation of the hemiaminal to produce benzamide as the major product (Scheme 27).



**Scheme 27.** Plausible reaction pathway for the ammoxidation and amidation of benzyl alcohol over supported gold catalysts.



[65] M.-H. So, Y. Liu, C.-M. Ho, K.-Y. Lam, C.-M. Che, *ChemCatChem* **2011**, *3*, 386.

[66] J. E. Parks, A. L. Balch, *J. Organomet. Chem.* **1974**, *71*, 453.

[67] A. Grirrane, A. Corma, H. Garcia, *Science* **2008**, *322*, 1661.

[68] A. Grirrane, A. Corma, H. Garcia, *Nat. Protoc.* **2010**, *11*, 429.

[69] T. Ishida, H. Watanabe, T. Takei, A. Hamasaki, M. Tokunaga, M. Haruta, *Appl. Catal. A* **2012**, *425–426*, 85.

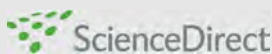
---

Received: May 14, 2012

Published online on July 16, 2012





available at [www.sciencedirect.com](http://www.sciencedirect.com)journal homepage: [www.elsevier.com/locate/chnjc](http://www.elsevier.com/locate/chnjc)

Article (Special Issue on the 2nd International Congress on Catalysis for Biorefineries (CatBior 2013))

## Highly selective formation of imines catalyzed by silver nanoparticles supported on alumina

Jerrick Mielby, Raju Poreddy, Christian Engelbrekt, Søren Kegnæs\*

DTU Chemistry, Technical University of Denmark, 2800 Kgs. Lyngby, Denmark

## ARTICLE INFO

## Article history:

Received 2 January 2014

Accepted 9 January 2014

Published 20 May 2014

## Keywords:

Heterogeneous catalysis

Silver nanoparticle

Oxidative dehydrogenation

Alcohol

Aldehyde

Imine

## ABSTRACT

The oxidative dehydrogenation of alcohols to aldehydes catalyzed by Ag nanoparticles supported on  $\text{Al}_2\text{O}_3$  was studied. The catalyst promoted the direct formation of imines by tandem oxidative dehydrogenation and condensation of alcohols and amines. The reactions were performed under mild conditions and afforded the imines in high yield (up to 99%) without any byproducts other than  $\text{H}_2\text{O}$ . The highest activity was obtained over 5 wt%  $\text{Ag}/\text{Al}_2\text{O}_3$  in toluene with air as oxidant. The reactions were also performed under oxidant-free conditions where the reaction was driven to the product side by the production of  $\text{H}_2$  in the gas phase. The use of an efficient and selective Ag catalyst for the oxidative dehydrogenation of alcohol in the presence of amines gives a new green reaction protocol for imine synthesis.

© 2014, Dalian Institute of Chemical Physics, Chinese Academy of Sciences.

Published by Elsevier B.V. All rights reserved.

## 1. Introduction

In recent years there has been rising demand for efficient solid catalyzed processes for the oxidation of alcohols for the production of fine and bulk chemicals [1]. Much effort has been devoted to the development of aerobic oxidation methods using molecular oxygen or air as the oxidant. Compared to the use of high valence inorganic metal oxides, such as chromate or permanganate, these methods are very attractive because oxygen is a cheap and abundant oxidant that produces water as the only byproduct [2].

Another attractive alternative is the oxidant-free dehydrogenation of alcohols to carbonyl compounds and molecular hydrogen [3]. Although tremendous advances have been achieved in the dehydrogenation of alcohols with homogeneous platinum-group metals [4–7], only a limited number of similar solid catalysts that are effective under mild reaction

conditions, have appeared to date. Recently, Kaneda et al. [8] used Ag supported on hydrotalcite (Ag/HT) for the dehydrogenation of alcohols under oxidant-free conditions. The reaction afforded high yields of the corresponding carbonyl compounds at 130 °C with the co-production of  $\text{H}_2$ . Shimizu et al. [9] reported that  $\text{Ag}/\text{Al}_2\text{O}_3$  showed higher catalytic activity than the conventional catalysts based on platinum group metals (such as  $\text{Rh}/\text{Al}_2\text{O}_3$  and  $\text{Pd}/\text{Al}_2\text{O}_3$ ), and suggested that the high activity was due to the presence of sub-nanometer sized Ag particles and the acidic and basic surface sites on  $\gamma\text{-Al}_2\text{O}_3$ . Furthermore, Shimizu et al. [10,11] showed that  $\text{Ag}/\text{Al}_2\text{O}_3$  could be used for amide synthesis and also for the direct synthesis of secondary amines via intermediate imine formation by the borrowing hydrogen mechanism when it is used together with a strong Lewis acid co-catalyst. Liu et al. [12] showed that with Ag nanoparticles, secondary amines could be formed from alcohols and amines via intermediate imine formation by

\* Corresponding author. Tel: +45-45252402; Fax: +45-45883136; E-mail: [skk@kemi.dtu.dk](mailto:skk@kemi.dtu.dk)

This work was supported by the Danish Council for Independent Research (10-093717, 12-127580).

DOI: 10.1016/S1872-2067(14)60033-4 | <http://www.sciencedirect.com/science/journal/18722067> | Chin. J. Catal., Vol. 35, No. 5, May 2014

the borrowing hydrogen mechanism. Similar reactions have also been shown possible with metals other than Ag [13,14]. Although reports on Ag catalyzed reactions is increasing, the application of supported Ag catalysts is still limited in liquid phase organic chemistry. Furthermore, the addition of additives such as a base is usually required to give high yields.

In this work, we showed that Ag supported on  $\text{Al}_2\text{O}_3$  was an active and highly selective catalyst for the formation of aldehydes from alcohols without the use of additives. Furthermore, we showed that Ag/ $\text{Al}_2\text{O}_3$  catalyzed the direct formation of imines by consecutive oxidative dehydrogenation and condensation of alcohols and amines as shown in Scheme 1.

The reactions were performed under mild reaction conditions with a number of different alcohols and amines, which demonstrated that the method was versatile and applicable to a broad range of substrates. Although the highest catalytic activity was obtained with 5 wt% Ag/ $\text{Al}_2\text{O}_3$  in toluene using air as oxidant, the reaction also occurred under oxidant-free conditions where the reaction was driven to the product side by the production of  $\text{H}_2$  in the gas phase [9].

## 2. Experimental

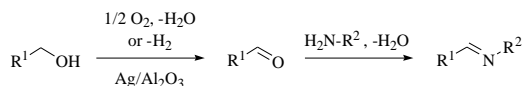
### 2.1. Catalyst preparation

A series of supported Ag catalysts were prepared by incipient wetness impregnation of the solid supports with an aqueous solution of  $\text{AgNO}_3$  to give 1, 5, and 10 wt% Ag on the support. Before each reaction, the impregnated and dried catalysts were reduced with 10%  $\text{H}_2/\text{N}_2$  in a tube oven for 2 h at 300 °C and a heating ramp of 5 °C/min.

The support materials investigated were various combinations of magnesium and aluminum oxides, including metal oxides ( $\text{Al}_2\text{O}_3$  and  $\text{MgAl}_2\text{O}_4$ ) and layered double hydroxides ( $\text{Mg}_6\text{Al}_2(\text{CO}_3)(\text{OH})_{16}$ , hydrotalcite, HT). All supports were purchased from commercial sources (Saint-Gobain and Sigma Aldrich) and used without further purification or pretreatment. For comparison, 5 wt% Au/ $\text{Al}_2\text{O}_3$  catalyst was prepared by the standard impregnation procedure. In addition, a HT-like catalyst was prepared by the co-precipitation of  $\text{AgNO}_3$ ,  $\text{Mg}(\text{NO}_3)_2$ , and  $\text{Al}(\text{NO}_3)_3$  in an aqueous alkaline solution of  $\text{Na}_2\text{CO}_3$  and NaOH using a modified literature procedure [15]. The amounts of metal nitrates used were calculated to give a final composition of 5 wt% Ag. The metal nitrates were dissolved in water and added dropwise to the alkaline solution under vigorous stirring. After ageing for 24 h, the catalyst was collected by filtration, washed in water, and dried at 90 °C overnight. Finally, the catalyst was reduced using the standard procedure.

### 2.2. Characterization

$\text{N}_2$  physisorption was performed on a Micromeritics ASAP 2020 surface area and porosimetry analyzer. The samples were outgassed in vacuum at 200 °C prior to measurement. The specific surface area ( $S_{\text{BET}}$ ) was calculated by the BET method. X-ray diffraction (XRD) analysis was carried out on a Huber G670 diffractometer operated in transmission mode with Cu



**Scheme 1.** Formation of imines by consecutive oxidative dehydrogenation and condensation of alcohols and amines using Ag/ $\text{Al}_2\text{O}_3$  as catalyst.

$\text{K}\alpha_1$  irradiation from a focusing quartz monochromator. The sample was fixed on a piece of tape. Transmission electron microscopy (TEM) was performed on a FEI Tecnai T20 G2 microscope operated at 200 kV. All specimens were dispersed in ethanol and left to dry on the TEM grids at room temperature before the analysis. The diameter of the nanoparticles was estimated from the measurements of about 100 particles.

### 2.3. Standard oxidation procedure

In a typical experiment, alcohol (2.0 mmol), amine (2.0 mmol), anisole (internal standard, 0.2 mmol), and toluene (6.0 ml) was charged into a reaction tube and connected to the reaction station (Radley Carousel 12 Plus). The reaction station provided stirring, heating and an atmosphere of Ar,  $\text{O}_2$  or atmospheric air at ambient pressure. The reaction tube was flushed with gas, heated to the desired temperature and then 100 mg catalyst was added. Unless otherwise noted, the reactions were performed at 100 °C for 24 h.

During the reaction, samples of 0.1 ml were periodically collected, filtered and analyzed by GC-FID and GC-MS using a HP-5 column from Agilent Technologies Inc. The amounts of substrates and products were quantified using anisole as an internal standard. The conversions were calculated from the conversion of alcohol. The reported values were consistent with the corresponding values calculated from the conversion of amine within  $\pm 5\%$ . The selectivity and yield were determined from the area of the product peak relative to the total area of all product peaks.

## 3. Results and discussion

### 3.1. Characterization

Table 1 shows the overview of the prepared catalysts. As expected,  $S_{\text{BET}}$  of all the catalysts were similar to those of the parent support, that is, the Ag loading only has a relatively small effect on the surface area.

The catalysts were also characterized by XRD. The results were as expected, but the co-precipitated HT-like catalyst displayed poor crystallinity. The diffraction peaks assigned to Ag on both the co-precipitated and impregnated catalysts were distinct. Figures 1–4 show TEM images and the size distribution of the nanoparticles of the 5 wt% Ag catalysts together with the XRD patterns.

The TEM results showed that the nanoparticle size distribution was relatively broad. As expected, the average size of the nanoparticles increased with the Ag loading. In general, the nanoparticles were evenly dispersed over the support and

**Table 1**  
Overview of the catalysts.

Entry	Catalyst	Ag(Au) loading (wt%)	S <sub>BET</sub> (m <sup>2</sup> /g)	Diameter (nm)
1	MgAl <sub>2</sub> O <sub>4</sub>	—	74	—
2	Ag/MgAl <sub>2</sub> O <sub>4</sub>	5	76	20–70
3	HT	—	135	—
4	Ag/HT	5	142	10–60
5	Ag/HT*	5	135	10–70
6	Al <sub>2</sub> O <sub>3</sub>	—	219	—
7	Ag/Al <sub>2</sub> O <sub>3</sub>	1	241	10–30
8	Ag/Al <sub>2</sub> O <sub>3</sub>	5	223	20–50
9	Ag/Al <sub>2</sub> O <sub>3</sub>	10	227	20–70
10	Au/Al <sub>2</sub> O <sub>3</sub>	5	217	10–50

\*Prepared by co-precipitation.

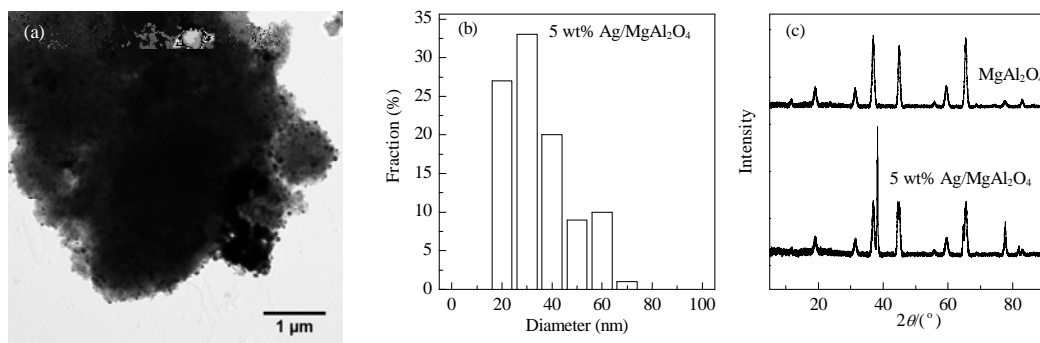
were < 30, < 50, and < 70 nm for the 1, 5, and 10 wt% Ag/Al<sub>2</sub>O<sub>3</sub> catalyst, respectively.

### 3.2. Catalytic activity

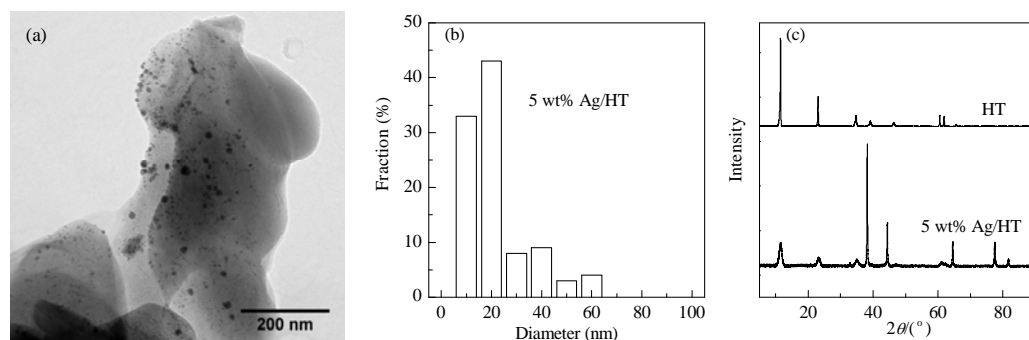
First, the dehydrogenation of benzyl alcohol to benzaldehyde was used as a model reaction to study the effect of the support material and Ag loading. Table 2 shows the conversion, selectivity, and yield from the oxidative dehydrogenation of benzyl alcohol under Ar (i.e. under oxidant-free conditions) at 100 °C for 24 h. Table 2 showed that the pure support materials were inactive for the reaction and that no reaction occurred

without a catalyst (Entry 11). In contrast, the Ag impregnated catalysts afforded benzaldehyde in moderate to good yields. The activity of 5 wt% Ag/MgAl<sub>2</sub>O<sub>4</sub> and the activity of 5 wt% Ag/HT were similar and they gave 17%–18% conversion with 70%–72% selectivity. However, the 5 wt% Ag/Al<sub>2</sub>O<sub>3</sub> surprisingly gave 60% conversion and 96% selectivity under the same reaction conditions. The co-precipitated Ag/HT\* catalyst did not give any conversion, while the 5 wt% Au/Al<sub>2</sub>O<sub>3</sub> only gave 8% yield. The main byproduct was benzyl benzoate.

Entries 7–9 in Table 2 shows the effect of the Ag loading. The conversion increased with the Ag loading up to 5 wt% and then decreased with further loading. Since the same amount of catalyst was used in the reactions the increase in conversion from 1 to 5 wt% was expected. However, when the Ag loading was increased to 10 wt% the conversion and selectivity decreased significantly. This may be explained by the increased size of the nanoparticles. It is noteworthy that both the conversion and the selectivity depended on the Ag loading and the nature of the support material. Recently Shimizu et al. [9] proposed a mechanism where the dehydrogenation of alcohol is favored by the special acid-base sites on Al<sub>2</sub>O<sub>3</sub>. In this mechanism, the reaction proceeds in three steps: (1) the reaction of the alcohol on a basic site to give an alkoxide and an adsorbed water molecule, (2) C-H activation of the alkoxide on the Ag nanoparticle to give a silver hydride species and a carbonyl compound, and (3) H<sub>2</sub> desorption from an alumina acid site.



**Fig. 1.** TEM image (a), size distribution (b), and XRD patterns (c) of the nanoparticles on 5 wt% Ag/MgAl<sub>2</sub>O<sub>4</sub>.



**Fig. 2.** TEM image (a), size distribution (b), and XRD patterns (c) of the nanoparticles on 5 wt% Ag/HT.

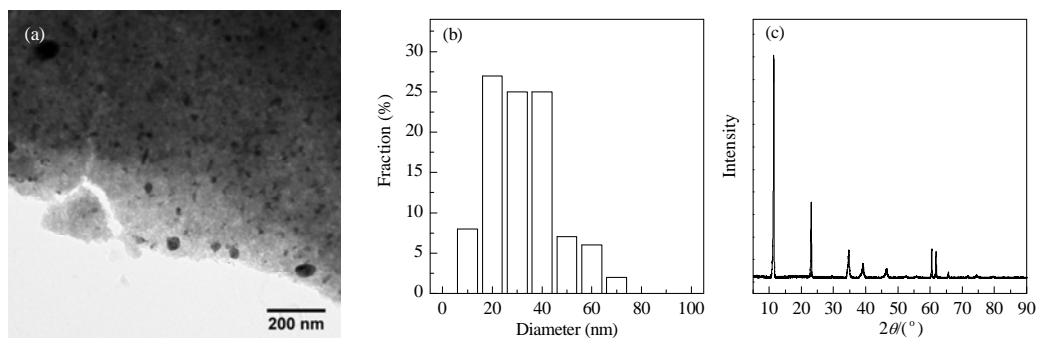


Fig. 3. TEM image (a), size distribution (b), and XRD pattern (c) of the co-precipitated nanoparticles on 5 wt% Ag/HT\*.

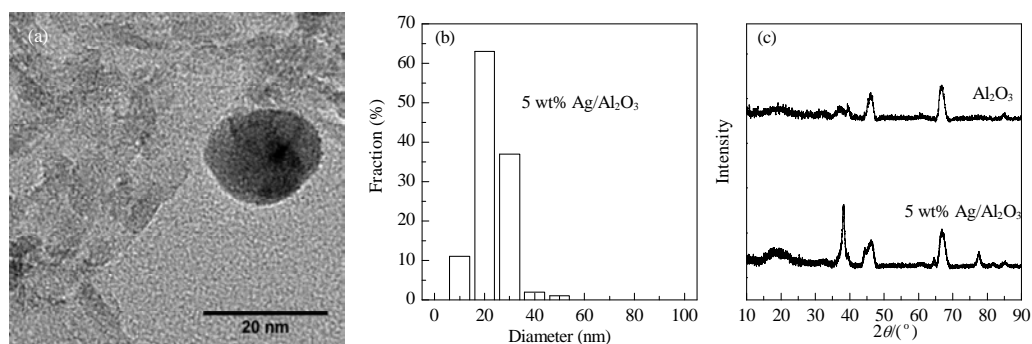


Fig. 4. TEM image (a), size distribution (b), and XRD patterns (c) of the nanoparticles on 5 wt% Ag/Al<sub>2</sub>O<sub>3</sub>.

The proposed mechanism may explain the higher activity of Ag on Al<sub>2</sub>O<sub>3</sub> with respect to other supports.

Based on the reasoning that the oxidative dehydrogenation is dependent on the abstraction of hydrogen by the Ag atoms and that a fast removal of this hydrogen is important for a high reaction rate, the reactions were also tested using atmospheric air and pure molecular oxygen. Under these reaction conditions, water was formed as the byproduct rather than molecular hydrogen.

Figure 5 show the yield of benzaldehyde as a function of reaction time over 5 wt% Ag/Al<sub>2</sub>O<sub>3</sub>. While the initial reaction rate

was the same, after 24 h, the reaction performed under air resulted in almost 50% higher yield than that under the inert Ar atmosphere and also higher than that under pure O<sub>2</sub>. These result suggested that only a small amount of oxygen was needed to efficiently remove the hydrogen from the Ag atoms to increase the catalytic activity. On the other hand, too high partial pressure of O<sub>2</sub> may decrease the catalytic activity, possibly by the oxidation of the active Ag atoms into inactive Ag<sub>2</sub>O [16]. The formation of Ag<sub>2</sub>O has been previously studied using a variety of different techniques [16,17].

Table 2

Effect of support material and Ag loading.

Entry	Catalyst	Conversion (%)	Selectivity (%)	Yield (%)
1	MgAl <sub>2</sub> O <sub>4</sub>	1	30	<1
2	5% Ag/MgAl <sub>2</sub> O <sub>4</sub>	17	70	12
3	HT	0	0	0
4	5% Ag/HT	18	72	13
5	5% Ag/HT*	0	0	0
6	Al <sub>2</sub> O <sub>3</sub>	5	20	1
7	1% Ag/Al <sub>2</sub> O <sub>3</sub>	28	3	1
8	5% Ag/Al <sub>2</sub> O <sub>3</sub>	60	96	57
9	10% Ag/Al <sub>2</sub> O <sub>3</sub>	15	60	9
10	5% Au/Al <sub>2</sub> O <sub>3</sub>	10	82	8
11	—	0	0	0

Reaction conditions: benzyl alcohol 2 mmol, anisole 0.2 mmol, toluene 6 ml, catalyst 100 mg, 24 h, 100 °C, under Ar.

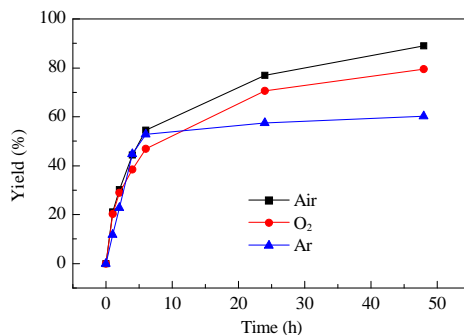


Fig. 5. Yield of benzaldehyde as a function of reaction time using 5 wt% Ag/Al<sub>2</sub>O<sub>3</sub> at 100 °C under atmospheric air, O<sub>2</sub>, and Ar.

**Table 3**

Effect of reaction temperature on the oxidation of benzyl alcohol to benzaldehyde.

Entry	Temperature (°C)	Conversion (%)	Selectivity (%)	Yield (%)
1	60	19	75	14
2	80	45	70	32
3	100	95	97	92


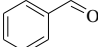
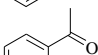
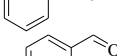
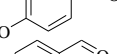
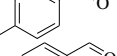
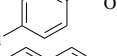
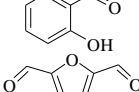
Reaction conditions: benzyl alcohol 2 mmol, anisole 0.2 mmol, toluene 6 ml, 5 wt% Ag/Al<sub>2</sub>O<sub>3</sub> 100 mg, 24 h, atmospheric air.

In order to investigate the effect of the temperature, the 5 wt% Ag/Al<sub>2</sub>O<sub>3</sub> catalyst was tested under atmospheric air for 24 h at different temperatures. As expected, the conversion decreased significantly as the temperature was decreased from 100 to 60 °C (Table 3). Furthermore, the formation of benzylbenzoate was suppressed at higher temperatures, which resulted in 95 % conversion with 97% selectivity at 100 °C.

A number of different alcohols were oxidized under the optimized reaction conditions in order to investigate the range of substrates that can be used (Table 4). All reactions were carried out over 5 wt% Ag/Al<sub>2</sub>O<sub>3</sub> for 24 h under atmospheric air at 100 °C. All the alcohols were converted into the corresponding carbonyl compounds. However, while the oxidation of benzyl alcohol reached almost full conversion in 24 h, the aliphatic 1-hexanol only reached 27% conversion (Table 4, Entry 1). This result suggested that the conversion of aliphatic alcohols required longer reaction time or higher temperatures than benzylic alcohols. The secondary alcohol 1-phenylethanol reached full conversion within 24 h and afforded the corresponding ketone acetophenone in 94% yield (Table 4, Entry 3). Entries 4–6 show the effect of different substituents at the *para* position of the benzyl alcohol. The decrease in conversion on going from *p*-OCH<sub>3</sub> to *p*-CH<sub>3</sub> to *p*-Cl suggested a linear free en-

**Table 4**

Oxidation of different alcohols over 5 wt% Ag/Al<sub>2</sub>O<sub>3</sub> under atmospheric air.

Entry	Product	Conversion (%)	Selectivity (%)	Yield (%)
1		27	74	20
2		95	97	92
3		100	99	99
4		100	98	98
5		96	98	94
6		46	97	45
7		100	99	99
8		23	73	17

Reaction conditions: alcohol 2 mmol, anisole 0.2 mmol, toluene 6 ml, 5 wt% Ag/Al<sub>2</sub>O<sub>3</sub> 100 mg, 24 h, 100 °C, atmospheric air.

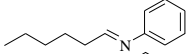
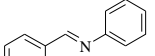

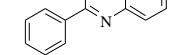
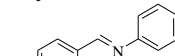
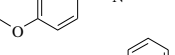
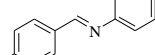
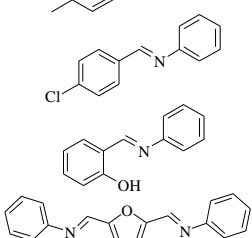
ergy relationship where substrates with electron donating substituents (*p*-OCH<sub>3</sub> and *p*-CH<sub>3</sub>) are more reactive than substrates with electron withdrawing substituents (*p*-Cl). These results indicated a positive charge build-up in the benzylic position during the rate determining step, which was in good agreement with the hydride abstraction step proposed by Shimizu et al. [9]. Furthermore, furan-2,5-dicarbaldehyde was obtained in 17% yield from the oxidation of 5-hydroxymethylfurfural (Table 4, Entry 8).

The optimized reaction conditions were used to study the direct formation of imines by the tandem oxidative dehydrogenation and condensation of alcohols and amines. The results of adding one equivalent of aniline to the reaction solution is shown in Table 5. All reactions were performed under the same reaction conditions and no further optimization was attempted for the individual substrates.

The results in Table 5 show that all the substrates reacted to give the corresponding imines with the exception of 1-hexanol and aniline, which did not react. Although the conversion of benzyl alcohol was decreased from 95% to 82% by the addition of amine, the selectivity to the desired product increased as less benzyl benzoate was formed. The formation of benzyl benzoate was due to the condensation of benzyl alcohol with benzoic acid (formed by over-oxidation or aldehyde disproportionation) or by the oxidation of a hemiacetal (formed by the reac-

**Table 5**

Oxidation of different alcohols in the presence of aniline over 5 wt% Ag/Al<sub>2</sub>O<sub>3</sub> under atmospheric air.

Entry	Product	Conversion (%)	Selectivity (%)	Yield (%)
1		0	—	—
2		82	98	81
3		71	95	68
4		95	98	94
5		100	99	99
6		65	98	64
7		100	68	68
8		20	80	16

Reaction conditions: alcohol 2 mmol, aniline 2 mmol, anisole 0.2 mmol, toluene 6 ml, 5 wt% Ag/Al<sub>2</sub>O<sub>3</sub> 100 mg, 24 h, 100 °C, atmospheric air.

tion of benzyl alcohol and benzaldehyde). In either case, the amine increased the selectivity by removing the benzaldehyde intermediate in a fast condensation step. For this reason, it is expected that even higher selectivity would be achieved by increasing the ratio of amine to alcohol. As expected, a similar trend in yield was observed for the three *para*-substituted alcohols, which indicated that the oxidation of the alcohol is the rate determining step of the overall reaction. 2-((phenylimino)-methyl)phenol was obtained in 68% yield due to the low selectivity, while the diphenylimine of HMF was obtained in 16% yield due to the low conversion.

The effect of different amines was also studied. Table 6 shows the conversion, selectivity, and yield from the reaction of benzyl alcohol with different amines, including benzyl amine, cyclohexylmethanamine, hexan-1-amine, and pentan-3-amine. All amine substrates reacted with benzyl alcohols to afford the desired products with high selectivity (> 94%). While the reaction with benzyl amine and cyclohexylmethanamine only gave 10% and 17% conversion, respectively, and pentan-3-amine gave 32% conversion. The highest conversion of 82% was obtained with aniline, followed by hexan-1-amine with 66% conversion.

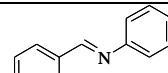
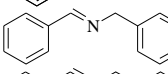
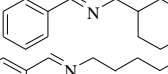
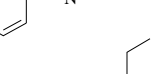
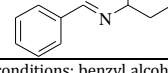
Compared to the previously reported results with Au-catalyzed imine synthesis [18–21], the supported Ag catalysts used here were different in several aspects. First, the Ag catalysts required higher temperatures than the Au catalysts that were active even at room temperature. Furthermore, the Au catalysts were not deactivated by high partial pressures of oxygen. On the other hand, Au catalysts required a strongly alkaline solution. In some systems this would be detrimental as various base-catalyzed side reactions can decrease the selectivity [2]. It is noteworthy that the supported Ag catalysts need no additives or co-catalysts and were even active under oxidant-free conditions with only one equivalent of amine.

#### 4. Conclusions

The Ag nanoparticles supported on Al<sub>2</sub>O<sub>3</sub> (Ag/Al<sub>2</sub>O<sub>3</sub>) is an efficient catalyst for the oxidative dehydrogenation of alcohols to aldehydes without any additives. This catalytic system can

**Table 6**

Oxidation of benzyl alcohol in the presence of different amines over 5 wt% Ag/Al<sub>2</sub>O<sub>3</sub> under atmospheric air.

Entry	Product	Conversion (%)	Selectivity (%)	Yield (%)
1		82	99	81
2		10	99	10
3		17	94	16
4		66	99	66
5		32	97	31

Reaction conditions: benzyl alcohol 2 mmol, amine 2 mmol, anisole 0.2 mmol, toluene 6 ml, 5 wt% Ag/Al<sub>2</sub>O<sub>3</sub> 100 mg, 24 h, 100 °C, atmospheric air.

also be used for the oxidative coupling of alcohols and amines to form the corresponding imines. The highest catalytic activity was obtained with 5 wt% Ag/Al<sub>2</sub>O<sub>3</sub> in toluene using atmospheric air as oxidant. Performing the reaction with pure oxygen resulted in decreased conversion, which suggested that active Ag atoms were oxidized to Ag<sub>2</sub>O. The reaction can also be performed under oxidant-free conditions, where the reaction was driven to the product side by the production of H<sub>2</sub> in the gas phase. The reactions were performed at relatively mild conditions (100 °C and atmospheric pressure) without any additives or co-catalysts and afforded the desired imines with high selectivity (up to 99%) from equivalent amounts of alcohols and amines. The reaction was performed with a number of different alcohols and amines to demonstrate the range and versatility of the reaction. The use of an efficient and selective Ag catalyst for the oxidative dehydrogenation of alcohols in the presence of amines is a new green reaction protocol for imine synthesis.

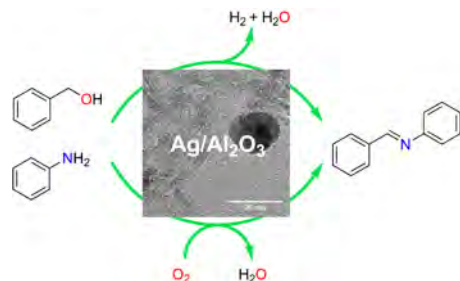
#### Graphical Abstract

*Chin. J. Catal.*, 2014, 35: 670–676 doi: 10.1016/S1872-2067(14)60033-4

#### Highly selective formation of imines catalyzed by silver nanoparticles supported on alumina

Jerrick Mielby, Raju Poreddy, Christian Engelbrekt, Søren Kegsnæs\*  
Technical University of Denmark, Denmark

A green method to synthesis imines by aerobic oxidative coupling of amines and alcohols under mild reaction conditions with Ag/Al<sub>2</sub>O<sub>3</sub> as catalyst was shown.



## References

- [1] Franz G, Sheldon R A. 'Oxidation', Ullmann's Encyclopedia of Industrial Chemistry. 6th Ed. Weinheim: Wiley-VCH, 2000
- [2] Mallat T, Baiker A. *Chem Rev*, 2004, 104: 3037
- [3] Friedrich A, Schneider S. *ChemCatChem*, 2009, 1: 72
- [4] Maggi A and Madsen R. *Organometallics*, 2012, 31: 451
- [5] Rigoli J W, Moyer S A, Pearce S D, Schomaker J M. *Org Biomol Chem*, 2012, 10: 1746
- [6] Esteruelas M A, Honczek N, Oliván M, Oñate E, Valencia M. *Organometallics*, 2011, 30: 2468
- [7] Boopathy G, Jing Z, David M. *Angew Chem Int Ed*, 2010, 49: 1468
- [8] Mitsudome T, Mikami Y, Funai H, Mizugaki T, Jitsukawa K, Kaneda K. *Angew Chem Int Ed*, 2008, 47: 138
- [9] Shimizu K-i, Sugino K, Sawabe K, Satsuma A. *Chem Eur J*, 2009, 15: 2341
- [10] Shimizu K-i, Ohshima K, Satsuma A. *Chem Eur J*, 2009, 15: 9977
- [11] Shimizu K-i, Nishimura M, Satsuma A. *ChemCatChem*, 2009, 1: 497
- [12] Liu H H, Chuah G-K, Jaenicke S. *J Catal*, 2012, 292: 130
- [13] Patil R D, Adimurthy S. *Asian J Org Chem*, 2013, 2: 726
- [14] Mielby J, Kegnaes S, Fristrup P. *ChemCatChem*, 2012, 4: 1037
- [15] Kirm I, Medina F, Rodríguez X, Cesteros Y, Salagre P, Sueiras J. *Appl Catal A*, 2004, 272: 175
- [16] Li W X, Stampfl C, Scheffler M. *Phys Rev Lett*, 2003, 90: 256102
- [17] Yamamoto R, Sawayama Y, Shibahara H, Ichihashi Y, Nishiyama S, Tsuruya S. *J Catal*, 2005, 234: 308
- [18] Kegnaes S, Mielby J, Mentzel U V, Christensen C H, Riisager A. *Green Chem*, 2010, 12: 1437
- [19] Soulé J-F, Miyamura H, Kobayashi S. *Chem Commun*, 2013, 49: 355
- [20] Grirrane A, Corma A, Garcia H. *J Catal*, 2009, 264: 138
- [21] Sun H, Su F Z, Ni J, Cao Y, He H Y, Fan K N. *Angew Chem Int Ed*, 2009, 48: 4390





# Formation of pyridine *N*-oxides using mesoporous titanium silicalite-1

Jerrick Mielby · Jacob Oskar Abildstrøm ·  
Susana Pérez-Ferreras · Søren Birk Rasmussen ·  
Søren Kegnæs

© Springer Science+Business Media New York 2014

**Abstract** Mesoporous titanium silicalite-1 (TS-1) prepared by carbon-templating is significantly more active than conventional TS-1 for the oxidation of pyridine derivatives using aqueous hydrogen peroxide as oxidant. The catalytic activity is increased by the system of mesopores that helps to overcome the configurational diffusion limitations within the microporous catalyst. The use of a carbon-template for generation of secondary porosity is more effective than desilication. The desilicated catalyst is slightly more active than conventional TS-1, probably due to a decrease of the mean diffusion path length. In contrast, carbon-templated mesopores provides an efficient transport throughout the zeolite, thus preventing deactivation due to product confinement. All catalysts were characterised by X-ray powder diffraction, scanning electron microscopy, UV–Vis spectroscopy and nitrogen physisorption. The results indicate that desilication may cause a surface densification of less catalytically active extra-framework Ti species. Carbon-templating is thus a more gentle and effective method for generating secondary porosity. Utilization of carbon-templated mesoporous TS-1 for oxidation of pyridine derivatives represents a new and environmentally friendly method to synthesise *N*-oxides.

**Keywords** Mesoporous TS-1 · *N*-oxides · Catalytic oxidation · Carbon templating · Desilication

J. Mielby · J. O. Abildstrøm · S. B. Rasmussen · S. Kegnæs (✉)  
Department of Chemistry, Technical University of Denmark,  
Kemitorvet 207, 2800 Kgs.Lyngby, Denmark  
e-mail: skk@kemi.dtu.dk

S. Pérez-Ferreras · S. B. Rasmussen  
Instituto de Catálisis y Petroleoquímica (ICP), Consejo Superior  
de Investigaciones Científicas (CSIC), Calle Marie Curie 2,  
Cantoblanco, 28049 Madrid, Spain

## 1 Introduction

Titanium silicalite-1 (TS-1) is possibly one of the most remarkable innovations in heterogeneous catalysis during the last 30 years. Since its discovery, a number of catalytic reactions have been commercialized, including phenol hydroxylation, [1] cyclohexanone ammoxidation [2] and propylene epoxidation [3].

TS-1 is a microporous zeolite with MFI structure where a small fraction of the tetrahedrally coordinated Si atoms is substituted by Ti. The high coordination ability of the isolated Ti sites and the strong hydrophobicity of the silicate structure make TS-1 an outstanding heterogeneous catalyst for oxidation of simple organic compounds with aqueous hydrogen peroxides. Unfortunately, the zeolite catalyst suffers from severe diffusion limitations, which is enhanced for larger and more bulky molecules. Since the reactants and products have to pass each other in pores with molecular dimensions (for MFI  $5.1 \times 5.6$  Å in diameter), the diffusion in zeolites is often orders of magnitude slower than both molecular and Knudsen diffusion. Several preparative strategies have been developed in the attempt to overcome these configurational diffusion limitations. In particular, much effort has been devoted to increase the diameter of the zeolite pores. Titanium containing zeolites with increased pore diameters was first reported by Bellussi et al. [4] with MEL ( $5.3 \times 5.4$  Å) and Serrano et al. [5] with MRE ( $5.3 \times 5.6$  Å). Later, zeolites structures with even larger pores have been reported, including BEA ( $5.6 \times 5.6$  Å) and MTW ( $5.6 \times 6.0$  Å) [6–8]. Unfortunately, the special chemical properties generally seem to disappear as the pore dimension increases. Consequently, a compromise that relieves the diffusion restraints, while maintaining the high activity and shape selectivity of TS-1, is often more desirable [9]. A different approach to overcome the diffusion limitations is to decrease the mean diffusion path

length. This is typically done by decreasing the size of the zeolite crystals (confined space synthesis) [10] or creating an additional porosity called secondary porosity. The secondary porosity can be generated by dealumination, desilication or detitanation of preformed zeolites [11–13]. Another route is to use structural templates, such as organosilanes, [14–16] carbon followed by calcination, [17, 18] or by indirect templating methods such as partial recrystallization [19] or controlled deposition [20].

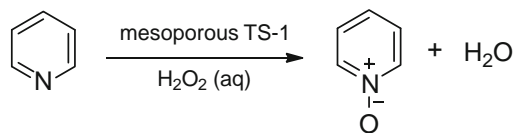
Here, we demonstrate that mesoporous TS-1 is significantly more active than conventional TS-1 for the oxidation of pyridine derivatives with aqueous hydrogen peroxide. The mesoporous TS-1 is prepared by carbon-templating following the method developed by Jacobsen et al. [21] In this process, a carbon source (e.g. carbon black pearls) is impregnated with the zeolite precursor before the material is subjected to a hydrothermal treatment to grow the zeolites crystal around the carbon-temple. During the subsequent calcination, the carbon-temple is removed by combustion to leave the mesoporous catalyst. Furthermore, we investigated the effect of desilicating both the conventional and mesoporous catalysts in strong base.

*N*-oxides are important chemical intermediates, which are used in the production of bulk commodities, high-valuable fine chemicals, agrochemicals and pharmaceuticals. Initially, the oxidation of pyridine to pyridine *N*-oxide was used as model reaction, but the successful oxidation of larger pyridine derivatives was also demonstrated. Based on the mild reaction conditions and high product selectivity we believe that the utilization of mesoporous TS-1 represents an attractive and environmentally friendly alternative to the current synthesis of *N*-oxides (Scheme 1).

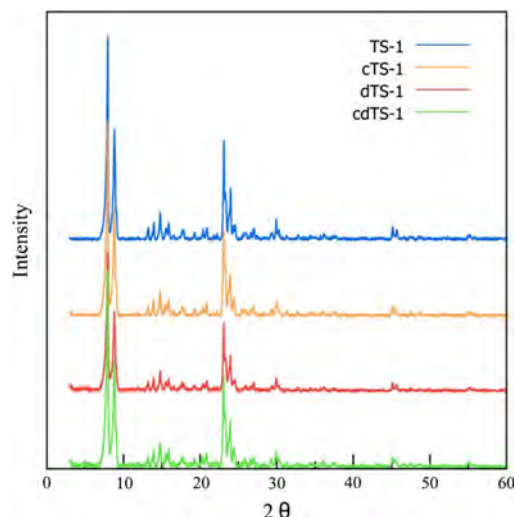
## 2 Results and discussion

### 2.1 X-ray powder diffraction

Figure 1 shows the X-ray powder diffraction (XRPD) patterns for the conventional (TS-1), carbon-templated (cTS-1), desilicated (dTTS-1) and the sample prepared by both carbon-templating and desilication (cdTS-1) containing around 1 wt% titanium (Si/Ti = 130). The diffraction



**Scheme 1** Oxidation of pyridine to the corresponding pyridine *N*-oxides using aqueous  $\text{H}_2\text{O}_2$  as oxidant and mesoporous TS-1 as catalyst



**Fig. 1** XRPD patterns of conventional (TS-1), carbon-templated (cTS-1), desilicated (dTTS-1) and both carbon-templated and desilicated catalysts (cdTS-1)

patterns were obtained after calcination to remove the structure directing agent and carbon-temple and show that all samples are highly crystalline and possess MFI structure.

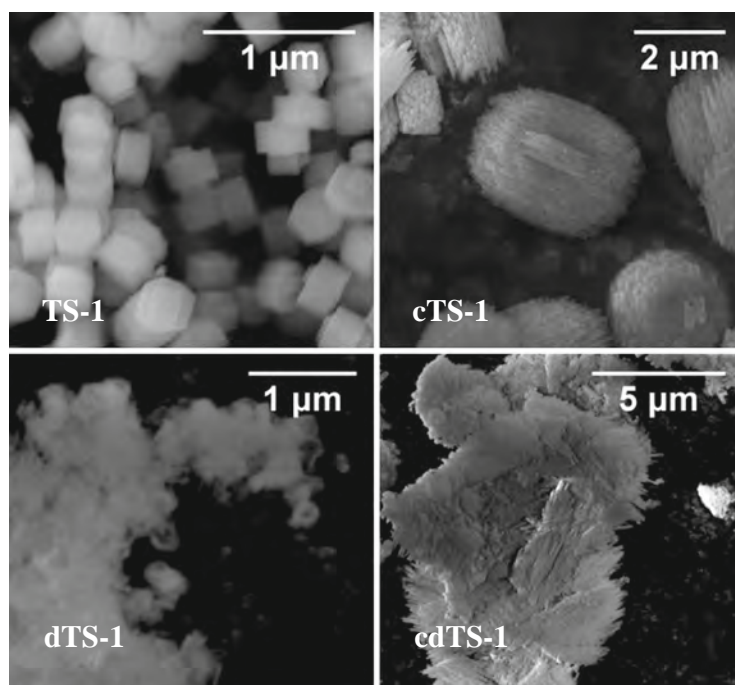
### 2.2 Scanning electron microscopy

Figure 2 shows scanning electron microscopy (SEM) images of conventional and mesoporous TS-1 before and after desilication. The images show that both the TS-1 and cTS-1 crystals are coffin shaped, although the carbon-templated cTS-1 crystals are generally larger and more irregular than the conventional TS-1 crystals. The length of the conventional TS-1 crystals ranges from 0.30 to 0.40  $\mu\text{m}$ , while the length of the mesoporous crystals ranges from 1.1 to 2.3  $\mu\text{m}$ . The most evident difference between TS-1 and cTS-1 is the non-crystallographic intracrystalline mesopores that perforates the surface of mesoporous catalyst. The rough surface features indicate that the catalyst possess high porosity. The SEM images of the conventional and mesoporous catalysts after desilication (dTTS-1 and cdTS-1, respectively) reveals that most of the regular zeolite features disappear with the strong base treatment.

### 2.3 Nitrogen physisorption

The textural properties of the synthesized materials were determined by nitrogen adsorption–desorption analysis. The observed Brunauer–Emmett–Teller surface area ( $S_{\text{BET}}$ ), external surface areas ( $S_{\text{ext}}$ ), micropore volume

**Fig. 2** SEM images of the prepared catalysts. Please note the different scale bars



**Table 1** Nitrogen sorption data for the investigated catalysts

Catalyst	Carbon-templated (c)	Desilicated (d)	$S_{\text{BET}}^{\text{a}}$ (m <sup>2</sup> /g)	$S_{\text{ext}}^{\text{b}}$ (m <sup>2</sup> /g)	$V_{\text{mic}}^{\text{c}}$ (cm <sup>3</sup> /g)	$V_{\text{tot}}^{\text{d}}$ (cm <sup>3</sup> /g)
TS-1	No	No	390	166	0.0915	0.224
cTS-1	Yes	No	346	225	0.0498	0.478
dTS-1	No	Yes	367	136	0.0981	0.448
cdTS-1	Yes	Yes	353	182	0.0731	0.622

<sup>a</sup> Calculated by the BET method

<sup>b</sup> Calculated by BJH method

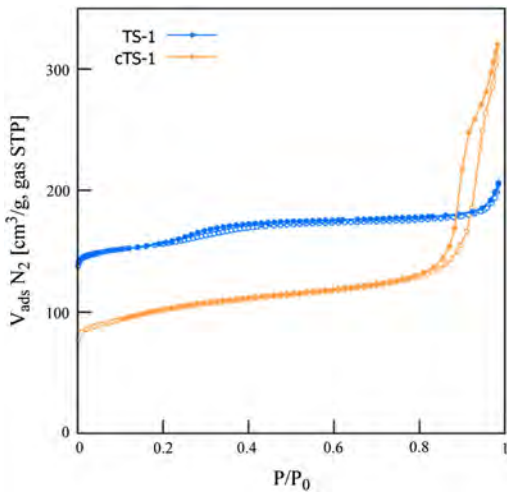
<sup>c</sup> Single point adsorption read at less than around 80 nm width at  $P/P_0 = 0.97$

<sup>d</sup> t-Plot method

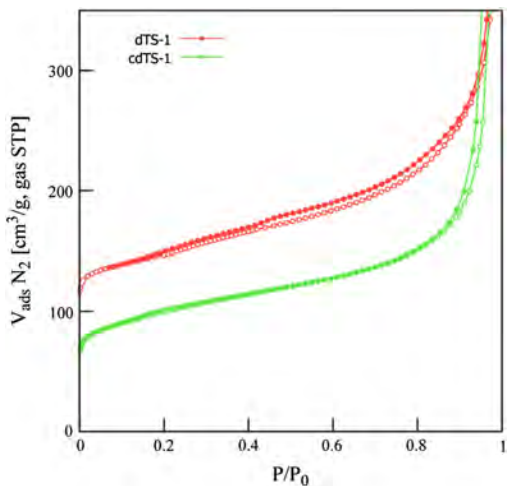
( $V_{\text{mic}}$ ) and total pore volume ( $V_{\text{tot}}$ ) are collated in Table 1. The BET surface area is less for dTS-1 with respect to TS-1 and this tendency is further enhanced for cdTS-1 and cTS-1. As expected, the samples exhibit increasing external surface area after the introduction of mesoporosity. cTS-1 has the highest external surface, dTS-1 somewhat lower, and cdTS-1 curiously has a value which corresponds with the average of cTS-1 and d-TS-1. The same is observed for the micropore volumes.

Figures 3 and 4 show the adsorption–desorption isotherms of the prepared catalysts. According to the IUPAC

classification of physisorption isotherms, the conventional TS-1 has a type I isotherm with a sharp transition in the adsorption branch at  $P/P_0 < 0.1$  and almost no adsorption at intermediate relative pressures. This is typical for purely microporous materials such as zeolites. At  $P/P_0 > 0.9$  further nitrogen uptake takes place due to the interparticle adsorption within the voids formed between the rather small zeolite particles as observed in the SEM analysis for conventional TS-1. In contrast, cTS-1, dTS-1 and cdTS-1 also have some character of type IV isotherms with moderate, but significant hysteresis loops, which is typical for mesoporous materials. The mesoporous samples created by carbon-templating (cTS-1 and cdTS-1) present hysteresis loops at  $P/P_0 > 0.86$  which can be attributed to the interparticle adsorption within the voids formed between the zeolite particles, or more likely due to creation of some very large pores, which would be in line with observation of large, SEM visible porosity in the cTS-1 sample. dTS-1 (and cdTS-1 to a smaller extent) show smaller hysteresis loops closing at  $P/P_0 > 0.42$  with less generation of mesopores compared to micropores. These are effects caused by the well-known, so-called TSE-effect, [22, 23] where capillary evaporation during desorption occurs via a hemispherical meniscus, separating the vapor and the capillary condensed phase [24].

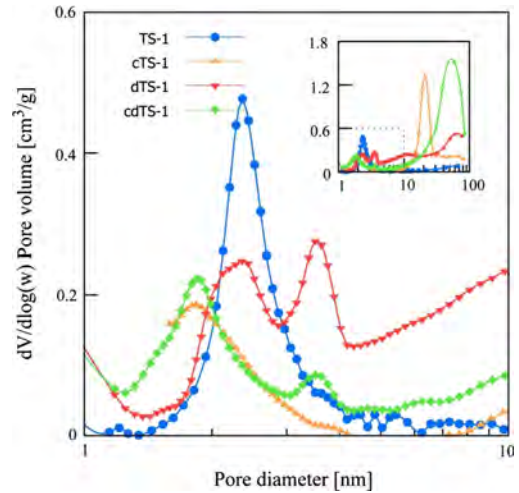


**Fig. 3** Nitrogen adsorption/desorption isotherms of TS-1 and cTS-1, respectively. The isotherm for TS-1 is offset by 50 for illustrative purposes



**Fig. 4** Nitrogen adsorption/desorption isotherms of dTS-1 and cdTS-1, respectively. The isotherm for dTS-1 is offset by 50 for illustrative purposes

Barrett–Joyner–Halenda analyses of desorption branch further indicate secondary mesopore distributions in the TS-1 derived catalysts. This mesoporosity is created at the expense of micropore volume as seen in Table 1, especially for cTS-1 and cdTS-1, and an increase of the external surface compared to the value of TS-1 is observed as mentioned above. Calcination of the carbon-template creates mesopores of around 19 nm in cTS-1, while the



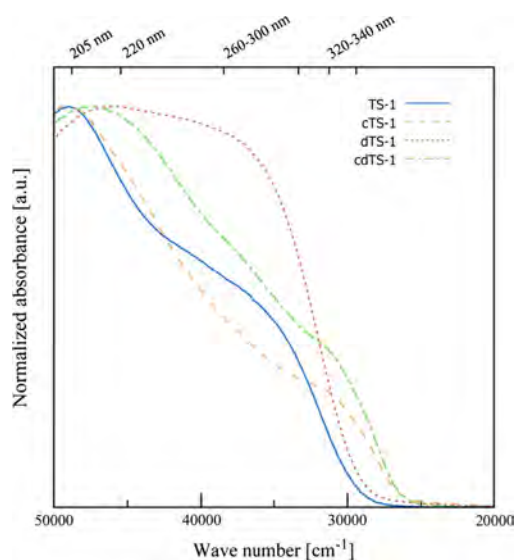
**Fig. 5** BJH pore size distribution from 1 to 10 nm based on the desorption isotherms. The inset shows the pore size distribution from 1 to 100 nm

subsequent desilication creates larger pores of around 60 nm in cdTS-1 (according to IUPAC notation materials with pores > 50 nm are classified as macroporous). The dTS-1 catalyst also exhibits macropores around 60 nm but in less amounts, see Fig. 5.

#### 2.4 UV–Vis diffuse reflectance spectroscopy

The UV–Vis spectrum of TS-1 in Fig. 6 shows a maximum at  $47,600\text{ cm}^{-1}$  (210 nm), which is characteristic for the charge-transfer of oxygen 2p electrons to the empty 3d orbital of Ti in tetrahedrally coordinated  $\text{Ti}(\text{OSi})_4$  species situated in hydrophobic zeolite frameworks. The slight shift to higher wavelengths at ca.  $45,500\text{ cm}^{-1}$  (220 nm) for the desilicated samples suggests the simultaneous presence of tetrahedral tripodal  $\text{Ti}(\text{OSi})_3\text{OH}$  and tetrapodal  $\text{Ti}(\text{OSi})_4$  species, [25] which might be a consequence of an increased surface density of  $\text{Ti}^{4+}$  due to the desilication process. This effect is only appreciable in cdTS-1 and dTS-1 (desilicated structures) and is not seen in cTS-1. Moreover dTS-1 shows a broad band at  $38,400\text{--}33,300\text{ cm}^{-1}$  (260–300 nm), which can be attributed to the partially polymerized hexa-coordinated non-framework Ti species, which contain Ti–O–Ti bonds [26, 27]. This strongly suggests densification of titania species, probably on the outside of the zeolite frameworks.

Furthermore, cTS-1 and cdTS-1 also shows a broad band between  $31,250$  and  $29,400\text{ cm}^{-1}$  (320–340 nm), which is typical for larger extra-framework  $\text{TiO}_2$  particles with a structure similar to anatase. This suggest that the



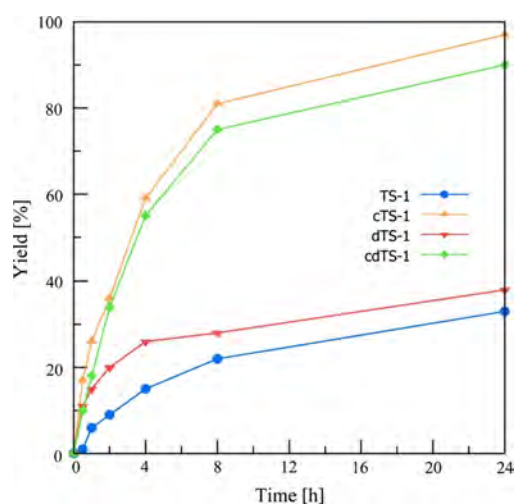
**Fig. 6** Reflectance (pseudo absorbance) UV-Vis spectra of the prepared catalysts

carbon-templating technique might also interfere with the active titania sites to some degree, perhaps by provoking some agglomeration of titania species near the mesopore channels, which could be speculated to occur from the creation of hotspots during the combustion of carbon. In summary, the tetrahedrally coordinated framework Ti species appear to be less affected by the carbon-templating compared to the desilication method.

## 2.5 Catalytic oxidation

Initially, the oxidation of pyridine was used as model reaction to compare the catalytic activity of the prepared TS-1 samples. All catalysts afforded the corresponding *N*-oxide with excellent selectivity (>99 %) and no other by-products were detected by gas chromatography. While TS-1 resulted in 30 % yield after 24 h at 60 °C, cTS-1 resulted in 97 % yield, dTS-1 resulted in 37 % and cdTS-1 resulted in 94 %. For comparison, a ‘blank’ reaction with no added catalyst resulted in 19 % yield under the same reaction conditions, which confirmed that the reaction rate was significantly enhanced in the presence of a catalyst.

The results presented in Fig. 7 show that the introduction of secondary porosity by carbon-templating and desilication significantly increases the catalytic activity. In the

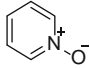
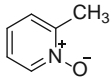
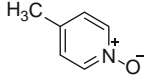
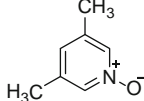


**Fig. 7** Yield of pyridine *N*-oxide at 60 °C using the prepared catalysts

beginning of the reaction the reaction rate was relatively similar for the three catalysts with secondary porosity. However, after 1 h of reaction the activity of dTS-1 decreases, possibly due to pore blocking or deactivation due to the extra-framework Ti species. After 4 h the activity of cdTS-1 is slightly decreased in comparison to cTS-1, which seems to have the most appropriate distribution of pores and Ti active sites.

Table 2 compiles the results from the oxidation of pyridine derivatives with different configuration and size. All examined pyridines, including pyridine, 4-methylpyridine, 2-methylpyridine and 3,5-dimethylpyridine were oxidized to form the corresponding *N*-oxides with more than 99 % selectivity. Pyridine and 4-methylpyridine were the only compounds that were also oxidized in absence of a catalyst. Since the partial negative charge on the N-atom is similar for 2- and 4-methylpyridine we believe that the relatively low yield of 4-methylpyridine may be caused by steric hindrance near the Ti active sites or as a consequence of poor product diffusion. Disregarding any possible electronic substituent effects, the results indicate that the reaction rate is highly dependent on the size and configuration of the substrate. It is noteworthy that the trend in yield with respect to the catalyst is the same for all substrates, i.e. cTS-1 > cdTS-1 > dTS-1 > TS-1, except for 4-methylpyridine where the yield is highest for cTS-1 but more or less the same for cdTS-1, dTS-1 and TS-1.

**Table 2** Yield of *N*-oxides after 24 h at 60 °C using the prepared catalysts

Product	Blank (%)	TS-1 (%)	cTS-1 (%)	dTS-1 (%)	cdTS-1 (%)
	19	30	97	37	94
	0	16	64	33	57
	10	17	23	17	16
	0	4	32	0	27

### 3 Conclusion

In conclusion, we have demonstrated that mesoporous TS-1 prepared by carbon-templating is significantly more active than conventional TS-1 for the oxidation of pyridine derivatives using aqueous hydrogen peroxide as oxidant. Furthermore, we found that the carbon-templated catalyst was more active than macroporous TS-1 prepared by desilication. Nitrogen physisorption and UV-Vis spectroscopy confirmed that carbon-templating is a more gentle and effective method for generating secondary porosity in TS-1. Based on the relatively mild reaction conditions and excellent product selectivity (>99 %) we believe that utilization of carbon-templated mesoporous TS-1 represents a new and environmentally friendly method to synthesize *N*-oxides.

## 4 Experimental section

### 4.1 Materials

Commercial carbon black particles (Black Pearls 2000, Carbot Corporation) with an average particle diameter of 12 nm were used as carbon-templating for the synthesis of mesoporous TS-1. The carbon black particles were dried at 110 °C for 24 h prior to use. All other reagents were of reagent grade and used without further purifications: tetraethylorthosilicate (TEOS, 98 wt%, Aldrich), tetraethylorthotitanate (TEOT, 98 wt%, Aldrich), tetrapropylammonium hydroxide (TPAOH, 40 wt%, Fluka), hydrogen peroxide (H<sub>2</sub>O<sub>2</sub>, 35 wt%, Aldrich), 1,4-dioxane (99.8 %, Aldrich),

pyridine (> 99.8 %, Fluka), 2-methylpyridine (98 %, Aldrich), 4-methylpyridine (98 %, Aldrich), 3,5-dimethylpyridine (> 98 %, Aldrich), ethanol (EtOH, 99 wt%, Aldrich) and deionized water.

### 4.2 Synthesis of conventional TS-1

The conventional TS-1 was prepared by the following procedure: A mixture of TEOS and TEOT (Si/Ti = 100) was added dropwise to a solution of TPAOH and water. The mixture was stirred for 1 h and then transferred to a Teflon-lined stainless steel autoclave (130 ml). The autoclave was heated to 180 °C for 24 h. The autoclave was cooled to room temperature and the material was thoroughly washed with water, filtered by suction and washed again several times (until neutral pH). The material was dried at room temperature overnight and then calcined for 24 h at 550 °C (heating 2 °C/min) to give a fine white product.

### 4.3 Synthesis of cTS-1 by carbon-templating

The cTS-1 catalyst was prepared by the following procedure: Pre-dried carbon black was impregnated to incipient wetness with a solution of TPAOH, water and ethanol. After evaporation of the ethanol (24 h at room temperature), the particles were impregnated with a mixture of TEOS and TEOT (Si/Ti = 100). The impregnated carbon black was put in a Teflon beaker and placed inside a Teflon-lined stainless steel autoclave (130 ml) containing enough water to produce saturated steam (15 ml) and heated to 180 °C for 72 h. The obtained material was washed and calcined following the same procedure as for the synthesis of conventional TS-1 described above.

### 4.4 Synthesis of dTS-1 and cdTS-1 by desilication

TS-1 and cTS-1 was prepared and calcined according to the procedures described above. The catalysts were then treated with a 0.1 M solution of NaOH at 65 °C for 30 min (8 mmol base/g catalyst). The desilicated catalysts were filtrated, washed thoroughly with demineralised water (until neutral pH) and dried at room temperature overnight. The weight of the catalysts was greatly reduced during the desilication.

### 4.5 Characterization

X-ray powder diffraction (XRPD) was measured in transmission mode using Cu-K $\alpha$  radiation from a focusing quartz monochromator and a HUBER G670 Guinier camera.

Nitrogen adsorption and desorption measurements were performed at liquid nitrogen temperature (77 K) on a Micromeritics ASAP 2420. The samples were outgassed in vacuum at 300 °C, 16 h prior to measurement. The (apparent) total surface areas were calculated according to the BET method. Pore size distributions were calculated with BJH method. External surface area, micropore area and micropore volume were determined by t-plot methods in the desorption branch. Total pore volume was calculated for pores around 80 nm width at  $P/P_0 = 0.97$ .

UV–Vis spectra were obtained with a VARIAN/CARY 5000 UV–Vis/NIR spectrophotometer equipped with diffuse reflectance unit (EL04114100), using deuterium (UV) and halogen quartz (Vis/NIR) as light sources and a photomultiplier and cooled PbS as detectors. Spectra were registered from 50,000 to 10,000  $\text{cm}^{-1}$  and obtained directly on the solid powder with no further treatment employing spectralon® as internal standard.

Scanning electron microscopy (SEM) was performed on Quanta 200 ESEM FEG microscope with the samples on a carbon film.

#### 4.6 Standard oxidation procedure

In a typical experiment, amine (5 mmol), dioxane (internal standard, 0.5 mmol), water (5 ml) and 30 mg of catalysts were charged to a reaction tube together with a stirring bar. The reaction tube was closed with a rubber septum and put in a reaction station (Radley Carousel 12 Plus) that provided stirring and heating for several reactions at the same time. The system was heated to 60 °C and the reaction time was started as hydrogen peroxide (7.5 mmol) was added to the reaction. Unless otherwise noted, the reactions were left for 24 h. All oxidations were carried out three times to ensure repeatability.

#### 4.7 Product analysis

During the reactions, samples of 0.1 ml were periodically collected, filtered and analysed by a combined GC-FID and GC–MS from Agilent Technologies Inc. The amounts of substrate and product were quantified using dioxane as internal standard. Products other than the desired *N*-oxides were only observed in negligible amounts. The deviation of the yield of the reactions, was within four percentage point of the presented results.

**Acknowledgments** We gratefully acknowledge the support of the Danish Council for Independent Research, Grant No. 10-093717 and Grant No. 12-127580. We would also like to thank for support from

the Spanish Ministry of Science and Innovation (project CTQ2011-25517), and Unidad de Apoyo from Catalysis Institute (ICP-CSIC).

#### References

1. B. Notari, *Stud. Surf. Sci. Catal.* **37**, 413–425 (1988)
2. M. Padovan, F. Genoni, G. Leofanti, G. Petrini, P. Roffia, A. Cesana, US Patent 4.968.842, (1990)
3. M. Taramasso, G. Perego, B. Notari, US Patent 4.410.501, (1983)
4. G. Bellussi, A. Carati, M. G. Clerici, A. Esposito, R. Millini, F. Buonomo, BE Patent 1.001.038, (1989)
5. D.P. Serrano, L. Hong-Xin, M.E. Davis, *J. Chem. Soc. Chem. Commun.* **10**, 745–747 (1992)
6. A. Cambor, A. Corma, A. Martinez, J. Pérez-Pariente, *Zeolites* **13**, 82–87 (1993)
7. M.A. Cambor, M. Costantini, A. Corma, L. Gilbert, P. Esteve, A. Martinez, S. Valencia, *Chem. Commun.* **11**, 1339–1340 (1996)
8. T. Blasco, M.A. Cambor, A. Corma, P. Esteve, J.M. Guil, A. Martinez, J.A. Perdigón-Melon, S. Valencia, *J. Phys. Chem. B* **102**, 75–88 (1998)
9. C. Perego, A. Carati, P. Ingallina, M.A. Mantegazza, G. Bellussi, *Appl. Catal. A* **221**, 63–72 (2001)
10. C. Madsen, C.J.H. Jacobsen, *Chem. Commun.* 673–674 (1999)
11. J.C. Groen, J.C. Jansen, J.A. Moulijn, J. Perez-Ramirez, *J. Phys. Chem. B* **108**, 13062–13065 (2004)
12. A.H. Janssen, I. Schmidt, C.J.H. Jacobsen, A.J. Koster, K.P. de Jong, *Micropor. Mesopor. Mater.* **65**, 59–75 (2003)
13. Y. Gao, H. Yoshitake, P. Wu, T. Tatsumi, *Micropor. Mesopor. Mater.* **70**, 93–101 (2004)
14. L. Chen, Y.M. Wang, M. He, *Mater. Res. Bull.* **46**, 698–701 (2011)
15. Y. Cheneviere, F. Chieux, V. Caps, A. Tuel, *J. Catal.* **269**, 161–168 (2010)
16. D.P. Serrano, R. Sanz, P. Pizarro, I. Moreno, *Appl. Catal. A* **435**, 32–42 (2012)
17. X. Wang, G. Li, W. Wang, C. Jin, Y. Chen, *Micropor. Mesopor. Mat.* **142**, 494–502 (2011)
18. Y. Fang, H. Hu, *Catal. Commun.* **8**, 817–820 (2007)
19. M.J. Verhoeft, P.J. Kooyman, J.C. Van der Waal, M.S. Rigutto, J.A. Peters, H. Van Bekkum, *Chem. Mater.* **13**, 683–687 (2001)
20. D. Trong On, S. Kaliaguine, *Angew. Chem. Int. Ed.* **41**, 1036–1040 (2002)
21. K. Johannsen, A. Boisen, M. Brorson, I. Schmidt, C.J.H. Jacobsen, *Stud. Surf. Sci. Catal.* **142**, 109–115 (2002)
22. O. Kadlec, M.M. Dubinin, *J. Colloid Interface Sci.* **31**, 479–489 (1969)
23. C.V.G. Burgess, D.H. Everett, *J. Colloid Interface Sci.* **33**, 611–614 (1970)
24. J.C. Groen, L.A.A. Peffer, J. Pérez-Ramírez, *Micropor. Mesopor. Mat.* **60**, 1–17 (2003)
25. P. Ratnasamy, D. Srinivas, H. Knözinger, *Adv. Catal.* **48**, 1–169 (2004)
26. G. Petrini, A. Cesana, G. De Alberti, F. Genoni, G. Leofanti, M. Padovan, G. Paparatto, P. Rofia, *Stud. Surf. Sci. Catal.* **68**, 761–766 (1991)
27. M. Bandyopadhyay, A. Birkner, M.W.E. Van den Berg, K.V. Klementiev, W. Schmidt, W. Grunert, H. Gies, *Chem. Mater.* **17**, 3820–3829 (2005)





# Oxidation of Bioethanol using Zeolite Encapsulated Gold Nanoparticles

Jerrik Mielby<sup>[a]</sup>, Jacob Oskar Abildstrøm<sup>[a]</sup>, Feng Wang<sup>[b]</sup>, Takeshi Kasama<sup>[c]</sup>, Claudia Weidenthaler<sup>[b]</sup> and Søren Kegnæs<sup>[a]\*</sup>

**Abstract:** With the on-going developments in biomass conversion, the oxidation of bioethanol to acetaldehyde may become a favorable and green alternative to the ethylene route. Here, we report a simple and effective method to encapsulate gold nanoparticles in zeolite silicalite-1 and demonstrate their high activity and selectivity for the catalytic gas-phase oxidation of ethanol. The zeolites are modified by a recrystallization process, which creates intra-particle voids and mesopores that facilitate the formation of small and disperse nanoparticles upon simple impregnation. The individual zeolite crystals comprise a broad range of mesopores and contain up to several hundred 2-3 nm gold nanoparticles that are distributed inside the zeolites rather than on the outer surface. The encapsulated nanoparticles have good stability and result in 50% conversion with 98% selectivity to acetaldehyde at 200°C, which (under the given reaction conditions) corresponds to 617 mmol acetaldehyde/mmol Au hour<sup>-1</sup>.

As a consequence of the continuing depletion of fossil resources, the future chemical industry must gradually rely on renewable resources such as biomass to produce bulk and fine chemicals. Bioethanol, which is primarily used as fuel or fuel additive, is already produced from biomass and reached a production of 114 billion liters in 2013 [1,2]. Crude bioethanol is produced by fermentation and contains up to 90% water which typically has to be removed before use [3]. The production of anhydrous bioethanol is a relatively energy demanding process and it has therefore been suggested that bioethanol could be converted into higher value-added chemicals via reactions that are not sensitive to the water content [4]. For instance, bioethanol can be used as a renewable resource for H<sub>2</sub> production by catalytic steam reforming [5] or for production of acetaldehyde [6], acetic acid [7] or ethyl acetate [8] by selective oxidation or dehydrogenation [9,10]. Currently, the main production of acetaldehyde is based on the oxidation of ethylene using a homogeneous catalytic system comprised of PdCl<sub>2</sub> and CuCl<sub>2</sub> (the Wacker process). As the cost of bioethanol is expected to decrease due to the technological developments in biomass processing, it seems likely that converting bioethanol to acetaldehyde may become a favorable and green alternative to the ethylene route.

Since the first report on the high catalytic activity for low-temperature CO oxidation [11], supported gold nanoparticles have been used for a number of reactions in organic chemistry. In particular, supported gold nanoparticles are highly active and selective catalysts for the aerobic oxidation of alcohols, including ethanol, in both liquid [4,7] and gas-phase [12,13]. Although the intimate mechanistic details are still not fully understood, it is generally accepted that several factors contribute to the high catalytic activity. In particular, the gold nanoparticles must typically be less than 10 nm in diameter, so that under-coordinated, reactive gold atoms exist in large numbers at the edges and corners of the particles [14]. However, like other metal catalysts, supported gold nanoparticles are prone to sintering, a thermal deactivation caused by Ostwald ripening or particle migration and coalescence [15]. The stability may be improved by tuning the catalyst composition and metal-support interactions [16] or by optimizing the three-dimensional distribution of the nanoparticles in ordered mesoporous materials [17]. Furthermore, highly stable catalysts have been achieved by encapsulation of individual nanoparticles in porous inorganic shells [18]. In 2010, Laursen *et al.* [19] reported the encapsulation of colloidal gold nanoparticles in zeolites during crystallization and recently Li *et al.* [20] reported the synthesis of single gold nanoparticles in hollow zeolites prepared by recrystallization in tetrapropylammonium hydroxide (TPAOH). The researches demonstrated that the zeolite encapsulated metal nanoparticles were extraordinary size-selective [21] and even remained active after calcination at high temperatures. Although encapsulation of single-nanoparticles is an effective and elegant concept, bottom-up approaches often require complex procedures and expensive additives that may prevent large-scale production.

Here, we report a simple and effective method to encapsulate gold nanoparticles in mesoporous silicalite-1 (Au/Recryst-S1) and demonstrate their high stability, catalytic activity and selectivity for the gas-phase oxidation of bioethanol to acetaldehyde. The preparation of Au/Recryst-S1 was based on impregnation of recrystallized silicalite-1 prepared by an alkaline dissolution-reassembly process in the presence of a surfactant. The alkaline dissolution was performed in an aqueous solution of ammonium hydroxide and cetyltrimethylammonium bromide (CTAB) and the reassembly was performed in an autoclave under hydrothermal conditions (see supporting information). Based on the detailed mechanism recently reported by Ivanova *et al.* [22,23], we propose that the alkaline dissolution breaks Si-O-Si bond inside the zeolite, which causes the formation of intra-particle voids and mesopores. At this stage the surfactant protects the zeolite from non-uniform leaching, which may result in the formation of large meso- and macropores [24,25]. Furthermore, the surfactant may diffuse into the zeolite where it can form micelles and serve as template for the condensation of extracted siliceous species during the hydrothermal reassembly [22]. The recrystallized zeolite is

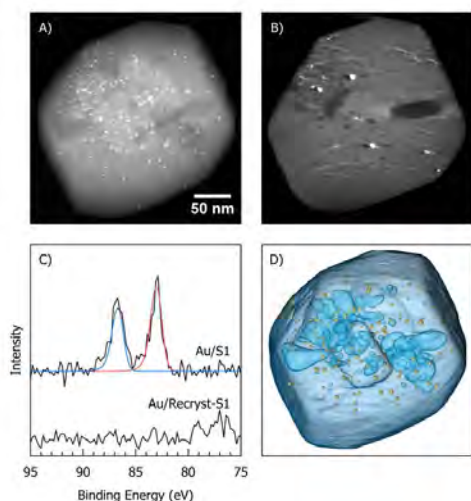
[a] J. Mielby, J. O. Abildstrøm and Assoc. Prof. Søren Kegnæs  
Department of Chemistry  
Technical University of Denmark  
Kgs. Lyngby, Denmark  
E-mail: skk@kemi.dtu.dk

[b] Dr. F. Wang and Dr. C. Weidenthaler  
Max-Planck-Institut für Kohlenforschung  
Mülheim an der Ruhr, Germany

[c] Dr. T. Kasama  
Center for Electron Nanoscopy  
Technical University of Denmark  
Kgs. Lyngby, Denmark

calcined in air to remove the surfactant, dried under vacuum and then impregnated with an aqueous solution of  $\text{HAuCl}_4$  which fills up the voids and mesopores. As the material is dried and then reduced under hydrogen, the confined space of the zeolite framework provide ideal conditions for the preparation of small and disperse gold nanoparticles inside the zeolite crystals [22,23].

Initially, the Au/Recryst-S1 catalyst was characterized by X-ray photoelectron spectroscopy (XPS). Compared to a conventional silicalite-1 catalyst with gold nanoparticles situated on the surface (Au/S1), we observed no signal at the Au  $4f_{7/2}$  level for the recrystallized catalyst, see Figure 1. Since XPS is a surface-sensitive analysis, the absence of gold photopeaks indicated that the gold was deposited inside the silicalite-1 crystals rather than on the outer surface.



**Figure 1.** A) STEM image of Au/Recryst-S1. B) Reconstructed cross-section of Au/Recryst-S1. C) XPS spectrum of the Au  $4f_{7/2}$  level of Au/S-1 and Au/Recryst-S1, respectively. D) 3D model of Au/Recryst-S1.

Scanning transmission electron microscopy (STEM) provided more detailed information about the exact situation and size distribution of the gold nanoparticles. Electron tomography was performed by collecting STEM images at incremental degrees of rotation around the center of the zeolite crystal shown in Figure 1A. Alignment and tomographic reconstruction of the collected images confirmed that the gold nanoparticles were situated inside the zeolite (See Figure 1B, Supporting Movie1). The gold nanoparticles were 2-3 nm in diameter and only a small fraction of the particles were situated on the surface of the zeolite. Furthermore, the tomographic reconstruction provided a unique insight into the voids and mesopores that were formed during the recrystallization process. Although there were no clear correlation between the distribution of nanoparticles and the internal mesopores, the observed porosity

was in good agreement with the  $\text{N}_2$  physisorption isotherm, which showed a typical H4 hysteresis loop that was nearly parallel at  $P/P_0 > 0.45$  (see supporting information). Figure 1D and supporting Movie 2 and 3 show a 3D reconstruction of the Au/Recryst-S1 catalyst.

In order to investigate the effect of the zeolite support, the catalytic activity of Au/Recryst-S1 was compared to three other gold silicalite-1 catalysts. The first catalyst was prepared by impregnation of pure silicalite-1 followed by drying and reduction (Au/S1). The second catalyst was prepared by impregnation of a carbon-templated mesoporous silicalite-1 (Au/Meso-S1) following the method developed by Jacobsen *et al.* [26]. It has previously been demonstrated that carbon-templating is an effective method to synthesize mesoporous zeolites and that the additional system of mesopores can increase the external surface area [27] and help to overcome diffusion limitations [28,29]. The third catalyst was prepared by impregnation of Silicalite-1 modified with 3-aminopropyl trimethoxysilane (APS) in refluxing toluene (Au/APS-S1). The surface modification was performed in order to improve the gold/support interaction [30] and assist the formation of small and disperse nanoparticles. Detailed synthetic procedures and characterization by X-ray powder diffraction, XPS, TEM and  $\text{N}_2$  physisorption analysis is described in the Supporting Information. An overview of the investigated catalysts is shown in Table 1.

**Table 1.** Overview of the investigated catalysts.

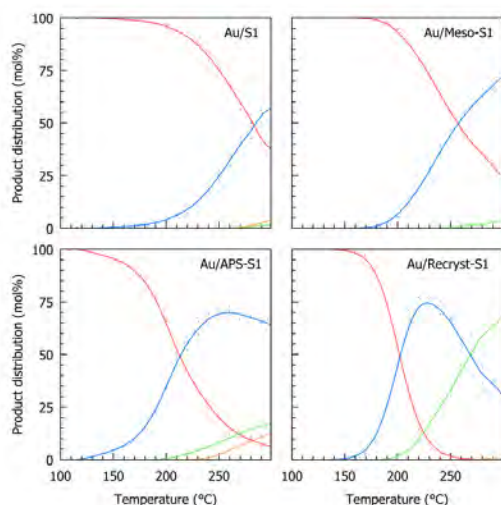
Catalyst	Nanoparticle size <sup>[a]</sup> (nm)	$S_{\text{ext}}^{\text{[b]}}$ ( $\text{m}^2/\text{g}$ )	$V_{\text{micro}}^{\text{[b]}}$ ( $\text{cm}^3/\text{g}$ )	$V_{\text{tot}}^{\text{[c]}}$ ( $\text{cm}^3/\text{g}$ )
1 wt% Au/S1	4.3±1.7	65	0.116	0.192
1 wt% Au/Meso-S1	3.3±1.4	139	0.100	0.304
1 wt% Au/APS-S1	2.4±0.7	80	0.118	0.201
1 wt% Au/Recryst-S1	2.6±0.5	102	0.124	0.232

[a] Average size based on measurements of ~250 particles by TEM. [b] Calculated by the t-plot method. [c] Determined from the isotherm adsorption branch at around  $P/P_0 = 0.95$ .

In a typical experiment, an aqueous solution of 10% ethanol was pumped into a evaporator together with He and atmospheric air corresponding to a molar ratio of  $\text{O}_2/\text{ethanol} = 1$ . The reactant gas was then passed through a fixed-bed reactor containing 100 mg fractionated catalyst. The reaction products were analyzed by an online GC-FID, while CO and  $\text{CO}_2$  were analyzed by an online NDIR detector.

Figure 2 shows the product distribution as function of the reaction temperature for the investigated catalysts. All catalyst was impregnated with 1 wt% Au, which allowed a direct comparison of the catalytic activity. The Au/S1 catalyst was highly selective towards acetaldehyde and reached 50% conversion at 280°C. The Au/Meso-S1 catalyst was more active and reached 50% conversion at 250°C. Only small amounts of  $\text{CO}_2$  and acetic acid were observed at temperatures above

250°C. The slightly higher activity of Au/Meso-S1 may be related to the increased external surface area, which results in a better dispersion of the Au nanoparticles [27]. The surface functionalized Au/APS-S1 catalyst was more active than both Au/S1 and Au/Meso-S1 and reached 50% conversion at 210°C. At temperatures above 240°C, however, the catalyst resulted in large amounts of acetic acid and CO<sub>2</sub>, which significantly decreased the acetaldehyde yield. Au/Recryst-S1 was the most active catalyst and reached 50% conversion with 98% selectivity to acetaldehyde at 200°C. Above 200°C, the selectivity to acetaldehyde started to decrease due to formation of acetic acid. At 270°C both acetaldehyde and acetic acid was formed in 50% yield. Surprisingly, no CO<sub>2</sub> was formed even at 300°C. The Au/Recryst-S1 catalysts also showed good stability and even after 100 h of reaction at 200°C the Au/Recryst-S1 was still far more active than a commercial Au/TiO<sub>2</sub> catalyst (see supporting information).



**Figure 1.** Product distribution of ethanol (red), acetaldehyde (blue), acetic acid (green) and CO<sub>2</sub> (orange) as function of the reaction temperature.

SiO<sub>2</sub> has often been described as an inert support because it does not contribute to the supply and activation of oxygen as opposed to reducible metal oxides such as TiO<sub>2</sub>, CeO<sub>2</sub> or Fe<sub>2</sub>O<sub>3</sub> [31]. This does not mean that Au/SiO<sub>2</sub> (here in the form of silicalite-1) cannot be active, but that high catalytic activity requires very small Au nanoparticles with a high number of metal-support interfacial sites. It has previously been suggested that these sites may provide hydroxyl groups that promote the reaction rate, presumably by participating in the reaction mechanism [32,33]. Our results demonstrate the importance of considering not only the size of the gold nanoparticles and the nature of the support material, but also the three-dimensional distribution and the structure of the gold-support interfacial sites.

In conclusion, we have developed a simple and effective method to encapsulate Au nanoparticles in recrystallized silicalite-1. The method is cost-effective, practical and results in a narrow size distribution of small nanoparticles that are situated inside the zeolite crystals, but remain readily accessible through the inherent microporous structure. The encapsulated nanoparticles were demonstrated to be highly active and selective for the catalytic gas-phase oxidation of ethanol to acetaldehyde. We therefore hope that impregnation of recrystallized zeolites will become a helpful tool in the development of many new nanostructured materials with unprecedented catalytic, magnetic and optical properties.

## Experimental Section

The detailed synthesis and characterization of all investigated catalysts by X-ray powder diffraction, XPS, TEM and N<sub>2</sub> physisorption analysis is given in the Supporting Information.

### Synthesis of 1 wt% Au/Recryst-S1

Tetraethyl orthosilicate (4.465 ml) was added dropwise to a tetrapropylammonium hydroxide solution (1.0 M, 7.265 ml) under stirring in a Teflon beaker. The mixture was stirred for 1 hour and then heated in a Teflon-lined stainless steel autoclave at 180°C for 24 h under autogeneous pressure. The product was collected by filtration, washed with water, dried at room temperature and then calcined for 20 hours at 550°C. The product silicalite-1 (1.0 g) was added to a solution of cetyl trimethylammonium bromide (0.7 g) in aqueous ammonium hydroxide (100 ml, 2.5 wt%) and stirred for 3 hours at room temperature. The solution was then transferred to a Teflon-lined stainless steel autoclave and heated to 140°C for 24 hours. The product was collected by filtration, washed with water, dried overnight and then calcined at 550°C for 5 hours to remove the surfactant. The recrystallized silicalite-1 (0.9900 g) was pre-dried in a vacuum oven at 50°C and then impregnated with an aqueous solution of HAuCl<sub>4</sub>·3H<sub>2</sub>O (0.0199 g) to incipient wetness. The material was dried at room temperature overnight and then reduced in Formier gas for 2h at 350°C to give the final gold catalyst.

### Gas-phase oxidation of ethanol

An aqueous solution of 10% ethanol (0.05 ml/min) was pumped into an evaporator at 165 °C together with air (12.4ml/min) and He (37.6 ml/min), which corresponded to a molar ratio of O<sub>2</sub>/ethanol=1. The preheated gas was then passed through a 3 mm stainless steel fixed-bed reactor containing 100 mg fractionated catalyst diluted with 100 mg of fractionated quartz (180-355 μm). The weight hourly space velocity was around 2.95 g ethanol/g catalyst h<sup>-1</sup>. The product gas was periodically analyzed every 12 min by an online GC-FID equipped with a standard non-polar column. All products were identified from gas samples by GC-MS and by the retention time of authentic samples on the online GC-FID. CO and CO<sub>2</sub> were detected by an online NDIR detector. All catalysts were tested under the same reaction conditions using a pre-programmed temperature profile from 110-300°C increasing in 10°C steps every hour to insure measurements at near steady state conditions.

## Acknowledgements

The authors gratefully acknowledge the support of the Danish Council for Independent Research, Grant No. 12-127580.

**Keywords:** encapsulated gold nanoparticles • zeolite • catalytic oxidation • bioethanol • acetaldehyde

- [1] OECD-FAO Agricultural Outlook 2013, OECD Publishing (2013); DOI: 10.1787/agr\_outlook-2013-en.
- [2] J. Goldemberg, *Science* **2007**, 315, 808.
- [3] S. Kumar, N. Singh, R. Prasad, *Renew. Sust. Energ. Rev.* **2010**, 14, 1830.
- [4] B. Jørgensen, S. E. Christiansen, M. L. D. Thomsen and C. H. Christensen, *J. Catal.* **2007**, 251, 332.
- [5] G. A. Deluga, J. R. Salge, L. D. Schmidt and E. E. Verykios, *Science* **2004**, 303, 933.
- [6] Y. Guan and E. J. M. Hensen, *J. Catal.* **2013**, 305, 135.
- [7] C. H. Christensen, B. Jørgensen, J. Rass-Hansen, K. Egeblad, R. Madsen, S. K. Klitgaard, S. M. Hansen, M. R. Hansen, H. C. Andersen and A. Rissager, *Angew. Chem.* **2006**, 45, 4648.
- [8] M. Nielsen, H. Junge, A. Kammer and M. Beller, *Angew. Chem.* **2012**, 51, 5711.
- [9] M. Murdoch, G. I. N. Waterhouse, M. A. Nadeem, J. B. Metson, M. A. Keane, R. F. Howe, J. Llorca and H. Idriss, *Nature Chem.* **2011**, 3, 489.
- [10] T. Takei, N. Iguchi and M. Haruta, *Catal. Surv. Asia* 2011, 15, 80.
- [11] M. Haruta, N. Yamada, T. Kobayashi, S. Iijima, *J. Catal.* 1989, 115, 301.
- [12] A. Simakova, V. I. Sobolev, K. Y. Koltunov, B. Campo, A.-R. Leino, K. Kordás and D. Y. Murzin, *ChemCatChem* **2010**, 2, 1535.
- [13] V. I. Sobolev, K. Yu. Koltunov, O. A. Simakova, A.-R. Leino and D. Y. Murzin, *Appl. Catal. A* **2012**, 433, 88.
- [14] N. Lopez, T. V. W. Janssens, B. S. Clausen, Y. Xu, M. Mavrikakis, T. Bligaard and J. K. Nørskov, *J. Catal.* **2004**, 223, 232.
- [15] T. W. Hansen, A. T. DeLaRiva, S. R. Challa and A. K. Datya, *Acc. Chem. Res.* **2013**, 46, 1720.
- [16] J. A. Farmer and C. T. Campbell, *Science* **2010**, 329, 933.  
17 G. Prieto, J. Zečević, H. Friedrich, K. P. de Jong and P. E. de Jong, *Nature Mater.* **2013**, 12, 34.
- [18] P. M. Arnal, M. Comotti and F. Schüth, *Angew. Chem.* **2006**, 118, 8404.
- [19] A. B. Laursen, K. T. Højholt, L. F. Lundegaard, S. B. Simonsen, S. Helveg, F. Schüth, M. Paul, J.-D. Grunwald, S. Kegnæs, C. H. Christensen and K. Egeblad, *Angew. Chem.* **2010**, 122, 3582.
- [20] S. Li, L. Burel, C. Aquino, A. Tuel, F. Morfin, J.-L. Rousset and D. Farrusseng, *Chem. Commun.* **2013**, 49, 8507.
- [21] S. Li, L. Burel, T. Boucheron, A. Tuel, D. Farrusseng and F. Meunier, *Chem. Commun.* **2014**, 50, 1824.
- [22] I. I. Ivanova and E. Knyazeva, *Chem. Soc. Rev.* **2013**, 42, 3671.
- [23] I. I. Ivanova, I. A. Kasyanov, A. A. Maerle and V. I. Zaikovskii, *Microporous Mesoporous Mater.* **2014**, 189, 163.
- [24] Y. P. Khidev, I. I. Ivanova, Y. G. Kolyagin, O. A. Ponomareva, *Appl. Catal.* **2012**, 441-442, 124.
- [25] V. V. Ordonsky, I. I. Ivanova, E. E. Knyazeva, V. V. Yuschenko and V. I. Zaikovskii, *J. Catal.* **2012**, 295, 207.
- [26] K. Johannsen, A. Boisen, M. Brorson, I. Schmidt and C. J. H. Jacobsen, *Stud. Surf. Sci. Catal.* **2002**, 142, 109.
- [27] C. H. Cristensen, I. Schmidt, A. Carlsson, K. Johannsen and K. Herbst, *J. Am. Chem. Soc.* **2005**, 127, 8098.
- [28] I. Schmidt, A. Krogh, K. Wienberg, A. Carlsson, M. Brorson and C. J. H. Jacobsen, *Chem. Commun.* **2000**, 2157.
- [29] J. Mielby, J. O. Abildstrøm, Susana Pérez-Ferreras, S. B. Rasmussen and S. Kegnæs, *J. Porous Mater.* **2014**; DOI: 10.1007/s10934-014-9800-0
- [30] L. M. Liz-Marzán, M. Giersig and P. Mulvaney, *Langmuir* **1996**, 12, 4329.
- [31] M. M. Schubert, S. Hackenberg, A. C. van Veen, M. Muhler, V. Plzak and R. J. Behm, *J. Catal.* **2001**, 197, 113.
- [32] B. N. Zope, D. D. Hibbitts, M. Neurock and R. J. Davis, *Science* **2010**, 330, 74.
- [33] M. S. Ide and R. J. Davis, *Acc. Chem. Res.*; DOI: 10.1021/ar400190